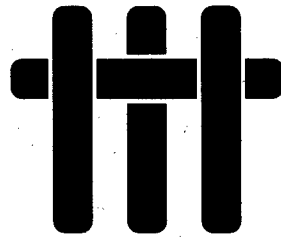


FINAL REPORT

University Research Initiative

Contract No.: N00014-92-J-1808

May 1996 - September 1997



Mechanism-Based Design for High-Temperature, High-Performance Composites

by

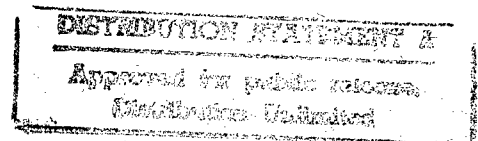
A.G. Evans & F.A. Leckie
University of California,
Santa Barbara, CA

and

J.W. Hutchinson
Harvard University,
Cambridge, MA

Cambridge University
Harvard University
Washington State University
University of Pennsylvania
University of Virginia

19980721 082



DTIC QUALITY INSPECTED 8

UNIVERSITY OF CALIFORNIA, SANTA BARBARA

BERKELEY • DAVIS • IRVINE • LOS ANGELES • RIVERSIDE • SAN DIEGO • SAN FRANCISCO



SANTA BARBARA • SANTA CRUZ

MATERIALS DEPARTMENT
COLLEGE OF ENGINEERING

SANTA BARBARA, CALIFORNIA 93106-5050
FAX (805) 893-8486

June 15, 1998

Defense Technical Information Center
Building 5, Cameron Station
Alexandria, VA 22304-6145

Re: University Research Initiative Final Report

Please find enclosed the Final Report for the University Research Initiative, entitled "Mechanism-Based Design for High-Temperature, High-Performance Composites," Contract No.: N00014-92-J-1808. We appreciate the support of DARPA and ONR for the performance of this research and the opportunity this program gave us to develop a truly collaborative team on this important subject.

Yours sincerely,

A handwritten signature in cursive script, reading "F A Leckie".

Frederick A. Leckie
Professor

2:(Lt)URI/mef

REPORT DOCUMENTATION PAGE			Form Approved OMB No. 0705-0188	
1. AGENCY USE ONLY (Leave blank)		2. REPORT DATE 980529	3. REPORT TYPE AND DATES COVERED FINAL REPORT 960501 TO 970930	
4. TITLE AND SUBTITLE Mechanism-Based Design for High Temperature/High Performance Composites			5. FUNDING NUMBERS N00014-92-J-1808	
6. AUTHOR(S) Evans, Anthony G. Leckie, Frederick A. Hutchinson, J.W.				
7. PERFORMING ORGANIZATION NAME(S) AND ADDRESS(ES) MATERIALS DEPARTMENT COLLEGE OF ENGINEERING UNIVERSITY OF CALIFORNIA SANTA BARBARA, CA 93106-5050			8. PERFORMING ORGANIZATION REPORT NUMBER	
9. SPONSORING/MONITORING AGENCY NAME(S) AND ADDRESS(ES) SCIENTIFIC OFFICE CODE: 1131N STEVEN G. FISHMAN OFFICE OF NAVAL RESEARCH 800 NORTH QUINCY STREET ARLINGTON, VIRGINIA 22217-5000			10. SPONSORING/MONITORING AGENCY REPORT NUMBER	
11. SUPPLEMENTARY NOTES				
12A. DISTRIBUTION/AVAILABILITY STATEMENT See Distribution List			12B. DISTRIBUTION CODE	
13. ABSTRACT (Maximum 200 words) The Final Report of the University Research Initiative project at UCSB on Mechanism-Based Design for High Temperature/High Performance Composites consists of four books. The books are entitled as follows: <u>1-Constituent Properties and Macroscopic Performance of CMC - I;</u> <u>2-Constituent Properties and Macroscopic Performance of CMC - II;</u> <u>3A-Constituent Properties and Macroscopic Performance of MMC, 3B-Constitutive Laws and Design;</u> <u>4-Measurement and Micro-Mechanisms</u>				
14. SUBJECT TERMS Ceramic Matrix Composites, Metal Matrix Composites, Design, Notch Strengths, Constitutive Laws, Measurement Techniques, Processing, Damage, Fatigue, Creep			15. NUMBER OF PAGES 1308	
			16. PRICE CODE	
17. SECURITY CLASSIFICATION OF REPORT UNCLASSIFIED	18. SECURITY CLASSIFICATION OF THIS PAGE UNCLASSIFIED	19. SECURITY CLASSIFICATION OF ABSTRACT UNCLASSIFIED	20. LIMITATION OF ABSTRACT	

**SUMMARY
OF
TABLE OF CONTENTS**

EXECUTIVE SUMMARY

BOOK 1: CONSTITUENT PROPERTIES AND MACROSCOPIC PERFORMANCE OF CMC - I

BOOK 2: CONSTITUENT PROPERTIES AND MACROSCOPIC PERFORMANCE OF CMC - II

BOOK 3:

Section A: CONSTITUENT PROPERTIES AND MACROSCOPIC PERFORMANCE OF MMC

Section B: CONSTITUTIVE LAWS AND DESIGN

BOOK 4: MEASUREMENT AND MICRO-MECHANISMS

Executive Summary

1. OBJECTIVE OF THE INITIATIVE

The objective of the program was to develop methodologies for implementing Metal Matrix (MMC) and Ceramic Matrix (CMC) composite materials that improve the efficiency of gas/aero-engines and reduce their environmental impact. These materials can operate at high temperatures and have the high strength to weight ratios which make them attractive candidates.

Development based on try and test methods is expensive and knowledge gained in this way can be quickly overcome by advancements in new materials and processes. The approach taken in this initiative was to demonstrate how the mechanisms which determine the properties of MMCs and CMCs can be related to both the manufacture and design of aero-engines. In this way the knowledge base and the design procedures provide a permanent framework which can accommodate advances in new materials and design concepts.

2. GENERAL STRATEGY

The overall program embraced property profiles, manufacturing, design and sensor development (Fig. 1) consistent with a concurrent engineering philosophy. For this purpose, the program has created networks with the other national composites activities. Research on MMCs was strongly coupled with the 3M Model Factory. Major links with Corning, SEP and Westinghouse were established for CMC manufacturing. *Design Team* activities were coordinated by exchange visits annually in February/March to Pratt and Whitney, General Electric, McDonnell Douglas and Corning. These visits served as a critique of the research plan, as a means of disseminating the knowledge and defining the research program for the next year.

The program strategy concerned with design attempted to provide a balance of effort between *properties and design* by conducting studies of mechanisms and property profiles, which intersect with a focused activity devoted to design problems (Fig. 2). The latter includes two foci, one on MMCs and one on CMCs. Each reflects differences in the property emphases required for design. The intersections with the

mechanism studies ensured that commonalties in behavior were identified, and facilitated the efficient transfer of models between MMCs and CMCs.

To foster the concurrent engineering philosophy, weekly seminars were organized at UCSB throughout the year, attended by all members of the team. Design group leaders presented regular status seminars.

Representatives from industry and members of the internal and external academic teams would meet annually for ten days at the beginning of each year. These meetings were organized so that mornings were devoted to formal presentations from industrial and academic participants. Afternoons were used to discuss topics which emerged from the formal presentations. Input from these sessions and from visits to industry determined the program for the following year.

3. ACHIEVEMENTS

Collaboration with industrial participants was crucial in identifying those components for which the introduction of MMC and CMC would improve engine performance. The importance of knowledge transfer became very evident and that suitable software was more efficient in this respect than were detailed reports. Addressing this problem has been a key contribution to the success of the program. Reference to this particular effort is made in the achievement summary.

3.1 The Bridging Mechanism

The presence of cracks in composite materials is inevitable for a number of reasons. Pre-existing cracks are introduced during the manufacturing process. Upon application of sufficient stress, matrix cracks form in CMCs, which have a brittle matrix. In MMCs cracks form by fatigue. Irrespective of their source, the bridging effects of fibers is the underlying mechanism which ensures the integrity of the system in the presence of cracks. The bridging mechanism is one of the basic concepts needed to appreciate the behavior of composite materials in terms of strength, fatigue and the ability to redistribute stress concentrations.

3.2 Global Load Sharing

The strength of composite materials in the direction of the fibers is dependent on the statistical strength of the fibers and the interface properties between the fiber and matrix. An important concept known as Global Load Sharing demonstrates the

conditions under which a fiber breaks when the load is transferred safely to its neighbors without catastrophic failure. Global Load Sharing provides an optimum measure against which the performance of fibrous systems can be judged, and has proven to be an essential concept in judging structural safety.

3.3 Software for Metal Matrix Composites

The properties of MMCs under the multi-axial states of stress occurring in practice depend on the statistical strength of the fibers, the elastic/plastic properties of the matrix and the strength of the fiber/matrix interface. It has been demonstrated that the complex behavior can be readily described by combining knowledge of the mechanisms with the results of a small number of discriminatory material tests. Software has been developed for the finite element ABAQUS system which can be used to predict the performance of complex components. Calculations have been performed on components identified by industry, such as a rotating bladed ring used in engine compressors, rods for exhaust panel control and in panels joined by bolted connections. Parametric studies illustrate the importance of the anisotropic properties of the composite and how they can be used to advantage in design.

3.4 Software for Ceramic/Matrix Composites

In contrast to metal matrix composites, for which the matrix is ductile, ceramic matrix composites have a brittle matrix which cracks when it reaches the so-called "matrix cracking stress". In spite of the constituent parts of CMCs being brittle, their interplay through the interface and fiber-bridging result in materials which demonstrate characteristics similar in some respects to those of ductile materials. For example, tests have demonstrated the ability of CMCs to redistribute stress concentrations to beneficial effect. Consequently, the holes and intersections which occur in practice can sustain loads several times those suggested by conventional elastic analysis. To take advantage of this characteristic quantitatively in design, constitutive equations have been developed which can be used in a finite element package. The finite element package is available as a UMAT routine or as a "hook" on the C-Stem system supported by General Electric together with NASA. Application of the finite element calculations demonstrate the degree of stress redistribution which occurs in panels penetrated by holes in combustor liners and in components subjected to bending induced by thermal loading.

Because the constitutive equations are mechanism-based, extension to include the effects of fatigue and creep are readily achieved. Fatigue and creep are also included in a UMAT routine of ABAQUS and as a "hook" in the C-Stem system.

3.5 Software for Technology Transfer

Detailed studies of the work carried out in 1992-1997 are available in the annual reports. It was quickly realized the amount of information is so extensive that effective communication with industry by means of reports and meetings is insufficient. It was described earlier how software has been introduced into ABAQUS and C-Stem for application in analysis. This software is essential for detailed design, but does not address the problem of transmitting those basic concepts which provide the core understanding essential for product development.

Two approaches have been developed. One approach which has proven to be very powerful is the Material Selector Software developed by Professor Ashby. It has been shown how material selection can be made systematic by the use of Design Indices which relate combinations of material properties to design function. The software produced is an excellent example of concurrent engineering which draws together very quickly concepts used at the early stages in design. The second approach was to use hypertext languages in which concepts such as bridging could be explained and the material data drawn together to perform design calculations. The hypertext format allows the designer to guide themselves through a learning process and at the same time provide the results of design calculations. The software was developed using Hypercard before the Web was generally available, which represents an obvious extension for future work.

3.6 Joining and Attachments

The strength/weight advantage of composite materials can be lost if attachments which join one component to another are not well designed. The complex geometry of joints can introduce additional failure mechanisms whose effects must be appreciated. Joints in metal matrix composites are usually accomplished by using a cladding of the matrix material. A test program has been completed on a variety of cladding geometries to determine their affect on the strength and fatigue properties of the joints. Failure maps have been produced which can be used directly in design.

Complex geometries have also been studied for joining CMCs. To simulate a circumstance commonly occurring in practice, tension panels perforated by holes (with or without pins) have been tested. Another geometry which is convenient and inexpensive consists of two straight panels bonded together by a circular panel. This design is vulnerable to failure by interlaminar debonding. Theoretical and experimental studies have quantified the conditions for this failure mechanism. Design graphs have been developed giving geometries which can be safely used in practice. The studies on joints and attachments have been supported by the stress calculations conducted using the software referred to in Sections 3.3 and 3.4, and to the methods which measure stress redistribution, referred to in Section 3.0.

3.7 Development Of Oxide/Oxide CMCs

Tests performed on SiC/SiC composites at temperatures in the range 750-900°C indicate that stress can be maintained for only a few hours. The source of this premature failure is a chemical reaction of oxygen with the coating at the fiber-matrix interface. It was deduced that this so called "Pest Effect" places a serious limit on the temperatures at which SiC/SiC materials can operate. Protective coatings on the fibers is a possible solution, which is being pursued by other laboratories. A different program was initiated here to synthesize CMCs based on oxide fibers and a porous oxide matrix, both of which have the advantage of being oxidatively stable. The process is now developed to the point that sizable panels can be produced on a regular basis. Despite the absence of a crack deflecting interface, it was discovered that the composite is tough and can sustain the strains expected to occur in thermally loaded components. Efforts are underway to fabricate a subscale combustor liner in collaboration with industry.

The mechanical properties have been extensively investigated. From the tests, constitutive equations have been formulated and introduced into the finite element package referred to in Section 3.4. No deterioration was observed in beams subjected to combinations of mechanical and cyclic thermal loading. The ability of the material to resist high thermal loading in hostile chemical and temperature conditions with little deterioration is promising.

3.8 Delamination And Stitching

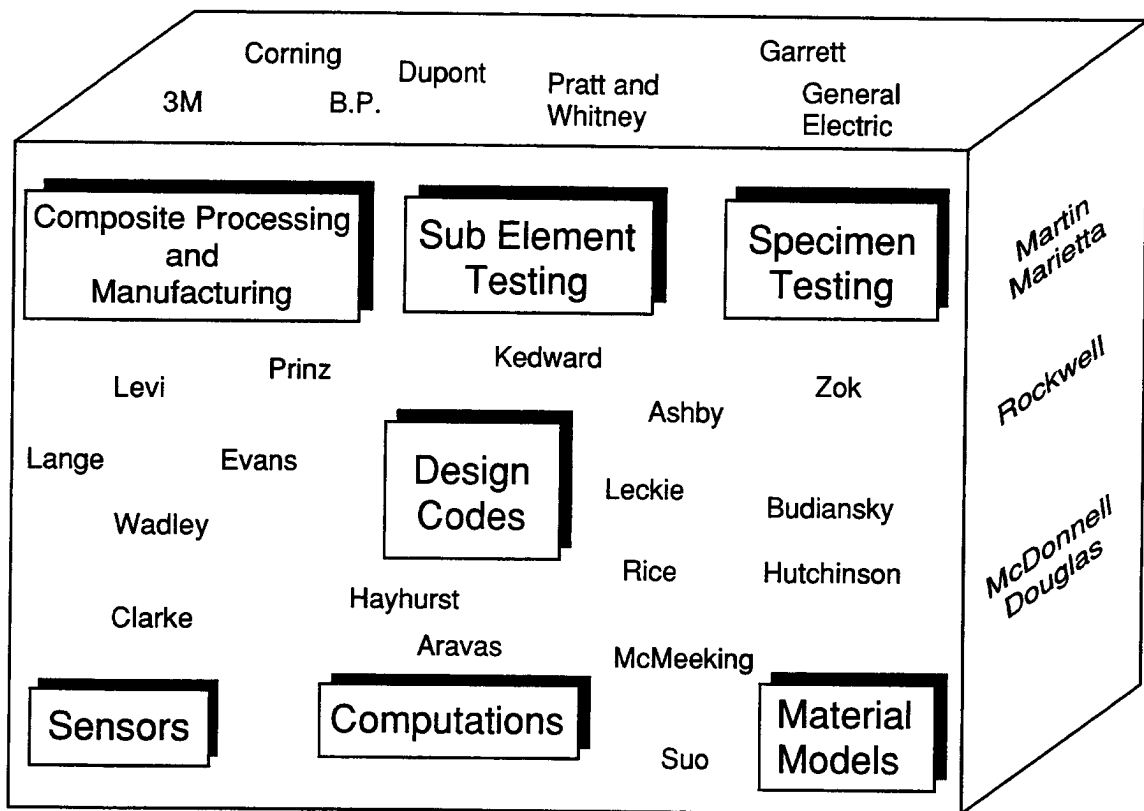
Delamination is a potential failure mechanism in composites subjected to high through-thickness thermal gradients, as well as in curved panels connecting

straight panels. Calculations have been completed which reduce to simple graphical representative combinations of loading and material properties to ensure delamination is suppressed. If it is not possible to fulfill the required conditions, it may be necessary to use through-thickness stitching. This problem has also been solved, and the amount of stitching required to prevent delamination is presented in simple graphical form.

3.9 Sensors

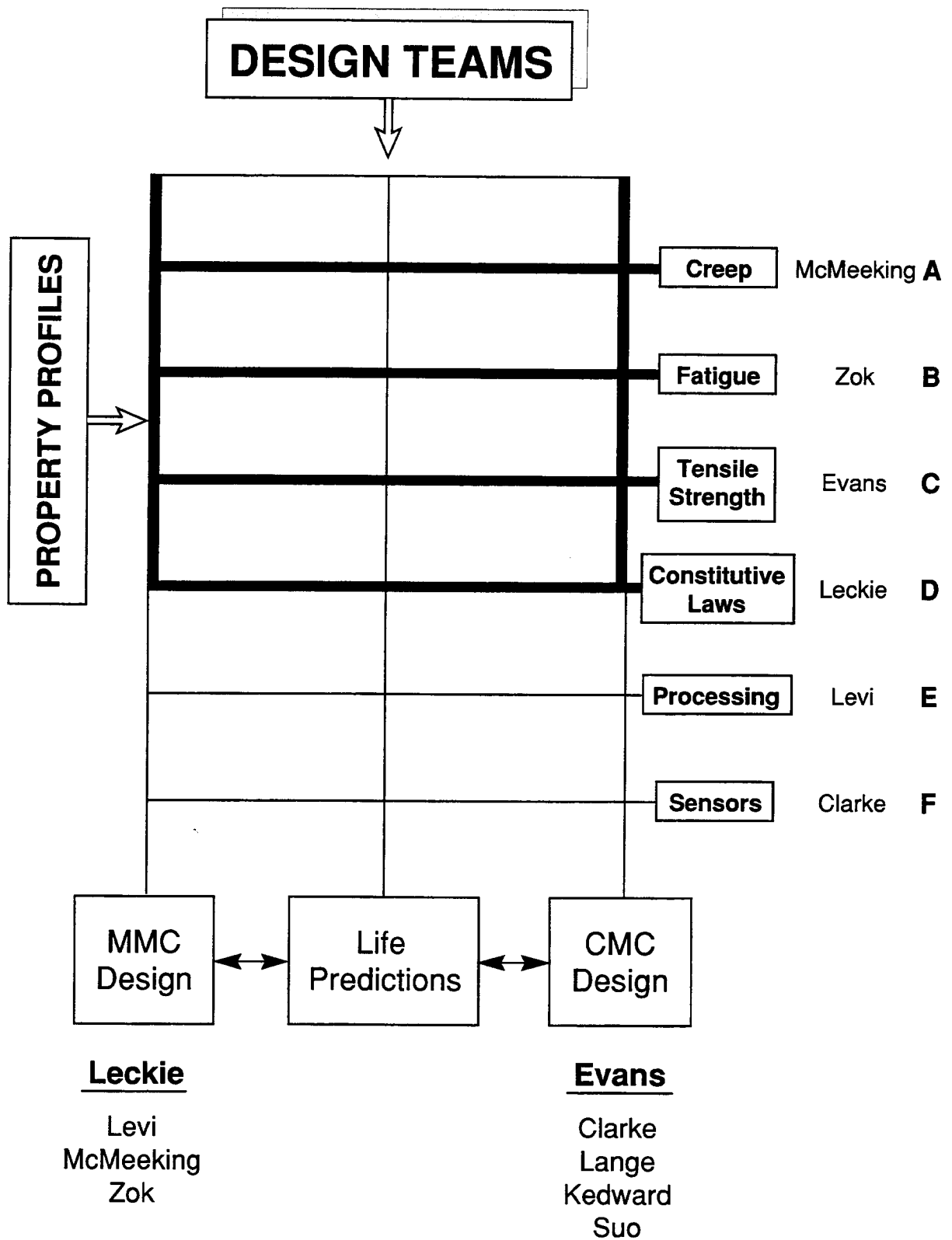
Two systems have been developed which measure stress at the micro and macro scale. At the micro-scale the procedure uses the change in frequency in the fluorescent emission which occurs when doped oxides are subjected to stress. The equipment has been used to measure the stress in individual fibers of composite materials with the result that the in-situ properties of the fibers have been measured and the results compared with the global load sharing model referred to in Section 3.1.

The second technique makes use of the elastic/thermal coupling which occurs in materials. By measuring small changes in temperature upon the application of in-plane cyclic loads, it is possible to infer the stress in materials with non-linear characteristics. The method demonstrates the beneficial stress redistribution which occurs in CMCs which rationalizes their notch strengthening characteristics.



Interactions of Areas Covered

Figure 1



Matrix Structure of Program

Figure 2

BOOK 1

CONSTITUENT PROPERTIES AND MACROSCOPIC PERFORMANCE OF CMC - I

Time Dependent Crack Initiation and Growth in Ceramic Matrix Composites	M.R. Begley B.N. Cox R.M. McMeeking	21
Creep Crack Growth with Small Scale Bridging in Ceramic Matrix Composites	M.R. Begley B.N. Cox R.M. McMeeking	33
Notch Strength of Ceramic Composites: Long Fibers, Stochastics, Short Fibers	B. Budiansky J.C. Amazigo	47
Damage, Fatigue and Failure of Ceramic-Matrix Composites	A. Burr F. Hild F.A. Leckie	59
Continuum Description of Damage in Ceramic-Matrix Composites	A. Burr F. Hild F.A. Leckie	85
Advances in Ceramic Composites Reinforced by Continuous Fibers	B.N. Cox F.W. Zok	137
Matrix Cracking in Ceramic Matrix Composites with Creeping Fibers	B.N. Cox D.B. Marshall R.M. McMeeking M.R. Begley	145
Delamination Resistance of Two Hybrid Ceramic Composite Laminates	W.A. Cutler F.W. Zok F.F. Lange P.G. Charalambides	159
Limit Stress Conditions for Weakly Bonded Fiber Composites Subject to Transverse Biaxial Tensile Loading	Z.-Z. Du F.W. Zok	169
Models of High-Temperature, Environmentally Assisted Embrittlement in Ceramic-Matrix Composites	A.G. Evans F.W. Zok R.M. McMeeking Z.-Z. Du	225
Creep Damage in SiC/SiC Composites	A.G. Evans C. Weber	233

Composite Laminates in Plane Stress: Constitutive
Modeling and Stress Redistribution due to Matrix
Cracking

G.M. Genin
J.W. Hutchinson

239

BOOK 2

CONSTITUENT PROPERTIES AND MACROSCOPIC PERFORMANCE OF CMC - II

Mechanical Performance of Ceramic Matrix Composite I-Beams	F.E. Heredia M.Y. He A.G. Evans	1
In-Plane Mechanical Properties of an All-Oxide Ceramic Composite	J.A. Heathcote X.-Y. Gong J. Yang U. Ramamurty F.W. Zok	13
The Processing and Performance of an All-Oxide Ceramic Composite	C.G. Levi J.Y. Yang B.J. Dalgleish F.W. Zok A.G. Evans	59
Notched Strength of Ceramic-Matrix Composites	W.P. Keith K.T. Kedward	93
Shear Damage Mechanisms in a Woven, Nicalon-Reinforced Ceramic-Matrix Composite	W.P. Keith K.T. Kedward	99
Effect of Matrix Grain Growth Kinetics on Composite Densification	O. Sudre F.F. Lange	107
Anisotropic Damage Evolution in Unidirectional Fiber Reinforced Ceramics	Y.M. Liu T.E. Mitchell H.N.G. Wadley	111
Elastic Properties of Laminated Calcium Aluminosilicate/Silicon Carbide Composites Determined by Resonant Ultrasound Spectroscopy	Y. Liu Y. He F. Chu T.E. Mitchell H.N.G. Wadley	151
The Influence of Fiber/Matrix Interface on the Mechanical Behavior of Nicalon SiC Fiber Reinforced Glass-Ceramic Composites	Y.M. Liu T.E. Mitchell H.N.G. Wadley	159
Effects of Off-Axis Loading on the Tensile Behavior of a Ceramic-Matrix Composite	C.S. Lynch A.G. Evans	165
Rupture Simulations for Unidirectional Ceramic Matrix Fiber Composites	R.M. McMeeking M.A. McGlockton B.N. Cox	177

Application of Weakest-Link Fracture Statistics to Fiber-Reinforced Ceramic-Matrix Composites	J.C. McNulty F.W. Zok	185
Notch-Sensitivity of Fiber-Reinforced Ceramic Matrix Composites: Effects of Inelastic Straining and Volume-Dependent Strength	J.C. McNulty F.W. Zok G.M. Genin A.G. Evans	195
Failure of a Porous Solid from a Deep Notch	P. Redanz N.A. Fleck R.M. McMeeking	239
Effect of Notch Root Radius on the Initiation Toughness of a C-Fiber/SiC-Matrix Composite	J.Y. Shen J.P. Hirth F.W. Zok J.A. Heathcote	265
Stress Rupture of an Enhanced Nicalon TM /SiC Composite at Intermediate Temperatures	T.E. Steyer F.W. Zok D.P. Walls	271

BOOK 3

Section A

CONSTITUENT PROPERTIES AND MACROSCOPIC PERFORMANCE OF MMC

Creep of Metal-Matrix Composites with Elastic Fibers — Part I: Continuous Aligned Fibers	C. Cheng N. Aravas	1
Creep of Metal-Matrix Composites with Elastic Fibers — Part II: A Damage Model	C. Cheng N. Aravas	37
Measurement of the Cyclic Bridging Law in a Titanium Matrix Composite and Its Application to Simulating Crack Growth	S.J. Connell F.W. Zok	61
Power-Law Matrix Creep in Fiber Composites Due to Transverse Stress Gradients	Z.-Z. Du A.C.F. Cocks R.M. McMeeking	71
The Effects of a Single Mode III Loading Cycle on Mode I Crack Initiation and Growth Toughnesses in a Cross-Ply $[90^\circ/0^\circ]_2$, Ti-6Al-4V/SiC _f Composite	S.V. Kamat J.P. Hirth F.W. Zok	93
A Shear Lag Model for a Broken Fiber Embedded in a Composite with a Ductile Matrix	C.M. Landis R.M. McMeeking	109
The Influence of Particle Size and Particle Fracture on the Elastic/Plastic Deformation of Metal Matrix Composites	C.-W. Nan D.R. Clarke	143
Modeling the Elastic-Plastic Deformation of Al/Al ₂ O ₃ Particulate Composites	C.W. Nan D.R. Clarke	155
Experimental Assessment of Fatigue Life and Failure Modes in a SiC/Ti Composite	T.E. Steyer F.W. Zok D.P. Walls	159
Strength Variability in Alumina Fiber-Reinforced Aluminum Matrix Composites	U. Ramamurty F.W. Zok F.A. Leckie H.E. Déve	197
Inelastic Deformation of Fiber Composites Containing Bridged Cracks	F.W. Zok M.R. Begley T.E. Steyer D.P. Walls	209

Section B

CONSTITUTIVE LAWS AND DESIGN

The Role of Scarf Angle in the Performance of Aluminum Matrix Composite Joints	D.D. Brink C.G. Levi A.C.F. Cocks F.A. Leckie	223
On Kink-Band Propagation in Fiber Composites	B. Budiansky N.A. Fleck J.C. Amazigo	235
Singularities in Bi-materials: Parametric Study of an Isotropic/Anisotropic Joint	R. Desmorat F.A. Leckie	253
Design and Life Prediction Issues for High-Temperature Engineering Ceramics and their Composites	A.G. Evans	273
Effect of Interface Undulations on the Thermal Fatigue of Thin Films and Scales on Metal Substrates	A.G. Evans M.Y. He J.W. Hutchinson	291
Failures at Attachment Holes in Brittle Matrix Laminates	G.M. Genin J.W. Hutchinson	303
Effect of Cyclic Thermal Loading on the Inplane Shear Strength of Fiber Reinforced MMC's	S. Jansson F. Leckie	333
Design Considerations and Mechanical Properties of SCS6/Ti 15-3 Metal Matrix Composite After Debond	S. Jansson K. Kedward	345
On the Behaviour of Metal Matrix Composites Subjected to Cyclic Thermal Loading	A.R.S. Ponter F.A. Leckie	355
Shakedown Limits for a Metal Matrix Composite	A.R.S. Ponter K.F. Carter J.M. Duggan	385
Effects of Cladding on the Tensile Properties of Titanium Matrix Composites	U. Ramamurty F.W. Zok F.A. Leckie	407
Role of Cladding in the Notched Tensile Properties of a Titanium Matrix Composite	U. Ramamurty F.W. Zok F.A. Leckie	413

Strength-Limited Design of Composite/Monolith
Transitions in Metallic Structures

F.W. Zok
M.Y. He
A.G. Evans
F.A. Leckie
H.E. Déve

423

BOOK 4

MEASUREMENT AND MICRO-MECHANISMS

A Photothermal Technique for the Determination of the Thermal Conductance of Interfaces and Cracks	J.R. Dryden K.R. McDonald A. Majumdar F.W. Zok	1
Determination of Fibre Strength Distributions from Bundle Tests Using Optical Luminescence Spectroscopy	J. He D.R. Clarke	41
Polarization Dependence of the Cr^{3+} R-Line Fluorescence from Sapphire and Its Application to Crystal Orientation and Piezospectroscopic Measurement	J. He D.R. Clarke	63
Residual Stresses in Dielectrics Caused by Metallization Lines and Pads	M.Y. He J. Lipkin D.R. Clarke A.G. Evans M. Tenhover	73
Convergent Debonding of Films and Fibers	M.Y. He A.G. Evans J.W. Hutchinson	81
A Model of Evolving Damage Bands in Materials	Y. Huang X.Y. Gong Z. Suo Z.Q. Jiang	91
Effect of Interfacial Carbon on Adhesion and Fracture Toughness of Gold-Sapphire Interfaces	D.M. Lipkin D.R. Clarke A.G. Evans	103
Estimating the Metal-Ceramic van der Waals Adhesion Energy	D.M. Lipkin J.N. Israelachvili D.R. Clarke	139
Laser-Ultrasonic Evaluation of Damage Unidirectional Ceramic Matrix Composites	Y.-M. Liu T.E. Mitchell H.N.G. Wadley	153
Fiber Optic Measurement of Residual Stress in Ti-6Al-4V/SiC Fiber Composites Using Cr^{3+} Doped Sapphire Fibers	G.T. Munger H.N.G. Wadley	163
Motions of Microscopic Surfaces in Materials	Z. Suo	179

Damage Evolution and Acoustic Emission Mechanisms in $\alpha_2\beta$ /SCS-6 Titanium Matrix Composites	D.J. Sypeck H.N.G. Wadley	281
Acoustic Emission Analysis of SCS-6 Fiber Fracture in Titanium Matrix Composites	D.J. Sypeck H.N.G. Wadley	313

TIME DEPENDENT CRACK INITIATION AND GROWTH IN CERAMIC MATRIX COMPOSITES

Matthew R. Begley
Harvard University
Cambridge, MA 02138

Brian N. Cox
Rockwell International
Thousand Oaks, CA 93017

Robert M. McMeeking
University of California, Santa Barbara
Santa Barbara, CA 93107

ABSTRACT

Matrix cracking in ceramic matrix composites with fine grained fibers at high temperatures will be governed by fiber creep, as relaxation of the fibers eliminates crack tip shielding. Using a time dependent bridging law which describes the effect of creeping fibers bridging a crack in an elastic matrix, crack growth initiation and history have been modeled. For a stationary crack, crack tip stress intensity factors as a function of time are presented to predict incubation times before subcritical crack growth. Two crack growth studies are reviewed: a constant velocity approximation for small-scale bridging, and a complete velocity history analysis which can be used to predict crack length as a function of time. The predictions are summarized and discussed in terms of identifying various regimes of crack growth initiation, subcritical growth, and catastrophic matrix cracking.

NOMENCLATURE

E_f, E_m	Young's modulus of the fibers and matrix
$E_L = fE_f + (1-f)E_m$	rule of mixtures composite Young's modulus
\bar{E}	composite modulus which accounts for orthotropy
f	fiber volume fraction
D	fiber diameter
B	creep coefficient of the fibers ($\dot{\epsilon}_f = \frac{\dot{\sigma}_f}{E_f} + B\sigma_f$)
$\beta = \frac{BE_f E_L}{2(1-f)E_m}$	modified creep coefficient of the fibers
τ	shear sliding stress at the fiber-matrix interface
$\sigma, \dot{\sigma}$	bridging stress, bridging stress rate
$\delta, \dot{\delta}$	total crack opening, total crack opening rate
$\lambda = \frac{D(1-f)^2 E_m^2}{4f^2 \tau E_f E_L^2}$	rate-independent bridging coefficient ($\delta = \lambda \sigma^2$)
$T = \frac{E_L}{(1-f)BE_f E_m}$	characteristic relaxation time of intact composite
K_c	critical stress intensity factor for matrix crack extension
K_∞	far-field applied stress intensity factor
$\sigma_{mc} = \left[\frac{12f^2 \tau E_f E_L^2 K_c^2}{D(1-f)E_m^3} \right]^{1/3}$	steady-state matrix cracking stress
$l = (\lambda \bar{E} K_c)^{2/3} = \lambda \bar{E} \sigma_{mc}$	characteristic length scale for the composite
$\delta_{mc} = \lambda \sigma_{mc}^2$	total crack opening at steady-state matrix cracking stress (for the rate-independent case)
$\Delta_{cr} = \frac{\lambda \bar{E}^2 \delta_{cr}}{l^2} = \frac{\delta_{cr}}{\delta_{mc}}$	normalized critical total crack opening governing fiber failure
a, \dot{a}	crack half length, crack tip velocity
$v_{ss} = \frac{\dot{a}}{\beta l}$	normalized steady-state crack velocity
$\bar{K}_\infty = \frac{\lambda \bar{E} K_\infty}{l} = \frac{K_\infty}{K_c}$	normalized applied stress intensity factor
$\bar{\epsilon} = \frac{\lambda \bar{E}^2 \epsilon}{l}$	normalized total fiber strain at the crack plane
$\bar{\epsilon}_{cr}$	normalized critical total strain to fiber failure
$(K_\infty)_{asym}$	asymptotic applied stress intensity factor at low crack speeds
α_{asym}	asymptotic bridge length at low crack speeds

1. INTRODUCTION

High strength ceramic fibers can be achieved by decreasing fiber grain size, which limits the flaw size. Ceramic matrix composites (CMCs) are made by combining these fibers with relatively coarse grained matrices. Since the role of the matrix is generally to provide ductility to the composite, the decrease in matrix strength due to large flaw sizes is not considered detrimental. The low temperature behavior of such composites has been studied extensively both experimentally and analytically, and is generally well understood¹.

The primary motivation for using such composites, however, is the high temperature capabilities of the ceramic constituents. At high temperatures, predicting composite performance becomes more complicated due to oxidation and creep²⁻³. The fine grained fibers are particularly susceptible to creep, as small grain sizes increase avenues for grain boundary diffusion. (The coarser grained matrix can be considered to behave elastically, as creep rates are significantly lower.) Crack bridging by intact fibers becomes time-dependent at high temperatures, as fiber creep causes crack closure forces to decay over time⁴⁻¹¹. Furthermore, cracks that can be considered benign at low temperatures may cause significant problems at high temperatures, as they may provide pathways for oxidation to occur in the interior of the composite or result in a loss of hermeticity¹². The room temperature question of crack stability thus changes to questions about when and how fast cracks grow.

This paper is intended to provide a summary of some recent work on predicting time dependent crack growth in CMCs caused by fiber creep at high temperatures. A time dependent bridging law has been developed to describe the effect of creeping fibers bridging a matrix crack in a composite whose matrix can be considered elastic⁴. This bridging law has been used to estimate the time needed to initiate crack growth from both fully bridged and partially bridged stationary cracks⁵. The issue of crack growth rate has been addressed in both the small-scale and large-scale bridging regimes⁶⁻⁷. Representative results are presented and used to discuss the issues raised by time dependent crack growth in both unidirectional and laminated CMCs.

In the crack behavior studied in this work, a finite crack tip stress intensity factor is assumed to exist. For analysis of initiation times, it is assumed that the crack geometry and loading is such that the crack tip stress intensity factor, K_{tip} , is less than the toughness of the matrix, K_c (adjusted for matrix volume fraction.) For crack growth studies, it is assumed that crack growth occurs under the condition that $K_{tip} = K_c$. The analyses and results are often similar to a cohesive zone approach in different materials¹³⁻¹⁴; however, it should be emphasized that the assumption of a finite stress intensity factor at the crack tip (based on the fact that the matrix remains elastic) leads to significant differences.

2. TIME DEPENDENT BRIDGING

The crack tip shielding provided by creeping fibers bridging a matrix crack can be analyzed by determining the relationship between the crack opening rate and bridging traction for a representative bridged section of the crack. Such cell models can then be integrated with traditional fracture mechanic relations to develop an integral equation which is solved for the closure forces in the bridged section of the crack. These closure forces are then used in the usual manner to predict the reduction in crack tip stress intensity factor.

A full derivation for a creeping fiber embedded in an elastic matrix results in the following bridging law, which incorporates the effects of frictional slip between the fiber and the matrix⁴:

$$\begin{aligned} \dot{\delta}(t) = & \frac{(1-f)^2 E_m^2 D}{2f^2 \tau E_f} \left\{ \frac{\sigma(t)}{E_L} + \frac{f B E_f^2}{E_L^2} \int_{-\infty}^t \sigma(\bar{t}) e^{-(t-\bar{t})/T} d\bar{t} \right\} \\ & \times \left\{ \frac{\dot{\sigma}(t)}{E_L} + \frac{B E_f \sigma(t)}{2(1-f) E_m} \left[1 + \frac{f E_f (f E_f - (1-f) E_m)}{E_L^2} \left\{ \int_{-\infty}^t \frac{\sigma(\bar{t})}{T \sigma(t)} e^{-(t-\bar{t})/T} d\bar{t} \right\} \right] \right\} \end{aligned} \quad (1)$$

D is the diameter of the fibers, f is the fiber volume fraction, B is the creep coefficient of the fibers; τ is the shear sliding stress between the fibers and the matrix, E_f , E_m , and E_L are the elastic moduli of the fiber, matrix and composite, respectively; and T is the characteristic relaxation time for the intact composite, given by $E_L/B(1-f)E_mE_f$.

For a growing crack, the convolution integrals in (1) (which reflect the history dependence of the bridging stress) complicate things, and the following simplified bridging law has been used in crack growth studies^{6,7};

$$\dot{\delta}(t) = 2\lambda\sigma(t)[\dot{\sigma}(t) + \beta\sigma(t)] \quad (2)$$

where λ is the rate-independent bridging coefficient, and β is a modified creep coefficient. (Please see the nomenclature table.) The assumptions that justify simplifying Eq. (1) to Eq. (2) are based on comparing the relative magnitudes of terms in full bridging law and neglecting smaller terms. In summary, Eq. (2) neglects creep of the fibers in the intact portion of the composite, which is acceptable during crack growth studies since creep in the slip region adjacent to the matrix crack, and the short time ($t \ll T$) response of Eq. (1), dominate the shielding effect of the fibers. Further details of these assumptions and their validity is discussed fully in [5-7].

3. TIME TO INITIATE CRACK GROWTH

For a given crack geometry and load level, the crack tip stress intensity factor may be beneath the critical stress intensity factor of the matrix, implying that some time is required to relax the shielding effect of the fibers to the point that crack growth occurs. Such a situation would arise when a matrix flaw exists that spans multiple fibers, provided the load is beneath the critical stress to propagate the bridged matrix crack. Another example is the case of an overload, where the applied load on the composite decreases; during the peak loading, the matrix crack is driven to the length where $K_{tip} = K_c$ for the peak load. If the load is subsequently decreased, K_{tip} falls beneath K_c and some time is required to decay the bridging tractions until crack growth occurs.

In the following calculations, the crack is assumed to be stationary; thus, the problem is simply to calculate the evolution of the bridging stress over time. The bridging stress profile at a given instant in time was then used to predict the instantaneous value of the crack tip intensity factor. The geometry is a fully bridged center crack of length $2a$ in an infinite panel. The crack tip stress intensity factor as a function of time is shown in Figure 1 for several different cases.

The curves compare the effects on the crack tip stress intensity factor of two different simplifications, for three different load levels. The solid lines were generated using the bridging stress profile generated by the solution of an integral equation derived using Eq. (2), the simplified bridging law. The dashed lines were calculated using the full bridging law and imposing a parabolic approximation for crack opening. (At high loads or for short cracks, the crack opening will be nearly parabolic; assuming the form of the profile allows the differential form of the integral equation to be reduced to a simple one degree of freedom differential equation.) It can be seen that at high loads the effect of the convolution integrals is negligible. As discussed in [5], even at lower loads the neglect of the convolutions is usually not significant. The discrepancy in Figure 1 between the two

calculations for the lowest load is mostly a result of the inaccuracy of the parabolic form used to reduce the integral equation.

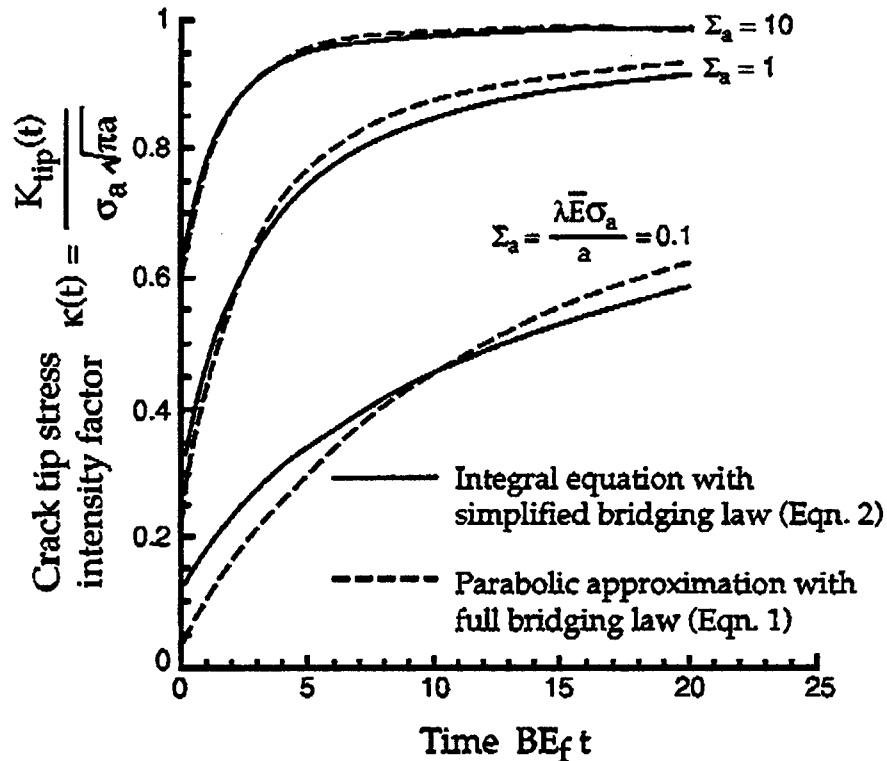


Figure 1

Two calculations for the crack tip stress intensity factor as a function of time for three different loads and the case where $f = 0.3$, $E_f = E_m = E_L = E$.

4. CONSTANT VELOCITY CRACK GROWTH: SMALL-SCALE BRIDGING

In situations where the length of the bridging zone is much smaller than the crack length, small-scale bridging is said to apply and the governing equations can be simplified from the general case. An example of such a scenario may occur in laminated CMCs, where cracks first appear in the 90° layers with fibers perpendicular to the loading direction. These cracks will advance into the adjacent 0° plies and arrest at room temperature; at loads much smaller than the matrix cracking stress, the bridging zone is much smaller than the total crack length.

The case being modeled here is a semi-infinite crack loaded with a far-field applied stress intensity factor, K_∞ , growing at a constant speed, v_{ss} ⁶. The bridging law dictating material behavior in the bridged zone is given as Eq. (2). Fibers fail in the wake of the crack and the bridging zone size remains constant. The solution represents a steady-state configuration, as the zone of creeping fibers bridging the crack propagates with the crack tip. The length of the bridging zone depends on the crack growth rate and is determined by a fiber failure criterion. Two failure criteria are presented here: a critical crack opening, Δ_{cr} , and a critical total strain in the fiber, $\bar{\epsilon}_{cr}$.

Figure 2 illustrates how crack velocity varies as a function of applied stress intensity factor K_{∞} for the two cases. For both cases, there is a rapid increase in crack velocity as the applied stress intensity factor is raised above the matrix toughness. The figure demonstrates the existence of upper and lower bounds on the applied loading. The assumption of a finite crack tip stress intensity factor dictates that a minimum K_{∞} exists, below which no crack growth will occur; this minimum is merely the matrix toughness. For applied loads above this value, fiber creep will decrease bridging tractions to drive crack growth, though perhaps at very small velocities.

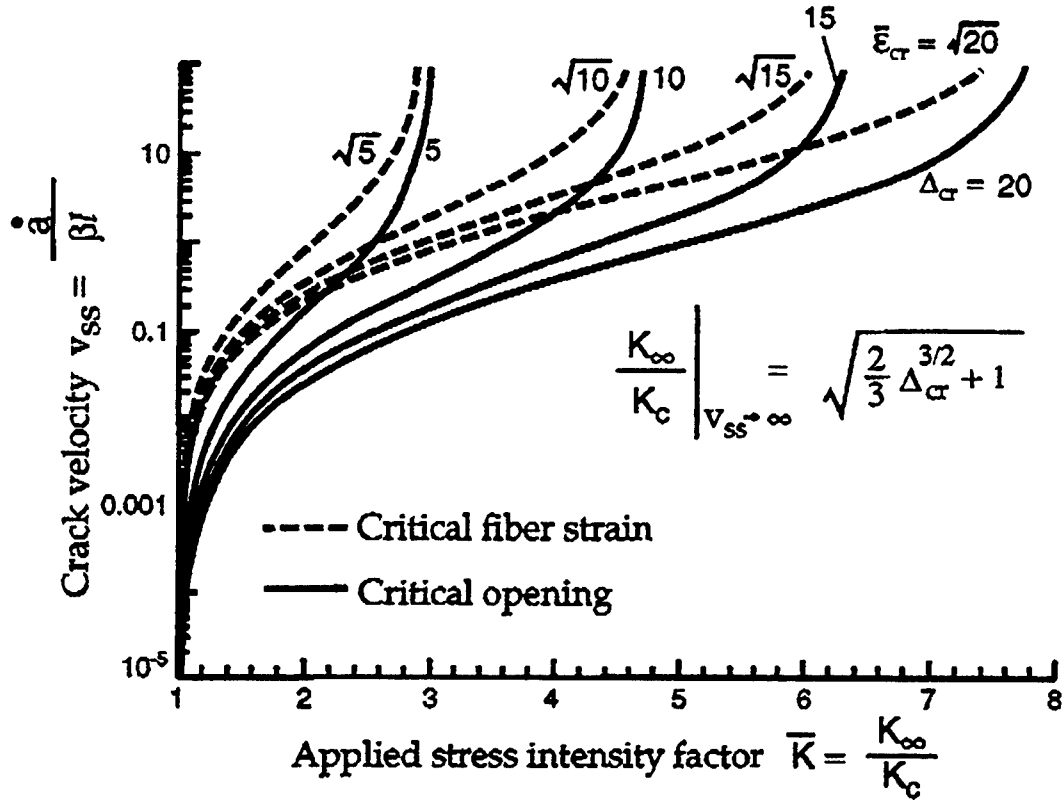


Figure 2
Steady-state crack velocity as a function of far-field applied stress intensity factor for two fiber failure criteria and the case where $f = 0.3$, $E_f = E_m = E_L = E$.

Since the simplified bridging law (given as Eq. 2) reduces to the appropriate rate independent bridging law in the limit of no creep, an upper limit exists. As the applied load increases towards the level at which bridging (without creep) is no longer effective enough to maintain $K_{tip} = K_c$, crack velocities tend toward infinity. Thus, the upper limit corresponds to load levels at which instantaneous matrix crack occurs.

One of the attractive results of the simplifying assumptions used in this analysis is that they allow closed form asymptotic solutions when crack speeds are low. The asymptotic dependence of the bridging zone length and crack velocity on the applied stress intensity factor are summarized below for the case where fiber failure is governed by a critical strain criterion;

$$\left(\frac{K_{\infty}}{K_c}\right)_{\text{asym}} = 1 + \frac{4}{\pi^{1/4}} \left(\frac{3E_f E_L}{4(1-f)E_m} \right)^{1/3} (\bar{E}_{cr})^{1/3} (v_{ss})^{2/3}; \quad (v_{ss} \rightarrow 0) \quad (3)$$

$$\left(\frac{\alpha}{l}\right)_{\text{asym}} = \frac{1}{4} \left(\frac{3E_L}{4(1-f)E_m} \right)^{4/3} (\bar{E}_{cr})^{4/3} (v_{ss})^{2/3} \quad (4)$$

These closed form solutions reveal a simple power law relationship between applied stress intensity factor and crack velocities that may be useful in comparing with experiments with very small bridging zones.

5. GENERAL TIME DEPENDENT CRACK GROWTH: LARGE-SCALE BRIDGING

Obviously, cracks may not grow at constant velocity, and the bridging length may be comparable to specimen dimensions. For such cases, full large-scale bridging have been performed to predict crack length and velocity as a function in time⁷. Fiber failure was not incorporated into the analysis. The geometry being considered is a center crack of length $2a$ in an infinite panel with a 'notch', or unbridged portion of matrix crack of lengths $2a_0$. Crack growth is assumed to occur with the condition that the crack tip stress intensity factor equals the matrix toughness. The numerical procedure is summarized in [7]; one attractive aspect of the technique used is that the bridging law has exactly the correct form in the limit of small time increments. Hence, the bridging behavior near the crack tip, where fibers are responding nearly elastically, is captured accurately. The results of these analyses are summarized in Figures 3 and 4.

Crack velocities as a function of crack length are shown in Figure 3 for several different values of applied nodes and several different notch sizes. The curves start at different initial values of crack length, corresponding to the case where $K_{tip} = K_c$ for the rate independent case. Thus, for these cases the initiation time discussed in section 3 is zero. All cases show that the crack will initially decelerate as the rate of decay of bridging tractions *decreases*. After the initial transient has finished, the crack accelerates monotonically, eventually becoming asymptotically independent of initial notch size.

The crack velocity as a function of crack length can be integrated to predict crack length as a function of time. Such results are shown in Figure 4 for one of the notch sizes in Figure 3 and the same load levels. The curves illustrate the large effect the deceleration transient will have on the overall crack growth; the larger the dip in the crack velocity curve, the larger the dwell time in Figure 4. For laminates, critical crack lengths at which catastrophic cracks cross the specimen may be short, i.e. equal to the ply thickness, emphasizing the importance of solutions in the transient regime.

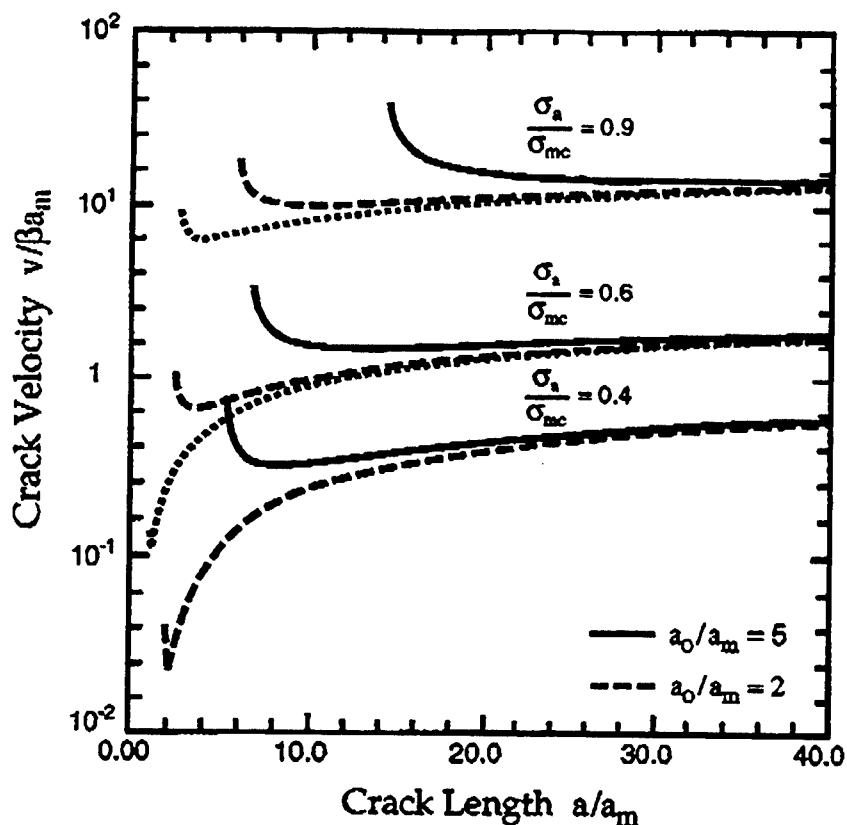


Figure 3

Crack velocity as a function of crack length for several values of applied load and notch sizes using the simplified bridging law

6. PREDICTING TIME DEPENDENT CRACK GROWTH IN CMCs

6.1 Crack growth initiation

For a given loading scenario, the first question to answer is whether or not crack growth starts immediately, or whether some time is required to decrease the shielding in bridged cracks. The answers lie in the *rate-independent* behavior of CMCs, which has been extensively studied; provided the loading rate is high enough, the composite constituents will initially respond elastically. The upper limit on the applied loading such that crack growth studies are applicable is the steady-state matrix cracking stress, which represents the load level at which matrix cracks will propagate across the composite catastrophically in a rate-independent manner.

For cracks created by load histories where the specimen or component is loaded monotonically beneath the matrix cracking stress, the transition to subcritical crack growth will be instantaneous. Both cracks grown from a notch in a unidirectional composite and cracks tunneling into 0° plies in a laminate will arrest at the crack length at which $K_{tip} = K_c$. Therefore, *any* amount of fiber creep will decrease crack tip shielding and cause crack growth; initiation times for these cases are zero. The crack length at which $K_{tip} = K_c$ with rate-independent behavior will be the initial condition used in the time dependent study. The rate independent behavior of both unidirectional CMCs and laminates is summarized in [15], which can be used to identify relevant starting geometries for time dependent studies.

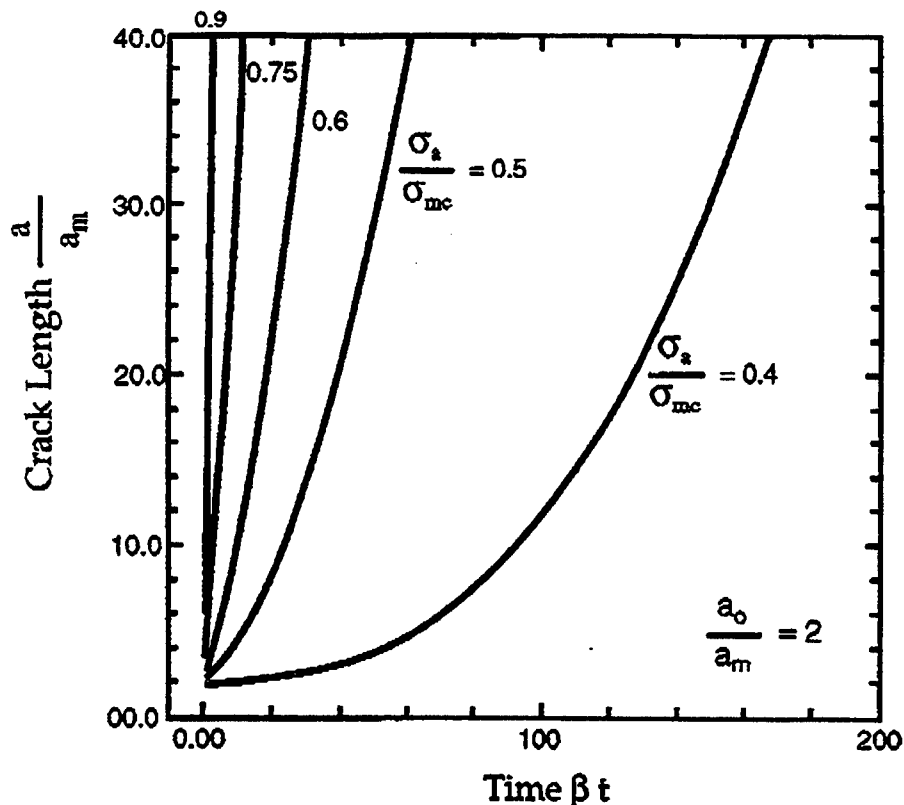


Figure 4

Crack length as a function of time calculated by integrating the curves in Figure 3

Initiation times will not be zero for cracks created by an overload, where the load applied to the composite decreases after some maximum. For these cases, the starting crack length is the length created by the maximum load, where $K_{tip}(\sigma_{max}) = K_c$. If the load drops, K_{tip} will fall below K_c , and the crack will remain stationary until fiber creep degrades shielding enough to cause crack growth. Obviously, such histories affect subsequent crack growth as fiber strains will accumulate. Further modeling and experiments are needed to discover the effect of creep prior to crack growth.

6.2 Regime of subcritical crack growth

Once crack growth has started, the relevant question to answer is when the cracks reach lengths that are undesirable. This is most likely the length at which the crack crosses the specimen, resulting in two halves of intact composite held together by creeping fibers. For laminates, the critical length at which cracks propagate unstably may be the 0° ply width, depending on the ratio of $0^\circ/90^\circ$ widths¹⁵.

Once the critical crack length has been identified, the models described in Sections 4 and 5 can be used to estimate the amount of time required to reach this length. Noting that a_m in Figure 3 is on the order of a tenth of a millimeter for most CMCs, it can be seen that most (if not all) of the relevant crack growth for typical laminates occurs during the transient period of crack growth. Thus, the pertinent regions Figures 3 and 4 are the ones where the normalized crack length a/a_m is less than 10 or so. For loads above 60% of the matrix crack stress, the time to reach a critical crack length is quite small, as the transient region becomes less and less pronounced. For such cases, matrix cracks quickly cross the

specimen and composite rupture is governed by the rupture behavior of the fibers loaded uniformly.

For loads significantly below the matrix cracking stress, velocities will may be quite small, implying that fibers have significant time to creep. Naturally, the fibers will exhibit a finite amount of creep ductility and for slower velocities, will fail during the subcritical crack growth. A transition exists then, between subcritical crack growth characterized by fiber failure in the wake of the crack⁶ and fiber failure *after* the crack has reached critical dimensions⁷. Experiments are needed to confirm this transition and evaluate the validity of the predictions presented here.

6.3 Appropriateness of the bridging law and single crack model

In general, bridging laws developed from cell models fail to capture certain aspects of bridging behavior. Notably, the equation presented here does not account for the possibility of "reverse" slip, where the direction of relative sliding between the fiber and the matrix changes sign. This is most likely to happen in regions of the bridging zone that are unloading. For stationary cracks, this is most likely to be the case, and further calculations are warranted. For growing cracks, however, it has been shown that growth is dominated by the near-tip behavior of the bridging region⁶⁻⁷. Near the crack tip, bridging fibers will be loaded rapidly and will respond nearly elastically, or with the 'short time' response of the bridging law. In this regime, both the possibility of 'reverse' slip and the convolution integrals in Eq. (1) can be reasonably neglected.

It should be pointed out that a single crack model does not account for the stress redistribution that will occur if multiple matrix cracks occur near a stress concentration. Multiple matrix cracks are common, and a more realistic bridging law which incorporates the effect of overlapping slip zones would be more useful. Additionally, different weight functions used in developing the integral equations could be used, to account for arrays of multiple cracks.

Despite the limitations on the bridging law outlined above, the results will be qualitatively consistent with more detailed analyses incorporating reverse slip and crack interaction. The essential features of the constitutive law for the bridging zone will not be changed by considering slip zone reversal or overlap; namely that the bridging stress increases with opening and decays with time. Most importantly, the details of appropriate bridging laws *always* require empirical calibration, preferably with crack growth data rather than micromechanical tests¹⁶. Regardless of the exact form of the bridging law, accurate predictions over a wide range of stress levels should be possible once the model is calibrated against experiments.

ACKNOWLEDGMENTS

MRB and RMM were supported by the University Research Initiative, ONR Contract No. N-0014-92-J-1808. BNC was supported by AFOSR Contract No. F49620-94-C-0030.

REFERENCES

- [1] Evans, A.G. and Zok, F.W., (1994). The physics and mechanics of fibre-reinforced brittle matrix composites. *J. Mat. Sci.*, **29**, 3857
- [2] Lamouroux, F., Steen, M. and Valles, J.L. (1994). Uniaxial tensile and creep behavior in an alumina fiber-reinforced ceramic matrix composite: I - Experimental study. *J. Euro. Ceram. Soc.*, **14**, 529

- [3] McNulty, J., Zok, F.W. and Evans, A.G., (1996). Fatigue and rupture of ceramic matrix composites at elevated temperature. Unpublished work
- [4] Begley, M.R., Evans, A.G. and McMeeking, R.M., (1995). Creep rupture in ceramic matrix composites with creeping fibers. *J. Mech. Phys. Sol.*, **43**, 727
- [5] Begley, M.R., (1996). Time dependent cracks in ceramic matrix composites: crack growth initiation. *Int. J. Sol. Structures*, in print
- [6] Begley, M.R., Cox, B.N. and McMeeking, R.M., (1996). Creep crack growth with small-scale bridging in ceramic matrix composites. *Acta Met.*, in print
- [7] Begley, M.R., Cox, B.N. and McMeeking, R.M., (1995). Time dependent crack growth in ceramic matrix composites with creeping fibers. *Acta Met.*, **43**, 3927
- [8] Henager, C.H. and Jones, R.H., (1993). High temperature plasticity effects in bridged cracks and subcritical crack growth in ceramic matrix composites. *Mat. Sci. & Engr. A*, **166**, 211
- [9] Henager, C.H. and Jones, R.H., (1994). Subcritical crack growth in CVI silicon carbide reinforced with Nicalon fibers: Experiment and model. *J. Am. Ceram. Soc.*, **77**, 2381
- [10] El-Azab, A. and Ghoniem, N.M., (1995). Investigation of incubation time for subcritical crack propagation in SiC-SiC composites. *J. Nuc. Mat.*, **219**, 101
- [11] Nair, S.V. and Gwo, T.J., (1993). Role of crack wake toughening on elevated temperature crack growth in a fiber reinforced ceramic matrix composite. *J. Eng. Mat. Tech.*, **115**, 273
- [12] Evans, A.G., Zok, F.W., McMeeking, R.M. and Du, Z.Z., (1996). Models of environmentally assisted embrittlement in ceramic matrix composites. *J. Am. Ceram. Soc.*, **79**, 2345
- [13] Knauss, W.G., (1993). Time dependent fracture and cohesive zones. *J. Eng. Mat. Tech.*, **115**, 262
- [14] Fager, L.-O., Bassani, J.L., Hui, C.-Y. and Xu, D.-B., (1991). Aspects of cohesive zone models and crack growth in rate-dependent materials. *Int. J. Fracture*, **52**, 119
- [15] Cox, B.N. and Marshall, D.B., (1996). Crack initiation in brittle fiber reinforced laminates. *J. Amer. Ceram. Soc.*, in press
- [16] Cox, B.N., (1995). Life prediction for bridged cracks. *Life Prediction for Titanium Matrix Composites*, ed. W.S. Johnson, J. Larsen and B.N. Cox, ASTM STP (ASTM, Philadelphia, 1995), in press



CREEP CRACK GROWTH WITH SMALL SCALE BRIDGING IN CERAMIC MATRIX COMPOSITES

M. R. BEGLEY¹, B. N. COX² and R. M. McMEEKING³

¹Division of Applied Science, Harvard University, Cambridge, MA 02138, ²Rockwell Science Center, 1049 Camino Dos Rios, Thousand Oaks, CA 91360 and ³Mechanical and Environmental Engineering Department, University of California, Santa Barbara, Santa Barbara, CA 93106, U.S.A.

(Received 26 March 1996; accepted 1 October 1996)

Abstract—Time-dependent crack growth in ceramic matrix composites with linearly creeping fibers in an elastic matrix is predicted for bridged regions that are much smaller than the crack length. The relationship between crack openings and bridging tractions was modeled previously and accounts for the mechanics of fiber pull-out while fibers are creeping. The length of the bridged zone is determined by a fiber failure criterion and the condition that the stress intensity factor at the crack tip equals the matrix toughness. Solutions that relate constant crack velocities to applied stress intensity factors are presented. Two fiber failure criteria are considered: a critical crack opening and a critical total strain in the fiber at the crack plane. When fiber failure is governed by a critical crack opening, bridging lengths will decrease with increasing velocity. For the case of a critical strain, the steady-state bridge length will increase with increasing velocity. Asymptotic analytical solutions are presented for cases where the crack velocity is small. © 1997 Acta Metallurgica Inc.

1. INTRODUCTION

The first load-induced damage observed in current fiber-reinforced ceramic matrix composites (CMCs) is usually matrix cracking [1]. Provided the fiber matrix interfaces are weak, the matrix cracks are bridged by intact fibers. If the cracks initiate at a sufficiently large notch, their growth is stable and crack arrest will occur at some finite crack length at stresses lower than the steady-state cracking stress, σ_{mc} , expected for infinite matrix cracks [2]. In unnotched laminates, the matrix cracks initiate as tunneling cracks in the 90° plies (Fig. 1) [3, 4], which can then be regarded as playing the role of the notch [5, 6]. Thus, if the 90° ply width is sufficiently large, the matrix cracks may again arrest at finite lengths for stresses lower than σ_{mc} [5, 6].

The macroscopic stiffness of the composite is compromised relatively slightly by finite matrix cracks. Much more serious softening is associated with multiple matrix cracks that span the whole specimen. Similarly, in applications demanding hermeticity, when either the ceramic composite must contain a gas or fluid or the fibers or fiber/matrix interfaces must be protected from a hostile environment, finite matrix cracks might be regarded as benign. Thus in many cases, the composite might be considered not to have failed as long as matrix cracks remain finite; and therefore, provided the arrest of cracks initiating from 90° plies or stress concentrators is permanent, the steady-state matrix cracking stress, σ_{mc} , may be used as a design limit.

At high temperatures, crack arrest will not be permanent, because of the onset of creep. In many CMCs, creep occurs first in the fibers, while the matrix remains elastic [7, 8]. Creep occurs preferentially in the fibers (single crystal fibers aside) because they are manufactured with small grain size to maximize strength. Since matrix cracks concentrate stress in bridging fibers, fibers will creep most in the wake of matrix cracks. The resulting reduction in crack tip shielding will allow previously arrested matrix cracks to resume propagation with growth rates determined by fiber creep.

A constitutive law to describe the decaying bridging tractions generated by creeping fibers coupled to the matrix by friction has already been developed by Begley *et al.* [9]. In a previous paper, this law was used to calculate crack growth rates for matrix cracks growing away from initial flaws (notches or 90° plies) when the fibers creep but never fail [10]. However, in that work it was shown that, at relatively low stresses, propagation times for the matrix cracks were long compared to the time required for the creep failure of fibers. Therefore, at low stresses, matrix crack propagation should be calculated in the presence of fiber failure.

In one limit of this process, the bridged region of the matrix crack will remain small compared to the total crack length: this is the limit of small scale bridging. Conditions near the crack tip are then approximately those of a semi-infinite crack with a finite bridged zone and the mechanics of crack growth can be investigated without regard to notch size or specimen geometry (Fig. 2).

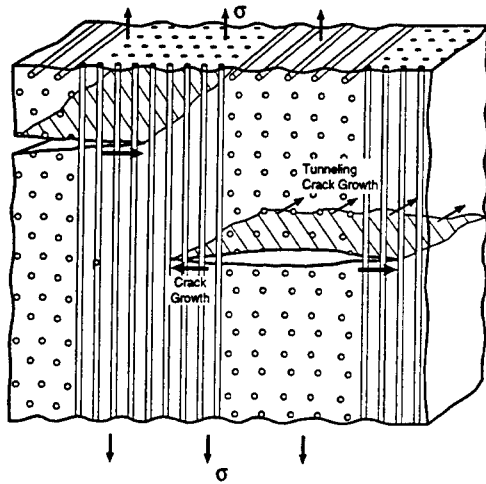


Fig. 1. Schematic of tunneling cracks in a 0/90° laminate.

The results presented in this work will show that small scale bridging will be favored when fiber failure is governed by a critical creep strain criterion. In this case, the length of the zone of bridging fibers decreases to zero with the applied stress intensity factor. Thus, small scale bridging conditions should be commonly found in specimens with machined notches at low stresses.

For naturally occurring matrix cracks in laminates, small scale bridging will be most relevant when the fracture toughness of the 90° ply is less than half that of the 0° plies, and the applied load is only slightly higher than that required to initiate matrix cracking by crack tunneling. In these conditions, the length of the bridging zone as the crack grows away from the

90° plies into the 0° plies (Fig. 1) will remain small compared to the 90° ply width [6].

In this paper, the mechanics of crack growth governed by fiber creep is examined in the small scale bridging limit. Crack growth is assumed to occur when the stress intensity of the matrix crack, K_{tip} , reaches a critical value, K_c , which is related to the matrix fracture toughness. The crack velocity is calculated as a function of applied stress intensity factor assuming a constant crack velocity, which corresponds to the attainment of a steady-state bridging configuration, which propagates with the crack tip. The constant velocity condition can strictly only be obtained at constant applied stress intensity factor. However, it will be well approximated under more general conditions and it is an instructive limit for study.

Two cases are considered, identified by different fiber failure conditions. In one case, fibers are assumed to fail (and thus no longer provide bridging tractions) when the total crack opening reaches a time-independent critical value. The other case assumes fibers fail when the total strain in the fibers (at the crack plane) reaches a constant critical value. The length of the bridging region is determined by imposing the conditions $K_{tip} = K_c$ and the fiber failure criterion.

1.1. Relationship to other rate-dependent bridged crack problems

The work presented here is similar in many regards to analyses previously applied to craze crack growth in polymers [11–16]. The literature on this subject is extensive; only a few examples are discussed here to highlight the essential physical differences with the case of matrix cracks in CMCs. All analyses of polymeric crazes assume that the stress intensity factor at the crack tip, i.e. at the end of the bridged zone nearest the uncracked material (see Fig. 2), is zero. Crack growth is then completely determined by the time-dependent responses of the bulk and crazing material and the criteria used to determine the formation and failure of the craze. The analysis provided by Kramer and Hart [15] is framed in terms of a non-zero stress intensity factor, but at the *trailing* end of the bridged zone; i.e. the applied stress distribution along the bridged zone is assumed to be the same as the stress distribution ahead of a crack in a linear elastic material.

Knauss and co-workers [11, 12] assume in modeling cracks in polymers that the craze length is determined by a critical strain criterion for the failure of fibrils that bridge intact regions of the bulk material. In their work, the bulk material is assumed to be linearly viscoelastic, with nonlinear viscoelastic deformation taking place in the craze. Fager and co-workers [13, 14] used a general power law to model the time-dependent deformation of the craze, and apply a damage parameter based on critical opening to determine when failure occurs in the

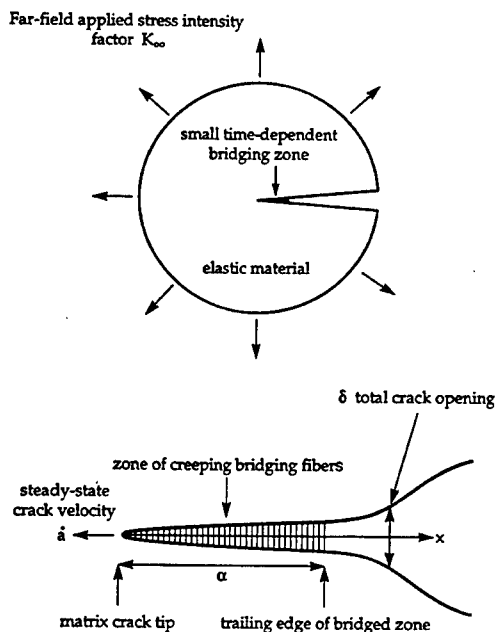


Fig. 2. Small scale bridging model.

bridging zone. The intact bulk material is assumed to be elastic. Kramer and Hart [15] predict failure of the bridging material according to a limiting stress based on the strength and spacing of fibrils in the craze zone. Schapery [16] assumes a general form describing the craze behavior and models the bulk material as linear viscoelastic. In Schapery's work, a variety of criteria are used for failure of the craze, including a critical crack opening and a critical amount of work done to the deforming material.

While the work presented here is similar to the analyses outlined above, it deals with different physical mechanisms, which lead to distinct crack growth characteristics. Since the matrix is elastic, it is more reasonable to assume that a finite stress intensity factor exists at the crack tip and that crack growth in the matrix is governed by its achieving a critical value. The assumption of a non-zero stress intensity factor at the crack tip is important: the steady-state matrix cracking commonly observed in CMCs under rate-independent conditions, which are a limit of the creep problem, could not be modeled otherwise. It has no analogue in polymers.

Time-dependent crack growth specific to CMCs has been investigated by Nair and co-workers [17, 18]. Crack growth is predicted as a function of time for a fully bridged center crack geometry, where the fiber-matrix interface creeps and the fibers and matrix are elastic. The mechanics of fiber bridging in their work differs significantly from those presented in this paper. Here the fibers are assumed to creep and the fiber-matrix interface properties are time-independent. This is more realistic for CMCs with interfaces whose phase composition is stable at service temperatures, a highly desirable condition that is a universal processing goal. Henager and Jones [7, 8] have provided experimental results for time-dependent crack growth in CMCs, and also a model based on the assumption that fibers creep. In their work, time-dependent crack growth is predicted by assuming that the fibers bridging a matrix crack behave according to a logarithmic creep law taken from experiments. However, their model neglects the debonding that occurs between the matrix and fibers near the crack plane, which is known to be critical in crack propagation in CMCs and to their damage tolerance. They also ignore the effects of fiber creep in the bulk material. More recently, El-Azab and Ghoniem [19] have used a time-dependent bridging law based on linear fiber creep and frictional sliding to predict how bridging tractions decay with time for a non-propagating crack.

Thus, while fibrous composites have been modeled in the literature cited above, the mechanics specific to bridging by creeping fibers coupled to the matrix by friction (i.e. a sliding region between the matrix and fibers near the crack plane) have not previously been included in creep crack growth models.

1.2. The time-dependent bridging law

The bridging law to be used here was derived previously [9], assuming the matrix is elastic and that slip occurs between the fibers and matrix with a time-independent sliding stress along a finite region adjacent to the matrix crack. Details of the full bridging law are given in the Appendix. In certain fairly common circumstances (outlined in the Appendix), the bridging stress, σ , at time t is related to the crack opening displacement, δ , by the differential equation

$$\dot{\delta}(t) = 2\lambda\sigma(t)[\dot{\sigma}(t) + \beta\sigma(t)] \quad (1)$$

where β is a modified creep coefficient:

$$\beta = \frac{BE_t E_L}{2(1-f)E_m} \quad (2)$$

and λ is the bridging law coefficient for the rate-independent case, i.e. [20, 21]

$$\delta = \lambda\sigma^2 \quad (3a)$$

$$\lambda = \frac{D(1-f)^2 E_m^2}{4f^2 \tau E_t E_L^2} \quad (3b)$$

with D the fiber diameter, f the fiber volume fraction, τ the interface friction stress, E_m and E_t the matrix and fiber Young's moduli respectively, and $E_L = fE_t + (1-f)E_m$.

2. PROBLEM FORMULATION

2.1. Development of governing integral equation

The crack velocity is assumed to be constant and the bridging tractions along the crack are fixed in coordinates translating with the crack tip. Therefore, the total opening rate of the crack at x can be written as

$$\dot{\delta}(x) = \frac{d\delta(x)}{dx} \dot{a} \quad (4)$$

where $\dot{\delta}(x)$ is the derivative with respect to time of the total crack opening at a specific distance x from the crack tip and \dot{a} is the steady-state crack velocity. The time derivative of the bridging traction can be treated in a similar manner, allowing the bridging law (1) to be written in the following form:

$$\frac{d\delta(x)}{dx} = 2\lambda\sigma(x) \left[\frac{d\sigma(x)}{dx} + \frac{\beta}{\dot{a}} \sigma(x) \right] \quad (5)$$

Integrating with respect to x yields the steady-state crack opening profile in terms of the steady-state bridging traction profile and the crack velocity:

$$\delta(x) = \lambda\sigma^2(x) + \frac{2\lambda\beta}{\dot{a}} \int_0^x \sigma^2(\bar{x}) d\bar{x} \quad (6)$$

The crack opening profile can also be written as the sum of the opening due to the applied stress intensity factor and the opening due to fiber bridging [22]:

$$\delta(x) = \frac{8 K_\infty}{E} \sqrt{\frac{x}{2\pi}} - \frac{4}{\pi E} \int_0^x \sigma(\bar{x}) \ln \left| \frac{\sqrt{x} + \sqrt{\bar{x}}}{\sqrt{x} - \sqrt{\bar{x}}} \right| d\bar{x}. \quad (7)$$

\bar{E} is a composite elastic modulus which accounts for orthotropy [23, 24] and α is the length of the bridging zone (see Fig. 2).

The crack growth criterion ($K_{ip} = K_c$) provides a relationship between the applied stress intensity factor, the bridging tractions, and the volume fraction adjusted matrix toughness (a known quantity). K_{ip} is expressed as the sum of the far-field applied stress intensity factor K_∞ and the stress intensity factor reduction due to fiber bridging [22]:

$$K_{ip} = K_\infty - \int_0^\alpha \sigma(\bar{x}) \sqrt{\frac{2}{\pi \bar{x}}} d\bar{x} = K_c. \quad (8)$$

Setting equation (6) equal to equation (7) and using equation (8) to substitute for K_∞ , the following integral equation for the bridging traction profile is obtained:

$$\frac{8 K_c}{E} \sqrt{\frac{x}{2\pi}} = \frac{4}{\pi E} \int_0^\alpha \sigma(\bar{x}) \left[\ln \left| \frac{\sqrt{x} + \sqrt{\bar{x}}}{\sqrt{x} - \sqrt{\bar{x}}} \right| - 2 \sqrt{\frac{x}{\bar{x}}} \right] d\bar{x} + \lambda \sigma^2(x) + \frac{2\lambda\beta}{a} \int_0^\alpha \sigma^2(\bar{x}) d\bar{x}. \quad (9)$$

Once the bridging traction profile is determined for a specified velocity, matrix toughness, and bridge length (determined by the fiber failure criterion), the applied stress intensity factor needed to maintain that velocity can be found via equation (8).

2.2. Determining the length of the bridging zone: fiber failure criteria

The length of the bridging zone is determined by evaluating either the crack opening or the total strain in the fiber at the end of the bridging zone, $x = \alpha$. The crack opening profile can be found directly from the bridging tractions using equation (6). Since the fiber at the end of the bridging zone is exposed to creep for the longest time, the crack opening and the total strain in the fiber will be largest there. However, the maximum fiber stress may be near the crack tip rather than at the trailing end of the bridged zone: see below.

If the criterion for fiber failure is maximum total strain, the fiber strain profile is found by replacing the time derivatives in the fiber creep law [given as

equation (A2.1)] with spatial derivatives, as was done for the bridging law. Since the stress in the fiber is equal to the volume fraction of fibers multiplied by the bridging traction, the fiber strain profile along the crack (evaluated at the matrix crack plane) is given by

$$\epsilon(x) = \frac{\sigma(x)}{E_f} + \frac{B}{a} \int_0^x \sigma(\bar{x}) d\bar{x}. \quad (10a)$$

The first term on the right-hand side represents the elastic strain, the second term the additional strain due to fiber creep. This expression is then used to determine the length of the bridging zone by maintaining the condition

$$\epsilon(\alpha) = \epsilon_{cr} \quad (\text{fiber strain criterion}) \quad (10b)$$

where ϵ_{cr} is a fixed critical value.

If the criterion for fiber failure is a critical crack opening, the bridged crack length is found by evaluating equation (6) and equating it to the critical value, δ_{cr} :

$$\delta(\alpha) = \lambda \sigma^2(\alpha) + \frac{2\lambda\beta}{a} \int_0^\alpha \sigma(\bar{x}) d\bar{x} = \delta_{cr} \quad (\text{critical opening criterion}). \quad (10c)$$

Since the problem is non-linear, iteration must be performed to determine the length of the bridging zone needed to maintain the failure criterion. Once the bridging length is found using equations (9) and (10b) [or (9) and (10c)], the applied stress intensity factor is found using equation (8).

2.3. Normalization of the governing integral equation and fiber failure criteria

Introduction of the rate-independent characteristic length scale (or bridging length scale) for the composite allows a convenient normalization of the governing equations. This quantity is given by [2]

$$l = (\lambda \bar{E} K_c)^{2/3}. \quad (11)$$

A matrix crack bridged by rate-independent (non-creeping) fibers approaches steady-state conditions when its length exceeds l . The steady-state matrix cracking stress, σ_{mc} , given by [20, 25]

$$\sigma_{mc} = \left[\frac{12 E_f E_m^2 f \tau K_c^2}{D E_m^2 (1-f) \bar{E}} \right]^{1/3} \quad (12)$$

is related to l by

$$l = \lambda \bar{E} \sigma_{mc}. \quad (13)$$

Using these reference values, the governing integral equation (9) can be rewritten in terms of non-

dimensional variables:

$$\frac{8}{\sqrt{2\pi}} \sqrt{\bar{X}} = \frac{4}{\pi} \int_0^{a/l} \Sigma(\bar{X}) \left\{ \ln \left| \frac{\sqrt{\bar{X}} + \sqrt{\bar{X}}}{\sqrt{\bar{X}} - \sqrt{\bar{X}}} \right| - 2\sqrt{\frac{\bar{X}}{\bar{X}}} \right\} d\bar{X} + \Sigma^2(X) + \frac{2}{v_{ss}} \int_0^x \Sigma^2(\bar{X}) d\bar{X} \quad (14)$$

where

$$v_{ss} = \frac{\dot{a}}{\beta l} \quad (15)$$

is the normalized steady-state crack speed;

$$\Sigma = \frac{\lambda \bar{E} \sigma}{l} = \frac{\sigma}{\sigma_{mc}} \quad (16)$$

is the normalized bridging traction; and $X \equiv x/l$ and $\bar{X} \equiv \bar{x}/l$. Note that the matrix toughness in equation (9) becomes unity when normalized.

Defining the normalized crack opening, Δ , by

$$\Delta \equiv \frac{\delta}{\delta_{mc}} = \frac{\lambda \bar{E}^2 \delta}{l^2} \quad (17)$$

equation (6) becomes

$$\Delta(X) = \frac{\lambda \bar{E}^2}{l^2} \delta(X) = \Sigma^2(X) + \frac{2}{v_{ss}} \int_0^{a/l} \Sigma^2(\bar{X}) d\bar{X}. \quad (18)$$

Consideration of the bridging tractions and openings in terms of steady-state rate-independent matrix cracking distinguishes the effects of fiber creep, as these quantities represent a limit in the absence of creep. The normalized applied stress intensity factor follows from equation (8):

$$\bar{K}_{\infty} = \frac{\lambda \bar{E} K_{\infty}}{l^{3/2}} = \frac{K_{\infty}}{K_c} = 1 + \int_0^{a/l} \Sigma(\bar{X}) \sqrt{\frac{\bar{X}}{\pi \bar{X}}} d\bar{X}. \quad (19)$$

The strain in the fibers at the matrix plane is normalized according to

$$\bar{\epsilon}(X) = \frac{\epsilon(X)}{\epsilon_{ss}} = \frac{\bar{E}}{E_f} \Sigma(\bar{X}) + \frac{2(1-f)E_m \bar{E}}{E_f E_L} \frac{1}{v_{ss}} \int_0^x \Sigma(\bar{X}) d\bar{X} \quad (20a)$$

where

$$\epsilon_{ss} = \frac{1}{\lambda \bar{E}^2} \quad (20b)$$

is the strain that would exist in an uncracked, non-creeping composite loaded to the steady-state matrix cracking stress, σ_{mc} . Critical values of $\bar{\epsilon}$ will usually be ~ 10 .

2.4. Numerical solution of the equations

The governing integral equation (14), can be solved by representing the bridging traction by smooth, parametric basis functions defined on small intervals; a non-linear matrix equation results which can be solved using standard methods. Such methods have become common and examples are available in Refs 26–28. The paper by Begley and McMeeking [28] provides details of the particular method used here.

3. RESULTS

3.1. Bridging traction distributions

Examples of bridging traction distributions for various crack speeds are given in Fig. 3(a), for the case where fiber failure is dictated by a critical crack opening. Each curve represents the resultant steady-state traction profile for a given crack speed. The bridging zone size depends on the steady-state crack velocity and the fiber failure criterion used. For higher crack speeds, the bridging traction profile approaches the distribution for the rate-independent case. The fibers are exposed to creep for shorter times and accumulate negligible creep strain, so that the bridging tractions have not relaxed much. The bridging stress profiles near the rate-independent limit show a significant stress concentration at the end of the bridging zone. At lower velocities, preferential creep relaxation where the fiber stress is highest attenuates this effect.

Bridging traction distributions for several crack speeds are shown in Fig. 3(b) for the case where a critical fiber strain governs fiber failure. The curves are similar in shape to the critical opening case, but now, as crack speed increases, the steady-state bridge length increases as well, as opposed to the critical opening case, where bridge lengths decrease with increasing velocity. This difference in bridge length dependence on crack velocity for the two cases is further discussed in Sections 3.5–3.6. It can be

Bridging law: $\delta = 2\lambda\sigma[\dot{\sigma} + \beta\sigma]$

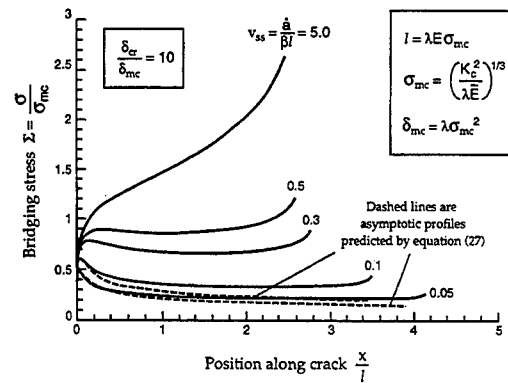


Fig. 3(a). Steady-state bridging stress distributions where fiber failure is governed by a critical opening for five different crack velocities.

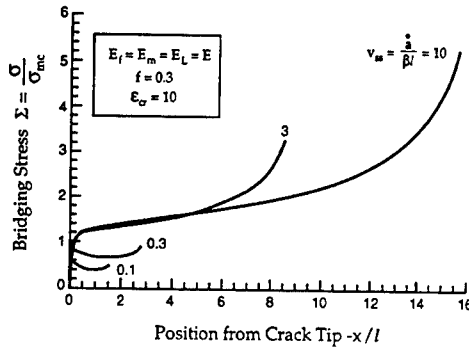


Fig. 3(b). Steady-state bridging stress distributions where fiber failure is governed by a critical fiber strain for five different crack velocities.

explained most easily by considering the asymptotic behavior of the system, which is analysed in Section 4.

As a result of the constant crack velocity assumption, the amount of time the fibers bridging the crack undergo creep is linear with distance from the crack tip. Thus, the bridging traction profiles shown in Fig. 3(a) and (b) also represent the stress history of a given fiber as the crack sweeps by; the distance from the crack tip can be reinterpreted as the time a fiber has been exposed to creep. As a fiber first enters the crack, it is quickly loaded and responds elastically; as the crack sweeps past, the fiber creeps and the bridging traction relaxes. When the fiber has almost reached the end of its life, the bridging traction due to the fiber rises because of the stress concentration at the end of the bridging zone.

The curves shown in Fig. 3(a) and (b) are qualitatively consistent with those compiled by Begley, Cox and McMeeking [10] for non-steady-state conditions. Both their work and the results presented here show the same characteristic peak in the bridging stress near the crack tip. However, comparison should not be taken too far. The results of Begley *et al.* [10] were generated for the case of a center crack under constant load, whereas the results presented here are for a semi-infinite crack with a constant applied stress intensity factor.

3.2. Fiber strain distributions

Several fiber strain distributions are shown in Fig. 4(a) and (b) for the case of equal matrix and fiber elastic moduli and a fiber volume fraction of 0.3. These curves were calculated using equation (10) and represent the strain in the fibers at the matrix crack plane. The solid lines are the total strain in the fibers as a function of distance from the crack tip, while the dashed lines show the creep strain contribution for each case. The elastic contribution to strain is thus the difference between the two curves. Since the curves in Fig. 4 were taken from results generated by assuming a critical failure strain, the maximum strain (which occurs at the end of the bridging zone) is the

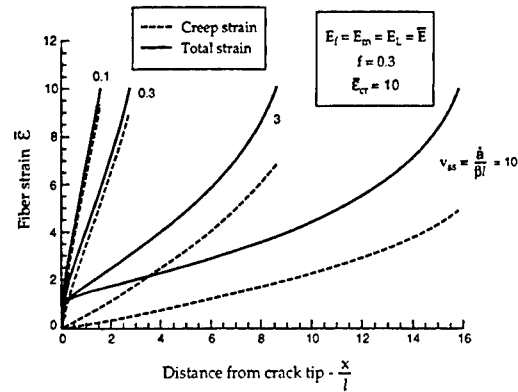


Fig. 4(a). Steady-state total fiber strain and creep strain distributions where fiber failure is governed by a critical fiber strain for five different crack velocities.

same for each profile. In contrast, the fiber strain at the end of the bridging zone is different in Fig. 4(b) for each case, as fiber failure is governed by a critical opening.

The curves in Fig. 4 for a crack velocity of $v_{ss} = 0.1$ illustrate that at low speeds, nearly all of the strain in the fibers is achieved via creep. As the crack velocity is increased, the amount of time during which the fibers undergo creep decreases significantly, and the elastic contribution to the strain increases. The curves also illustrate that bridging lengths will either decrease or increase with crack velocity, depending on the fiber failure criterion. This behavior was evident in Fig. 3(a) and (b) and is discussed in detail in subsequent sections.

The strain profiles have no simple connection to the crack opening profiles; the crack opening files corresponding to the cases shown in Fig. 4(a) and (b) must be calculated via equation (17) using the bridging traction profile that results from the solution of equation (14).

3.3. Crack velocity as a function of applied stress intensity factor

The steady-state crack velocity is shown in Fig. 5 as a function of applied stress intensity factor

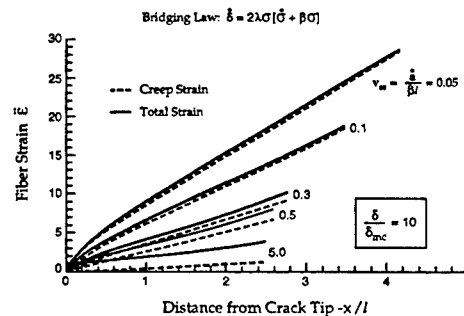


Fig. 4(b). Steady-state total fiber strain and creep strain distributions when fiber failure is governed by a critical opening for five different crack velocities.

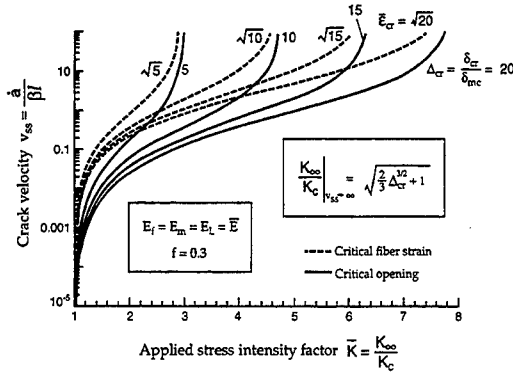


Fig. 5. Steady-state crack velocity as a function of applied stress intensity factor for four values of the two fiber failure criteria.

criterion of critical opening and the dashed lines to the criterion of critical fiber strain. For both cases, as the applied stress intensity factor is increased above the effective matrix toughness, the crack velocity increases rapidly. Decreasing the critical value governing fiber failure for either criterion will increase the steady-state crack velocity for a given applied stress intensity factor. The general trend of these curves is easily explained; as the crack velocity increases, the relaxation of bridging tractions decreases and higher loads are needed to overcome the more effective bridging.

In these plots, $\bar{K}_{\infty} = 1$ (i.e. $K_{\infty} = K_c$) represents a lower threshold for crack growth. At zero velocity, creep completely relaxes the bridging tractions and crack growth occurs at the toughness of the monolithic matrix material adjusted for the volume fraction of the fibers.

There is also an upper threshold on the applied stress intensity factor. At high velocities, creep in the fibers is negligible and the system responds in a rate-independent manner. In this limit only, the critical opening displacement and strain criteria [equations (10b) and (10c)] are related simply by $\bar{\epsilon}_{cr} = \sqrt{\Delta_{cr}}$. Furthermore, for the rate-independent limit, there exists a critical applied stress intensity factor that causes unstable matrix cracking. Its value can be found analytically by applying the J-integral along a path at the crack faces and equating it to the J-integral taken in the far field, thus relating K_{∞} to an integral of the rate-independent bridging law [29, 30]. The result is the following expression for the critical applied stress intensity factor as the crack velocity approaches infinity:

$$\left(\frac{K_{\infty}}{K_c} \right)_{v_{ss} \rightarrow \infty} = \sqrt{\frac{2}{3} \Delta_{cr}^{3/2} + 1}$$

$$= \sqrt{\frac{2}{3} \bar{\epsilon}_{cr}^3 + 1} \quad \bar{\epsilon}_{cr} = \sqrt{\Delta_{cr}}; \quad v_{ss} \rightarrow \infty. \quad (21)$$

The curves in Fig. 5 illustrate this upper limit and the concurrence of the two criteria when $\bar{\epsilon}_{cr} = \sqrt{\Delta_{cr}}$ as $v_{ss} \rightarrow \infty$.

3.4. Bridging length behavior for the critical crack opening criterion

The bridging length as a function of crack speed is shown in Fig. 6 for the critical opening criteria. The curves show that the maximum bridge length is obtained as $v_{ss} \rightarrow 0$, and that larger critical openings always result in larger bridge lengths for a given crack velocity. The minimum bridge length is apparently not achieved as the crack velocity tends towards infinity; the numerical results show a shallow minimum in the bridge length at a finite crack velocity.

The bridge length for zero velocity corresponds to the location where the crack opening for an unbridged crack equals the critical opening. In the limit when the crack speed goes to zero, the bridging tractions are completely relaxed via creep and the crack opening profile is merely that of an unbridged crack. As the crack speed tends towards infinity, the system responds nearly rate-independently and the resulting bridge length is the same as the length that would result from rate-independent bridging analysis.

The schematic of Fig. 7 shows why the bridge length must be smaller in the limit of infinite velocity than it is for zero velocity for the critical crack opening criterion. The crack profile at zero velocity tends towards a parabola whose curvature at the crack tip is consistent with $K_{tip} = K_c$. The bridge length is determined by the intersection of this parabola with the ordinate $\delta = \delta_{cr}$. At very high velocity, the profile must approach this same parabola near the crack tip; but in the far wake of the crack, it must approach a parabola whose curvature is consistent with K_a . Since $K_a > K_c$ at any velocity greater than zero, the far-wake

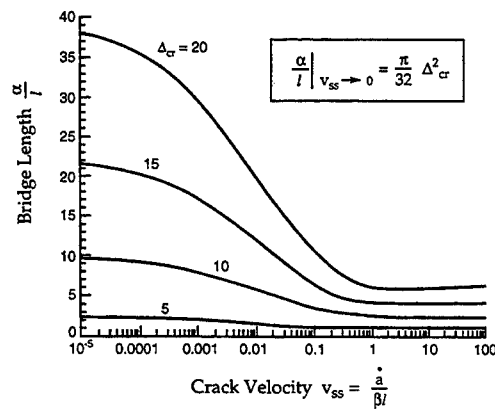


Fig. 6. Bridge length as a function of steady-state crack velocity for critical crack opening fiber failure criterion.

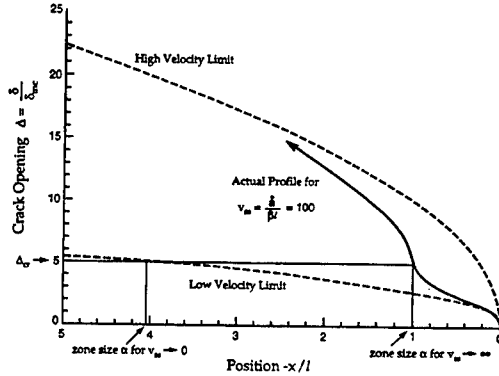


Fig. 7. Schematics of limiting crack profiles at zero and very large crack velocities, with bridging zones marked off for critical opening criterion.

limiting profile must lie above the near-tip limiting profile. The high velocity profile must take on a shape similar to that shown in Fig. 7. Its intersection with the ordinate $\delta = \delta_{cr}$ must define a shorter bridge zone.

There is no plot corresponding to Fig. 7 for the critical strain criterion. The utility of Fig. 7 derives from the existence of an easily analysed crack configuration that is asymptotically independent of velocity. In the critical strain case, the crack profile has no such limit. The profile behaves according to the asymptotic results derived in Section 4.

3.5. Bridging length behavior of the critical fiber strain criterion

The relationship between bridge length and steady-state crack velocity is illustrated in Fig. 8 for eight different critical strains. The elastic moduli of the matrix and fibers were assumed to be the same, and the fiber volume fraction used was $f = 0.3$. Varying the fiber volume fraction and the ratio of elastic moduli does not qualitatively change the results.

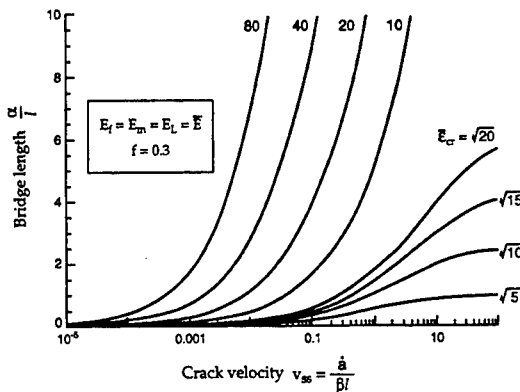


Fig. 8. Bridge length as a function of steady-state crack velocity for critical strain fiber failure criterion.

For critical strains < 10 (e.g. $\epsilon_{cr} = \sqrt{20}$, $\sqrt{15}$, $\sqrt{10}$, and $\sqrt{5}$ in Fig. 8), the bridging length asymptotes to values only a few times greater than 1 as the crack velocity increases. As for the critical opening criterion, as the crack velocity increases, crack growth is governed by the rate-independent limit. The strains in the fibers at the notch for the rate-independent case are relatively small, however, and significantly higher loads and bridge lengths are required to satisfy higher critical strains. Thus, when larger critical values ($\epsilon_{cr} \geq 10$) are used, the bridge lengths become exceedingly large as the crack velocity increases. For values typical of ceramic matrix composites, these longer bridge lengths are of the order of tens of millimeters. Accurate numerical results are difficult for these cases, as the significantly longer bridge lengths require a large number of grid points in the discretization of the bridging traction profile; and numerical instabilities set in when $\alpha \gg 1$ [26, 31]. Therefore, calculations were limited to the range shown in Fig. 8.

Figures 6 and 8 show very different bridging lengths for the two fiber failure criteria. When critical openings are used, the bridging length decreases with increasing crack velocity, whereas the opposite trend is observed for the case of a critical fiber strain. The bridging length behavior for the two cases can be directly compared by noting that the critical strain values in Fig. 8 and the critical opening values in Fig. 6 were chosen to give coincident crack configurations in the high velocity limit. Consider, for example, the curve for $\Delta_{cr} = 10$ in Fig. 6 and the curve for $\epsilon_{cr} = \sqrt{10}$ in Fig. 8. The bridging length dependence on velocity for the critical strain case and the connection between bridging lengths and bridging stress magnitudes can best be explained by considering the asymptotic behavior for low velocities, presented in the next section.

4. ASYMPTOTIC LIMITS FOR SLOW CRACK GROWTH

4.1. Asymptotic result for the bridging stress profile

When crack growth is very slow, creep in the fibers has significant time to relax the bridging tractions, resulting in a crack opening profile that is not much different from the parabolic opening due to the applied load:

$$\delta(x) \approx \eta \sqrt{x} \quad (22)$$

where

$$\eta = \frac{8K_c}{\bar{E}\sqrt{2\pi}} \quad (23)$$

This expression can be combined with the steady-state crack opening profile predicted by the bridging law [expression (1)] to formulate the following differential equation for the bridging stress profile:

$$\frac{dy}{dx} + \frac{2\beta}{a} y = \frac{\eta}{2\lambda} \frac{1}{\sqrt{x}} \quad (24)$$

where $y \equiv \sigma^2$.

The solution to equation (24) yields the bridging stress profile at very slow crack speeds:

$$\sigma(x) = \left[\frac{\eta\sqrt{\pi}}{2\lambda} \left(\frac{a}{2\beta} \right)^{1/2} \times e^{-2\beta x/a} \operatorname{erfi} \left\{ \left(\frac{2\beta}{a} x \right)^{1/2} \right\} \right]^{1/2} \quad (25)$$

where $\operatorname{erfi}(x)$ is the imaginary error function, defined by

$$\operatorname{erfi}(x) = -i \operatorname{erf}(ix). \quad (26)$$

Using the normalizations presented in Section 2.3 and equation (23) to eliminate η , the normalized bridging stress profile will be

$$\Sigma(X) = \frac{\sigma(X)}{\sigma_{mc}} = \left(\frac{4}{\pi} \right)^{1/2} v_{ss}^{1/4} \times e^{-X/v_{ss}} \left\{ \operatorname{erfi} \left[\left(\frac{2X}{v_{ss}} \right)^{1/2} \right] \right\}^{1/2}. \quad (27)$$

This asymptotic form of the bridging stress profile can be used to predict the system behavior at very low crack speeds. The profiles predicted by equation (27) have been superimposed on the numerical results in Fig. 3(a) for the two lowest velocities. The agreement between the numerical results and the asymptotic prediction improves with decreasing velocity.

4.2. Asymptotic behavior of the bridged zone very near the crack tip

The bridging stress profile very near the crack tip can be examined by noting that at small values of x , the exponential term in equation (27) goes to unity and the imaginary error function can be approximated by the first term in a series expansion in $X^{1/2}$ [32]. The normalized bridging stress profile very near the crack tip is then given by

$$\Sigma(X) \approx \frac{2}{\pi^{1/4}} X^{1/4} \quad \text{for } \frac{X}{v_{ss}} \ll 1. \quad (28)$$

This expression can be used with equation (20) to predict the normalized strain distribution:

$$\bar{\epsilon}(X) \approx \frac{2\bar{E}}{E_f} \left(\frac{X}{\pi} \right)^{1/4} + \frac{\sqrt{8}}{\pi^{1/4}} \frac{(1-f)\bar{E}E_m}{E_f E_L} \left(\frac{1}{v_{ss}} \right)^{3/4} X \quad (29)$$

where the first term on the right-hand side represents elastic fiber strain and the second creep strain. Thus the creep strain is asymptotically linear in x and, since it varies as $v_{ss}^{-3/4}$, it dominates the total strain for very low crack velocities. These trends are borne out in the log-log plot of Fig. 9. Extremely close to the crack

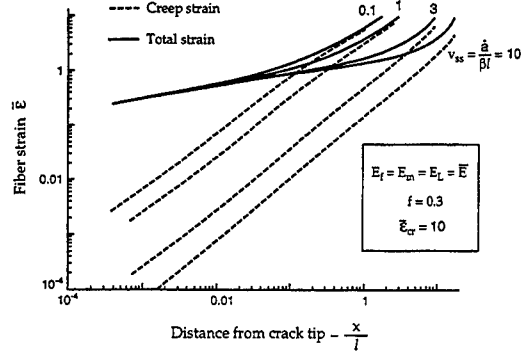


Fig. 9. Fiber strain distributions for critical strain fiber failure criterion shown on a log-log scale.

tip, the total strain is dominated by the elastic contribution, leading to $\bar{\epsilon} \propto X^{1/4}$, which can also be seen in Fig. 9.

4.3. Asymptotic dependence of the applied stress intensity factor and the bridge length on crack velocity

When the steady-state crack velocity $v_{ss} = \dot{a}/\beta l \ll 1$, equation (27) can be approximated by [24]

$$\Sigma(X) \approx (v_{ss})^{1/2} \left(\frac{1}{2X} \right)^{1/4} \quad \frac{X}{v_{ss}} \gg 1. \quad (30)$$

The corresponding strain profile results from combining equation (30) with equation (20):

$$\bar{\epsilon}(X) = \frac{\bar{E}}{E_f} \left\{ (v_{ss})^{1/2} \left(\frac{1}{2X} \right)^{1/4} + \frac{4(1-f)E_m}{3E_L} \left(\frac{1}{v_{ss}} \right)^{1/2} (2X)^{3/4} \right\} \quad \frac{X}{v_{ss}} \gg 1. \quad (31)$$

Under the condition $X/v_{ss} \gg 1$, the second term (creep strain) dominates equation (31), allowing the strain profile to be approximated as

$$\bar{\epsilon}(X) = \frac{4(1-f)E_m\bar{E}}{3E_f E_L} \left(\frac{1}{v_{ss}} \right)^{1/2} (2X)^{3/4} \quad \frac{X}{v_{ss}} \gg 1. \quad (32)$$

Equation (30) can be used with equation (19) to predict the asymptotic dependence of the applied stress intensity factor on the steady-state crack velocity. The bridging length in the resulting equation is removed by applying the fiber failure criterion via equation (10b) or (10c). For the case of a critical opening, the asymptotic limit for the applied stress intensity factor is given by

$$\left(\frac{K_{\infty}}{K_c} \right)_{\text{asym}} \approx 1 + \frac{1}{2\pi^{1/4}} \left(\frac{\delta_{cr}}{\delta_{mc}} \right)^{1/2} (v_{ss})^{1/2} \quad (v_{ss} \rightarrow 0). \quad (33)$$

The asymptotic dependence of the normalized bridge length for the case of a critical opening is obtained

directly from evaluating equation (22) at $x = \alpha$:

$$\left(\frac{\alpha}{l}\right)_{\text{asym}} = \frac{\pi}{32} \left(\frac{\delta_{\alpha}}{\delta_{mc}}\right)^2 (v_{ss} \rightarrow 0). \quad (34)$$

Here the bridging length is independent of v_{ss} for small v_{ss} , which is confirmed by the shape of the full solutions in Fig. 6. The quadratic dependence on δ_{cr} reflects the limiting parabolic crack opening.

For the case where fiber failure is governed by a critical strain, the asymptotic limit for the applied stress intensity factor can be derived using equation (30) in conjunction with equations (19) and (32), resulting in

$$\left(\frac{K_{\infty}}{K_c}\right)_{\text{asym}} = 1 + \frac{4}{\pi^{1/4}} \left(\frac{3E_f E_L}{4(1-f)E_m}\right)^{1/3} (\bar{\epsilon}_{cr})^{1/3} (v_{ss})^{2/3} \times (v_{ss} \rightarrow 0). \quad (35)$$

For the same criterion, the asymptotic variation of the bridge length can be found by evaluating equation (32) at $x = \alpha$ and inverting:

$$\left(\frac{\alpha}{l}\right)_{\text{asym}} = \frac{1}{4} \left(\frac{3E_L}{4(1-f)E_m}\right)^{4/3} (\bar{\epsilon}_{cr})^{4/3} (v_{ss})^{2/3}. \quad (36)$$

Thus the bridge length will go to zero as the crack velocity approaches zero, in contrast to the behavior in the critical opening case. These results can be used to check the numerical results given in Figs 5 and 6 for the case of small velocities. The numerical results for the bridging length vs velocity for the critical strain case are re-plotted on a log-log scale in Fig. 10 to highlight the power-law dependence. The slope of the lines is $2/3$ at low v_{ss} , in agreement with equation (36).

Further insight into why the bridging lengths decrease with decreasing velocity for the critical strain case follows from considering the length of time, t_a , for which the fiber at the end of the bridging zone is exposed to creep. From the steady-state

velocity assumption,

$$t_a = \frac{\alpha}{v_{ss}}. \quad (37)$$

Combining this with the asymptotic result (36) for the bridge length gives

$$t_a = \frac{1}{4} \left(\frac{1}{v_{ss}}\right)^{1/3} \left(\frac{3E_L \bar{\epsilon}_{cr}}{4(1-f)E_m}\right)^{4/3}.$$

Therefore, as the crack velocity approaches zero, the amount of time during which the last surviving fiber is exposed to creep goes to infinity. Even though the bridging stress applied by the fiber decreases with velocity as well, the decrease in bridging traction due to slower velocities is not nearly as sensitive to crack speeds. The bridging length will therefore tend to zero as the crack speed decreases.

The shorter bridging lengths in the critical strain case (for a given crack speed) do not necessarily imply larger bridging tractions than in the critical opening case, as the applied stress intensity factor for the critical strain case will be lower as well. To fully understand the interplay between shorter bridging lengths, crack tip stress intensity factors, and bridging lengths, the asymptotic relations given by equations (33)–(38) must be examined critically.

5. DISCUSSION

5.1. Implications of a finite stress intensity factor at the crack tip

The trends in bridging length behavior are qualitatively similar to those presented for craze growth in polymers. The work of Knauss and Losi [11, 12] illustrates that when fibril failure is governed by a critical strain, bridging lengths decrease with decreasing velocity. The critical opening case is similar to the results of Fager *et al.* [13], showing decreasing bridge length with increasing velocity. In general for both criteria, the craze literature reports the same trends of increasing velocity with increasing applied stress intensity factor.

While the general trends are similar, the assumption of a finite stress intensity factor at the matrix crack tip results in significant differences at low velocities. When $K_{tip} = 0$, the crack profile must be cuspidal. When $K_{tip} \neq 0$, it is asymptotically parabolic. The algebraic relationship between applied stress intensity factor and the crack velocity found here is therefore peculiar to the problem of a crack in an elastic matrix.

And, of course, the lower threshold on K_{∞} , namely $K_{\infty} = K_c$ (see Fig. 5), does not exist unless a finite stress intensity factor occurs at the matrix crack tip. For CMCs where the matrix is elastic, there exists a threshold in the applied loading below which crack growth will not occur: this is the applied stress intensity factor which is equal to the matrix toughness adjusted for the fiber volume fraction.

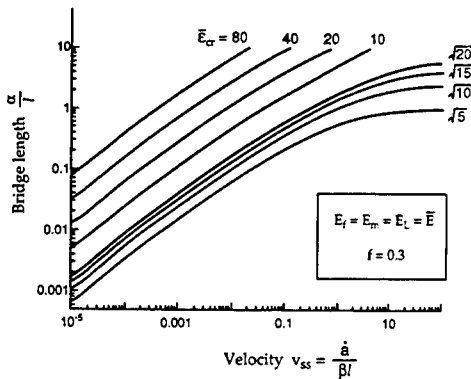


Fig. 10. Bridge length as a function of steady-state crack velocity for critical strain fiber failure criterion shown on a log-log scale.

5.2. Influence of the assumed form of the bridging law

At very high velocities there are significant differences as well. In general, the cohesive zone analyses of the craze literature predict a power-law relationship between the crack velocity and the applied stress intensity factor at high velocities [14]. This is a result of the assumed form of the bridging law, a power-law dependence of crack opening rate on the bridging stress. Such behavior predicts no upper limit on the applied stress intensity factor. In contrast, the bridging law used here has a rate-independent component that dominates at high velocities as creep effects become negligible. Thus, one of the attractive features of the work presented here is that a connection is made with previous analyses for rate-independent CMCs. The phenomenon of instantaneous matrix cracking above a critical applied load is predicted by using a bridging law that is still valid in regimes where creep effects are negligible.

5.3. Pertinence of small scale bridging conditions

Whatever the expected length of the zone of intact bridging fibers, it is possible in principle to satisfy the conditions of small scale bridging in a large enough specimen with a large enough notch. But in practice small scale bridging will be most easily achieved if the bridging zone is very small. Thus the ease of preparing specimens for studying the small scale bridging limit depends on the prevailing fiber failure criterion: only in materials in which fiber failure occurs at a critical strain can arbitrarily small bridging zones be obtained (Fig. 8). For these materials, small scale bridging should always be obtainable simply by going to lower applied stresses.

This is indeed likely to be the usual case. The critical fiber strain criterion is the more physically reasonable, as discussed in the following section.

5.4. Appropriateness of fiber failure criteria

When materials with creeping ceramic fibers are considered, the critical fiber strain criterion is clearly the more relevant of the two criteria used here. While the critical opening criterion has no obvious direct physical basis for the case of creeping ceramic fibers, it has been used previously as a bridging failure criterion and may be relevant to other material systems. Additionally, the total crack opening is a parameter that may be easier to measure experimentally than fiber strain, which would be particularly difficult to quantify on a fiber-by-fiber basis.

The critical strain for fiber failure could be based on creep rupture data taken directly from creep tests performed on bare fibers and thus related to the creep ductility of the fibers. For typical SiC/SiC composite near 1200°C, a strain of 1% translates into the normalized value $\bar{\epsilon}_{cr} = 52$. Therefore, higher values for $\bar{\epsilon}_{cr}$ than those shown in Fig. 5 are also of interest. For critical strains near or above 1%, the applied

stress intensity factor must be very high to generate elastic strains at the notch of the requisite magnitude. In this regime, the bridge lengths become very large.

The fiber failure criterion could alternatively have been based on a critical value of creep strain rather than total strain. At low velocities, where the creep strains dominate, this would make negligible difference. At higher velocities, the results would be significantly different, since the creep contribution to fiber strain disappears as the time fibers are exposed to creep goes to zero. Choosing a critical creep strain implies that the bridge lengths would be enormous at high velocities, as longer and longer bridge lengths would be necessary to expose the fibers to creep to achieve sufficient creep strains. In the limit of rate-independent cracking (i.e. $v_{ss} \rightarrow \infty$), bridge lengths would go to infinity. The small scale bridging assumption implied by the steady-state analysis presented here would not then be satisfied.

Because of the qualitatively different trends in bridging length for different failure criteria, experimental measurements of bridging zone length vs crack speed (i.e. applied stress intensity factor) would be useful in empirical discrimination of the models.

It is plausible that a fiber failure criterion based on stress would be more realistic in some regimes, either a temperature-dependent fiber strength or a fracture stress based on a characteristic flaw size in the fibers. The traction profiles of Fig. 3 suggest possible instability in this case. There are two crack locations at which the stress exhibits a local maximum, one at the trailing edge of the bridging zone and one behind the crack tip. If failure can occur behind the crack tip, it is feasible that steady-state propagation would give way to a pulsing or stick-slip motion, involving alternation between states with long and short bridging zones. Further calculations appear warranted to pursue this curiosity.

Lastly, it should be pointed out that in some cases, oxidation will play an important role in the fiber failure mechanism. In these situations, the amount of time during which the fibers are exposed to oxidation (i.e. when the fibers are in the crack wake) will influence the lifetime of the fiber. While assuming a critical time to failure of the fibers would be attractive due to its simplicity, it fails to account for the stress dependence of the oxidation failure mechanism. The coupled stress-time dependence of fiber failure presents significant difficulties and was not considered here.

6. SUMMARY

Crack growth has been predicted for regimes where bridging lengths are small compared to total crack lengths. Using two different fiber failure criteria to establish the steady-state bridge length, crack velocities are shown to increase as the applied stress intensity factor is increased. When fiber failure is governed by a critical crack opening, bridge lengths

decrease with increasing velocity; assuming a critical total fiber strain results in an opposite trend. Asymptotic results are given (and verified by numerical calculations) for regimes of very slow crack growth. Very different behavior from similar analyses for polymers is predicted as a result of a non-zero stress intensity factor at the matrix crack tip and a bridging law which accounts for frictional sliding. Small scale bridging conditions in experiments should be expected at low stresses when fiber failure is governed by a critical strain criterion.

Acknowledgements—MRB and RMM were supported by the Advanced Research Projects Agency through the University Research Initiative, ONR Contract N00014-92-J-1808. BNC was supported by the U.S. AFOSR, Contract No. F49620-94-C-0030.

REFERENCES

- Evans, A. G. and Marshall, D. B., *Acta metall. mater.*, 1987, **37**, 2567.
- Cox, B. N. and Marshall, D. B., *Acta metall. mater.*, 1994, **42**, 341.
- Beyerle, D. S., Spearing, S. M. and Evans, A. G., *J. Am. Ceram. Soc.*, 1992, **75**, 3321.
- Lamoureux, F., Steen, M. and Valles, J. L., *J. Europ. Ceram. Soc.*, 1994, **14**, 529.
- Xia, C., Carr, R. R. and Hutchinson, J. W., *Acta metall. mater.*, 1993, **41**, 2365.
- Cox, B. N. and Marshall, D. B., *J. Am. Ceram. Soc.*, 1996, **79**, 1181.
- Henager, C. H. and Jones, R. H., *Mater. Sci. Engng A*, 1993, **166**, 211.
- Henager, C. H. and Jones, R. H., *J. Am. Ceram. Soc.*, 1994, **77**, 2381.
- Begley, M. R., Evans, A. G. and McMeeking, R. M., *J. Mech. Phys. Solids*, 1995, **43**, 727.
- Begley, M. R., Cox, B. N. and McMeeking, R. M., *Acta metall. mater.*, 1995, **43**, 3927.
- Knauss, W. G., *J. Engng Mater. Technol.*, 1993, **115**, 262.
- Knauss, W. G. and Losi, G. U., *J. appl. Mech.*, 1993, **60**, 793.
- Fager, L.-O., Bassani, J. L., Hui, C.-Y. and Yu, D.-B., *Int. J. Fracture*, 1991, **52**, 119.
- Fager, L.-O. and Bassani, J. L., *J. Engng Mater. Technol.*, 1993, **115**, 252.
- Kramer, E. J. and Hart, E. W., *Polymer*, 1984, **25**, 1667.
- Schapery, R. A., *Int. J. Fracture*, 1975, **11**, 141.
- Nair, S. V., Jakus, K. and Lardner, T. J., *Mech. Mater.*, 1991, **12**, 229.
- Nair, S. V. and Gwo, T.-J., *J. Engng Mater. Technol.*, 1993, **115**, 273.
- El-Azab, A. and Ghoniem, N. M., *J. Nuclear Mater.*, 1995, **219**, 101.
- McCartney, L. N., *Proc. R. Soc. Lond.*, 1987, **A409**, 329.
- Hutchinson, J. W. and Jensen, *Mech. Mater.*, 1990, **9**, 139.
- Tada, H., Paris, P. C. and Irwin, G. R., *The Stress Analysis of Cracks Handbook*. Del Research, St. Louis, MO, 1985.
- Sih, G. C., Paris, P. C. and Irwin, G. R., *Int. J. Fracture Mech.*, 1965, **1**, 189.
- Bao, G. and McMeeking, R. M., *Acta metall. mater.*, 1994, **42**, 2415.
- Aveston, J., Cooper, G. A. and Kelly, A., in *Conference Proceedings of the National Physical Laboratory*. IPC Science and Technology Press, Surrey, England, 1971, p. 15.
- Cox, B. N. and Marshall, D. B., *Acta metall. mater.*, 1991, **39**, 579.
- Cox, B. N. and Rose, L. R. F., *Mech. Mater.*, 1994, **19**, 39.
- Begley, M. R. and McMeeking, R. M., *Mater. Sci. Engng A*, 1995, **200**, 12.
- Rose, L. R. F., *J. Mech. Phys. Solids*, 1987, **34**, 383.
- Budiansky, B., Hutchinson, J. W. and Evans, A. G., *J. Mech. Phys. Solids*, 1986, **34**, 167.
- Hughes, B. D. and White, L. M., *Q. J. appl. Math.*, 1979, **32**, 445.
- Handbook of Mathematical Functions*, ed. M. Abramowitz and I. A. Stegun, Applied Mathematics Series 55, National Bureau of Standards, 1964.
- Marshall, D. B., Cox, B. N. and Evans, A. G., *Acta metall. mater.*, 1985, **33**, 2013.
- DiCarlo, J. A. and Morscher, G. N., *Failure Mechanisms in High Temperature Composite Materials*. ASME AD-Vol. 22/AMD-Vol. 122, 1991, p. 15.
- Simon, G. and Bunsell, A. R., *J. Mater. Sci.*, 1984, **19**, 3658.
- McLean, M., *Comp. Sci. Technol.*, 1985, **23**, 37.

APPENDIX 1

Nomenclature

E_t, E_m	Young's modulus of fibers and matrix, respectively
$E_L = fE_t + (1-f)E_m$	Rule of mixtures composite Young's modulus
\tilde{E}	composite modulus which accounts for orthotropy
f	fiber volume fraction
D	fiber diameter
B	creep coefficient of fibers
$\beta = \frac{BE_tE_L}{2(1-f)E_m}$	modified creep coefficient of the fibers
τ	shear sliding stress at fiber-matrix interface
$\sigma, \dot{\sigma}$	bridging stress, bridging stress rate
$\delta, \dot{\delta}$	total crack opening, total crack opening rate
$\lambda = \frac{D(1-f)^2E_m^2}{4f^2\tau E_t E_L^2}$	rate-independent bridging coefficient ($\delta = \lambda\sigma^2$)
$T = \frac{E_L}{(1-f)BE_tE_m}$	characteristic relaxation time of intact composite
\dot{a}	steady-state crack velocity
K_c	critical stress intensity factor for matrix crack extension
K_∞	far-field applied stress intensity factor
α	length of bridged region of matrix crack
ϵ_{cr}	critical total strain needed to rupture fibers
$\sigma_{mc} = \left[\frac{12f^2\tau E_t E_L^2 K_c^2}{D(1-f)E_m^3} \right]^{1/3}$	steady-state matrix cracking stress
$l = (\lambda \tilde{E} K_c^2)^{2/3} = \lambda \tilde{E} \sigma_{mc}$	characteristic length scale for composite
$\delta_{mc} = \lambda \sigma_{mc}^2$	total crack opening at steady-state matrix cracking stress (for the rate-independent case)
$\Sigma = \frac{\lambda \tilde{E} \sigma}{l} = \frac{\sigma}{\sigma_{mc}}$	normalized bridging stress
$\Delta = \frac{\lambda \tilde{E}^2 \delta}{l^2} = \frac{\delta}{\delta_{mc}}$	normalized total crack opening
$v_{ss} = \frac{\dot{a}}{\beta l}$	normalized steady-state crack velocity

$\bar{K}_\infty = \frac{\lambda \bar{E} K_\infty}{l} = \frac{K_\infty}{\bar{K}_c}$	normalized applied stress intensity factor
$\epsilon_{ss} = \frac{l}{\lambda \bar{E}^2}$	strain in uncracked, non-creeping composite loaded to steady-state matrix cracking stress
$\bar{\epsilon} = \frac{\epsilon}{\epsilon_{ss}}$	normalized total fiber strain at crack plane
$\bar{\epsilon}_{cr}$	normalized critical total strain to fiber failure
Δ_{cr}	normalized critical total opening to fiber failure
$(K_\infty)_{asym}$	asymptotic applied stress intensity factor at low crack speeds
α_{asym}	asymptotic bridge length at low crack speeds
t_a	time during which fiber at end of bridging zone is exposed to creep

APPENDIX 2

Details of the bridging law

The bridging law derivation [9, 10] is based on a cell model similar to the elastic case [20, 21, 33]. The fibers are assumed to creep linearly, according to

$$\dot{\epsilon}_f = \frac{\dot{\sigma}_f}{E_f} + B\sigma_f \quad (\text{A2.1})$$

where $\dot{\epsilon}_f$ is the axial strain rate of the fiber, E_f is the Young's modulus of the fibers, and $\dot{\sigma}_f$ and σ_f are the axial stress rate and stress, respectively, applied to the fiber. B is the creep coefficient of the fibers. (Creep data for SiC fibers can be found in Refs [34] and [35].)

The relationship between the crack opening rate and the stress and stress rate applied to the cell model is given by

$$\begin{aligned} \dot{\delta}(t) = & \frac{(1-f)^2 E_m D}{2f^2 \tau E_f} \\ & \times \left\{ \frac{\sigma(t)}{E_L} + \frac{BfE_f^2}{E_L^2} \int_{-\infty}^t \sigma(\tau) e^{-(t-\tau)/T} d\tau \right\} \\ & \times \left\{ \frac{\dot{\sigma}(t)}{E_L} + \frac{BE_f \sigma(t)}{2(1-f)E_m} \left[1 + \frac{fE_f(fE_f - (1-f)E_m)}{E_L^2} \right] \right. \\ & \times \left. \left\{ \int_{-\infty}^t \frac{\sigma(\tau)}{T\sigma(t)} e^{-(t-\tau)/T} d\tau - 1 \right\} \right\} \quad (\text{A2.2}) \end{aligned}$$

where $\dot{\delta}(t)$ is the total opening rate of the matrix cracks as a function of time t ; $\sigma(t)$ and $\dot{\sigma}(t)$ are the stress and stress rate, respectively, applied to the cell model; E_m and $E_L = fE_f + (1-f)E_m$ are the matrix Young's modulus and the composite Young's modulus, respectively, τ is the shear sliding stress between the fibers and the matrix; D is the diameter of the fibers; and f is the fiber volume fraction. The characteristic relaxation time, T , for the intact material is given by

$$T = \frac{E_L}{(1-f)BE_f E_m} \quad (\text{A2.3})$$

The exponential terms in the bridging law given as equation (A2.2) result from the creep behavior of the composite material. The relaxation time T is the same as the value derived in McLean's model [36] for an intact material where the fibers creep linearly and the matrix is elastic.

In most situations, the term

$$\int_{-\infty}^t \frac{\sigma(\tau)}{T\sigma(t)} e^{-(t-\tau)/T} d\tau - 1 \quad (\text{A2.4})$$

is less than unity; additionally, for many materials the term $fE_f(fE_f - (1-f)E_m)/E_m^2$ is negligible. The product of these two can therefore reasonably be neglected, significantly simplifying the bridging law. If the times considered are much smaller than the characteristic time T , the first convolution in equation (A2.2) can be neglected as well. With neglect of the first convolution and the term containing equation (A2.4), the bridging law simplifies to

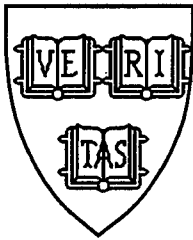
$$\dot{\delta}(t) = 2\lambda\sigma(t)[\dot{\sigma}(t) + \beta\sigma(t)] \quad (\text{A2.5})$$

where β is a modified creep coefficient, given as

$$\beta = \frac{BE_f E_L}{2(1-f)E_m} \quad (\text{A2.6})$$

and λ is the bridging law coefficient for the rate-independent case (such that $\beta = 0$) where $\delta = \lambda\sigma^2$ [20, 21]:

$$\lambda = \frac{D(1-f)^2 E_m^2}{4\tau f^2 E_L^2} \quad (\text{A2.7})$$



MECH 269

**NOTCH STRENGTH OF CERAMIC COMPOSITES:
LONG FIBERS, STOCHASTICS, SHORT FIBERS**

Bernard Budiansky
Division of Applied Sciences
Harvard University
Cambridge, MA 02138

and

John C. Amazigo
Department of Mathematics
University of Nigeria
Nsukka, Nigeria

In Nonlinear Analysis of Fracture, Proceedings of IUTAM Symposium held in Cambridge, U.K., 3-7 September 1995, Edited by J.R. Willis, Cambridge, U.K., Kluwer Academic Publishers, 1997.

NOTCH STRENGTH OF CERAMIC COMPOSITES: LONG FIBERS, STOCHASTICS, SHORT FIBERS

BERNARD BUDIANSKY
Division of Applied Sciences
Harvard University, Cambridge, MA 02138, USA

JOHN C. AMAZIGO
Department of Mathematics
University of Nigeria, Nsukka, Nigeria

Abstract

The tensile strength of an aligned-fiber ceramic composite containing an initial, through-the-fibers flaw is examined, and comparative studies are made of the effects of long fibers having deterministic tensile strengths, long fibers with stochastic strengths, and short fibers. Long-fiber reinforcement by perfectly uniform fibers having deterministic strengths has already been investigated extensively, and early studies of the effects of statistical variations in fiber strength associated with random fiber flaws (Thouless and Evans, 1988; Sutcu, 1989) indicated that long fibers having stochastic strengths could, paradoxically, provide significantly higher composite notch strengths than comparable fibers having uniform tensile strengths. The essential reason for this is that the randomly flawed fibers can suffer breaks in the interior of the composite, and then continue to carry load as well as enhance energy dissipation as they are pulled out of the matrix. A similar pullout effect can be induced by use of sufficiently short fibers, even when their strength is deterministic (Budiansky and Cui, 1995).

The influences on composite strength of these various fiber types are revisited and reviewed here. Particular attention is given to the question of "notch-sensitivity", which in the present context means the effect of the length of a major crack-like flaw on the overall composite strength.

1. Introduction

The configuration shown in Figure 1 illustrates a 2D model problem for the assessment of notch sensitivity. An infinite aligned-fiber composite containing a through-the-fibers flaw (or "notch") of length $2a_0$ is subjected to uniform tension σ at infinity. The fibers of radius R have volume concentration c_f and are held in the matrix by an interface friction of maximum magnitude τ . We assume further a matrix fracture toughness $K_{II}=0$; this simplifying assumption (Suo et al., 1993) introduces little error (Budiansky and Cui,

1994). Figure 1 shows long fibers, but a similar picture, and the same notation and assumptions will be used for aligned, but randomly located short fibers having uniform lengths.

In the analysis of the strength of the notched composite, some additional simplifications will be made. We will assume that an isolated matrix crack aligned with the initial flaw will emanate from each flaw tip (Figure 1) when load is applied to the composite. In actuality, fiber composites suffer multiple, closely spaced matrix cracks, with a concentrated density of such cracks near the notch tips. Like crack-tip plasticity in metals, such localized matrix cracks tend to relieve fiber stress concentration at the flaw tips, and so ignoring them makes the calculations of

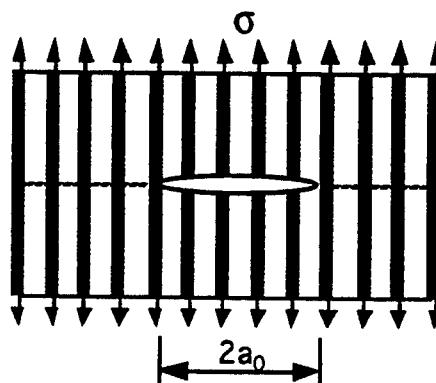


Figure 1. Flawed composite.

the composite strength conservative. Finally, we will be using an idealized bridging model, wherein the forces applied to the composite by fibers that bridge the matrix crack will be modeled via distributed spring stresses applied to the matrix crack faces, rather than by distributed friction along the fibers in a boundary layer in the interior of the composite. This too tends to concentrate flaw-tip stresses unrealistically, leading to conservative strength estimates, as shown in the "large-scale sliding" study by Xia et al (1994). Nevertheless, comparisons of the relative effectiveness of various kind of fibers may remain approximately valid, and the simplified analyses can be expected to provide lower bounds to the strength of the composite in the presence of a notch.

We will denote the strength of the composite by σ_s , and let σ_0 be the strength of the unflawed (but matrix-cracked) composite. Then the knockdown factor σ_s/σ_0 is a measure of the notch sensitivity.

2. Long Fibers, Deterministic Fiber Strength

The pertinent results found by Budiansky and Cui (1994) will be summarized. Figure 2 illustrates the bridging model in which the crack-face fiber stresses σ_f were smeared out into bridging stresses $p=c_f\sigma_f$ related by a bridging law to the crack-face opening displacement δ . We define the characteristic length

$$L = RS/\tau \quad (1)$$

where S is the fiber strength, and introduce the parameter

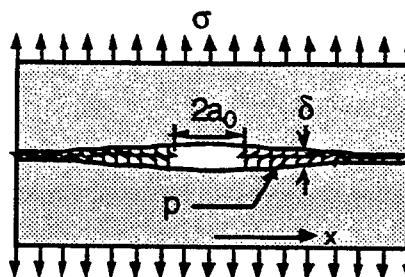


Figure 2. Crack-face spring bridging.

$$\Lambda(S) = \left(\frac{E}{2c_m E_m} \right) \sqrt{\frac{E_f}{S}} \quad (2)$$

where E_f , E_m , and E are the fiber, matrix, and composite moduli, and $c_m = 1 - c_f$ is the matrix volume fraction. In terms of the non-dimensional crack opening defined by

$$w = 8\Lambda^2(\delta/L) \quad (3)$$

the bridging relation

$$f \equiv \frac{p}{c_f S} = \sqrt{w} \quad (4)$$

was used. (See Xia et al (1994) and Budiansky et al (1995) for discussions of the provenance and limitations of this bridging law.) The criterion for fiber failure is $f=1$, and when this occurs at the ends of the original flaw, failure of the composite ensues.

Because $K_m=0$, the matrix cracks will extend out to infinity. With $\xi=x/a_0$

$$w(\xi) - w(1) = \left(\frac{16}{\pi} \right) \left(\frac{\omega a_0}{L} \right) \int_1^\infty f(t) \log \left| \frac{t^2 - \xi^2}{t^2 - 1} \right| dt. \quad (5)$$

governs the distribution $f(\xi)$ of the non-dimensional bridging stress. Here, via (4), $w=f^2$, and with ν equal to the Poisson's ratio of the composite, the parameter ω is defined as

$$\omega = \frac{(1-\nu^2)c_f E_f E}{2A c_m^2 E_m^2} = O(1). \quad (6)$$

Here $A=O(1)$ is a parameter that accounts for the orthotropy of the composite (Budiansky and Cui, 1994). Overall equilibrium requires the imposition of the auxiliary condition

$$\int_1^\infty [f(\xi) - f(\infty)] d\xi = f(\infty). \quad (7)$$

With $\sigma_0 = c_f S$, the results for the strength ratio σ_s/σ_0 vs. $\omega a_0/L$ shown in Figure 3 were found by setting $f(1)=w(1)=1$, solving (5) and (7) for $f(\xi)$, and identifying σ_s/σ_0 with $f(\infty)$.

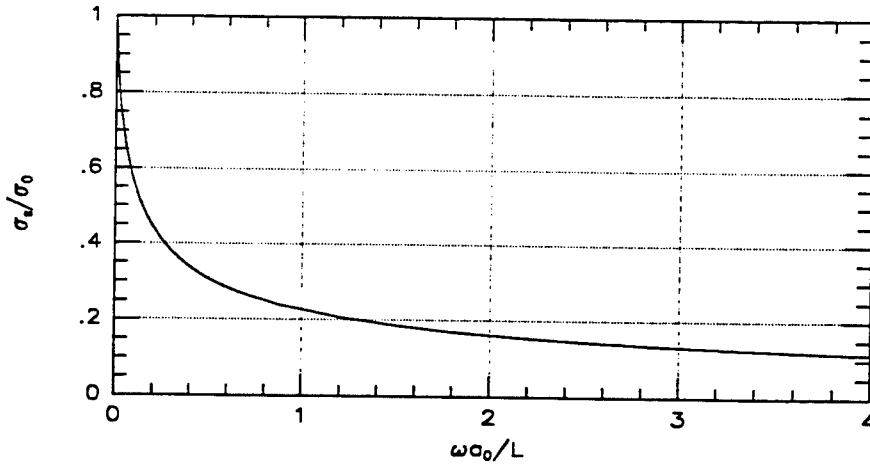


Figure 3. Notch sensitivity, deterministic fiber strength.

(We omit the details of the numerical solution.)

For an SiC/CAS composite, the nominal values $R=7\text{ }\mu\text{m}$, $S=2\text{ GPa}$, and $\tau=20\text{ MPa}$ give the characteristic length $L=700\text{ }\mu\text{m}$. For $c_f=.4$, $E_f=200\text{ GPa}$, and $E_m=100\text{ GPa}$, we have $E \approx c_f E_f + c_m E_m = 140\text{ GPa}$, and the values $\nu=.25$ and $A=.97$ (Budiansky and Cui, 1994) give $\omega \approx 1.5$. The consequent theoretical notch sensitivity as a function of the half-crack-size a_0 in millimeters, illustrated in Figure 4, is alarming; but in fact, the experiments by Cady et al (1995) on a notched, 0/90 SiC/CAS composite laminate exhibited essentially no notch sensitivity.

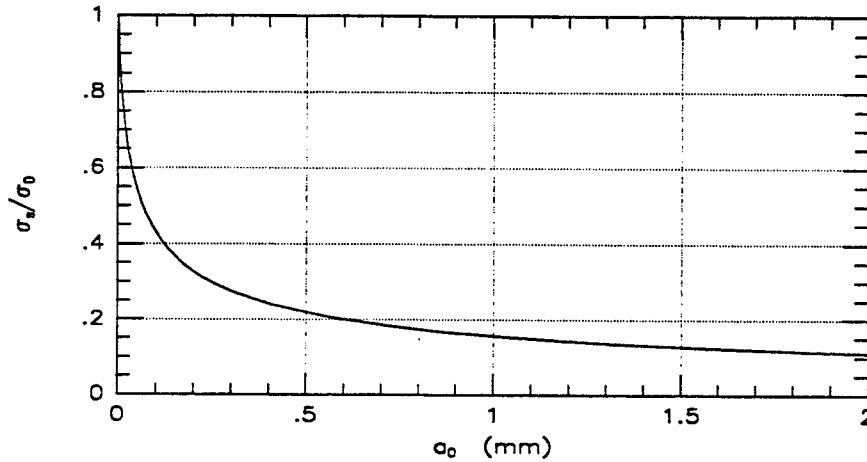


Figure 4. Notch sensitivity, deterministic fibers; example (SiC/CAS).

3. Long Fibers, Stochastic Fiber Strengths

We turn now to consideration of the effect on notch sensitivity of fibers having strengths governed by a Weibull strength distribution. Suppose that the occurrence of inherent flaws in a long fiber obeys a Poisson distribution specified by the probability $N[S]dx$ that the tensile strength of any element dx along the fiber is less than S . The Weibull assumption is that $N[S]$ is proportional to some power S^m . A useful formulation of this law is

$$N[S] = \frac{1}{L} \left[\frac{\Gamma(1 + 1/m) S}{S_L} \right]^m \quad (8)$$

where S_L is the average strength of fibers of length L , and Γ is the gamma function. We illustrate the significance of the size of the Weibull parameter m in Figure 5, which shows the probability-density function $q(S/S_L)$ for the strength ratio S/S_L of fibers of length L . The values of m shown more-or-less cover the range that has been reported for various fibers. For $m=\infty$ the fiber strength is deterministic, with $S=S_L$; m 's less than 2 are unlikely. The validity of Eq. (8) would imply that LS_L^m is invariant, and that the curves in Figure 5 are independent of L . (But experiments by Zok et al (1993) indicate that a simple Weibull distribution does not really account adequately for the presence of the distinct fiber flaw populations associated with pristine fibers and those introduced

during composite processing.)

The effective single-matrix-crack bridging law associated with fibers having Weibull strength distributions was studied by Thouless and Evans (1989), and has been

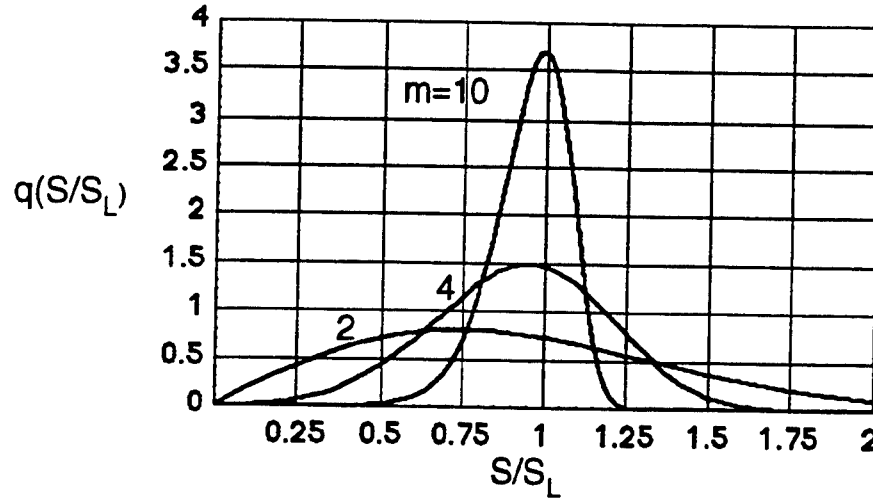


Figure 5. Fiber-strength probability densities for several Weibull exponents.

rederived, with corrections, by Budiansky and Amazigo (to be published). We define the new characteristic length L and the stress S_L by stipulating that the relation

$$L = S_L R / \tau \quad (9)$$

be satisfied by fibers of length L and their average strength S_L ; and we keep the definition (2) for the parameter Λ , with S replaced by S_L . Then, with w still defined by Eq. (3), the bridging law (4) generalizes into the form

$$\frac{P}{c_f S_L} \equiv f(w; m, \Lambda) = \sqrt{w} e^{-\alpha_m w^{(m+1)/2}} + \int_{\frac{w}{4\Lambda^2}}^{\sqrt{w}} \alpha_m e^{-\alpha_m s^{m+1}} \left[s - \frac{w}{4\Lambda^2} \right]^{m+1} ds \quad (10)$$

for $w < 16\Lambda^4$; for $w > 16\Lambda^4$ the integral is dropped. Here α_m is just the constant

$$\alpha_m = \frac{[\Gamma(1 + 1/m)]^m}{m+1} \quad (11)$$

(If the average strength S_g is known for a standard gage length L_g of fibers, then L and S_L may be found from the formulas

$$\frac{L}{L_g} = \left(\frac{S_g R}{\tau L_g} \right)^{\frac{m}{m+1}}, \quad \frac{S_L}{S_g} = \left(\frac{S_g R}{\tau L_g} \right)^{-\frac{1}{m+1}} \quad (12)$$

that follow from Eq. (9) and the connection $LS_L^m = L_g S_g^m$.)

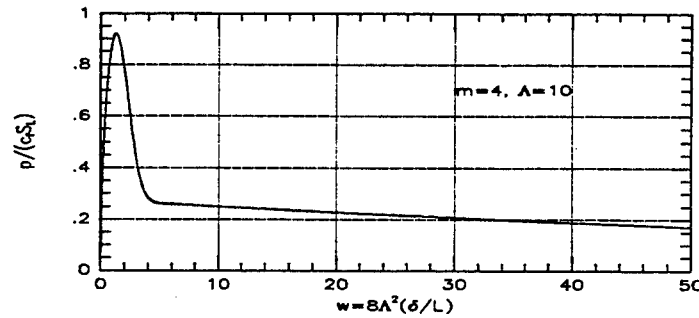


Figure 6. Bridging law, stochastic fiber strength; $m=4$, $\Lambda(S_L)=10$.

The bridging law (9) can be evaluated by numerical integration, and an example is shown in Figure 6, for $m=4$ and $\Lambda(S_L)=10$. Typically, in contrast to the deterministic law (4), which confines w to the narrow range $(0,1)$, the curve for stochastic fibers is considerably more broad in its early stage, and then transitions to a very long, low, gradually falling portion.

The integral equation (5) and the auxiliary relation (7) continue to apply to the model problem, with w given in terms of $f=p/(c_f S_L)$ by numerical inversion of the bridging relation. But the strength σ_s is now set by the maximum value achieved by the applied stress σ during opening of the matrix crack. The normalizing value σ_0 for the strength of the unnotched composite is identified with the peak value of p (Figure 6) in the bridging law. The maximum values of $p/(c_f S_L)$ are nearly independent of Λ , and decrease from unity only a little as m decreases. (For $m=2$ and $\Lambda=10$, $[p/(c_f S_L)]_{\max}=0.87$.)

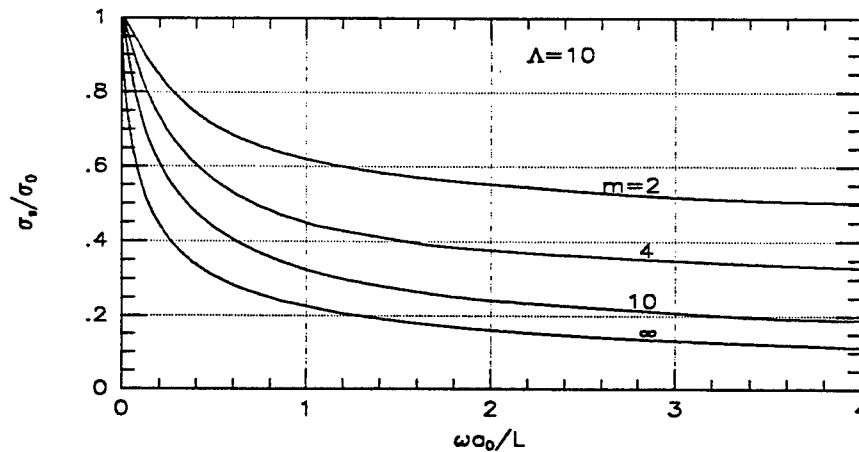


Figure 7. Notch sensitivity, stochastic fiber strengths; $\Lambda(S_L)=10$

We show in Figure 7 the non-dimensional results found for notch sensitivity, for $m=2, 4, 10$, and the deterministic case $m=\infty$ given in the previous section. For each m ,

we used $\Lambda(S_L)=10$. (For $m=\infty$ the strength does not depend on Λ , and additional numerical calculations have indicated that the notch strength is not very sensitive to Λ for the small notch sizes that are of interest in the study of notch sensitivity. For each finite m , the strength does become nearly proportional to Λ for very long notches.)

The curves of Figure 7 give a clear indication of the diminished notch sensitivity associated with decreasing values of the Weibull exponent. Note, however, that the characteristic length L in the non-dimensional abscissa depends on m , as does the normalizing value σ_0 for the unnotched composite. An explicit presentation of notch sensitivity estimates for SiC/CAS composites is shown in Figure 8, on the following basis. We suppose that for a standard gage length of 25.4 mm (1 inch), the measured average fiber strength S_g is 2 GPa for each m . With the same choices $R=7 \mu\text{m}$ and $\tau=20$ GPa made earlier for deterministic fibers, we used Eqs. (11) and (12) to calculate the characteristic lengths L and associated strengths S_L shown in Table I for the several m 's. Then, with $\omega=1.5$ (for the choices $c_f=.4$, $E_f=200$ GPa, and $E_m=100$ GPa used earlier) the results in Figure 7 produced the curves of Figure 8. (This introduces a small error, because $\Lambda=10$ was used for each of the curves in Figure 7, and the actual values of $\Lambda(S_L)$ for each m , also given in Table I, are a little different.)

The trends exhibited in Figure 8 confirm the reduced notch sensitivity to be expected from composites containing fibers having a statistical spread of breaking strengths. But some notch sensitivity survives in the millimeter-size notch range even for $m=2$, and so stochastics alone would not account for the Cady et al (1995) notch-insensitivity observations in SiC/CAS. Perhaps a combination of stochastic fiber strengths, multiple matrix cracking, and the Xia et al (1994) large-scale sliding effect will ultimately be needed to understand their notch-insensitivity data.

Table I
Stochastic fiber parameters

m	L (mm)	S_L (GPa)	$\Lambda(S_L)$
2	2.3	6.6	6.4
4	1.4	4.1	8.2
10	1.0	2.8	9.9
∞	.7	2.0	11.7

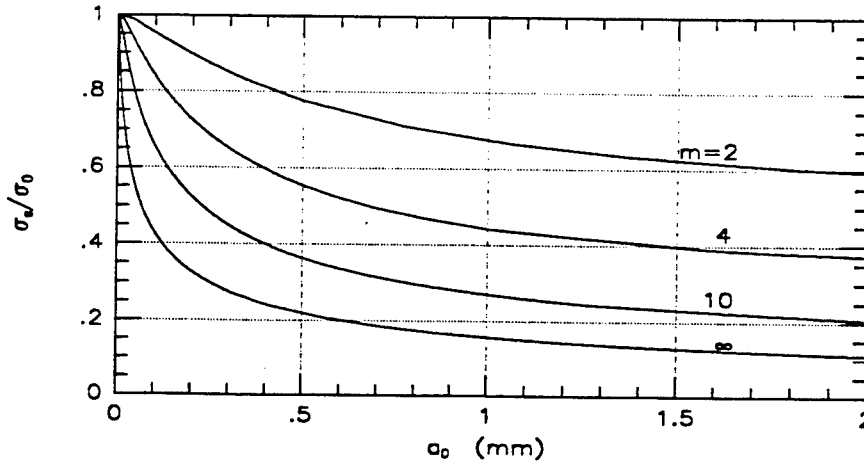


Figure 8. Notch sensitivity, stochastic fiber strengths; example (SiC/CAS).

There are several ways to rationalize the decreased notch sensitivity provided by stochastic fiber strengths. When weaker fibers break in the interior of the matrix they continue to inhibit crack opening as they slide out, allowing the fibers that are stronger than average to sustain their bridging constraint. The "softer" bridging law vis-a-vis the deterministic one tends to reduce the concentration of fiber stress near the notch. And from a related energy viewpoint, there is more dissipation associated with the pullout of broken fibers (Kelly and Macmillan 1985). So short fibers that would always pull out before they break should lead to less notch sensitivity. This was explored by Budiansky and Cui (1995), and is reviewed in the next section.

4. Short Fibers

We illustrate in Figure 9 randomly arrayed, aligned short fibers, or whiskers, in the composite containing an unbridged notch, with matrix cracks emanating from the notch tips. (Sophisticated, detailed analyses of matrix-crack-bridging by randomly inclined short fibers have been conducted by Li and his associates (e.g. Li et al, 1991), mostly in the context of reinforced cementitious materials.

The emphasis by Budiansky and Cui was on the notch-strength implications of aligned fibers, and involved much more primitive modeling.)

Reverting to the assumption of a deterministic fiber strength S suggests the concept of an "optimal" fiber length $L=RS/\tau$, as the largest length consistent with pullout before fiber fracture, regardless of a bridging fiber location with respect to the matrix crack. Retreating a bit from the modeling of long fibers, we assume that the fibers are rigid. If we let $e \leq L/2$ denote the length of a particular bridging-fiber segment that is being pulled out, then its crack-face fiber stress σ_f is related to the crack opening δ by $\sigma_f(\delta; e) = 2\tau(e-\delta)/R$ for $\delta \leq e$, and vanishes for $\delta > e$. Averaging σ_f over all e 's between zero and $L/2$, and writing $p = c_f(\sigma_f)_{ave}$ gives the optimal-fiber bridging law

$$\begin{cases} 2p/(c_f S) = [1 - 2\delta/L]^2 & (0 \leq \delta \leq L/2) \\ = 0 & (\delta > L/2) \end{cases} \quad (13)$$

The maximum bridging stress is $\sigma_0 = c_f S/2$, and this is also the reference composite strength for vanishing notch size. Now the matrix crack does not have to extend to infinity, even though the matrix toughness K_m is assumed to vanish; the finite value of bridging stress for $\delta=0^+$ makes it possible for K to vanish at the tip of a matrix crack of finite length ($b - a_0$). In contrast to Eq. (5), the integral equation

$$1 - \sqrt{f(\xi)} = 2\varepsilon_f \eta (a_0/L) \left(\frac{\sigma}{\sigma_0} \sqrt{\beta^2 - \xi^2} - \frac{1}{\pi} \int_1^\beta f(t) \log \left| \frac{\sqrt{\beta^2 - \xi^2} + \sqrt{\beta^2 - t^2}}{\sqrt{\beta^2 - \xi^2} - \sqrt{\beta^2 - t^2}} \right| dt \right) \quad (14)$$

with $\beta = b/a_0$, governs $f = p/\sigma_0$ in the range $1 \leq \xi \leq \beta$. Here the parameter η is

$$\eta = \frac{2(1-\nu^2)c_f E_f}{AE} = O(1) \quad (15)$$

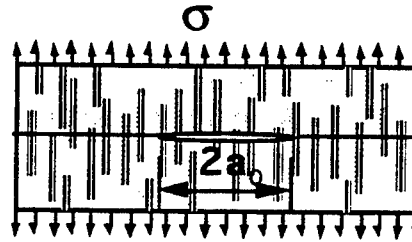


Figure 9. Notched short-fiber composite.

and $\epsilon_f = S/E_f$ is the fiber fracture strain. To meet the requirement of zero stress intensity factor at the matrix crack tip, the scalar condition

$$\frac{\sigma}{\sigma_0} = \frac{2}{\pi} \int_1^\beta \frac{f(\xi) d\xi}{\sqrt{\beta^2 - \xi^2}} \quad (16)$$

must also be satisfied. For specified values of the notch-size parameter $\epsilon_f \eta (a_0/L)$, the strength ratio σ_s/σ_0 (Figure 10) was determined as the peak value of σ/σ_0 , for increasing values of β , in the numerical solution of (15) and (16) for $f(\xi)$ and σ/σ_0 .

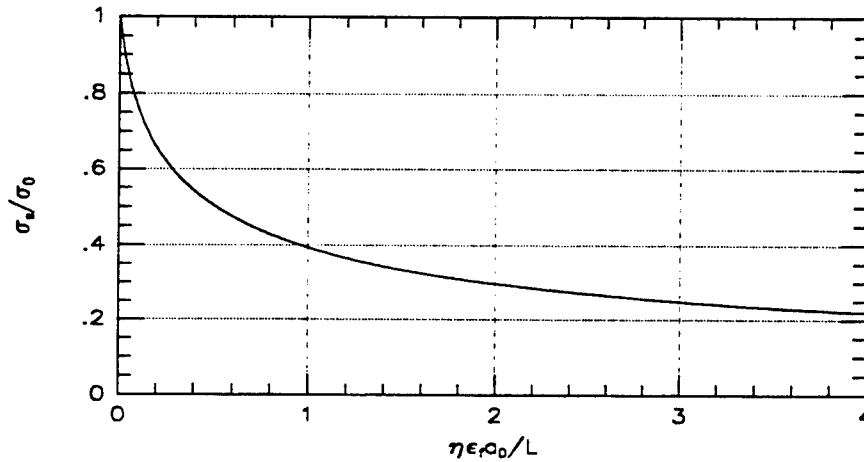


Figure 10. Notch sensitivity, optimal short fibers.

Actually, the abscissa in Figure 10 does not depend on S , but the form shown makes it easy to see that "optimal" short fibers should generally give less notch sensitivity than that given in Figure 3 for deterministic long fibers. The curves look similar, the η and ω parameters are both of order one, and the L parameters for long and short fibers should have comparable sizes. But the presence in the short-fiber abscissa of the factor $\epsilon_f = S/E_f$, which is around .01, means that for a given notch size a_0 , the knockdown factor is much less for short fibers. But we should remember that the normalizing strength parameter σ_0 is only $c_f S/2$ in the short-fiber case, instead of $c_f S$ for long fibers; however, short fibers in whisker form tend to have higher nominal strengths.

We will now finish up by showing an example for a hypothetical CAS matrix containing SiC whiskers. We presume an SiC whisker strength $S=4$ GPa, whisker radius $R=3$ μm , and keep $\tau=20$ MPa as the interface friction; this gives an optimal short-fiber length $L=600$ μm . The value $E_f=4$ GPa for the whisker modulus gives $\epsilon_f=.01$, and with $c_f=.4$, $E_m=100$ GPa, we get $E=220$ GPa, and $A=.88$ (Budiansky and Cui, 1994) for $\nu=.25$. These numbers give $\eta=1.55$, and then Figure 10 produces the short-fiber example in Figure 11, shown together with the curves reproduced from Figure 8 for stochastic and deterministic long fibers. Although various properties of the short and long fibers in this comparison differ, they reflect reasonable estimates for whiskers and fabricated fibers.

In this example, the optimal short fibers provide very comforting notch insensitivity, performing much better than even stochastic long fibers with $m=2$.

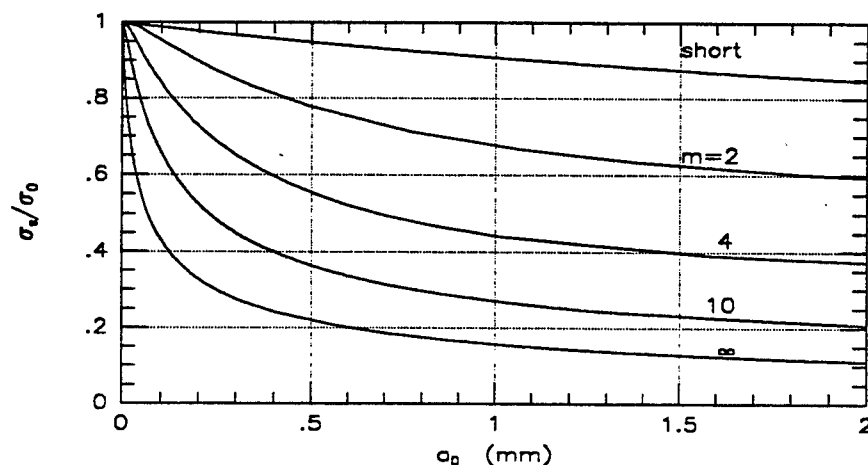


Figure 11. Notch sensitivity examples (SiC/CAS); short fibers, stochastic long fibers.

5. Acknowledgements

This work was partially supported by an ARPA University Research Initiative grant to the University of California at Santa Barbara, and by the Division of Applied Sciences, Harvard University.

6. References

- Budiansky, B. and Cui, Y.L. (1994) On the tensile strength of a fiber-reinforced ceramic composite containing a crack-like flaw. *J. Mech. Phys. Solids* **42**, 1-19.
- Budiansky, B., Evans, A.G., and Hutchinson, J.W. (1995) Fiber-matrix debonding effects on cracking in aligned fiber ceramic composites. *Int. J. Solids Structures* **32**, 315-328.
- Budiansky, B. and Cui, Y.L. (1995) Toughening of ceramics by short aligned fibers. *Mech. Matls.* **21**, 139-146.
- Cady, C.M., Mackin, T.J., and Evans, A.G. (1995) Silicon carbide/calcium aluminosilicate: a notch-insensitive ceramic-matrix composite. *J. Am. Ceram. Soc.* **78**, 77-82.
- Kelly, A., and Macmillan, N.H. (1985) *Strong Solids*, Clarendon Press, Oxford.
- Li, V.C., Wang, Y., and Backer, S. (1991) A micromechanical model of tension-softening and bridging toughening of short random fiber reinforced brittle matrix composites. *J. Mech. Phys. Solids* **39**, 607-625.
- Suo, Z., Ho, S., and Gong X. (1992) Notch ductile-to-brittle transition due to localized inelastic band. *ASME J. Engr. Mat. Tech.* **115**, 319-326.
- Sutcu, M. (1989) Weibull statistics applied to fiber failure in ceramic composites and work of fracture. *Acta. Metall.* **37**, 651-661.
- Thouless, M.D., and Evans, A.G. (1988) Effects of pullout on the mechanical properties of ceramic-matrix composites. *Acta. Metall.* **36**, 517-522.
- Xia, Z.C., Hutchinson, J.W., Evans, A.G., and Budiansky, B. (1994) On large scale sliding in fiber-reinforced composites. *J. Mech. Phys. Solids* **42**, 1139-1158.
- Zok, F.W., X Chen, X., and Weber, C.H. (1995) Tensile strength of SiC fibers. *J. Am. Ceram. Soc.*, **78**, 1965-1968.

Symposium on Applications of Continuum Damage Mechanics to Fatigue and Fracture

Damage, Fatigue and Failure of Ceramic-Matrix Composites

A. BURR,¹ F. HILD¹ and F.A. LECKIE²

¹Laboratoire de Mécanique et Technologie, E.N.S. de Cachan / C.N.R.S. / Université Paris 6
61, avenue du Président Wilson, F-94235 Cachan Cedex, France.

²Department of Mechanical and Environmental Engineering
University of California, Santa Barbara CA 93106-5070, USA.

The basic mechanisms related to the degradation of ceramic-matrix composites submitted to monotonic and cyclic load histories are matrix cracking, interfacial debonding and sliding, interfacial wear and eventually fiber breakage and fiber pull-out. These mechanisms are studied within the framework of Continuum Damage Mechanics by using results of micromechanical analyses. An explicit expression of the Helmholtz free energy density is derived in the case of monotonic load conditions. In particular, internal variables are carefully chosen to describe the degradation mechanisms (e.g., a damage parameter characterizing matrix cracking, another modeling fiber breakage) and written in a more appropriate format to allow the derivation of constitutive equations applicable to structural calculations.

In the case of cyclic load histories, the gradual degradation of the interface is described by interfacial wear. The constitutive equation is rewritten to incorporate interfacial wear. The effect of stress redistribution is analyzed.

In the case of monotonic and cyclic load histories the failure conditions are written in terms of macrocrack initiation conditions. Failure conditions are compared with ultimate tensile strength predictions. Fatigue failure conditions are summarized in a map in which three different regimes appear depending on the stress amplitude in fatigue.

TITLE OF SYMPOSIUM, JOURNAL, OR MANUAL:

Applications Of Continuum Damage Mechanics To Fatigue And Fracture, STP 1315

AUTHORS' NAME:

Alain Burr¹, François Hild¹ and Frederick A. Leckie²

TITLE OF PAPER:

Damage, Fatigue And Failure Of Ceramic-Matrix Composites

PAPER ID #: 451

AUTHORS' AFFILIATIONS

¹Post-Graduate Researcher and Research Assistant Professor, respectively,
Laboratoire de Mécanique et Technologie, E.N.S. Cachan / C.N.R.S. / Université Paris 6,
61, avenue du Président Wilson, F-94235 Cachan Cedex, France.

²Professor, Department of Mechanical and Environmental Engineering
University of California, Santa Barbara CA 93106-5070, USA.

ABSTRACT: Matrix-cracking, interfacial debonding and sliding, fiber breakage and fiber pull-out induce loss of stiffness, inelastic strains, hysteresis loops, and crack closure. These mechanisms are analyzed within the framework of Continuum Mechanics through the introduction of internal variables. Two models which are faithful to the micromechanical analysis are studied. They provide guidance on the choice of the relevant internal variables to model the mechanical behavior of unidirectional fiber-reinforced composites. Ultimate strength properties of fiber-reinforced composites are derived and compared with results related to localization. Extensions to cyclic load histories are given and are discussed in terms of ultimate strength reached after cycling.

KEY WORDS: matrix-cracking, debonding, fiber-breakage, interfacial shear strength, interfacial wear, ultimate strength, Continuum Damage Mechanics, state potential, internal variables, fatigue failure maps.

Introduction

The basic mechanisms related to the degradation of ceramic-matrix composites submitted to monotonic and cyclic load histories are matrix cracking, interfacial debonding and sliding, interfacial wear and eventually fiber breakage and fiber pull-out. These mechanisms are studied within the framework of Continuum Damage Mechanics by using results of micromechanical analyses. An explicit expression of the Helmholtz free energy density is derived in the case of monotonic load conditions. In particular, internal variables are carefully chosen to describe the degradation mechanisms (e.g. a damage parameter characterizing matrix cracking, another one modeling fiber breakage) and written in a more appropriate format to allow the derivation of constitutive equations applicable to structural calculations.

In the case of cyclic load histories, the gradual degradation of the interface is modeled by an interfacial wear law. The evolution laws of some state variables have to be rewritten to account for interfacial wear.

In the case of monotonic and cyclic load histories the failure conditions are written in terms of macrocrack initiation conditions (i.e. localization conditions). Failure conditions are compared with ultimate tensile strength predictions. In fatigue, failure conditions are summarized by the introduction of a shear stress map in which three different regimes appear depending on the stress amplitude in fatigue.

Matrix Cracking Mechanism

A Continuum Mechanics formulation applied to fiber-reinforced Ceramic Matrix Composites (CMCs) is written within the framework of the Thermodynamics of Irreversible Processes. The first step in establishing such a model is to identify the internal variables which define the state of the material. The second step is to determine the expression of the state potential in terms of the state variables and the third one to define the evolution laws of the internal variables. The state potential $\bar{\psi}$ is made up of the sum of two terms: viz. the elastic energy density $\bar{\psi}_e$ and the stored

energy density $\bar{\psi}$. The elastic part is directly related to the applied load. The stored energy density is the result of residual stress fields which gives rise to macroscopic strains with no applied load. By considering two elastic steps, the total free energy density can be evaluated following a so-called 'cut and paste' technique introduced by Volterra [1]. This approach will be used to study the degradation of fiber-reinforced composites.

General Expression of the Free Energy Density

Loading a composite consisting of a brittle matrix supported by stronger fibers, usually causes multiple matrix cracking which is accompanied by interfacial debonding and sliding. In the following, we assume that the whole matrix-cracking process occurs at load levels lower than the fiber breakage mechanism, and therefore the former mechanism will first be analyzed. The matrix cracks, which are assumed to be perpendicular to the fiber directions, cause a stiffness reduction when the applied stress $\bar{\sigma}$ is tensile. Furthermore it is the closure of the cracks which indicates the onset of increased stiffness when the specimen is subsequently loaded in compression. We will use elementary cells of length L , characterizing the average crack spacing, and consisting of two different materials (m) and (f) as shown in Fig. 1, where E is the Young's modulus of the unbroken composite, E_m that of the matrix (m), and E_f that of the fiber (f). The presence of matrix cracks implies a potential energy density change $\Delta\bar{\varphi}_c$

$$\Delta\bar{\varphi}_c = \frac{\bar{\sigma}^2}{E} \bar{\omega}_c \quad (1)$$

where

$\bar{\omega}_c$ = quantity depending on the crack density.

The cracking mechanism is dissipative and does not store energy: it only influences $\bar{\psi}_e$.

Debonding followed by sliding gives rise to inelastic strains and hysteresis loops. To describe these phenomena, different models have been proposed [2, 3]. They all consider a friction length l_f here assumed to be equal to the debond length l_d (Fig. 1). Similarly to cracking, which is a mode I mechanism, debonding *per se* is purely dissipative. When debonding and slip occur simultaneously, a self-balanced microscopic stress field is introduced. The corresponding strains in the matrix and in the fiber are denoted by $\Delta\epsilon_m(z)$ and $\Delta\epsilon_f(z)$, respectively, where z is the current coordinate. By application of the principle of virtual work, an overall inelastic strain $\bar{\epsilon}_{in}$ can be derived [4]

$$\bar{\epsilon}_{in} = \frac{1}{L} \int_0^L \Delta\epsilon_f(z) dz \quad (2)$$

Since the additional stress field is self-balanced the debonding and sliding processes are able to store energy. This result shows that to fully characterize both mechanisms the knowledge of the stored energy density $\bar{\psi}_s$ is crucial. It is expressed as the total elastic energy density associated with the residual stress field

$$\bar{\psi}_s = \frac{1}{L} \int_0^L \frac{1}{2} \left[f E_f \Delta\epsilon_f^2(z) + (1-f) E_m \Delta\epsilon_m^2(z) \right] dz \quad (3)$$

where

f = volume fraction of part (f).

The matrix cracking process described by an internal damage variable complies with the requirement of a fully dissipative mechanism. In a Continuum Mechanics framework, the presence of a crack results in a stiffness reduction defined by an internal damage variable D [5].

In the framework of Continuum Damage Mechanics, the potential energy change can be written as follows

$$\Delta \bar{\psi}_c = \frac{\bar{\sigma}^2}{2E} \frac{D}{1-D} \quad (4)$$

and the corresponding Gibbs' elastic energy density of a damaged material is written as $\bar{\psi}_e = \bar{\sigma}^2 / 2E(1-D)$.

To characterize fully the debonding and sliding mechanisms two variables are needed. The first one is the inelastic strain $\bar{\epsilon}_{in}$, and the second denoted by d , which is usually proportional to the debond length l_d is introduced to define the stored energy

$$\bar{\psi}_s = \frac{E}{2} \frac{\bar{\epsilon}_{in}^2}{d} \quad (5)$$

In addition to the total strain $\bar{\epsilon}$, the total free energy density $\bar{\psi}$ is therefore dependent on three internal variables are required: one damage variable D modeling matrix cracking and related to the average crack spacing, two variables $\bar{\epsilon}_{in}$ and d describing debonding and sliding, and related to the debond length and the crack opening

$$\bar{\psi} = \frac{E(1-D)}{2} (\bar{\epsilon} - \bar{\epsilon}_{in})^2 + \frac{E}{2} \frac{\bar{\epsilon}_{in}^2}{d} \quad (6)$$

The associated forces are defined as follows

$$\bar{\sigma} = \frac{\partial \bar{\psi}}{\partial \bar{\epsilon}}, \quad Y = -\frac{\partial \bar{\psi}}{\partial D}, \quad y = -\frac{\partial \bar{\psi}}{\partial d}, \quad X = \frac{\partial \bar{\psi}}{\partial \bar{\epsilon}_{in}} \quad (7.1,2,3,4)$$

Eqn. (7.1) defines the macroscopic stress $\bar{\sigma}$. Eqn. (7.2) defines the energy release rate density Y playing a similar role as the energy release rate G in Linear Elastic Fracture Mechanics.

Combining Eqns. (7.1) and (7.2), one shows that the energy release rate density Y is proportional to the square of the effective stress $\bar{\sigma} / (1-D)$. Similarly, Eqn. (7.3) defines the stored energy density y released during debonding and sliding. Since the variable d depends upon the details of the interfacial behavior, the definition of its associated force is also dependent upon the interfacial behavior. Lastly, Eqn. (7.4) defines the back stress $\bar{\chi}$ related to debonding and sliding. Again its exact value depends upon the interfacial behavior.

To determine the evolution laws of the internal variables, two ways can be followed. The first one is using simulations of the complete micromechanical model along the lines developed for instance by Feillard et al. [6] to get the evolution of crack spacing L and debond length l_d and then the state potential. The second one is by performing experiments. The damage variable D is obtained by measuring the initial unloading modulus (Fig. 2) and the corresponding inelastic strain is $\bar{\epsilon}_{in}$. Applications of these kind of identification procedure can be found in [7].

Relationship between Internal Variables and Microscopic Quantities

In this sub-section, expressions of the three internal variables D , $\bar{\epsilon}_{in}$ and d are derived for specific cases (Fig. 1). Using a shear lag analysis [8], the damage variable D can be shown to be linked to the average crack spacing L by the relation

$$\frac{D}{1-D} = \frac{(1-f)E_m}{fE_f} \frac{\tanh\beta L}{\beta L} \quad (8)$$

where the constant β is a function of the elastic and geometric properties of the fiber and the matrix and is on the order of 10 mm^{-1} for many CMCs. The strain distribution $\Delta\epsilon_f(z)$ in the friction zone in the part (f) is assumed to be linear and characterized by a constant interfacial shear strength τ_0 [9]. It is also assumed that the debond strength is negligible so that there is no

longitudinal stress jump at the crack tip [3]. When debonding occurs, the inelastic strain $\bar{\epsilon}_{in}$ is then given by

$$\bar{\epsilon}_{in} = \frac{\tau_0 l_d^2}{E_f R_f L} \quad (9)$$

where

R_f = fiber radius, m, and

l_d = debond length (inversely proportional to τ_0), m.

Eqns. (2) and (9) show that the inelastic strain is a function of the average crack spacing as well as the debond length. The definition of the variable d is directly obtained from its definition in the expression of the stored energy $\bar{\psi}_s$ given in Eqn. (3)

$$d = \frac{3}{4} \frac{(1-f)E_m l_d}{fE_f L} \quad (10)$$

The damage variable d defines the size of the slip zone related to the crack spacing length l_d/L .

Effect of Stress Redistribution due to Matrix Cracking

To study the ability of CMCs to redistribute stresses, a two bar structure is analyzed (see Fig. 3.1) which describes the effect of a strain concentration. This example is representative of more complex configurations (e.g. plates with holes, notched specimens, pin-loaded structures) for which strain concentrations occur. The length and cross sectional area of bar (1) are L and $(1-f)S$, and of bar (2) are kL and fS . This model allows variation of the load distribution in the bars and consequently the stress concentration. To simplify the analysis, only matrix cracking is modeled by the introduction of the damage variable D (i.e., no inelastic strain). The damage variable evolves provided any local stress is greater than the matrix cracking stress σ_{mc} up to the

ultimate strength σ_u . When a constant load $S\Sigma$ is applied, three different regimes can be defined. First, when the stress level is low (i.e., $\Sigma/\sigma_{mc} < 1-f+f/k$), there is no cracking ($\sigma_1 < \sigma_{mc}$, $\sigma_2 < \sigma_{mc}$) and the two bars behave elastically thereby defining an *elastic* regime. Second, for higher stress levels ($1-f+f/k \leq \Sigma/\sigma_{mc} < k(1-D_1)(1-f)+f$), the shortest bar (i.e., bar (1)) experiences cracking ($\sigma_1 \geq \sigma_{mc}$) whereas the longest one is still elastic. This condition is defined as *confined cracking*. The upper bound of this regime shows that the effect of confined cracking is a reduction of the stress concentration from an initial value of k to $k(1-D_1)$ assumed to be greater than 1. Third, for very high stress levels (i.e., $k(1-D_1)(1-f)+f < \Sigma/\sigma_{mc}$), the two bars experience matrix cracking and that defines a regime of *extensive cracking*. The third regime exists provided the ultimate strength σ_u is not exceeded. When $\sigma_u/\sigma_{mc} < k(1-D_u)$, where D_u is the damage parameter at the ultimate, the extensive cracking regime is excluded. On the other hand, when $\sigma_u/\sigma_{mc} \geq k(1-D_u)$, the extensive cracking regime exists. When the strain concentration is low (i.e., $\sigma_u/\sigma_{mc} \geq k$), the latter regime will always occur.

Wear Mechanism during Cyclic Loading

Under cyclic loading, wear may take place at the fiber/matrix interface because of stress reversals [10]. An estimate of the effect of cyclic loading on the mechanical behavior is possible when the influence of interfacial wear is included in the model. The effect of wear is to a change of the residual stress field induced by debonding and sliding. Therefore as the number of cycles N increases, there is a variation of the associated additional strains $\Delta\epsilon_m(z,N)$ and $\Delta\epsilon_f(z,N)$. By inspection of Eqns. (2) and (3), there is a direct influence of wear on the inelastic strain as well as the damage variable d . Thus to write the evolution laws during fatigue, one needs to model the evolution of wear as a function of the number of cycles.

We assume that $\Delta\epsilon_m(z,N) = \Delta\epsilon_m(z)\Phi(N)$ and $\Delta\epsilon_f(z,N) = \Delta\epsilon_f(z)\Phi(N)$ when a constant stress amplitude is applied, where Φ is a decreasing function with the number of cycles ($\Phi(0)=1$). If the interfacial behavior is modeled by a constant interfacial shear strength the previous hypothesis can be rewritten in terms of the evolution of the interfacial shear strength $\tau(N)$ as a

function N : $\tau(N) = \tau_0 \Phi(N)$ [11]. The evolution of the variables $\bar{\epsilon}_{in}(N)$ and $d(N)$ can be related to the initial values $\bar{\epsilon}_{in0}$ and d_0 reached during the first cycle by

$$\bar{\epsilon}_{in}(N) = \frac{\bar{\epsilon}_{in0}}{\Phi(N)}, \quad d(N) = \frac{d_0}{\Phi(N)} \quad (11)$$

Effect of Stress Redistribution due to Debonding during Fatigue

The model is now used to assess the stress redistribution during fatigue of the two-bar structure depicted in Fig. 3.1. The key mechanisms to consider are matrix cracking model by D and debonding and sliding described by $\bar{\epsilon}_{in}$. When the local stress is greater than the matrix cracking stress σ_{mc} , the damage variable and the inelastic strain grow until the total strain reaches a critical value ϵ_u . For the case when the cyclic load has a constant maximum value $S\Sigma$, three different regimes can again be identified. The *elastic* regime is the same as for a constant load condition when the behavior is everywhere elastic (when $\Sigma/\sigma_{mc} < 1-f+f/k$). The *confined cracking* regime is defined by $1-f+f/k \leq \Sigma/\sigma_{mc} < k(1-D_1)(1-f)+f-(1-D_1)(1-f)E\alpha_1\Phi(N)/\sigma_{mc}$, when the shortest bar (1) experiences cracking so that debonding and wear occur. In this regime, the most loaded bar (1) experiences a decrease of the maximum stress level $\sigma_1(N) = (\Sigma - fE\alpha_1\Phi(N)/k)/(1-f+f/k(1-D_1))$ as the number of cycles N increases, therefore the damage variable D_1 remains constant. The effect of confined cracking is to reduce the stress concentration. Third, for very high stress levels (when $k(1-D_1)(1-f)+f-(1-D_1)(1-f)E\alpha_1\Phi(N)/\sigma_{mc} < \Sigma/\sigma_{mc}$), the two bars experience cracking, debonding and wear: it is an *extensive cracking* regime. The boundary between the two regimes is defined by the following condition depicted in Figs. 4

$$\frac{\Sigma}{\sigma_{mc}} = k(1-f)(1-D_1) + f - \frac{(1-f)(1-D_1)E\alpha_1\Phi(N)}{\sigma_{mc}} \quad (12)$$

The third regime exists provided the maximum accumulated strain ϵ_u is not reached. The failure condition is represented by the condition $\epsilon_1 < \epsilon_u$ that can be expressed as $\Sigma/\sigma_{mc} < E\epsilon_u/k\sigma_{mc}$ $[k(1-D_1)(1-f)+f]-(1-f)(1-D_1)E\alpha_1\Phi(N)/\sigma_{mc}$. In many composites, ϵ_u is very well approximated by the ultimate tensile strain under monotonic load conditions and the dimensionless parameter $E\epsilon_u/\sigma_{mc}$ varies between 4 and 8 for many composite materials [12]. When $E\epsilon_u/\sigma_{mc}k \leq 1$, the extensive cracking regime will never be reached because failure occurs prior to reaching the confined/extensive regime boundary. Conversely, when $E\epsilon_u/\sigma_{mc}k > 1$, the extensive cracking regime will occur. If $\Phi(N \rightarrow +\infty) \leq [\{k(1-D_1)-1\}(1-f)+f/k]\sigma_{mc}/(1-f)(1-D_1)E\alpha_1$ fatigue life is infinite in the confined cracking regime (Fig. 4.1). On the other hand when $\Phi(N \rightarrow +\infty) > [\{k(1-D_1)-1\}(1-f)+f/k]\sigma_{mc}/(1-f)(1-D_1)E\alpha_1$ there is no fatigue endurance in the confined cracking regime (Fig. 4.2) and one number of cycles can be defined: N_1 so that $\Phi(N_1) = [\{k(1-D_1)-1\}(1-f)+f/k]\sigma_{mc}/(1-f)(1-D_1)E\alpha_1$. In Fig. 4, all the results are written in terms of a reference number of cycles N_0 modeling the shear stress decay. In many CMCs, N_0 is on the order of 10 to 100 and can be smaller for SiC/CAS composites [12]. This study will be complete if fiber breakage is modeled since for many composites it is the key mechanism leading to final failure.

Fiber Breakage Mechanism

A unit cell of length L_R is considered where the matrix crack spacing is $2L$. The length L_R is the *recovery* length and refers to twice the longest fiber that can be pulled out and cause a reduction in the load carrying capacity. Away from a fiber break, as in the case of matrix cracking, the fiber stress builds up through the stress transfer across the sliding fiber-matrix interface. If the interfacial shear stress τ is assumed to be constant, the recovery length is related to the maximum stress in the fiber by [13]

$$L_R = \frac{R_f T}{\tau_0} \quad (13)$$

where

T = reference stress (i.e., fiber stress in the plane of the matrix crack), Pa.

The model now discussed takes account of three features induced by fiber breakage and fiber pull-out, viz. the reduction in stiffness due to fiber breakage, the inelastic strains due to fiber pull-out, and the hysteresis loops. The details of the unloading and reloading process are complex and to avoid this difficulty it is useful to introduce the crack opening displacement δ , which characterizes the material state related to the reverse friction. The crack opening displacement δ is also useful in determining the conditions when closure occurs. To characterize the state of the composite, four quantities are required. These are the overall strain $\bar{\epsilon}$, the friction length L_F , the percentage of broken fibers, P_F , within the recovery length $L_R = 2L_F$, and the crack opening displacement, δ . To derive the free energy density associated to a loading sequence, we consider two different elastic steps to reach the same state. The first step consists in moving the unbroken fibers wrt. the broken fibers with no external load by an amount δ over a length L_F . The elastic density associated with this process is given by [14]

$$\bar{\psi}^s = \frac{fE_F}{2} \left(\frac{\delta}{L_F} \right)^2 P_F \frac{4-3P_F}{3} \quad (14)$$

and the opening displacement δ induces an overall inelastic strain $\bar{\epsilon}_{in}$

$$\bar{\epsilon}_{in} = \frac{\delta}{L_F} P_F \quad (15)$$

The second step, during which no friction occurs, consists in adding an elastic loading from the previous state. It involves an additional elastic energy density given by

$$\bar{\psi}^e = \frac{fE_F}{2} \left(\bar{\varepsilon} - \bar{\varepsilon}_{in} \right)^2 \quad (16)$$

The total free energy density is then the sum of the two energies. A more convenient expression for the free energy is obtained by using state variables in a modified form. The state variables are the total strain, $\bar{\varepsilon}$, the damage variable modeling the percentage of broken fibers, $D = P_F$, and the inelastic strains $\bar{\varepsilon}_{in}$ due to the crack opening displacement δ modeling fiber pull-out. The free energy density $\bar{\psi}$ can then be written in terms of the new internal variables

$$\bar{\psi} = \frac{fE_F}{2} \left(\bar{\varepsilon} - \bar{\varepsilon}_{in} \right)^2 + \frac{fE_F}{2} \frac{4-3D}{3D} \bar{\varepsilon}_{in}^2 \quad (17)$$

The thermodynamic forces associated with the new state variables are respectively given by

$$\bar{\sigma} = \frac{\partial \bar{\psi}}{\partial \bar{\varepsilon}} = fE_F \left(\bar{\varepsilon} - \bar{\varepsilon}_{in} \right) \quad (18.1)$$

$$Y = - \frac{\partial \bar{\psi}}{\partial D} = \frac{2fE_F}{3} \left(\frac{\bar{\varepsilon}_{in}}{D} \right)^2 \quad (18.2)$$

$$\bar{X} = \frac{\partial \bar{\psi}}{\partial \bar{\varepsilon}_{in}} = fE_F \left(\frac{4\bar{\varepsilon}_{in}}{3D} - \bar{\varepsilon} \right) \quad (18.3)$$

where

Y = energy release rate density associated with fiber breakage, Jm^{-3} , and

\bar{X} = back-stress, Pa.

When the fibers are assumed to exhibit a statistical variation of strength that obeys a two-parameter Weibull law, the evolution laws of the damage variable and the inelastic strain are given by [14]

$$D = 1 - \exp \left[- \left(\frac{E_f \bar{\epsilon}_M}{S_c} \right)^{m+1} \right], \quad \bar{\epsilon}_{in} = \frac{1}{2} \bar{\epsilon}_M D \quad (19)$$

with

$$S_c^{m+1} = \frac{L_0 S_0^m \tau}{R_f} \quad (20)$$

where

$\bar{\epsilon}$ = current strain,

$\bar{\epsilon}_M$ = maximum strain,

S_c = characteristic strength, Pa,

m = shape parameter,

S_0 = stress scale parameter, Pa,

L_0 = gauge length, m, and

τ = interfacial shear strength, Pa.

Provided the fibers are subject to global load sharing, the load transmitted from each failed fiber is shared equally among the intact fibers, the ultimate tensile strength $\bar{\sigma}_{UTS}$ is then scaled by the characteristic strength [15] S_c according to

$$\bar{\sigma}_{UTS} = f S_c F(m) \quad (21)$$

The function F depends upon the shape parameter m and whether localization happens or not before the peak stress [13, 16, 17]. To assess the ultimate tensile strength, the function F is given by [13]

$$F(m) = \left(\frac{2}{m+2} \right)^{1/(m+1)} \frac{m+1}{m+2} \quad (22)$$

and to calculate the localization tensile strength, the function F can be written as [17]

$$F(m) = \frac{1}{2} \left(\frac{1}{m+1} \right)^{1/(m+1)} \left\{ 1 + \exp \left(- \frac{1}{m+1} \right) \right\} \quad (23)$$

Eqns. (20) and (21) show that the interfacial shear resistance τ is a key parameter. If wear is involved, it is expected that the interfacial shear strength τ decreases as the number of cycles N increases as discussed earlier. The simple model of interfacial wear introduced previously can be used directly to evaluate the residual ultimate strength of fatigued CMCs [11]. The drawback of this simple wear model is that the influence of the load ratio is not modeled. In the following we will introduce another wear mechanism accounting for the load ratio R .

Fatigue Failure Maps

When cyclic stress experiments are performed on CMCs, it is known that the first cycle is often the most damaging in reducing of shear strength [10]. Therefore, following the first reversal of sliding, the frictional shear stress is assumed to decrease from τ_0 to τ_∞ . Upon first loading to a maximum stress σ , a friction length $2L_{F0}$ is reached ($L_{F0} \leq L$) over which the shear strength is equal to τ_0 (see Figs. 5). Upon unloading to $\sigma - \Delta\sigma = R\sigma$ a shear stress reversal occurs over a length L_{U1} , for which the interfacial shear strength is equal to τ_∞ . Upon reloading to σ there is shear stress reversal over the length L_{U1} for which the interfacial shear strength is still τ_∞ ; together with σ , sliding evolves from L_{F0} to L_{F1} , for which the interfacial shear stress is τ_0 . As the number of cycles N increases, there is an increase of $L_{F(N+1)}$ and $L_{U(N+1)}$ [18]. A key parameter is involved: $\gamma = (\tau_0 - \tau_\infty) / (\tau_0 + \tau_\infty)$, $0 < \gamma < 1$. It measures the amount of wear. Provided subcritical crack propagation does not exist, there is no further matrix cracking under cyclic loading conditions. However, fiber breakage may occur since the longitudinal stress in the fibers increases as a result of wear. In the following, we will neglect this phenomenon.

There are three cases to be considered. In case #1, $L > L_{FN}$, the condition for matrix cracking saturation is not reached. For case #2, $L_{UN} \leq L \leq L_{FN}$, matrix cracking saturation occurs and the friction characteristics involve τ_0 and τ_∞ . For case #3, $L_{UN} > L$, matrix cracking saturation takes place but the friction characteristics only involve τ_∞ (Fig. 5.2). An equivalent shear stress is defined to determine fatigue properties (Fig. 6.1). The evolution of the latter is given by

$$\frac{\tau^*(N)}{\tau_0} = \begin{cases} \frac{1-\gamma}{1-\gamma R - (1-R)\gamma^{N+1}} & L \geq L_{FN} \\ 1 - \frac{\gamma}{1-\gamma} \frac{(1-R)(1-f)E_m \sigma R_f}{2fE\tau_0 L} (1-\gamma^N) & L_{UN} \leq L < L_{FN} \\ \frac{1-\gamma}{1+\gamma} = \frac{\tau_\infty}{\tau_0} & L < L_{UN} \end{cases} \quad (24)$$

from which the shear stress map shown in Fig. 6.2 can be obtained. When $N = 0$, $\tau^*(0) = \tau_0$ since no reversal occurred. On the other hand, when $N = +\infty$, since $\gamma < 1$, the maximum value of $\tau^*(\infty) = \tau_0(1-\gamma)/(1-\gamma R)$ and the minimum value of $\tau^*(\infty) = \tau_\infty$. This last result shows that τ_∞ can only be reached if saturation takes place during cycling ($L < L_{FN}$) and complete reversal occurs at least one cycle over a length L ($L < L_{UN}$). This map is useful for deriving the ultimate fatigue strength according to Eqns. (21) and (24). Under monotonic loading conditions, the value of τ in Eqn. (21) is taken equal to τ_0 , whereas under cyclic loading conditions, it is taken equal to $\tau^*(N)$. It is worth noting that these results include directly the amplitude effect by the presence of the load ratio R .

Conclusions

The basic mechanisms related to the degradation of ceramic-matrix composites submitted to monotonic and cyclic load histories were studied within the framework of Continuum Damage Mechanics by using results of micromechanical analyses. An explicit expression of the Helmholtz free energy density was derived in the case of monotonic load conditions. In

particular, internal variables are carefully chosen to describe the degradation mechanisms (viz. matrix cracking, fiber breakage). In the case of cyclic load histories, the gradual degradation of the interface was modeled by the introduction of the effect of interfacial wear. The effect of stress redistribution is analyzed on two-bar structures.

In the case of monotonic and cyclic load histories the failure conditions are written in terms of macrocrack initiation conditions (i.e. localization conditions). Failure conditions are close to the ultimate tensile strength predictions. In fatigue, failure conditions are summarized by the introduction of a shear stress map in which three different regimes appear depending on the stress amplitude in fatigue. These maps are useful to derived the ultimate tensile strength after cycling.

References

- [1] Volterra, V., "Sur l'équilibre des corps élastiques multiplement connexes," Annales Scientifiques de l'Ecole Normale Supérieure, Paris, Vol. 24, No. 3, 1907, pp 401-518.
- [2] Aveston, J., Cooper, G. A. and Kelly, A., "Single and Multiple Fracture," National Physical Laboratory: Properties of Fiber Composites, IPC Science and Technology Press, Surrey (UK), 1971, pp 15-26.
- [3] Hutchinson, J. W. and Jensen, H. M., "Models for Fiber Debonding and Fiber Pull-Out in Brittle Composites with Friction," Mech. Mat., Vol. 9, 1990, pp 139-163.
- [4] Burr, A., Hild, F. and Leckie, F. A., "Micro-Mechanics and Continuum Damage Mechanics," Arch. Appl. Mech., Vol. 65, No. 7, 1995, pp 437-456.
- [5] Lemaitre, J. and Dufailly, J., "Modélisation et identification de l'endommagement plastique des métaux," 3ème congrès français de mécanique, Grenoble (France), 1977,.
- [6] Feillard, P., Désarmot, G. and Favre, J. P., "Theoretical Aspects of the Fragmentation Test," Comp. Sci. Tech., Vol. 50, 1994, pp 265-279.
- [7] Hild, F., Burr, A. and Leckie, F. A., "Matrix Cracking and Debonding in Ceramic-Matrix Composites," Int. J. Solids Struct., Vol. 33, No. 8, 1996, pp 1209-1220.

- [8] Cox, H. L., "The Elasticity and the Strength of Paper and other Fibrous Materials," Br. J. Appl. Phys., Vol. 3, 1952, pp 72-79.
- [9] Kelly, A. and Tyson, W. R., "Tensile Properties of Fibre-Reinforced Metals: Copper/Tungsten and Copper/Molybdenum," J. Mech. Phys. Solids, Vol. 13, 1965, pp 329-350.
- [10] Rouby, D. and Reynaud, P., "Fatigue Behaviour Related to Interface Modification During Load Cycling in Ceramic-Matrix Fibre Composites," Comp. Sci. Tech., Vol. 48, 1993, pp 109-118.
- [11] Evans, A. G., Zok, F. W. and McMeeking, R. M., "Fatigue of Ceramic Matrix Composites," Acta Metall. Mater., Vol. 43, No. 3, 1995, pp 859-875.
- [12] Heredia, F. E., "UCSB CMCs Survey," Report, Materials Department, University of California, Santa Barbara, 1995.
- [13] Curtin, W. A., "Theory of Mechanical Properties of Ceramic Matrix Composites," J. Am. Ceram. Soc., Vol. 74, No. 11, 1991, pp 2837-2845.
- [14] Hild, F., Burr, A. and Leckie, F. A., "Fiber Breakage and Fiber Pull-Out of Fiber-Reinforced Ceramic-Matrix Composites," Eur. J. Mech. A/Solids, Vol. 13, No. 6, 1994, pp 731-749.
- [15] Henstenburg, R. B. and Phoenix, S. L., "Interfacial Shear Strength Studies Using the Single-Filament-Composite Test. Part II: A Probability Model and Monte Carlo Simulations," Polym. Comp., Vol. 10, No. 5, 1989, pp 389-406.
- [16] Curtin, W. A., "Fiber Pull-Out and Strain Localization in Ceramic Matrix Composites," J. Mech. Phys. Solids, Vol. 41, No. 1, 1993, pp 35-53.
- [17] Hild, F. and Burr, A., "Localization and Ultimate Strength of Fiber-Reinforced Ceramic-Matrix Composites," Mech. Res. Comm., Vol. 21, No. 4, 1994, pp 297-302.
- [18] Burr, A. and Hild, F., "Ultimate Tensile Strength during Fatigue of Fiber-Reinforced Ceramic-Matrix Composites," Mech. Res. Comm., Vol. 22, No. 4, 1995, pp 401-406.

Figure Captions

FIG. 1--Elementary cell.

FIG. 2--Schematic stress/strain curve.

FIG. 3--(1): Two-bar structure,

(2): Stress redistribution map exhibited by matrix cracking.

FIG. 4--Stress redistribution map exhibited by debonding and sliding when

$$(1): \Phi(N \rightarrow +\infty) \leq \frac{\left[\left\{ k(1-D_1) - 1 \right\} (1-f) + f - \frac{f}{k} \right] \sigma_{mc}}{(1-f)(1-D_1)E\alpha_1},$$

$$(2): \Phi(N \rightarrow +\infty) > \frac{\left[\left\{ k(1-D_1) - 1 \right\} (1-f) + f - \frac{f}{k} \right] \sigma_{mc}}{(1-f)(1-D_1)E\alpha_1}.$$

FIG. 5--Shear stress profile along the fiber direction during one unloading (1) - reloading (2) sequence.

FIG. 6--(1): Depiction of the equivalent shear stress $\tau^*(N)$,

the symbol  denotes the slope of a pointed straight line.

(2): Shear stress map when $\tau_\infty / \tau_0 = 0.2$, $R = 0$.

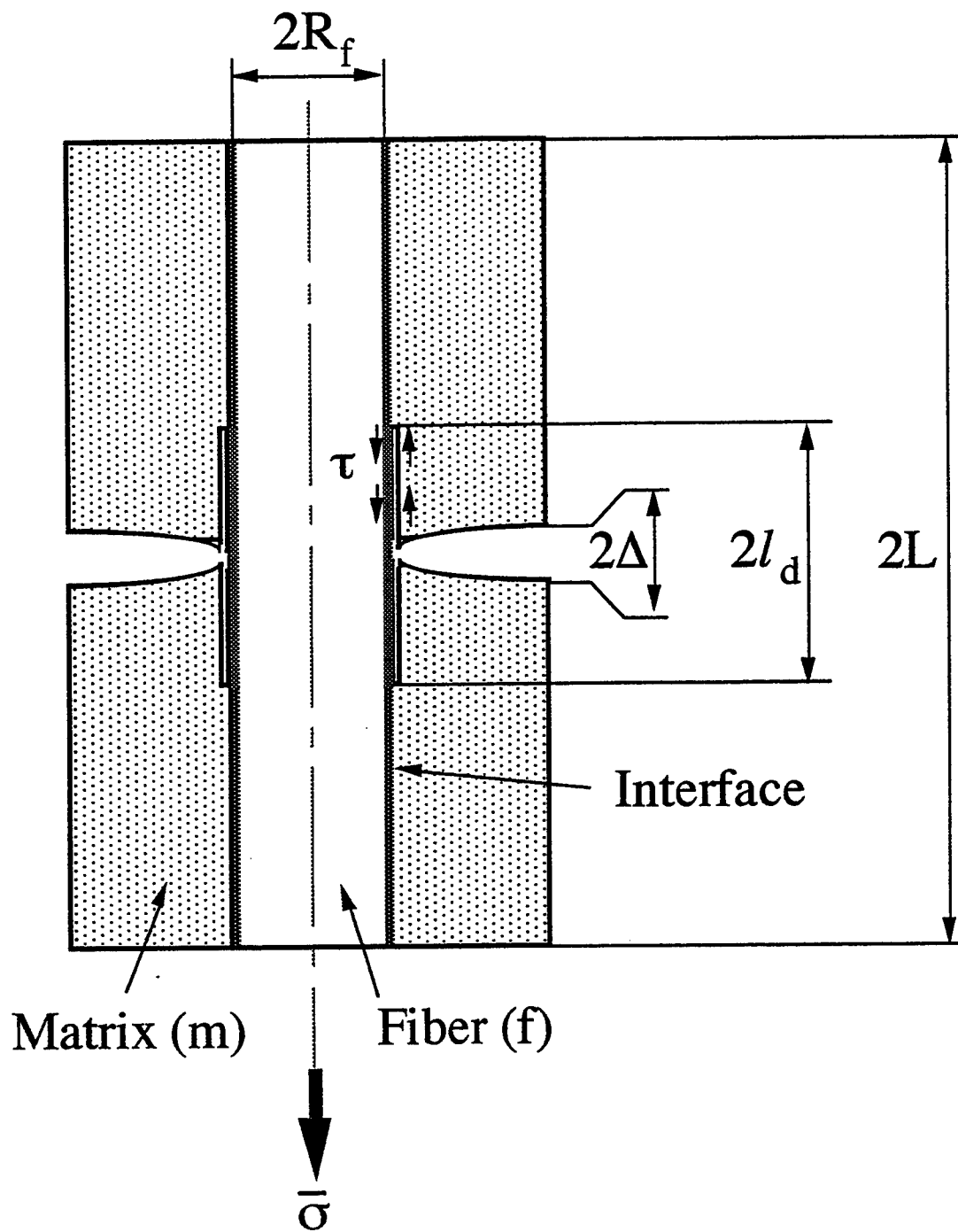


Figure 1 -- Burr; Hild and Leckie

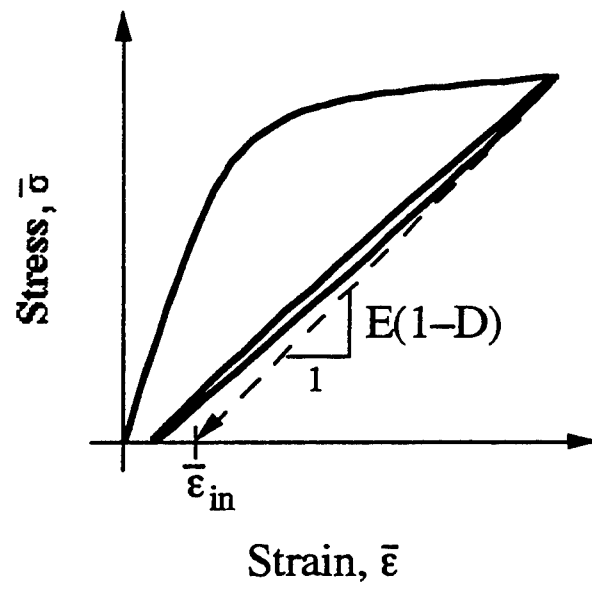
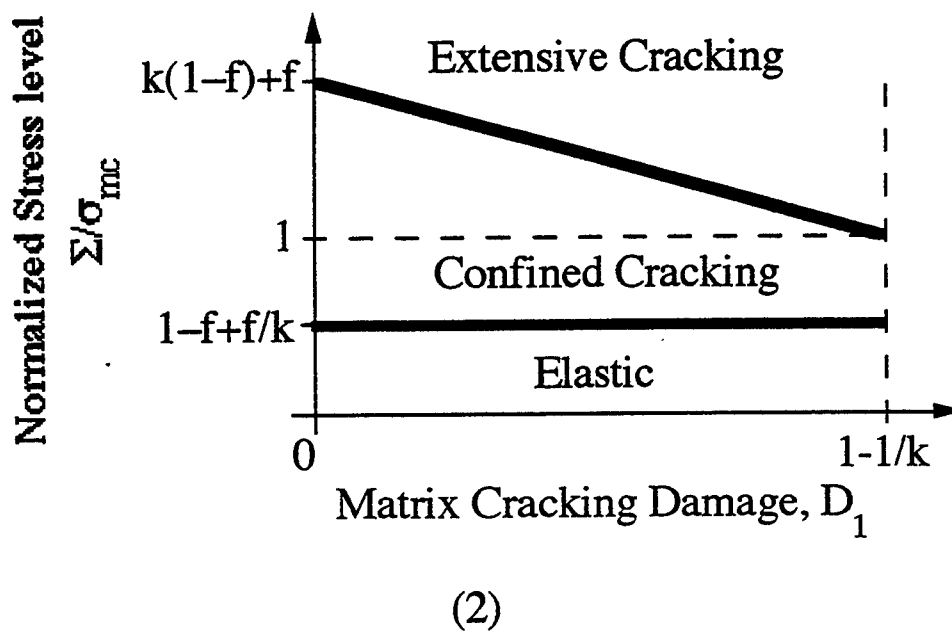
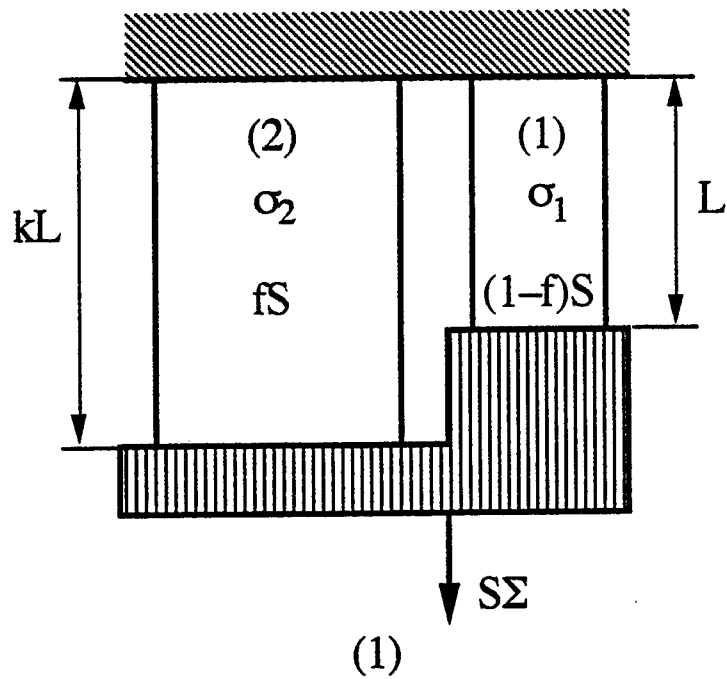
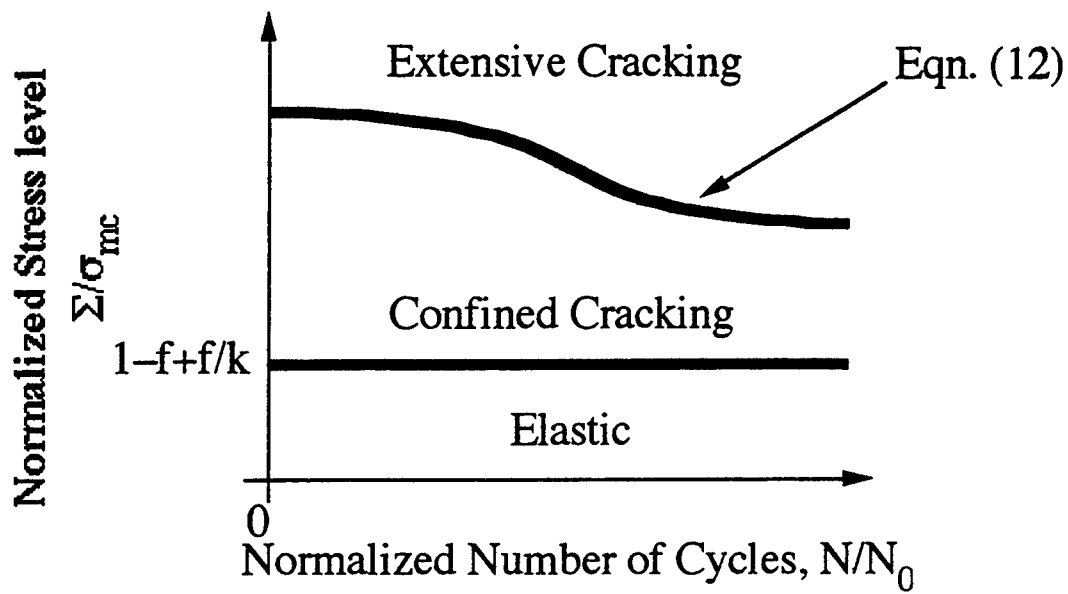


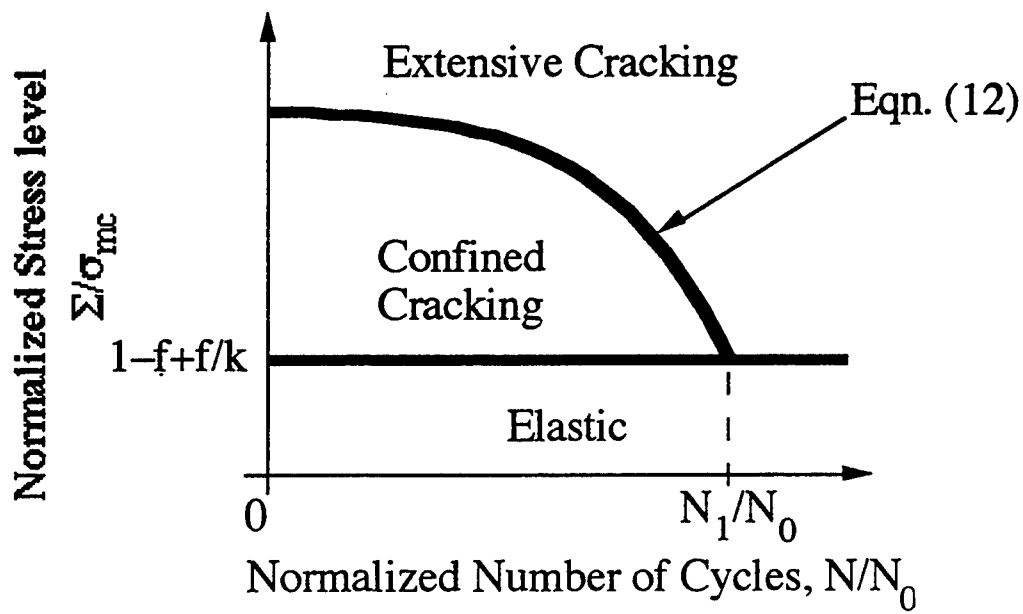
Figure 2 -- Burr; Hild and Leckie



Figures 3.1-2 -- Burr; Hild and Leckie

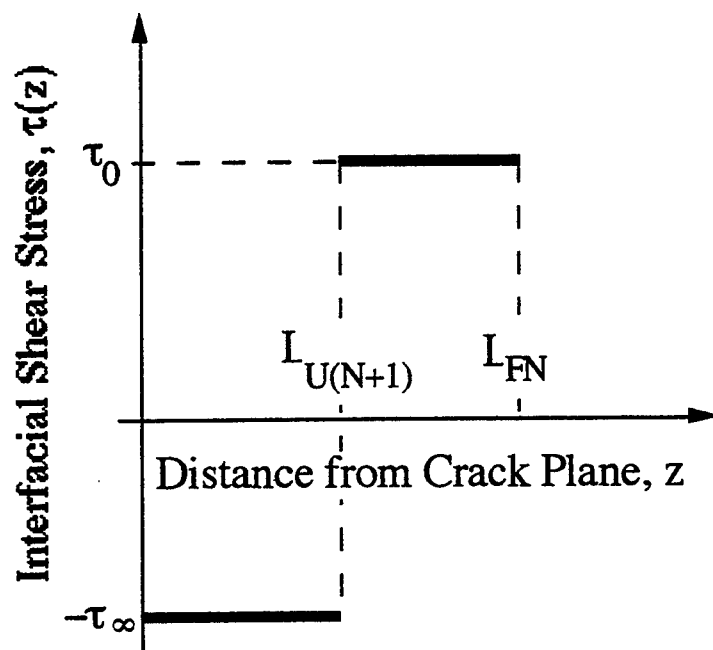


(1)

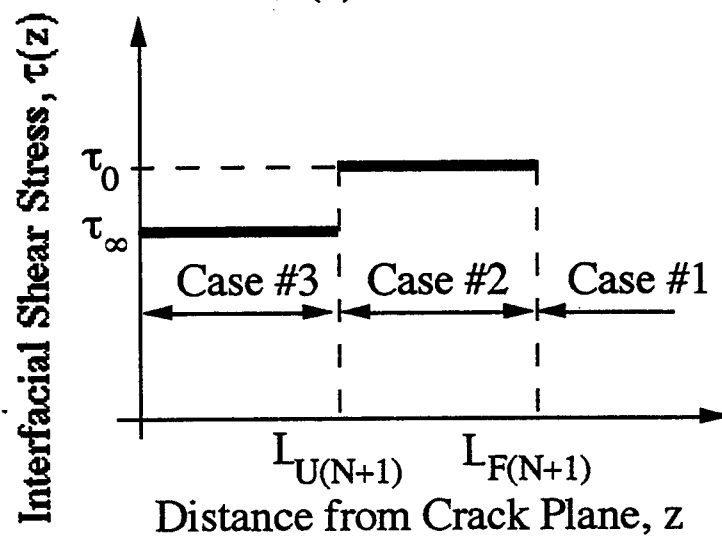


(2)

Figures 4.1-2 -- Burr; Hild and Leckie

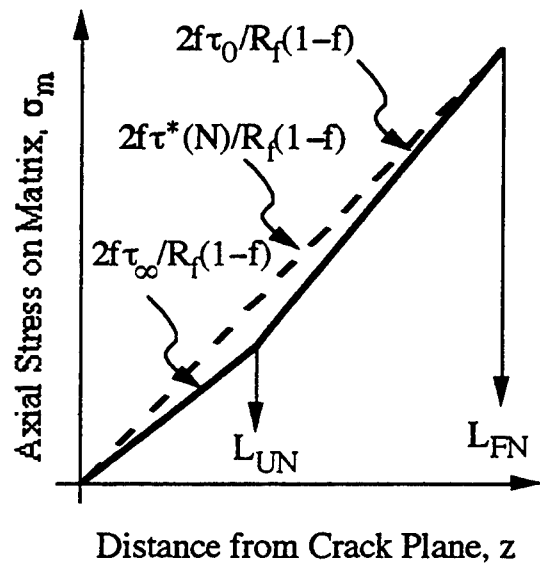


(1)

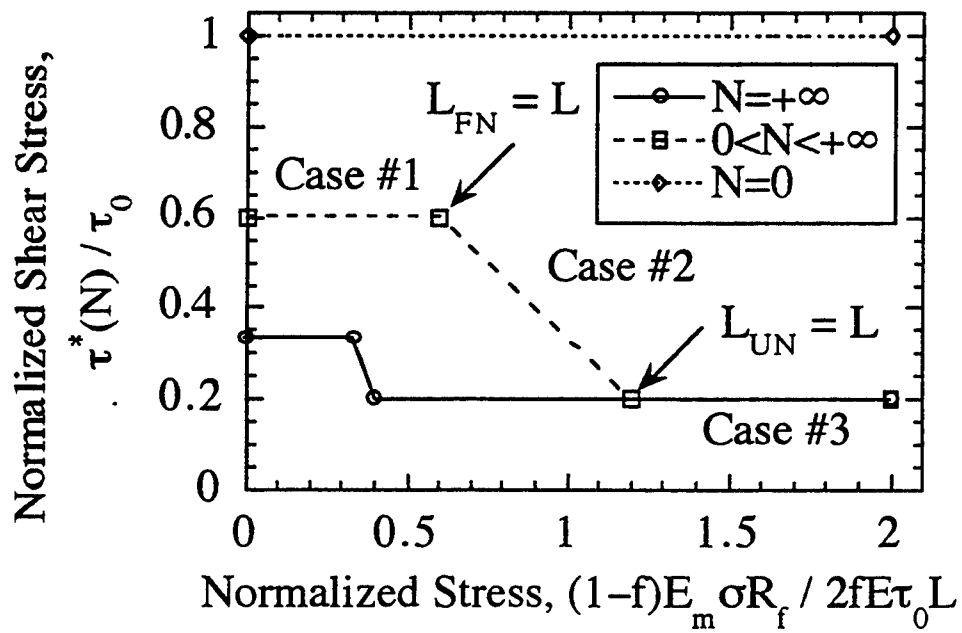


(2)

Figures 5.1-2 -- Burr; Hild and Leckie



(1)



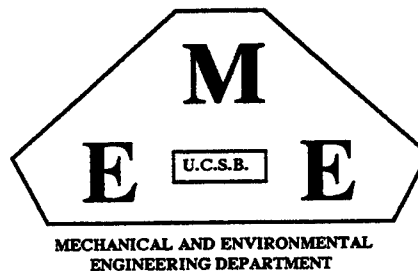
(2)

Figures 6.1-2 -- Burr; Hild and Leckie

CONTINUUM DESCRIPTION OF DAMAGE IN CERAMIC-MATRIX COMPOSITES

By

Alain Burr,¹ François Hild,^{1,*} and Frederick A. Leckie²



¹ Laboratoire de Mécanique et Technologie,
E.N.S. de Cachan / C.N.R.S. / Université Paris 6
61 avenue du Président Wilson, F-94235 Cachan Cedex, France.

² Department of Mechanical and Environmental Engineering, College of Engineering
University of California, Santa Barbara CA 93106-5070, U.S.A.

* to whom correspondence should be addressed.

CONTINUUM DESCRIPTION OF DAMAGE IN CERAMIC–MATRIX COMPOSITES

By

Alain Burr, François Hild, and Frederick A. Leckie

Abstract

A constitutive law is proposed for Ceramic–Matrix Composites which models matrix–cracking, sliding, fiber–breakage, and fiber pull–out. These different mechanisms induce loss of stiffness, inelastic strains, hysteresis loops, and crack closure. The features are analyzed within the framework of Continuum Damage Mechanics by the introduction of physical internal variables identified previously in material science investigations. The procedure is applied to a SiC/SiC [0/90] laminate composite using the results of pure tension tests of two laminate orientations. Each test involves a series of loading and unloading sequences. In order to verify the material description the behavior of an Iosipescu shear test is predicted using a Finite Element calculation and the results are compared with experiment.

1. Introduction

This study is concerned with the behavior of ceramics reinforced by continuous ceramic fibers. It has been demonstrated by Aveston et al. [1971] that following matrix-cracking, sliding occurs at the fiber-matrix interface which causes inelastic deformations. The presence of matrix cracks and inelastic deformations may impart to the material the ability to redistribute stresses. In fact the results of experiments on notched panels on SiC/CAS composites [Cady et al., 1995b] suggest the capacity of the material to redistribute stresses is sufficiently high for this material to be notch-insensitive. The ability to redistribute stress is an important property since design studies indicate that working stresses are sufficiently high for matrix-cracking to be unavoidable in regions of stress concentration.

The micromechanics which describes interface debonding and sliding has been established by Hutchinson and Jensen [1990] and Evans et al. [1994]. In contrast to the early phenomenological studies [Ladevèze, 1983] the intention of the present study is to develop a continuum description of the damage processes which is mechanism-based and which may be used to describe the behavior of Ceramic-Matrix Composites (CMCs) under the conditions of multiaxial stress occurring in practice. Since crack spacing at saturation is small [Beyerley et al., 1992] in most CMCs, Continuum Damage Mechanics is an appropriate means of describing degradation since changes in elastic moduli measured on a macroscopic level provide a simpler and more robust means of measuring damage than does microscopic measurement of crack density, which requires the average of many readings before reliable values are established [Jansson & Leckie, 1993].

By combining Continuum Damage Mechanics (CDM) [Lemaitre, 1992] with the micromechanical studies referred to previously, constitutive equations are developed which lend themselves to the finite element procedures commonly used in practice [Zienkiewicz & Taylor, 1989; Hibbitt et al., 1993]. The CDM formulation applied to reinforced

composites is written within the framework of the Thermodynamics of Irreversible Processes [Coleman & Gurtin, 1967; Rice, 1971; Germain et al., 1983]. The first step in establishing such a model is to identify the internal variables which define the state of the material. The second step is to determine the expression of the state potential in terms of the state variables and the third one to define the evolution laws of the internal variables.

The model is developed along the lines described, for instance, by Ashby [1992]. As mentioned earlier, the aim of the model is to be applied to structural applications. The degradation mechanisms are first determined by analyzing unidirectional CMCs in Section 2. The model is then extended to multidirectional systems in Section 3 by modeling the same mechanisms. The procedure described in the previous paragraph constitutes the general framework in which the model is written. In Section 4, the model identification is developed. In particular the number of tests constitutive of the input to the parameter tuning are discussed. The procedure is applied to continuous fiber SiC/SiC composites in a [0/90] lay-up for which suitable experimental data are available [Pluvinage, 1991] Section 5 is concerned with the prediction of a Iosipescu shear experiment. The results are compared with experimental data. This last section constitutes a first validation of the model.

2. The Tensile Stress-Strain Relationship for Unidirectional CMCs

Post-mortem analyses of broken specimens indicate the presence of arrays of microcracks in the matrix which are accompanied by debonding and friction at the fiber-matrix interface. Hutchinson and Jensen [1990] and Evans et al. [1994] have analyzed the behavior of unidirectional CMCs in tension by considering the unit cell shown in Fig. 1, when matrix-cracking of spacing $2L$ is accompanied by debonding and sliding at the interface over a friction length $2L_F$. The micromechanics analysis can predict the one-

dimensional macroscopic stress-strain response shown in Fig. 2. The microcracks are usually aligned with the principal stress or strain directions. By studying a cracked panel with crack of length $2a$ in a cell of area $4LW$ (Fig. 3), the reduction in stiffness may be estimated. If the initial behavior of the elementary cell is isotropic and elastic, and Young's modulus is E , it can be shown that the stiffness loss depends on the crack density defined as $\pi a^2 / 4LW$. By assuming plane stress conditions, and that the crack interactions can be neglected, a first approximation for the reduced elastic modulus \tilde{E} can be written as

$$(1) \quad \frac{\tilde{E}}{E} = \frac{1}{1 + 2 \frac{\pi a^2}{4LW}}$$

This relationship can be recast in the framework of CDM [Lemaitre & Chaboche, 1978] as

$$(2) \quad \frac{\tilde{E}}{E} = 1 - D$$

where

$$(3) \quad D = \frac{2 \frac{\pi a^2}{4LW}}{1 + 2 \frac{\pi a^2}{4LW}}$$

is the damage variable associated with the crack density. When D is small, a first order solution to Eqn. (3) is given by

$$(4) \quad D \approx 2 \frac{\pi a^2}{4LW}$$

so that the damage variable is proportional to the crack density. In the case of constituents with different elastic properties, D depends upon the elastic properties of the two constituents, as well as on the geometry (i.e., the ratios a/R and a/L , see Fig. 1, where R is the fiber radius). The uniaxial stress–strain relationship becomes

$$(5) \quad \sigma = \frac{\bar{\sigma}}{1-D} = E \bar{\varepsilon}$$

The elementary cell illustrated in Fig. 1 has been analyzed by various authors [H & J, 1990; E et al., 1994], but a different analytic approach is now used which follows the thermodynamic developments of Rice [1971] and Germain [1983] and which can be formulated conveniently in one and three dimensions alike. This is done by calculating the internal elastic energy density in the unit cell [Hild et al., 1996] caused by matrix–cracking, debonding and sliding at the interface. Two 'cut and paste' steps are used to evaluate the elastic energies following approaches introduced by Volterra [1907] and applied to the analysis the elastic behavior of homogeneous and isotropic media by considering the elastic properties of a cut cylinder [V, 1907; Love, 1927] as well as inclusions in an infinite medium [Eshelby, 1957] or to the study creeping materials [Cocks & Leckie, 1987]. The first step consists in moving the unbroken part (2) with respect to the broken part (1) with no external load by an amount Δ_s over a length l_F (Fig. 4). Because of interfacial sliding, this displacement Δ_s gives rise to a self-balanced linear stress field along a length l_F in parts (1) and (2) when the interfacial behavior is assumed to be characterized by a constant shear strength. By integration over l_F and then averaging over the total length L , the elastic energy density associated with this process is given by

$$(6) \quad \psi^s = \frac{2}{3} \frac{fE_1(1-f)E_2}{E} \left\{ \frac{\Delta_s}{l_F} \right\}^2 \frac{l_F}{L}$$

The crack opening displacement Δ_s due to slip induces an irreversible or inelastic strain α expressed as

$$(7) \quad \alpha = \frac{fE_1}{E} \frac{\Delta_s}{L}$$

The second step consists of an elastic loading of the damaged system so that the elastic energy density is given by

$$(8) \quad \psi^e = \frac{1}{2} E (1-D) (\bar{\epsilon} - \alpha)^2$$

The total elastic energy density is the sum of the two elements of the energy densities so that

$$(9) \quad \psi = \frac{1}{2} E (1-D) (\bar{\epsilon} - \alpha)^2 + \frac{2}{3} \frac{fE_1(1-f)E_2}{E} \left\{ \frac{\Delta_s}{l_F} \right\}^2 \frac{l_F}{L}$$

For convenience the energy density can be expressed in a more compact form by using state variables which are the total strain $\bar{\epsilon}$, the damage variable D modeling the loss of stiffness due to the cracking mechanism, the inelastic strain α derived previously (Eqn. (7)), and the damage variable $d = 3fE_1l_F / 4(1-f)E_2L$ which defines the size of the slip zone related to the average crack spacing. The friction length saturates when the cracking process stops ($L = l_F$) along with cracking damage D . Upon loading, all the internal variables vary (since L , l_F and Δ_s evolve), whereas upon unloading, the only variable to vary is the inelastic strain α (only Δ changes), the other variables are constant. The elastic energy density in terms of the new internal variables is [H et al., 1996]

$$(10) \quad \psi = \frac{1}{2} E (1-D) \left(\bar{\varepsilon} - \alpha \right)^2 + \frac{1}{2} E \left(\frac{\alpha^2}{d} \right)$$

The forces associated with the state variables $(\bar{\varepsilon}, D, d, \alpha)$ are respectively given by

$$(11.1) \quad \bar{\sigma} = \frac{\partial \psi}{\partial \bar{\varepsilon}} = E (1-D) (\bar{\varepsilon} - \alpha)$$

$$(11.2) \quad Y = - \frac{\partial \psi}{\partial D} = \frac{E}{2} (\bar{\varepsilon} - \alpha)^2$$

$$(11.3) \quad y = - \frac{\partial \psi}{\partial d} = \frac{E}{2} \left(\frac{\alpha}{d} \right)^2$$

$$(11.4) \quad X = \frac{\partial \psi}{\partial \alpha} = - \bar{\sigma} + E \frac{\alpha}{d}$$

These associated forces are useful in particular to determine the relevant forces driving each mechanism. Matrix cracking is assumed to be driven by Y , which plays an identical role as the energy release rate G in the framework of Linear Elastic Fracture Mechanics. From a micromechanical analysis [H et al., 1996] it can be shown that the back-stress is dependent on the applied stress $\bar{\sigma}$, therefore the driving force of the inelastic strains can be taken as the stresses acting in the same direction. The same assumption can be made when the evolution of the damage variable d related to sliding is analyzed, i.e. the driving force of d can be chosen to be its associated force y , or the applied stress $\bar{\sigma}$.

In the present approach the growth laws of the internal variables (D, d, α) are established from macroscopic quantities measured in the course of unloading and reloading sequences. To this end use is made of the solution of the response of the unit cell (Fig. 1) when subjected to an unloading/reloading sequence during which the magnitude of the shear stress remains constant.

The expressions obtained from the analysis for the residual stress ρ_1 and the internal variables D, d, α in terms of the macroscopic quantities shown in Fig. 2 are given respectively by [H et al., 1996]

$$(12.1) \quad \frac{-\rho_1}{E} = \left(\sqrt{\frac{\bar{\epsilon}_{in} + 2\delta\bar{\epsilon}}{4\delta\bar{\epsilon}}} - 1 \right) (\bar{\epsilon}_M - \bar{\epsilon}_{in} - 2\delta\bar{\epsilon})$$

$$(12.2) \quad D = \frac{\bar{\epsilon}_M \bar{D} - \bar{\epsilon}_{in} \bar{D} - 2\delta\bar{\epsilon}}{\bar{\epsilon}_M - \bar{\epsilon}_{in} - 2\delta\bar{\epsilon}}$$

$$(12.3) \quad \frac{d}{4} = \frac{\sqrt{(\bar{\epsilon}_{in} + 2\delta\bar{\epsilon})\delta\bar{\epsilon}}}{\bar{\epsilon}_M - \bar{\epsilon}_{in} - 2\delta\bar{\epsilon}}$$

$$(12.4) \quad \alpha = \frac{d}{2} \frac{\bar{\sigma}_M - \rho_1(1-D)}{E(1-D)}$$

where $-\rho_1 E_1 / E$ is the residual stress in the broken layer (1). Equations (12) are only valid when a constant shear strength characterizes the interfacial behavior, and lastly Eqn. (12.4) is only valid for monotonic loading conditions.

By performing a series of unloading/reloading sequences the internal variables can be determined from experiment using Eqns (12). The residual stress ρ_1 is calculated from Eqn. (12.1) and it is a test of the effectiveness of the model that the same value of the residual stress is obtained for each loading sequence. The values of D and d are given by applying Eqns (12.2) and (12.3) respectively. The information is now available to complete the calculation for Eqn. (12.4). The corresponding associated forces are obtained by the expressions given in Eqns. (11). The relationship between the internal variables and the associated forces can then be investigated by knowing the driving forces of each state variable. It is this method which is proposed to model the behavior of CMC laminates.

3. CMCs with Multidirectional Fiber Systems

The one-dimensional investigation is now extended to a [0/90] laminate composite and to a [0/90] woven composite subjected to multiaxial plane stress states. In this paper, only monotonic loading conditions are analyzed, even though the present framework can be easily extended to cyclic loading conditions and to non-proportional loading conditions. Following established procedures, the properties of each layer are first determined and those of the composite are then calculated by ensuring compatibility conditions.

The components of each layer consist of the matrix, the fiber and the interface, with f being the fiber volume fraction. The fiber direction defines the 1-2 axes. The axes x - y correspond to the principal axes of the strains in the ceramic matrix. The definition of the axes used at the constituent, layer and composite levels are shown in Fig. 5. Following Section 2, the loss of stiffness due to matrix-cracking and fiber-breakage is first established and this is followed by the influence of the slip at the interface.

3.1. Elastic Energies of the Composite Associated with Matrix-Cracking and Fiber-Breakage

3.1.1. Constituent Level: Matrix and Fiber

The initial behavior of the matrix is assumed to be isotropic. The presence of cracks leads the behavior to become anisotropic. The assumption is made that cracking occurs normal to the y -direction (e.g. maximum principal strain direction) in the matrix. Under the hypothesis of monotonic loading condition, only one damage variable is needed to model matrix-cracking, and is denoted by D_{my} . The study of a cracked system normal to one direction shows that the Young's modulus along that direction as well as the shear modulus

are altered [Budiansky & O'Connell, 1976; Chaboche, 1982] and that the expression of the elastic energy density of the matrix is

$$(13.1) \quad \psi_m = \frac{1}{2} \frac{E_m (\varepsilon_{mxx}^2 + 2\nu_m(1-D_{my})\varepsilon_{mxx}\varepsilon_{myy} + (1-D_{my})\varepsilon_{myy}^2)}{1-\nu_m^2(1-D_{my})} + 2\tilde{G}_m(D_{my})\varepsilon_{mxy}^2$$

with

$$\tilde{G}_m(D_{my}) = \frac{G_m}{1 + \left(\frac{D_{my}}{1 - D_{my}} \right) \frac{1}{2(1+\nu_m)}}$$

It is assumed that the fibers are aligned along the 1-direction and that fiber-breakage is perpendicular to the fiber direction. Therefore the elastic energy density is given by

$$(13.2) \quad \psi_f = \frac{1}{2} (E_f (1 - D_{f1}) \varepsilon_{f11}^2 + E_f \varepsilon_{f22}^2) + 2\tilde{G}_f(D_{f1}) \varepsilon_{f12}^2$$

The expression of the stresses in the matrix $\underline{\underline{\sigma}}_m$ and in the fibers $\underline{\underline{\sigma}}_f$ are obtained by partial differentiation of the elastic energy density with respect to the strain tensors $\underline{\underline{\varepsilon}}_m$ and $\underline{\underline{\varepsilon}}_f$ respectively

$$(14.1) \quad \underline{\underline{\sigma}}_m = \frac{\partial \psi_m}{\partial \underline{\underline{\varepsilon}}_m}$$

$$(14.2) \quad \underline{\underline{\sigma}}_f = \frac{\partial \psi_f}{\partial \underline{\underline{\varepsilon}}_f}$$

and the associated forces to the damage variables are defined as

$$(14.3) \quad Y_{my} = \frac{\partial \psi_m}{\partial D_{my}}$$

$$(14.4) \quad Y_{fl} = \frac{\partial \psi_f}{\partial D_{fl}}$$

These generalized forces are the energy release rate densities associated with matrix-cracking and fiber-breakage, respectively. They play similar roles as the force Y introduced in Section 2, and therefore are assumed to be the driving forces of the damage variables.

3.1.2. Layered Composite

When the composite consists of layers of unidirectional fibers with different orientations, the laminate properties are determined by applying laminate theory to the properties of individual layers.

3.1.2.1. Layer Level

A layer consists of fibers aligned along one orientation (the 1-direction) embedded in a matrix. To determine the behavior of this layer, micro-interface compatibility conditions are written in terms of the strains $\underline{\underline{\epsilon}}^L$ and stresses $\underline{\underline{\sigma}}^L$ on the layer level. These conditions are the compatibility and the equilibrium between a fiber (tensors $\underline{\underline{\epsilon}}_f$ and $\underline{\underline{\sigma}}_f$) and the surrounding matrix (tensors $\underline{\underline{\epsilon}}_m$ and $\underline{\underline{\sigma}}_m$), which takes place in that system. Therefore, it is more convenient to write the conditions in the 1-2 material frame as follows,

$$(15.1) \quad \epsilon_{m11} = \epsilon_{f11} = \epsilon_{11}^L$$

$$(15.2) \quad f_m \sigma_{m11} + f_f \sigma_{f11} = \sigma_{11}^L$$

$$(15.3) \quad f_m \varepsilon_{m22} + f_f \varepsilon_{f22} = \varepsilon_{22}^L$$

$$(15.4) \quad \sigma_{m22} = \sigma_{f22} = \sigma_{22}^L$$

$$(15.5) \quad f_m \varepsilon_{m12} + f_f \varepsilon_{f12} = \varepsilon_{12}^L$$

$$(15.6) \quad \sigma_{m12} = \sigma_{f12} = \sigma_{12}^L$$

When the principal strain directions do not coincide with the material frame, Eqns. (14.1–2) have to be rewritten in the 1–2 frame. The application of Eqns. (15) then defines the elastic properties of the layer

$$(16.1) \quad \underline{\underline{\sigma}}^L = \underline{\underline{E}}^L(D_{my}, D_{fl}) : \underline{\underline{\varepsilon}}^L$$

From Eqn. (16.1), the elastic energy density ψ^L associated with matrix–cracking and fiber–breakage on the layer level can be written as

$$(16.2) \quad \psi^L = \frac{1}{2} \underline{\underline{\varepsilon}}^L : \underline{\underline{E}}^L(D_{my}, D_{fl}) : \underline{\underline{\varepsilon}}^L$$

Matrix cracking and fiber breakage are dissipative mechanisms which do not store energy. Therefore they influence only the reversible (i.e., elastic) part of the free energy density.

3.1.3. Composite Level

For simplicity, the case of two layers at 0 and 90 degrees are considered. The micromechanical quantities associated with the 0 degree layer are superscripted by ⁰⁰, and those at 90 degrees by ⁹⁰. The elastic behavior of the composite system is determined by applying classical laminate theory. The compatibility condition and global equilibrium allow to get the overall stresses $\underline{\underline{\sigma}}$ and strains $\underline{\underline{\varepsilon}}$

$$(17.1) \quad \underline{\underline{\varepsilon}} = \underline{\underline{\varepsilon}}^{00} = \underline{\underline{\varepsilon}}^{90}$$

$$(17.2) \quad \underline{\underline{\sigma}} = f^{00} \underline{\underline{\sigma}}^{00} + f^{90} \underline{\underline{\sigma}}^{90}$$

By solving Eqns. (17) and using Eqn. (16.1), the overall behavior of the composite is defined as

$$(18.1) \quad \underline{\underline{\sigma}} = \underline{\underline{E}}(\underline{\underline{D}}_{my}^{00}, \underline{\underline{D}}_{my}^{90}, \underline{\underline{D}}_{fl}^{00}, \underline{\underline{D}}_{fl}^{90}) : \underline{\underline{\varepsilon}}$$

with

$$\underline{\underline{E}}(\underline{\underline{D}}_{my}^{00}, \underline{\underline{D}}_{my}^{90}, \underline{\underline{D}}_{fl}^{00}, \underline{\underline{D}}_{fl}^{90}) = f^{00} \underline{\underline{E}}(\underline{\underline{D}}_{my}^{00}, \underline{\underline{D}}_{fl}^{00}) + f^{90} \underline{\underline{E}}(\underline{\underline{D}}_{my}^{90}, \underline{\underline{D}}_{fl}^{90})$$

From Eqn. (18.1), the elastic energy density ψ^D associated with matrix-cracking and fiber-breakage on the composite level can be written as

$$(18.2) \quad \psi^D = f^{00} \psi^{00} + f^{90} \psi^{90}$$

with

$$\psi^{00} = \frac{1}{2} \underline{\underline{\varepsilon}} : \underline{\underline{E}}^{00}(\underline{\underline{D}}_{my}^{00}, \underline{\underline{D}}_{fl}^{00}) : \underline{\underline{\varepsilon}}$$

$$\psi^{90} = \frac{1}{2} \underline{\underline{\varepsilon}} : \underline{\underline{E}}^{90}(\underline{\underline{D}}_{my}^{90}, \underline{\underline{D}}_{fl}^{90}) : \underline{\underline{\varepsilon}}$$

3.1.2. Woven Composite

Woven composites are another architecture commonly used. Eqns. (16) can be used also for woven architectures. This approximation is relevant when two different damage

mechanisms can be exhibited in the tows at 0 and 90 degrees. Also, the effects due to fiber cross-over are neglected. Therefore the results developed so far can be extended to woven architectures.

However, there may be some situations in which the distinction between the matrix of the tows at 0 and 90 degrees is more difficult to make because there is only one matrix-cracking mechanism. In place of Eqns. (16) for the single layer, the equilibrium and compatibility conditions are given by the following equations written in the 1-2 frame

$$(19.1) \quad \epsilon_{m11} = \epsilon_{f11}^1 = \epsilon_{11}$$

$$(19.2) \quad \sigma_{m11} = \sigma_{f11}^2$$

$$(19.3) \quad (1+f_m) \sigma_{m11} + f_f \sigma_{f11}^1 = 2\sigma_{11}$$

$$(19.4) \quad \epsilon_{m22} = \epsilon_{f22}^2 = \epsilon_{22}$$

$$(19.5) \quad \sigma_{m22} = \sigma_{f22}^1$$

$$(19.6) \quad (1+f_m) \sigma_{m22} + f_f \sigma_{f22}^2 = 2\sigma_{22}$$

$$(19.7) \quad f_m \epsilon_{m12} + f_f \epsilon_{f12}^1 = \epsilon_{12}$$

$$(19.8) \quad \sigma_{m12} = \sigma_{f12}^1 = \sigma_{f12}^2 = \sigma_{12}$$

By solving Eqns. (19), and noting that there exists only one degradation mechanism taking place in the matrix characterized by one damage variable D_{my} and two degradation mechanisms associated with fiber-breakage in the 0 and 90 degree directions (D_{f1}^{00} , D_{f1}^{90}), the overall behavior of the composite is defined as

$$(20.1) \quad \underline{\underline{\sigma}} = \underline{\underline{E}}(D_{my}, D_{f1}^{00}, D_{f1}^{90}) : \underline{\underline{\epsilon}}$$

The elastic energy density ψ^D associated with matrix-cracking and fiber-breakage on the composite level can be written as

$$(20.2) \quad \psi^D = \frac{1}{2} \underline{\underline{\varepsilon}} : \underline{\underline{E}}(D_{my}, D_{fl}^{00}, D_{fl}^{90}) : \underline{\underline{\varepsilon}}$$

3.2. State Potential Associated with Debonding and Fiber Pull-Out

Inelasticity is essentially due to sliding at the interface between the fiber and the matrix. Sliding is involved in debonding as well as fiber pull-out. From a micromechanical point of view, this sliding can take place as soon as a crack is bridged by fibers. In a CDM formulation, only the equivalent homogenous sliding and the associated forces are considered. By considering equivalent homogeneous sliding on the composite level, there is no way to distinguish the contributions due to fiber/matrix debonding and sliding, and inter-layer delamination. However, in most CMCs delamination is not as critical as in polymeric matrix composites for which the Young's moduli differences are far more important. Therefore, the cell model used to describe cracking and sliding is that shown in Fig. 1. The analysis that has been done on a 1-D model (given in Section 2) can be formally extended to give the expression of the elastic energy density due to sliding of a layered composite along the 1-2 directions [Burr et al., 1995]

$$(21) \quad \psi^S(\underline{\underline{\alpha}}, \underline{\underline{d}}) = \frac{1}{2} \bar{\bar{E}} \left(\frac{\alpha_{11}^2}{d_{11}} + \frac{\alpha_{22}^2}{d_{22}} \right) + \frac{1}{2} \bar{\bar{G}} \left(\frac{\alpha_{12}^2}{d_{12}} \right)$$

with

$$\bar{\bar{E}} = \frac{f^{00}E^{00}f^{90}E^{90}}{f^{00}E^{00} + f^{90}E^{90}}$$

$$\bar{\bar{G}} = \frac{f^{00}G^{00}f^{90}G^{90}}{f^{00}G^{00} + f^{90}G^{90}}$$

3.2.1. State laws

The following development deals with layered CMCs. By using the results of Section 2, the total elastic energy density of the composite is the sum of the elastic energy density of the damaged composite ψ^D and the elastic energy density due to debonding and sliding ψ^S

$$(22) \quad \psi = \frac{1}{2} (\underline{\underline{\varepsilon}} - \underline{\underline{\alpha}}) : \underline{\underline{E}}(D_{my}^{00}, D_{my}^{90}, D_{fl}^{00}, D_{fl}^{90}) : (\underline{\underline{\varepsilon}} - \underline{\underline{\alpha}}) + \psi^S(\underline{\underline{\alpha}}, \underline{\underline{d}})$$

The force associated with total strain is

$$(23.1) \quad \underline{\underline{\sigma}} = \frac{\partial \psi}{\partial \underline{\underline{\varepsilon}}} = \underline{\underline{E}}(D_{my}^{00}, D_{my}^{90}, D_{fl}^{00}, D_{fl}^{90}) : (\underline{\underline{\varepsilon}} - \underline{\underline{\alpha}})$$

and corresponds to the macroscopic stress. The associated force to the damage variables modeling matrix-cracking and fiber-breakage are

$$(23.2) \quad Y_i = \frac{\partial \psi}{\partial D_i}$$

where $D_{i=1;4} = \{D_{my}^{00} ; D_{my}^{90} ; D_{fl}^{00} ; D_{fl}^{90}\}$, and $Y_{i=1;4} = \{Y_{my}^{00} ; Y_{my}^{90} ; Y_{fl}^{00} ; Y_{fl}^{90}\}$ represent the corresponding energy release rate densities due to matrix-cracking and fiber-breakage. The associated force to the damage variables modeling sliding are

$$(23.3) \quad \underline{\underline{\gamma}} = \frac{\partial \psi}{\partial \underline{\underline{d}}} = \frac{\partial \psi^S}{\partial \underline{\underline{d}}}$$

where $\underline{d} = \{d_{11} ; d_{22} ; d_{12}\}$, and \underline{y} correspond to the energy release rate densities due to debonding and sliding. The associated forces to the inelastic strains $\underline{\alpha}$ are

$$(23.4) \quad \underline{X} = \frac{\partial \psi}{\partial \underline{\alpha}} = -\underline{\sigma} + \frac{\partial \psi^S}{\partial \underline{\alpha}}$$

and represent the back-stresses in the sliding zone.

3.2.2. Evolution laws

The identification procedure is performed on a $[0/90]_s$ laminate architecture of CMCs. The first step is to define all the internal state variables needed to model the material behavior. The three total strain variables, (e.g., ε_{11} , ε_{22} , ε_{12}), are given either from experiment or as input from a F.E. calculation. The four damage variables $D_{i=1;4} = \{D_{my}^{00} ; D_{my}^{90} ; D_{fl}^{00} ; D_{fl}^{90}\}$ are used to define the change in the elastic properties, with $D_m = \{D_{my}^{00} ; D_{my}^{90}\}$ is the set of damage variables modeling matrix-cracking, and $D_f = \{D_{fl}^{00} ; D_{fl}^{90}\}$ is the set of damage variables modeling fiber-breakage. Assuming the damage evolution laws, $D_m(Y_m)$ and $D_f(Y_f)$ are functions of the associated forces $Y_m = \{Y_{my}^{00} ; Y_{my}^{90}\}$, and $Y_f = \{Y_{fl}^{00} ; Y_{fl}^{90}\}$ respectively, then only two evolution laws, one for each mechanism, are sufficient to compute the four components of damage. The three damage variables, $\{d_{11} ; d_{22} ; d_{12}\}$, define the sliding distances, with d_{11} or d_{22} being associated with sliding in the fiber directions and d_{12} associated with shear sliding. Consequently only two evolution laws are needed, $d_{11}(y_{11})$ or $d_{22}(y_{22})$, and $d_{12}(y_{12})$.

For the same reasons, two evolution laws for the inelastic strains, $\alpha_{11}(X_{11})$ or $\alpha_{22}(X_{22})$, and $\alpha_{12}(X_{12})$ define the evolution of the three inelastic strains, $\{\alpha_{11} ; \alpha_{22} ; \alpha_{12}\}$. In conclusion, the model has 13 state variables, three of which are

strain inputs and the remaining 10 micromechanical internal variables are derived from 6 evolution laws. Therefore, the set S of state variables is (Table 1)

$$(24.1) \quad S = \left\{ \underline{\underline{\varepsilon}} ; \underline{\underline{\alpha}} ; D_{i=1,4} ; \underline{\underline{d}} \right\}$$

and the associated forces F are (Table 1)

$$(24.2) \quad F = \left\{ \underline{\underline{\sigma}} ; \underline{\underline{X}} ; Y_{i=1,4} ; \underline{\underline{y}} \right\}$$

The second step is to define the relevant tests required to identify the growth of the six internal variables. This is achieved from unloading/reloading tests performed at regular intervals and measuring the macroscopic inelastic strain upon complete unloading, $\bar{\varepsilon}_{in}$, the macroscopic damage of the composite, \bar{D} , and the maximum hysteresis loop width, $\delta\bar{\varepsilon}$ (Fig. 2). Using Eqns. (12), the internal variables can be calculated.

When tension is applied at 45 degrees on a $[0/90]_s$ layered composite, the macroscopic damage variable, \bar{D}^{45} , is related to the microscopic damage variables taking place in the matrix alone, $\left\{ D_{my}^{00} ; D_{my}^{90} \right\}$, by using the transformation rules given in the Appendix. Moreover, in this particular case, the two damage variables D_{my}^{00} and D_{my}^{90} have the same value. Therefore, the evolution law, $D_m(Y_m)$, is directly given by the evolution of the macroscopic damage of the composite \bar{D}^{45} (Fig. 6).

The evolution law of the damage variable associated with fiber-breakage, $D_f(Y_f)$, is found from measurement of the macroscopic damage \bar{D}^{00} (Fig. 6) in a tension test at 0 degree on the $[0/90]$ which has been compensated by the contribution matrix-cracking which is calculated from the results of the first test.

Similarly, the evolution laws of the state variables related to sliding, $\alpha_{11}(X_{11})$ or $\alpha_{22}(X_{22})$, and $d_{11}(y_{11})$ or $d_{22}(y_{22})$ are known from the evolution of the macroscopic inelastic strain upon complete unloading $\bar{\varepsilon}_{in}^{00} = \alpha_{11}(\bar{\sigma}_{11}=0)$, the macroscopic damage of the

composite, D^{00} , and the maximum hysteresis loop width, $\delta\bar{\epsilon}^{00}$, using generalized micromechanics relations (Eqns. 12)

$$(25.1) \quad \frac{-\rho_1^{00}}{E^{00}} = \left(\sqrt{\frac{\bar{\epsilon}_{in}^{00} + 2\delta\bar{\epsilon}^{00}}{4\delta\bar{\epsilon}^{00}}} - 1 \right) (\bar{\epsilon}_m^{00} - \bar{\epsilon}_{in}^{00} - 2\delta\bar{\epsilon}^{00})$$

$$(25.2) \quad D^{00} = \frac{\bar{\epsilon}_M^{00} \bar{D}^{00} - \bar{\epsilon}_{in}^{00} \bar{D}^{00} - 2\delta\bar{\epsilon}^{00}}{\bar{\epsilon}_M^{00} - \bar{\epsilon}_{in}^{00} - 2\delta\bar{\epsilon}^{00}}$$

$$(25.3) \quad \frac{d_{11}}{4} = \frac{\sqrt{(\bar{\epsilon}_{in}^{00} + 2\delta\bar{\epsilon}^{00})\delta\bar{\epsilon}^{00}}}{\bar{\epsilon}_M^{00} - \bar{\epsilon}_{in}^{00} - 2\delta\bar{\epsilon}^{00}}$$

$$(25.4) \quad \alpha_{11} = \frac{d_{11}}{2} \frac{\bar{\sigma}_M^{00} - \rho_1^{00}(1-D^{00})}{E^{00}(1-D^{00})}$$

Finally, returning to the results of the tension test at 45 degrees on a $[0/90]_s$ layered composite (Fig. 6), the evolution laws of the state variables related to sliding, $\alpha_{12}(X_{12})$ and $d_{12}(y_{12})$ are given by the following relationships similar to those calculated by the micromechanical analysis

$$(26.1) \quad \frac{d_{12}}{4} = \frac{\bar{\epsilon}_{in}^{45}}{\bar{\epsilon}_M^{45} - 2\bar{\epsilon}_{in}^{45}}$$

$$(26.2) \quad \alpha_{12} = \frac{d_{12}}{2} \frac{\bar{\epsilon}_M^{45}}{1 + \frac{d_{12}}{2}}$$

In this analysis, it can be noticed that the residual stress $-\rho_1^{45}$ in the tension direction is equal to zero, and therefore $\bar{\epsilon}_{in}^{45} = 2\delta\bar{\epsilon}^{45}$, which leads to the above results. Equations (25) can be used to predict the overall behavior of the analyzed CMC. However, they are valid

provided the interfacial behavior can solely be modeled by a constant interfacial shear strength. This is not the only model available to study CMCs. Therefore the evolution laws of the damage variables as well as the inelastic strains are determined by direct measurement of their values at different stress levels. The drawback of this approach is that the model is not completely identified since the damage variables related to debonding and sliding are not identified. Therefore the part of the free energy that is stored is not fully determined since it depends upon the details of the interfacial behavior. The stress/strain relationship however is known and thus a structural analysis can be performed.

In summary, only two tests, on the same architecture, enable us to extract all six evolution laws that define the behavior of the material (see Fig. 6). Two tensile tests are sufficient when the back-stresses are computed (therefore the damage variables related to debonding and sliding). In the following it will be shown that two tests are still sufficient as long as the evolution of the inelastic strain α_{12} can be obtained by the analysis of one of the tensile tests.

4. Model Identification

The identification is performed on a $[0/90]_s$ laminate architecture of a SiC/SiC composite using the experimental results of Pluvinaige [1991]. Only two tension tests are used to establish the evolution laws of the damage quantities and the inelastic strains.

The first step is to consider the elastic properties. Inspection of the composite [P, 1991] indicates the presence of porosity in the matrix. Because the model is mechanism-based, the only means of accounting for this porosity is by an initial non-zero matrix damage quantity, D_{m0} . The measurement of Young's Moduli E^{00} and E^{45} respectively for a 0 degree and 45 degree tension tests combined with their analytic expressions gives the value of the initial non-zero isotropic damage quantity, $D_{m0} = 0.7$, which affects *only the initial elastic properties*. This damage value is consistent with experimental observations of

initial porosities due to the Chemical Vapor Infiltration technique used to process these materials [P, 1991].

The evolution laws of the state variables are written in terms of the associated forces. Therefore, the evolution of the damage variables is written as a function of the strain energy release rate densities. The evolution of the inelastic strains is written in terms of the corresponding back-stresses. It can be shown that the back-stresses are linearly proportional to the macroscopic stresses as shown in Eqns. (23.4) and (25.4). For the sake of simplicity, the evolution of the inelastic strains is thus written in terms of the macroscopic stresses. Lastly, the evolution of the damage variable \underline{d} is not explicitly needed in the present approach since only monotonic loading conditions are considered (see Section 2) and no particular statement is made concerning the interfacial behavior (see Section 3).

From the analysis of a tension test at 0 degree, the maximum hysteresis loop width is close to half of the corresponding inelastic strain upon complete unloading. It is concluded from Eqn. (25.1) that the macroscopic residual stresses are very small and will therefore be neglected.

The variation of D_m with Y_m obtained from the experimental data is shown in Fig. 7.1. Since matrix cracking is related to the presence of randomly distributed flaws, an appropriate form of evolution law which can fit the data shown in Fig. 7.1 is given by a Weibull law [1939; 1951]

$$(27) \quad D_m = D_{sat} \left(1 - \exp \left[- \left(\frac{Y_m - Y_{mth}}{Y_{m0}} \right)^{m_m} \right] \right)$$

The values that fit the data of Fig. 7.1 are

$$(28) \quad D_{sat} = 1.0 \quad Y_{mth} = 0. \text{ Jm}^{-3} \quad Y_{m0} = 0.6 \text{ Jm}^{-3} \quad m_m = 1.2$$

The threshold energy release rate density Y_{mth} has a zero value in accordance with the hypothesis of no macroscopic residual stresses. The parameters Y_{m0} and m_m are directly related to the evolution of cracking density as a function of applied stress. The damage parameter at saturation has a very high value in agreement with the fact that average crack spacing is very small for these composites [P, 1991]. The evolution laws for matrix damage having been determined, the fiber-breakage damage D_f can be plotted, as a function of Y_f . Using Curtin's relationship [1991] for fiber damage, the evolution law is given by

$$(29) \quad D_f = 1 - \exp \left[- \left(\frac{Y_f}{Y_{f0}} \right)^{(m_f+1)/2} \right]$$

In the following computations, it was assumed that during the matrix-cracking process, only few fibers break. Therefore, no attempt was made to identify the previous parameters.

Lastly, the expression used to fit the evolution laws for the inelastic strains shown in Figs. 7.2 and 7.3 are

$$(30) \quad \alpha_i = \frac{\langle \sigma_i - \sigma_{th} \rangle}{\sigma_0}$$

$$(31) \quad \alpha_{12} = \frac{\langle \tau_{eq} - \tau_{th} \rangle}{\tau_0} \text{Sign}(\tau_{12})$$

The material parameters of Eqns. (30) and (31) are related to the interfacial behavior.

The introduction of the expression for τ_{eq} comes from the observation that the stress/strain curves obtained for tensile tests at 45 degrees and shear tests at 0 degree almost coincide for CMC systems. This observation appears to apply for a whole class of materials: SiC/SiC, SiC/CAS, SiC/C, C/C composites [Cady et al., 1995a] and

presumably SiC/Al₂O₃ composites [Heredia et al., 1995]. One choice for τ_{eq} which satisfies this requirement is given by

$$(32) \quad \tau_{eq} = \sqrt{\left| \tau_{12} \left[\tau_{12} + \frac{3}{2}(\sigma_{11} + \sigma_{22}) \right] \right|}$$

Similar behavior is observed in concrete for which both the hydrostatic and shear stress states influence the inelastic deformations [Drucker & Prager, 1956] The definition of the equivalent shear stress given in Eqn. (32) enables us to identify all the evolution laws by analyzing two tensile tests. This hypothesis is crucial and will be checked in Section 5. The constants in Eqns. (30) and (31) which define the inelastic strains are given by (see Figs. 7.2 and 7.3)

$$(33) \quad \begin{aligned} \sigma_{th} &= 88 \text{ MPa} & \sigma_0 &= 480 \text{ GPa} \\ \tau_{th} &= 154 \text{ MPa} & \tau_0 &= 64.8 \text{ GPa} \end{aligned}$$

This model is implemented in the industrial Finite Element code ABAQUS [H et al., 1993] via a user material (UMAT) routine. This allows to investigate more complex loading conditions on a structural level. The Finite Element procedure was checked by analyzing pure tension tests at 0 and 45 degrees. The comparisons in terms of stress–strain between the experiments and the computations are shown in Figs. 8. There is a good agreement between the model and the experiments used to identify the model.

5. Analysis of Experiments on SiC/SiC Composites

When the availability of materials is restricted to planar form, the most usual means of obtaining shear data is to subject the Iosipescu specimen [Iosipescu, 1967] to shear force

[P, 1991]. In order to investigate the suitability of the Iosipescu test as a means of obtaining shear data, a Finite Element analysis has been performed using the constitutive equations described and identified previously. The Iosipescu specimen shown in Fig. 9 is subjected to shear loading and measurement of the shear properties of the material are obtained by plotting the average stress at the minimum section against the shear strain measured by strain gauges placed at the center of the specimen. It is known that the shear stress at the minimum section of this specimen is sensibly constant when the material is elastic and isotropic, but it is not known if the constant shear stress assumption is valid when cracking occurs. In addition to verifying the suitability of the Iosipescu specimen, the tests provide an opportunity to measure the ability of the constitutive equations to predict the behavior of a component in which the stress state is different from those used in the identification procedure.

The plot of the average stress against the strain at the center of the specimen is shown in Fig. 10. This prediction agrees with the experimental observations to within 5%. The stress-strain shear curve at the center of the ligament is also shown in Fig. 10. It can be seen that the average stress-strain shear curve *underestimates* the actual stresses. The difference, which is not large, is the result of the assumption that the shear stress and strain are almost uniform across the minimum section. The results of the finite element analysis shown in Fig. 11 indicate that the shear stress at the minimum section is essentially constant therefore justifying the use of the Iosipescu specimen as a means of obtaining shear data. Lastly, the hypothesis made to write the evolution of the inelastic strain α_{12} (Eqn. (31)) as a function of the equivalent shear stress τ_{eq} (Eqn. (32)) seems reasonable when the results of prediction of the Iosipescu test is compared with the experiments. Figure 11 also compares the shear stress profile for the linear elastic and non-linear calculations when the external load level is identical. The effect of non-linear stress/strain behavior allows the stresses to be redistributed when compared to a purely linear elastic calculation. This effect can be measured by the ratio of the average to maximum shear

stresses in the elastic calculation (0.93) and in the non-linear analysis (0.95). This difference is not important since the shear stress profile is almost constant in the ligament even for a linear elastic computation.

6. Conclusions

A CDM model is proposed for CMCs which is mechanisms-based. The laws which relate the growth of the internal state variables to their associated forces have been derived from the unloading-reloading paths during tensile experiments for two different directions. The ability of the model to predict the response to another state of stress suggests the advantage of a mechanism-based approach.

When applied to SiC/SiC [0/90] lay-ups, the present model has 10 internal variables, viz. three inelastic strains modeling sliding, three damage variables describing the amount of debonding and four damage variables accounting for matrix-cracking and fiber-breakage in the two plies. It is shown that only two different experiments in tension are needed to identify the growth laws of the ten internal variables. The model has the potential to be applied to other material configurations (e.g., SiC/CAS, SiC/C, C/C, and presumably SiC/Al₂O₃ composites) and architectures (e.g., woven configurations). Furthermore, the general framework presented herein has been applied to room temperature configurations and monotonic loading conditions. However extensions to cyclic load histories as well as high temperature applications can be included with minimal change to the state potential formulations. Evolution laws will have to be modified slightly.

The reliability of the Iosipescu test is confirmed as a means of average stress-strain shear data, and the constitutive equations are able to predict the shear properties correctly. However, it is shown that the average shear properties may be slightly different from the actual stress-strain shear data in the center of the ligament. Therefore the identification of

the shear properties based upon the measurements on an Iosipescu test are, strictly speaking, only an approximation of the actual response in pure shear.

The ability of stress redistribution due to the non-linearity of the stress/strain curve has been shown in the case of the Iosipescu experiment. Stress redistribution is important for structural applications and needs to be further studied on other types of structures and load configurations (e.g., plates with holes, notches, pin-loaded structures). This work is still under way.

Acknowledgments

This work was supported by the Advanced Research Project Agency through the University Research Initiative under Office of Naval Research Contract No. N-00014-92-J-1808.

Nomenclature

a	crack size
α	inelastic strain
$\underline{\underline{\alpha}}$	inelastic strain tensor
α_i	inelastic strain component in the i -direction ($i=11$ or 22)
$\alpha_{11}, \alpha_{22}, \alpha_{12}$	components of the inelastic strain tensor $\underline{\underline{\alpha}}$ in 1–2 frame
d	damage variable due to debonding and slip
$\underline{\underline{d}}$	debonding and sliding damage tensor
d_{11}, d_{22}, d_{12}	components of the debonding and sliding damage tensor $\underline{\underline{d}}$ in 1–2 frame
$D, D_m, D_{my}, D_{my}^{00}, D_{my}^{90}$	damage variables modeling matrix cracking
$\bar{D}, \bar{D}^{00}, \bar{D}^{45}$	macroscopic damage variables
$D_f, D_{f1}, D_{f1}^{00}, D_{f1}^{90}$	damage variables modeling fiber-breakage
D_i	set of damage variables
$D_{sat}, Y_{mth}, Y_{m0}, m_m$	parameters of the evolution law of matrix-cracking damage
Δ_s	crack opening displacement due to slip
$\delta\bar{\epsilon}, \delta\bar{\epsilon}^{00}, \delta\bar{\epsilon}^{45}$	maximum hysteresis loop width
E, E_1, E_2, E_m, E_f	Young's moduli
E^{00}	Young's modulus of the 0-degree layer in the fiber direction
E^{90}	Young's modulus of the 90-degree layer in the fiber direction
\bar{E}	equivalent Young's modulus
\tilde{E}	Young's modulus of a damaged material
$\underline{\underline{E}}(D_{my}, D_{f1}^{00}, D_{f1}^{90})$	fourth order elastic tensor on the composite level of a woven composite
$\underline{\underline{E}}(D_{my}^{00}, D_{my}^{90}, D_{f1}^{00}, D_{f1}^{90})$	fourth order elastic tensor on the composite level
$\underline{\underline{E}}^L(D_{my}, D_{f1})$	fourth order elastic tensor on the layer level

$E_{\equiv}^{00}(D_{my}^{00}, D_{f1}^{00})$	fourth order elastic tensor of the 0-degree layer
$E_{\equiv}^{90}(D_{my}^{90}, D_{f1}^{90})$	fourth order elastic tensor of the 90-degree layer
$\bar{\varepsilon}$	macroscopic strain
$\underline{\underline{\varepsilon}}$	overall strain tensor
$\varepsilon_{11}, \varepsilon_{22}, \varepsilon_{12}$	component of the strain tensor $\underline{\underline{\varepsilon}}$ in 1-2 frame
$\underline{\underline{\varepsilon}}_f^i$	strain tensor in the fiber aligned along the i-direction
$\varepsilon_{f11}, \varepsilon_{f22}, \varepsilon_{f12}$	component of the strain tensor $\underline{\underline{\varepsilon}}_f$ of the fiber in 1-2 frame
$\bar{\varepsilon}_{in}$	inelastic strain upon complete unloading ($\bar{\sigma}=0$)
$\bar{\varepsilon}_{in}^{00}, \bar{\varepsilon}_{in}^{45}$	macroscopic inelastic strain upon complete unloading
$\underline{\underline{\varepsilon}}^L, \underline{\underline{\varepsilon}}^{00}, \underline{\underline{\varepsilon}}^{90}$	strain tensor on a layer level
$\varepsilon_{mxx}, \varepsilon_{myy}, \varepsilon_{mxy}$	components of the strain tensor $\underline{\underline{\varepsilon}}_m$ of the matrix in x-y frame
$\varepsilon_{m11}, \varepsilon_{m22}, \varepsilon_{m12}$	components of the strain tensor $\underline{\underline{\varepsilon}}_m$ of the matrix in 1-2 frame
$\bar{\varepsilon}_M, \bar{\varepsilon}_M^{00}, \bar{\varepsilon}_M^{45}$	maximum applied strain
f, f_f	fiber volume fraction
f_m	matrix volume fraction
f^{00}, f^{90}	volume fraction of the 0 degree and the 90 degree layer
F	set of associated forces
G	energy release rate
\bar{G}	equivalent shear modulus
\tilde{G}_f	shear modulus of the damaged fiber embedded in the matrix
G_m, \tilde{G}_m	shear modulus of the undamaged and damaged matrix
G^{00}	shear modulus of the 0-degree layer
G^{90}	shear modulus of the 90-degree layer
L	crack spacing
l_F	friction length (assumed to be equal to debond length l_d)
ν_m	Poisson's ratio of the matrix

R	fiber radius
S	set of state variables
ψ	Helmholtz free energy density (state potential)
ψ^D	elastic energy density on the composite level
ψ^e	elastic (or reversible) free energy density
ψ_f	elastic energy density of the fiber
ψ^s	stored free energy density
ψ^S	elastic energy density due to debonding and sliding of a composite
ψ^L	elastic energy density on the layer level
ψ_m	elastic energy density of the matrix
ψ^{00}	free energy densities of the layer at 0 degree
ψ^{90}	free energy densities of the layer at 90 degrees
ρ_1	residual stress in the matrix
ρ_1^{00}	residual stress in the broken part of the 0 degree layer
σ	effective (or microscopic) stress
$\bar{\sigma}$	macroscopic stress
$\underline{\underline{\sigma}}$	overall stress tensor
$\sigma_{11}, \sigma_{22}, \tau_{12}$	components of the stress tensor $\underline{\underline{\sigma}}$ in 1-2 frame
$\underline{\underline{\sigma}}_f$	stress tensor of the fiber
$\underline{\underline{\sigma}}_f^i$	stress tensor in the fiber aligned along the i -direction
σ_i	stress applied to the composite in the i -direction ($i=11$ or 22)
$\underline{\underline{\sigma}}^L, \underline{\underline{\sigma}}^{00}, \underline{\underline{\sigma}}^{90}$	stress tensor on a layer level
$\underline{\underline{\sigma}}_m$	stress tensor of the matrix
$\bar{\sigma}_M, \bar{\sigma}_M^{00}$	maximum applied stress
$\sigma_{th}, \sigma_0, \tau_{th}, \tau_0$	parameters of the evolution law of the inelastic strains
τ_{eq}	equivalent shear stress
W	width

X	back-stress
$\underline{\underline{X}}$	back-stress tensor
X_{11}, X_{22}, X_{12}	components of the back-stress tensor $\underline{\underline{X}}$ in 1-2 frame
y	debonding and friction energy release rate density
$\underline{\underline{y}}$	energy release rate density tensor due to debonding and friction
y_{11}, y_{22}, y_{12}	components of the energy release rate density tensor $\underline{\underline{y}}$ in 1-2 frame
Y	cracking energy release rate density
Y_f, Y_{fl}	energy release rate densities associated with fiber-breakage
Y_{f0}, m_f	parameters of the evolution of fiber-breakage damage
Y_i	set of energy release rate densities
Y_m, Y_{my}	energy release rate densities associated with matrix-cracking
:	contraction wrt. two indices

References

- Ashby, M. F., 1992, Physical Modeling of Materials Problems, *Mat. Sci. Tech.*, **8**, 102-111.
- Aveston, J., Cooper, G. A., Kelly, A., 1971, Single and Multiple Fracture, National Physical Laboratory: Properties of Fiber Composites, IPC Science and Technology Press, Surrey (UK), 15-26.
- Beyerley, D., Spearing, S. M., Zok, F. W., Evans, A. G., 1992, Damage, Degradation and Failure in a Unidirectional Ceramic-Matrix Composite, *J. Am. Ceram. Soc.*, **75**, n° 10, 2719-2725.
- Budiansky, B., O'Connell, R. J., 1976, Elastic Moduli of a Cracked System, *Int. J. Solids Struct.*, **12**, 81-97.
- Burr, A., Hild, F., Leckie, F. A., 1995, Micro-Mechanics and Continuum Damage Mechanics, *Arch. Appl. Mech.*, **65**, n° 7, 437-456.
- Cady, C., Heredia, F. E., Evans, A. G., 1995a, In-Plane Mechanical Properties of Several Ceramic-Matrix Composites, *J. Am. Ceram. Soc.*, **78**, n° 8, 2065-2078.
- Cady, C., Makin, T. J., Evans, A. G., 1995b, Silicon Carbide Calcium Aluminosilicate - A Notch-Insensitive Ceramic-Matrix Composite, *J. Am. Ceram. Soc.*, **78**, n° 1, 77-82.
- Chaboche, J.-L., 1982, Le concept de contrainte effective appliquée à l'élasticité et à la viscoplasticité en présence d'un endommagement anisotrope, *Colloque international du CNRS*, **295**, 31-43.
- Cocks, A. C. F., Leckie, F. A., 1987, Creep Constitutive Equations for Damaged Materials, in *Advances in Applied Mechanics*, Academic Press, New-York, **25**, 239-294.
- Coleman, D. B., Gurtin, M. E., 1967, Thermodynamics with Internal Variables, *J. Chem. Phys.*, **47**, 597-613.

- Curtin, W. A., 1991, Exact Theory of Fiber Fragmentation in Single-Filament Composite, *J. Mat. Sci.*, **26**, 5239-5253.
- Drucker, D. C., Prager, W., 1956, Soil Mechanics and Plastic Analysis of Limit Design, *Quat. of Appl. Math.*, **14**, .
- Eshelby, J. D., 1957, The determination of the elastic field of an ellipsoidal inclusion and related problems, *Proc. Roy. Soc. London, A* **241**, 376-396.
- Evans, A. G., Domergue, J.-M., Vagaggini, E., 1994, Methodology for Relating the Tensile Constitutive Behavior of Ceramic matrix Composites to Constituent Properties., *J. Am. Ceram. Soc.*, **77**, n° 6, 1425-1435.
- Germain, P., Nguyen, Q. S., Suquet, P., 1983, Continuum Thermodynamics, *J. Appl. Mech.*, **50**, 1010-1020.
- Heredia, F. E., Evans, A. G., Anderson, C. A., 1995, Tensile and Shear Properties of Continuous Fiber-Reinforced SiC/Al₂O₃ Composites Processed by Melt Oxidation, *J. Am. Ceram. Soc.*, **78**, n° 10, 2790-2800.
- Hibbitt, H. D., Karlsson, B. I., Sorensen, P., 1993, Abaqus, version 5.3.
- Hild, F., Burr, A., Leckie, F. A., 1996, Matrix Cracking and Debonding in Ceramic-Matrix Composites, *Int. J. Solids Struct.*, **33**, n° 8, 1209-1220.
- Hutchinson, J. W., Jensen, H. M., 1990, Models for Fiber Debonding and Fiber Pull-Out in Brittle Composites with Friction, *Mech. Mat.*, **9**, 139-163.
- Iosipescu, N., 1967, New Accurate Procedure for Single Shear Testing of Metals, *J. Mater.*, **2**, 537-566.
- Jansson, S., Leckie, F. A., 1993, The Mechanics of Failure of Silicon Carbide Fiber-Reinforced Glass-Matrix Composites, *Acta Metall. Mat.*, **40**, n° 11, 2967-2978.
- Ladevèze, P., 1983, Sur une théorie de l'endommagement anisotrope, LMT Cachan, Report No. 34.
- Lemaitre, J., 1992, A Course on Damage Mechanics, Springer-Verlag, Berlin (Germany).

- Lemaitre, J., Chaboche, J.-L., 1978, Aspect phénoménologique de la rupture par endommagement, *J. Méc. Appl.*, **2**, n° 3, 317-365.
- Love, A. E. H., 1927, The Mathematical Theory of Elasticity, Cambridge University Press, Cambridge (UK).
- Pluinage, P., 1991, Etude expérimentale et simulation numérique du comportement mécanique de matériaux composites SiC/SiC. Influence des paramètres de stratification et d'élaboration., Thèse d'Université, Université Bordeaux 1.
- Rice, J. R., 1971, Inelastic Constitutive Relations for Solids: An Internal Variable Theory and its Application to Metal Plasticity, *J. Mech. Phys. Solids*, **19**, 433-455.
- Volterra, V., 1907, Sur l'équilibre des corps élastiques multiplement connexes, *Annales Scientifiques de l'Ecole Normale Supérieure, Paris*, **24**, n° 3, 401-518.
- Weibull, W., 1939, A Statistical Theory of the Strength of Materials, Roy. Swed. Inst. Eng. Res., 151.
- Weibull, W., 1951, A Statistical Distribution Function of Wide Applicability, *J. Appl. Mech.*, **18**, n° 3, 293-297.
- Zienkiewicz, O. C., Taylor, R. L., 1989, The Finite Element Method, McGraw-Hill, London (UK), 4th edition.

Appendix

Let us consider a lamina with initial principal directions of orthotropy given by 1 and 2. The initial principal directions of orthotropy, or material directions, often do not coincide with the loading directions given by x and y (Fig. 5). The z -axis is perpendicular to the plan (1-2) and (x - y).

Under plane stress conditions, an elastic stress-strain relation in the material directions can be written in terms of the compliance matrix $\{S\}$

$$(A1.1) \quad \begin{pmatrix} \epsilon_{11} \\ \epsilon_{22} \\ \gamma_{12} \end{pmatrix} = \begin{pmatrix} S_{11} & S_{12} & 0 \\ S_{12} & S_{22} & 0 \\ 0 & 0 & S_{66} \end{pmatrix} \begin{pmatrix} \sigma_{11} \\ \sigma_{22} \\ \tau_{12} \end{pmatrix}$$

or in terms of the stiffness matrix $\{Q\}$

$$(A1.2) \quad \begin{pmatrix} \sigma_{11} \\ \sigma_{22} \\ \tau_{12} \end{pmatrix} = \begin{pmatrix} Q_{11} & Q_{12} & 0 \\ Q_{12} & Q_{22} & 0 \\ 0 & 0 & Q_{66} \end{pmatrix} \begin{pmatrix} \epsilon_{11} \\ \epsilon_{22} \\ \gamma_{12} \end{pmatrix}$$

If we now consider the same expression written in the loading directions, the general stress-strain relation leads to a full compliance matrix $\{\bar{S}\}$

$$(A2.1) \quad \begin{pmatrix} \epsilon_{xx} \\ \epsilon_{yy} \\ \gamma_{xy} \end{pmatrix} = \begin{pmatrix} \bar{S}_{11} & \bar{S}_{12} & \bar{S}_{16} \\ \bar{S}_{12} & \bar{S}_{22} & \bar{S}_{26} \\ \bar{S}_{16} & \bar{S}_{26} & \bar{S}_{66} \end{pmatrix} \begin{pmatrix} \sigma_{xx} \\ \sigma_{yy} \\ \tau_{xy} \end{pmatrix}$$

or to a full compliance matrix $\{\bar{Q}\}$

$$(A2.2) \quad \begin{pmatrix} \sigma_{xx} \\ \sigma_{yy} \\ \tau_{xy} \end{pmatrix} = \begin{pmatrix} \bar{Q}_{11} & \bar{Q}_{12} & \bar{Q}_{16} \\ \bar{Q}_{12} & \bar{Q}_{22} & \bar{Q}_{26} \\ \bar{Q}_{16} & \bar{Q}_{26} & \bar{Q}_{66} \end{pmatrix} \begin{pmatrix} \varepsilon_{xx} \\ \varepsilon_{yy} \\ \gamma_{xy} \end{pmatrix}$$

The relationship between the compliance matrix in the material directions, $\{S\}$, and in the loading directions, $\{\bar{S}\}$ can be written as follows

$$(A3.1) \quad \{\bar{S}\} = \{T\}^T \{S\} \{T\}$$

and the relationship between the stiffness matrix in the material directions, $\{Q\}$, and in the loading directions, $\{\bar{Q}\}$ can be written as follows

$$(A3.2) \quad \{\bar{Q}\} = \{T\}^{-1} \{Q\} \{T\}^{-T}$$

where the superscript T denotes the matrix transpose, and $\{T\}$ the transformation matrix associated with a positive rotation of angle θ of principal axes about z from material axes (Fig. 1)

$$(A4) \quad \{T\} = \begin{pmatrix} \cos^2\theta & \sin^2\theta & -2\sin\theta \cos\theta \\ \sin^2\theta & \cos^2\theta & 2\sin\theta \cos\theta \\ \sin\theta \cos\theta & -\sin\theta \cos\theta & \cos^2\theta - \sin^2\theta \end{pmatrix}$$

Table 1

Table 1: Thermodynamic variables modeling elasticity, matrix cracking, debonding and sliding, fiber breakage and pull-out.

MECHANISM	STATE VARIABLES			ASSOCIATED FORCES	
		Observable	Internal		
ELASTICITY	Total strain	$\underline{\underline{\varepsilon}}$		$\underline{\underline{\sigma}}$	Stress
MATRIX CRACKING	Damage variables	..	D_m^{00} D_m^{90}	Y_m^{00} Y_m^{90}	Energy release rate densities
FIBER BREAKAGE	Damage variables		D_f^{00} D_f^{90}	Y_f^{00} Y_f^{90}	Energy release rate densities
DEBONDING	Inelastic strain		$\underline{\underline{\alpha}}$	$\underline{\underline{X}}$	Back-stress
& SLIDING	Damage variables		d_{11} d_{22} d_{12}	y_{11} y_{22} y_{12}	Energy release rate densities

Figure Captions

Figure 1: Elementary cell containing a crack. A debond zone is characterized by the debond length $2l_F$, and the average crack spacing is $2L$.

Figure 2: Stress, $\bar{\sigma}$, versus strain, $\bar{\epsilon}$, during a loading–unloading–reloading sequence.

Figure 3: Elementary cell of size $2L \times 2W$ containing a crack of size $2a$.

Figure 4: Motion of the unbroken part (2) with respect to the broken part (1) with no external load by an amount Δ_s over a length l_F .

Figure 5: The initial principal directions of orthotropy, or material directions, 1 and 2 often do not coincide with the loading directions x and y . The angle θ measures their respective orientation.

Figure 6: Flow chart of the identification procedure.

Figure 7: Experimental and identified evolution of
(1): the matrix–cracking damage variable D_m as a function of the strain energy release rate density associated with matrix–cracking Y_m ,
(2): the inelastic strains α_{11} (or α_{22}) as a function of the stress σ_{11} (or σ_{22}),
(3): the inelastic strains α_{12} as a function of the equivalent stress τ_{eq} .

Figure 8: Experimental and identified evolution of the tensile stresses σ_{11} as a function of the tensile strains ϵ_{11} in

(1): a tension test on a [0/90] SiC/SiC lay-up at 0 degree,

(2): a tension test on a [0/90] SiC/SiC lay-up at ± 45 degrees.

Figure 9: Iosipescu specimen configuration.

Figure 10: Experimental and predicted evolution of the average shear stresses σ_{12} as a function of the shear strains γ_{12} in a Iosipescu test on a [0/90] SiC/SiC lay-up. This evolution is compared with the evolution of the shear stresses σ_{12} as a function of the shear strains γ_{12} in the center of the specimen.

Figure 11: Shear stress profile in the ligament of the Iosipescu specimen when the shear strain γ_{12} in the center of the specimen is equal to 0.007 as a function of the relative distance y/b from the center of the ligament for a linear and non-linear computation.

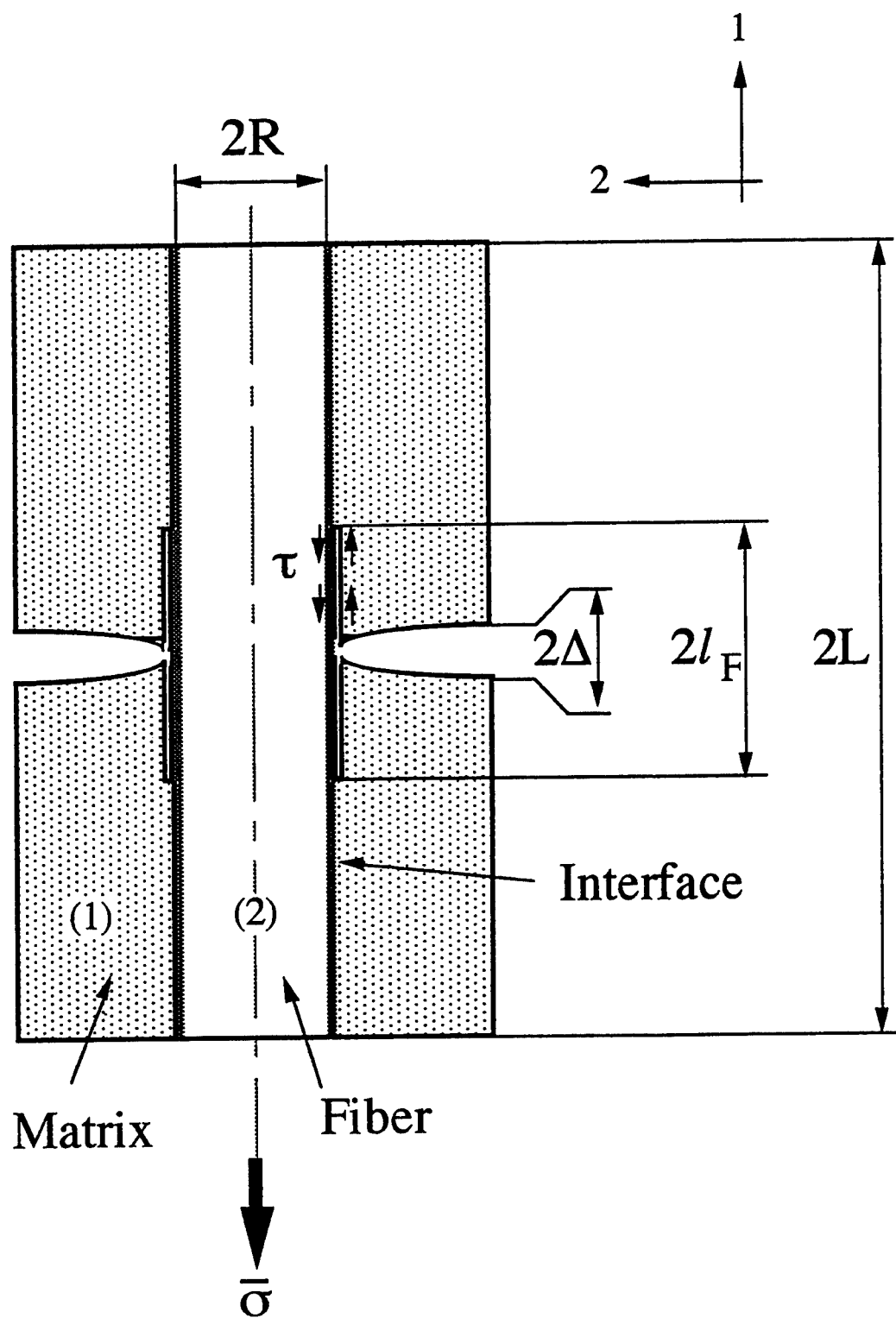
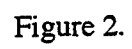


Figure 1.



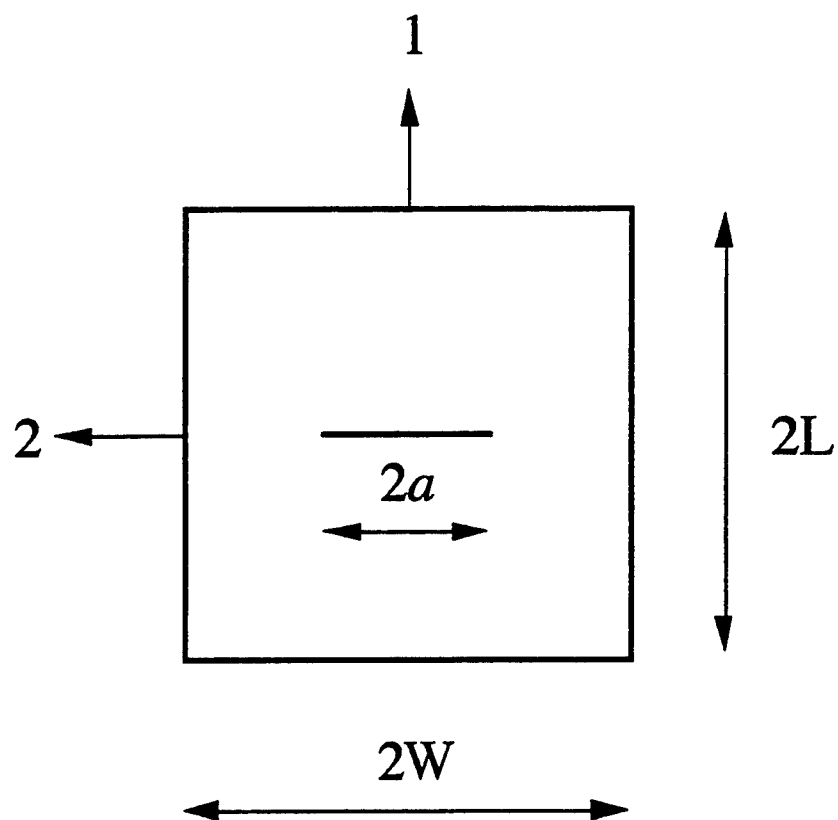


Figure 3.

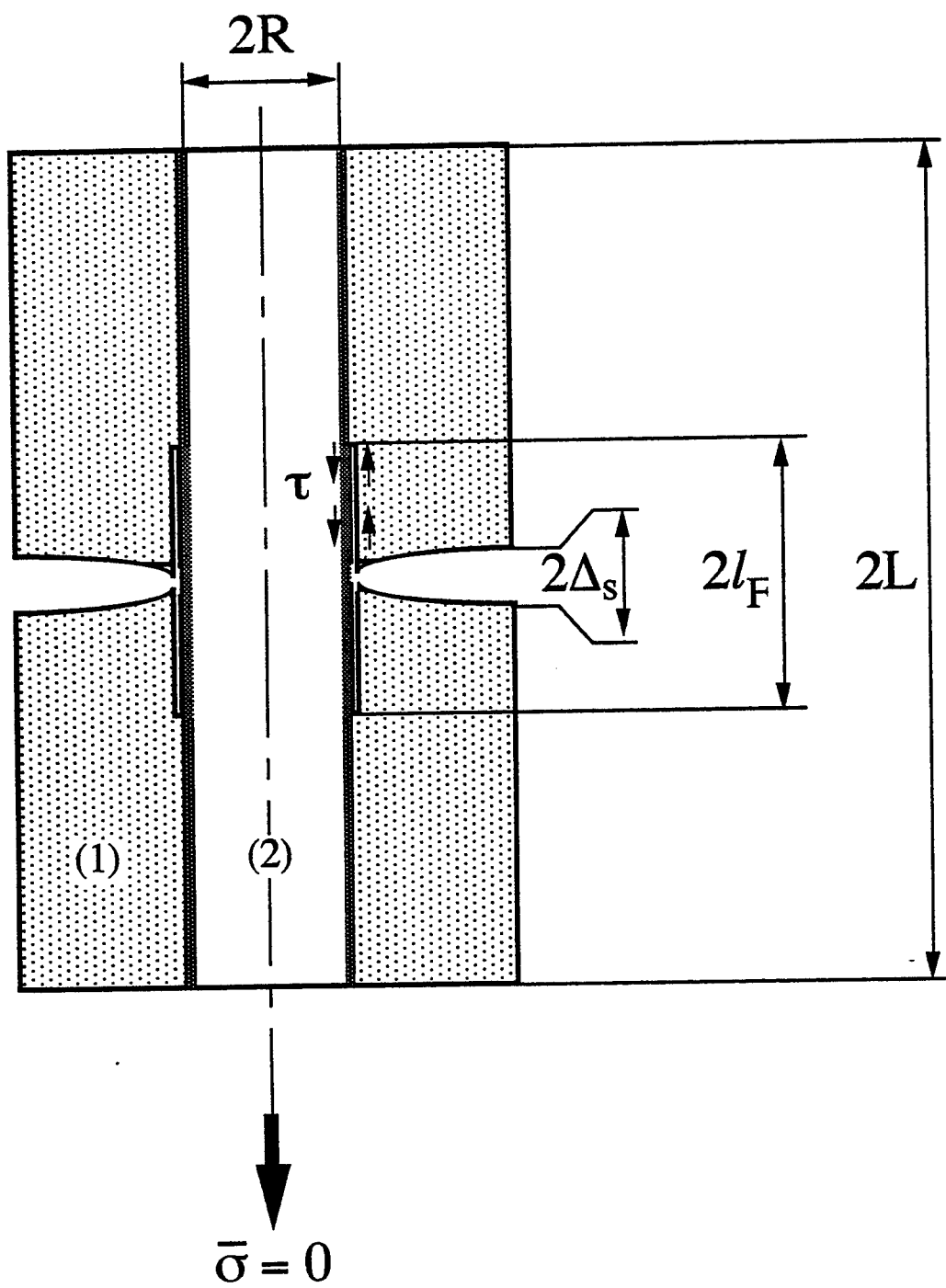


Figure 4.

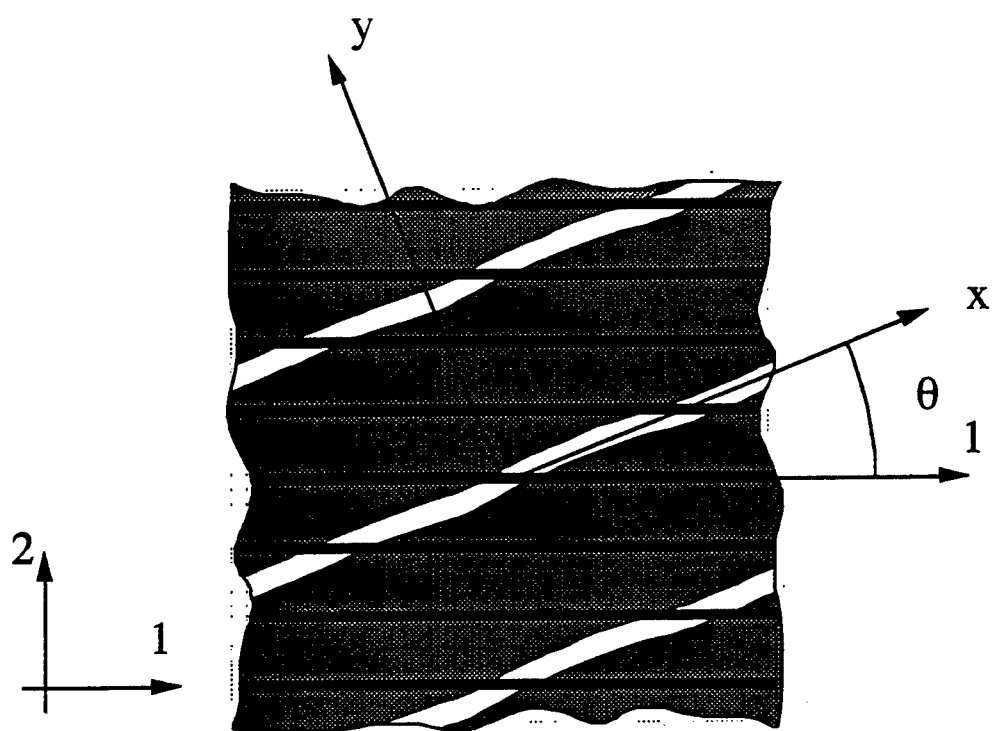


Figure 5.

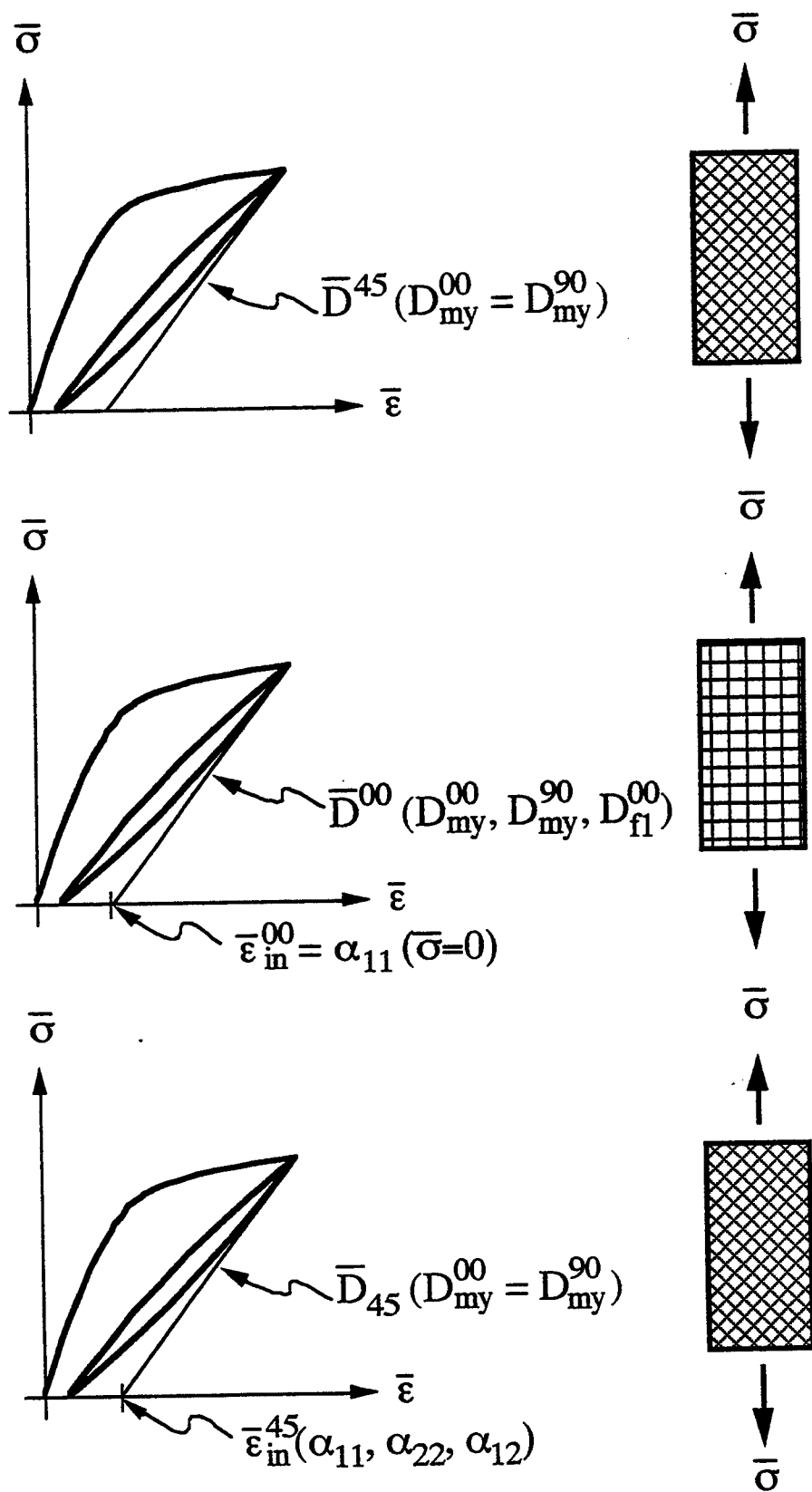


Figure 6.

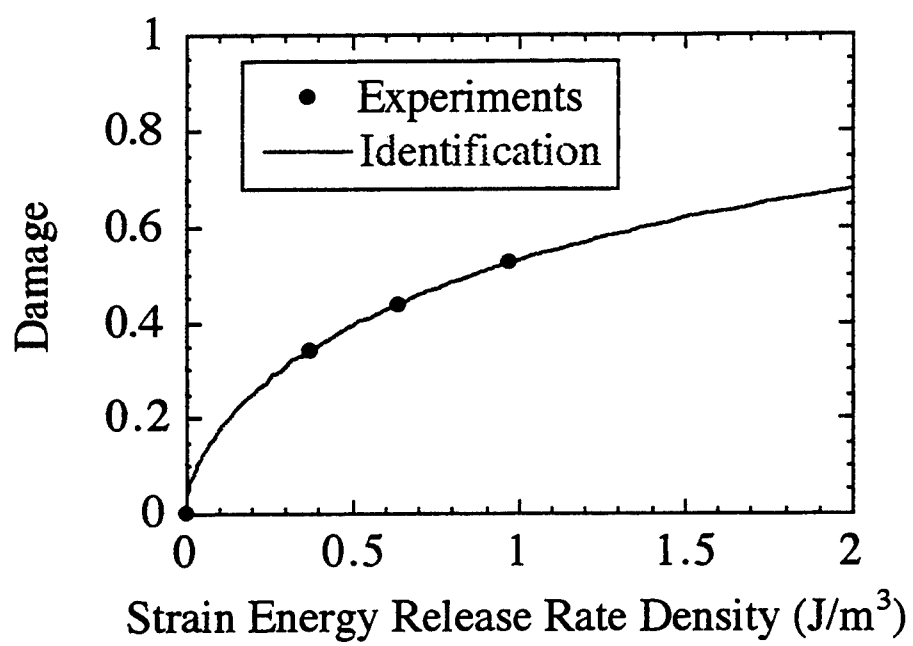


Figure 7.1

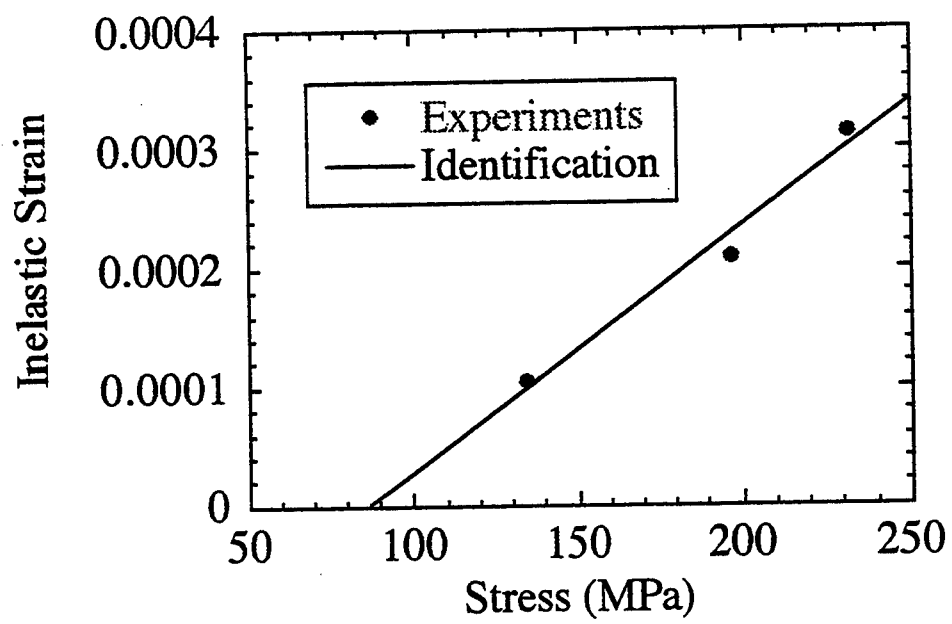


Figure 7.2

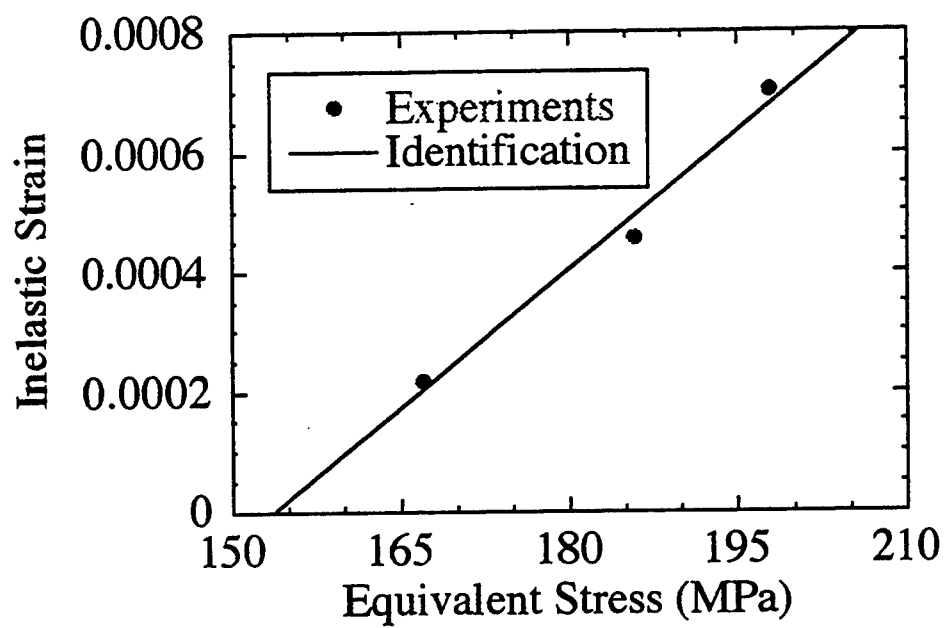


Figure 7.3

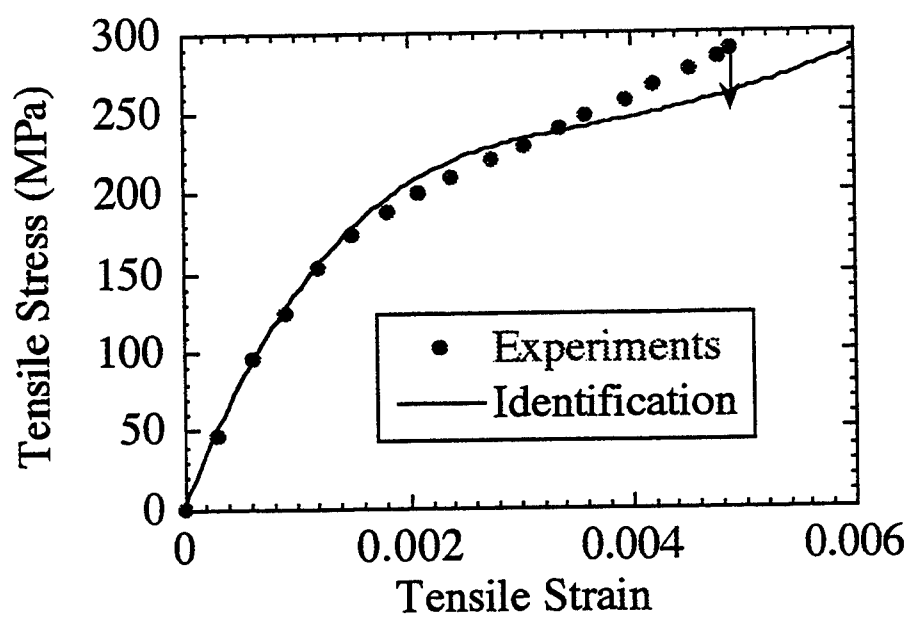


Figure 8.1

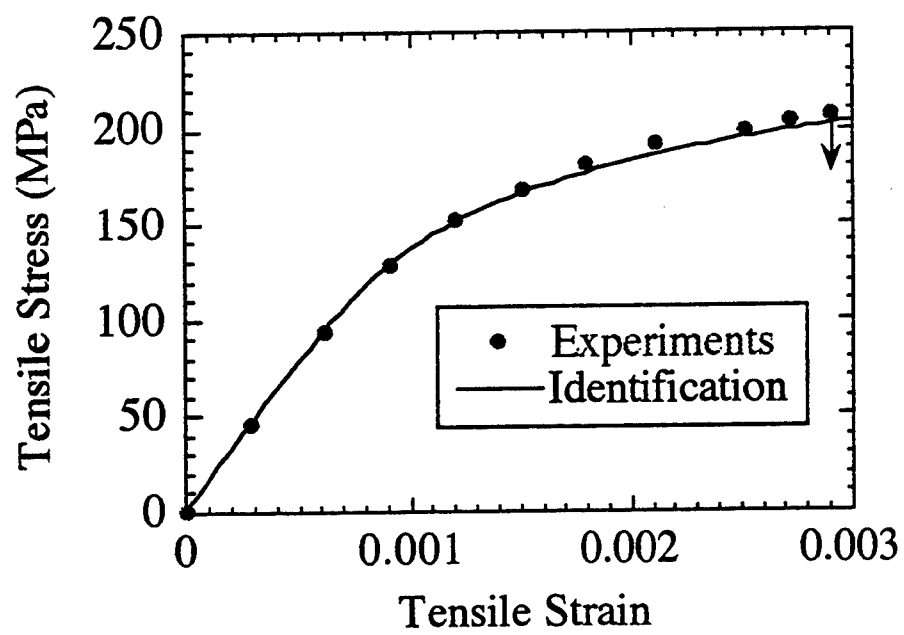


Figure 8.2

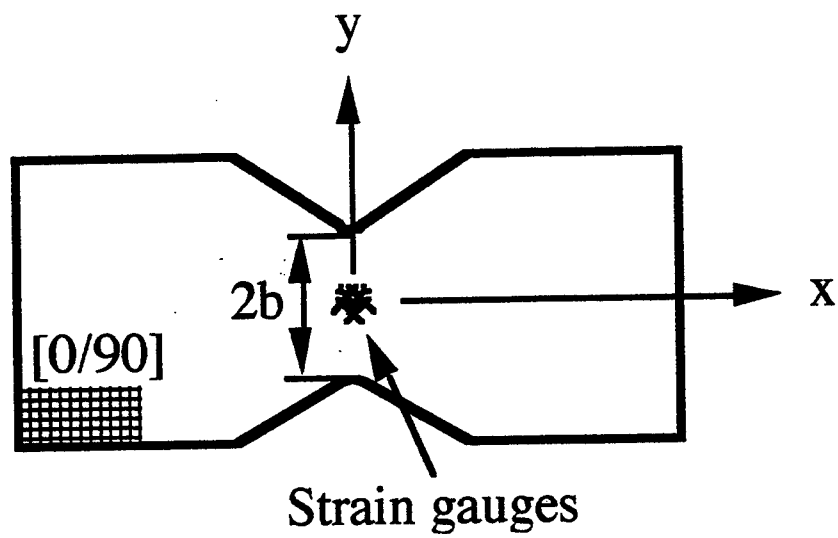


Figure 9.

Advances in ceramic composites reinforced by continuous fibers

Brian N Cox* and Frank W Zok†

Ceramic matrix composites reinforced with continuous fibers are on the verge of insertion into hot engineering structures. Yet current research is only beginning to attack some of the most critical problems. Key developments in the last 24 months include the formulation of constitutive laws for continuum mechanics analyses; the discovery of stable weak oxide-oxide interface systems; the analysis of how fiber creep limits life at high temperatures; confrontation of the problem of oxidation peeling at intermediate temperatures in SiC based systems; re-examination of the maxim that interfaces must be weak; and the advent of textile reinforcement as the solution to delamination problems.

Addresses

*Rockwell Science Center, 1049 Camino Dos Rios, PO Box 1085, Thousand Oaks, CA 91358, USA

†Materials Department, University of California at Santa Barbara, CA 93106, USA

Current Opinion in Solid State & Materials Science 1996, 1:666-673

© Current Chemistry Ltd ISSN 1359-0286

Abbreviation

CMCs ceramic matrix composites

Introduction

The period covered by this review (1995 and the beginning of 1996, with selected inclusion of papers from 1994) marks a major epoch in the history of research into continuous fiber reinforced ceramic matrix composites (CMCs). From the early 1980s, when CMC research first enjoyed large scale funding and the attention of significant groups all over the world, effort has been concentrated on a simple paradigm of the ideal CMC. It must have a weak fiber/matrix interface to allow energy absorption during fracture by the deflection of cracks, in the complete absence of any dislocation based toughening. Freed of stress concentration when the matrix cracked, strong fibers would continue to bear high loads. This approach to protecting CMCs from intrinsic flaws, notches, and damage was pursued almost entirely in the context of unidirectionally reinforced CMCs, with aligned loads; and mostly in terms of room temperature phenomena. It is now very well understood. (See [1,2] for recent articles covering many aspects of work up to 1995.)

Structural applications almost never involve uniaxial stresses; and the long sought pay-off for CMCs will certainly come at high temperatures. Now we see at last the reduction of micromechanical models and our detailed understanding of matrix cracking and statistical fiber failure to constitutive laws suitable for use in finite element calculations of structures under complex

loads. The serious difficulties of ensuring durability at high temperatures are being confronted; oxidation peeling of SiC fibers at intermediate temperatures, fiber creep at higher temperatures, and the chemical stability of interfaces are all hot topics. Textile reinforcement, especially with 3D architecture, has appeared as the solution to the unavoidable vulnerability of brittle matrix composites to delamination. And even the central axiom that CMCs cannot be tough unless the fiber/matrix interfaces are weak is now being challenged.

Modeling the inelastic regime

Major progress has been made in the last year or two in developing design and reliability codes suitable for field use from the wealth of micromechanical models in the CMC literature. Effort has focused on generating constitutive laws for insertion into finite element models, with the goal of reducing the treatment of nonlinearity in CMCs to standard continuum mechanics.

Nonlinearity in CMCs at room temperature involves matrix cracking, stochastic fiber fracture, damage localization, and fiber pullout. Two groups have presented exhaustive studies for unidirectional composites of the relation between micromechanical properties (including the interfacial friction stress, residual stresses, constituent elastic moduli, fiber radius, and fiber volume fraction) and the macroscopic stress-strain response under aligned loads prior to damage localization and ultimate failure [3-9]. Prior and well established models of matrix cracks bridged by sliding fibers are used as the physical basis for modeling. Micromechanical properties are deduced directly from experimental hysteresis loops, obviating any detailed tests of interface conditions, for example fiber pullout or pushout tests. One group has couched its work in the language of micromechanics more familiar to the CMC community [3*,4*,5]; the other in the language of continuum damage mechanics, but with a thermodynamic potential function derived from the same micromechanics [6,7,8**,9]. They offer equivalent treatments of nonlinearity up to localization, with some variations in the point of view and in the level of micromechanical detail used in fitting data. Both sets of work are essential reading. More empirical (probably unnecessarily so) treatments of nonlinearity in unidirectional CMCs have also appeared [10].

Recent extensions of the continuum damage approach also deal with predicting the onset of damage localization, which is required to model ultimate failure and the notch sensitivity of strength [11]. Localization and subsequent fiber pullout involve distributions of flaw strengths and stress redistribution effects which are complex and not generally well known in a particular material. There

is a commensurate increase in the number of material parameters to be determined by calibrating experiments. Applications to circumferentially reinforced rotors have been presented, but proof of the predictive power of localization models is not yet convincing [11].

Dealing with more complex fiber architectures is also much more challenging. The response of a 0/90° laminate prior to localization under loads aligned with the 0° fibers is the easiest case, since the cracking evolution is best understood [5]. Damage in textile CMCs involves much more complicated cracking patterns, for which micromechanical models are relatively crude (and not certain to improve, because of the difficulties of dealing with the tortuous heterogeneity of textiles). Continuum damage approaches are necessarily more empirical.

Likewise, highly empirical approaches are most credible for multiaxial or off-axis loading, even in unidirectional CMCs. A general method for developing multiaxial constitutive laws up to localization has been demonstrated for plane stress cases, using a combination of standard tension, compression, and shear test data [12*]. When the constitutive laws are embedded in finite element calculations of strain distributions around a stress concentrator, encouraging agreement is obtained with measured strain fields. Stiffness changes under off-axis loading have been measured ultrasonically [13].

This area of work represents the culmination of efforts to qualify CMCs as structural materials. Current activity focuses on dealing with rate dependent behaviour at high temperature, fatigue effects, and weakest link fracture statistics (volume effects).

Fracture and notch sensitivity

Tensile tests performed on specimens containing holes or notches have demonstrated that many CMCs are relatively notch-insensitive [14–16, 17*, 18*, 19, 20, 21*]. The net-section stress at fracture is typically 80–100% of the unnotched strength: considerably higher than the value calculated on the basis of the elastic stress concentration factor. Indeed, in some instances, there appears to be evidence of notch strengthening [14]. Measurements of in-plane strains (using moiré interferometry [18*]) and stresses (using SPATE [14–16, 17*]) have shown that strain concentrations are essentially unchanged by the inelastic deformation but stress concentrations are reduced dramatically. However, even in the most notch-insensitive materials, stress concentrations are not eliminated altogether, yet the net section strength is essentially equal to the unnotched strength. Similar conclusions have been reached from finite element simulations which incorporate the inelastic deformation [12*].

These results suggest that the failure stress should exhibit volume dependence, being highest when the volume

under most stress is small (as it is ahead of a notch). If so, the strength should follow weakest-link scaling. Comparisons of strengths in tension and bending (taking into account the nonlinear stress distributions) support this hypothesis (McNulty JC, Zok FW, unpublished data). Issues related to strength variability are addressed in more detail elsewhere in this journal [22].

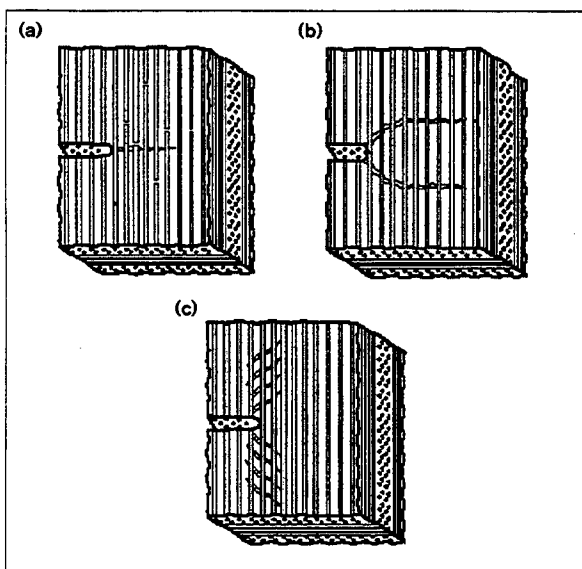
The degree of notch sensitivity is influenced by the nature of the inelastic deformation occurring ahead of the notches (Fig. 1). In some materials (e.g. Nicalon™/calcium aluminosilicate), a damage zone of multiple matrix cracks forms ahead of the notch, which has an analogous effect to the plastic zone in metals (designated Class II behavior by Evans [23*]). In others (e.g. C/C), nonlinearity arises from shear bands oriented parallel to the tensile direction (Class III behavior [23*]). In more brittle CMCs, fracture occurs by the propagation of a dominant mode I crack, with fiber failure and pullout in the crack wake, but with minimal inelastic deformation elsewhere (Class I behavior [23*]). Models of strength for Classes I and III have been developed, based on line-spring representations of the inelastic processes [24**, 25]. Models that take into account large scale sliding [26**] indicate that the maximum fiber stress in the bridging zone is somewhat lower than that predicted from the line-spring models; the latter are thus expected to provide conservative predictions for the stresses at the onset of fiber failure.

Some censure is due to several authors over loose claims that a given material has been found to be notch insensitive. This generally fallacious conclusion has been based on tests performed with relatively small notches: typically 1–5 mm. Moreover, there has been almost no discussion of the effects of notch shape (circular holes versus sharp slits). In the presence of sufficiently large, sharp notches, the strength must follow the Griffith relation and the material must be notch-sensitive (as is even the most ductile metal). Researchers should identify the length scales associated with the bridging processes and hence the notch sizes and shapes for which notch sensitivity will occur.

Compressive failure

Compressive failure of CMCs has remained largely unexplored. Some evidence exists that compressive strengths [27*] fall below tensile strengths [28*]. In CMCs with weak or porous matrices, observations to date [27*] show that compressive failure involves kink band formation within fiber bundles (plies or tows), similar to the prevalent failure mechanisms in polymer matrix composites (laminates and textiles). In this case, compressive strength will be governed by the initial misalignment of segments of fiber bundles and the shear strength of the matrix. Compressive failure also involves interply and intraply delamination, which will probably be the principal mechanisms of failure in CMCs with nonporous, relatively strong matrices.

Figure 1



Schematics of three classes of cracking found in unidirectional or cross-ply CMCs. (a) Class I, matrix cracking plus fiber failure; (b) Class II, matrix cracking, no fiber failure; (c) Class III, shear damage by matrix cracking. (Additional stress redistribution mechanisms exist in textile CMCs, because of the strong role played by heterogeneity on the scale of fiber tows or bundles. Their identification is a topic of current research.)

Fatigue

Fatigue failure occurs in most CMCs. The dominant mechanism at room temperature in CMCs based on oxide or SiC fibers involves matrix cracking on the first loading cycle, followed by debonding and cyclic sliding along the fiber-matrix interfaces. Repeated sliding causes wear of the fiber coatings, leading to a reduction in the interface sliding stress and a corresponding reduction in the fiber bundle strength [29,30]. It can also lead to higher permanent inelastic strains and a reduction in the hysteresis modulus. The latter effects may be important for dimensional stability. The wear process is also likely to produce flaws in the fibers, further reducing the bundle strength. Such effects have been seen in fiber-reinforced titanium matrix composites (by comparing the strengths of fibers extracted from composites before and after fatigue), but not in CMCs, partly because of the difficulty of extracting fibers from ceramic matrices. Typically, the fatigue thresholds are $\geq 75\%$ of the ultimate tensile strength (UTS) and the retained strengths following fatigue loading are almost equal to the UTS. However, limited data suggest that the fatigue threshold is reduced by notches (relative to the notched tensile strength) and negative stress ratios [31].

While fatigue effects in CMCs with SiC or oxide fibers appear to be mainly related to interfacial degradation, with minimal fiber damage, carbon fibers can be entirely worn away by fatigue. Thus generally severe fatigue effects are found in CMCs based on carbon fibers [32].

Delamination

Whether toughness is achieved in a CMC by incorporating weak fiber/matrix interfaces or a porous or otherwise weak matrix around fiber bundles, strength under loads acting normal to the fiber direction will be seriously impaired. Thus while laminated CMCs exhibit encouraging in-plane toughness, they remain vulnerable to delamination. Delamination can be resisted to some degree by in-plane fibers crossing the fracture plane obliquely, but the work of fracture remains well below 1 kJm^{-2} [33,34]. Laminates of 2D fabrics (e.g., plain or satin weave) are equally vulnerable.

The delamination problem is one of the main reasons CMCs are not yet preferred for load bearing components in high performance applications such as turbine engines. Current designs require them to sustain mainly thermal loads. Even then, thermal gradients present severe delamination risks. Hutchinson and Lu [35] have explored how a delamination crack interrupts heat flow, producing thermal stresses and crack tip stress intensities. The design limit implied for thermal gradients is quite stringent for realistic parameter values.

The obvious way to suppress delamination is by incorporating through-thickness reinforcement, for example, by stitching, 3D weaving, or inserting short rods. Very encouraging precedents exist in polymer composites [36,37]. While the processing challenges remain largely unaddressed by the ceramics community, data for other composite systems and theory lead the way. Through-thickness reinforcement bridges delamination cracks, often creating an analogue of the steady state matrix crack familiar from Mode I aligned loading of CMCs [38]. A lower bound therefore exists for the critical load, regardless of delamination crack length. This allows simple design rules to be formulated. The minimum volume fraction of through-thickness reinforcement required to suppress delamination is usually only a few percent or less [39]. For the thermal gradient problem in particular, through-thickness reinforcement also transports heat across a delamination crack, reducing crack-induced thermal stresses [35].

Thermal properties

To minimize thermal stress, CMCs must have high thermal conductivity along with low thermal expansion and stiffness. Despite their importance in determining the performance of CMC structures, thermal properties have received relatively little attention, with a few notable theoretical studies. Models have been developed to

account for degradation in the thermal expansion and conductivity of cross-ply laminates in the presence of periodic matrix cracks [40,41*]. The models highlight the importance of the Biot numbers associated with fiber matrix interfaces, bridged matrix cracks in longitudinal plies, and unbridged cracks in transverse plies, along with the corresponding crack densities. The through-thickness conductivity can also be impaired by the presence of porosity. The effects of porosity and fiber waviness have been incorporated into a cell model for plain weave architectures [42]. As noted earlier, knowledge of the through-thickness thermal properties is particularly important in design because of the low delamination resistance of CMCs.

A review of the models and the experimental work covering the past decade can be found in [43]. Despite progress in the development of models for the thermal properties of composites, a critical assessment of the models has been hampered by the lack of experimental data on the thermal properties of the constituents (especially the fibers) and the conductance of fiber-matrix interfaces.

Creep

Environment and phase stability aside, the design bounds of CMCs under aligned loads are set by creep.

In glass matrix composites, creep occurs predominantly in the matrix. In unidirectional glass matrix composites, high creep rates in the matrix under transverse loads cause considerable creep anisotropy. In asymmetrically laid-up laminates or in the presence of stress gradients, creep anisotropy within plies will compromise dimensional stability [44]. In CMCs designed for higher temperatures, which have nonglass matrices, the situation is reversed. Polycrystalline fibers are fabricated with fine grains for strength, which are usually smaller than the grains in the matrix. It is therefore the fibers that creep first. Considerable progress has now been made towards understanding the important consequences of this. Under sustained loads, matrix cracks, which would be arrested and remain stable at room temperature, exhibit stable, time dependent growth as fiber creep degrades the shielding effects of bridging fibers [45–47*,48]. The steady state matrix cracking stress is no longer a lower bound for nonlinearity and ultimate failure [49]. Constitutive laws have been derived for bridging fibers that creep [50*,51] (as well as for creeping interfaces [52]), the incubation of crack growth from prior matrix flaws has been modeled [51], and crack growth trends have been detailed [53]. Global creep plasticity in the presence of multiple matrix cracks is now well understood [47*,50*]. Possible failure modes for 0/90° laminates with creeping fibers have been mapped in terms of fundamental material parameters [49,54].

Matrix cracking moderated by creeping fibers appears to be the critical failure path for CMCs in high temperature

structural applications under aligned loads and when environmental degradation has been controlled. Current research focuses on notch sensitivity, where the combination of matrix cracking and the stress concentration of the notch accelerate creep rupture of fibers [46*,55]. Fiber creep encourages the dominance of a single matrix crack, since it tends to relieve stresses on parallel matrix cracks which have initiated upon the first loading. This contrasts with cracking at room temperature, where many cracks are usually found, even next to very sharp notches [14].

The creep properties of the fibers are obviously critical in setting design limits and for determining lifetime. Much is yet to be understood. For example, some early experiments have shown challengingly complex relationships between morphological changes and creep rates in Nicalon™ fibers [56,57]; and both creep rates and strength are likely to be affected by interactions between fibers and either interphases or the matrix (Morscher GN, unpublished data). Developing creep resistant fibers and establishing confidence in their performance remain central problems in the CMC field.

A peripheral field is developing in the potential (distant future!) application of SiC-based CMCs in fusion reactors. SiC is favoured for its low nuclear activation rate. Creep failure remains central, but is now coupled with radiation damage [58,59].

Oxidation embrittlement

The problem of oxidation embrittlement continues to plague SiC-based CMCs. The embrittlement involves oxygen ingress through matrix cracks and the subsequent reaction of oxygen with both the fiber coatings and the fibers [60,61*]. It occurs as a so-called pest phenomenon, being worst at temperatures lower than those of intended service. At higher temperatures, oxidation products near the external surfaces tend to seal cracks and inhibit further oxygen ingress. (Yet high temperature interfacial degradation is still a potential problem [62].) The pest temperature can be determined by mechanical testing of tensile specimens subject to a temperature gradient along the specimen length: the gradient being produced by (localized) induction heating near the gauge center [61*]. Typically, the pest temperatures are in the range 600–800°C. These temperatures are considerably lower than those usually used for high temperature testing of CMCs. Consequently, the embrittlement phenomenon can be readily overlooked.

Additional complications arise because of the inherent instability of Nicalon™ fibers (the most common fiber currently used in CMCs). Experiments on SiC/Nicalon™ minicomposites (single tow composites) confirm that failure at elevated temperatures is, in some instances, dominated by the strength degradation of the fibers alone (Morscher GN, unpublished data). Composites containing Hi-Nicalon™ fibers with BN coatings appear to be more

stable, although a critical assessment of their performance under conditions that accentuate the embrittlement has yet to be performed.

A rudimentary model has been developed to predict the rupture time under static loading [60]. More refined models are needed to take into account in a more realistic way the nature of the oxidation processes and the mechanisms responsible for fiber strength degradation. Some thermodynamic calculations have been performed to identify the dominant reaction products formed when BN and SiC are present with oxygen [63]. These have been limited to a temperature of 1100°C, considerably higher than the pest temperature. The kinetics and thermodynamics of these reactions and their effects on strength degradation in the pest regime are poorly understood.

The growing recognition of the prevalence of the embrittlement phenomenon in virtually all SiC-based CMCs has led to the development of all-oxide CMCs. These are described in a subsequent section of this review. Barring a significant materials breakthrough, in cases where SiC-based systems must endure long term exposure, the design stress will have to be limited to the matrix cracking stress, as this represents the threshold below which embrittlement is suppressed. Two strategies for improving upon the cracking stress could be adopted: stronger, fully dense matrices, produced, for example, by melt infiltration, rather than chemical vapor infiltration (which usually results in large pores at which cracks initiate); or the use of hybrid laminates comprising alternating layers of fiber reinforced CMCs and fully dense ceramic sheets. The latter approach has been demonstrated [64], although it is expected to be limited in its use to components with relatively simple geometry or those which can be produced using a tile construction.

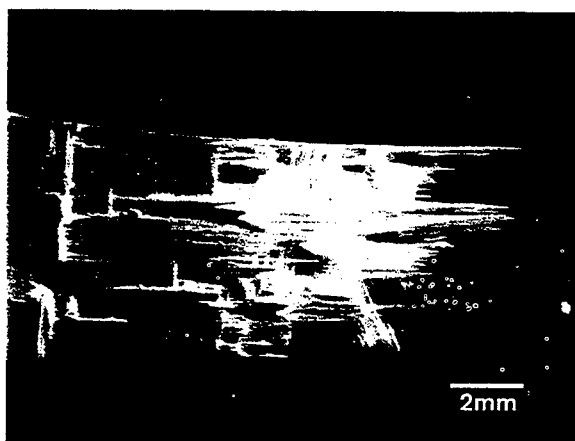
Materials development

The most eye-catching advance of the last two years in chemistry has been the advent of monazites and closely related structures, for example, xenotimes, as interface coatings and matrices in all-oxide composites. When prototypical LaPO_4 is deposited on Al_2O_3 fibers (with care to maintain accurate 1:1 La:P stoichiometry), a weak interface is formed which is extremely stable up to at least 1600°C [65•,66•]. The processing required appears to be simple and reproducible enough and the base materials sufficiently low in cost that monazites may well eliminate degradation by interphase reactions as a life limiting process in all-oxide composites. If so, this is a major breakthrough. There is substantial new activity in monazite processing and applications.

Tough oxide-oxide CMCs with strong fiber/matrix interfaces have now also been demonstrated. Crack deflection characteristics like those seen in wood have been achieved without fiber/matrix debonding by bundling fibers in a

porous matrix that offers easy splitting paths [67•,68]. (Other wood-like ceramics presented recently are really porous monoliths [69].) The propensity for splitting in CMCs can be enhanced by compressive residual stresses in the matrix [70]. Weak matrices and fiber entanglement within fiber bundles must also favour splitting [28]. Precedents in polymer and carbon-carbon composites suggest that especially effective toughening mechanisms for strong interface CMCs exist in textile composites [71]: fiber bundles fail as units, but neighboring bundles are protected from stress concentration by easy splitting between bundles; and 3D architectures bind failed fiber bundles together to large strains, giving exceptional values of work of fracture. Model brittle/brittle composites have been devised to demonstrate the benefits of interlocking 3D architectures [72•].

Figure 2



Bending fracture in an oxide-oxide CMC made from woven fiber tows with no fiber coating (strong interfaces). Note the irregular crack path and the extent of fiber bundle pullout, reminiscent of wood. (Courtesy BD Dalgleish, U Ramamurty, and CG Levi.)

Wood-like fracture has now also been observed in weak-interface systems, including fibrous Si_3N_4 -BN [73] and monazite composites.

While the progress with all-oxide CMCs is exciting, their inherent disadvantages persist. Oxides generally exhibit higher thermal expansion and lower thermal conductivity than SiC-based CMCs and will therefore have to sustain higher stresses and temperatures in thermal applications. Moreover, the creep resistance of currently available oxide fibers is markedly inferior to that of SiC fibers (e.g., Hi-Nicalon™).

Problems remain with chemical stability in carbon fiber CMCs [74–76] and oxide-oxide CMCs with BN interface coatings [77].

Interfaces

The mechanics of fiber/matrix interfaces and their relation to bridged cracks and thence the constitutive properties of CMCs are mature areas of research (e.g. [78]). One substantial and still fairly original recent effort has addressed the role of interface roughness. Roughness has been measured on several typical systems [79] and its effect on fiber pullout relations has been measured and modeled [80*,81,82]. Quantitative predictions of roughness effects remain difficult, because the roughness is geometrically complex. In some cases, roughness appears to cancel the effect of Poisson's contraction of a loaded fiber [80*], validating the assumption of uniform interfacial friction stresses, which has been popular because of its simplicity. But generally, determining the relation between interfacial conditions and fracture behaviour probably always requires calibrating fracture experiments [83]. It has been proposed that roughness effects can be controlled by incorporating a compliant fiber coating to accommodate mismatch strains caused by unseated asperities [84–86].

Substantial rate effects in stress-strain curves have been measured in SiC/glass composites [87*]. The material is stronger and exhibits lower cracking densities at higher strain rates. These effects have been assigned tentatively to environmentally assisted matrix cracking (effective at low strain rates) and an increase in the interfacial friction stress with strain rate (see also the section on Fatigue).

Since weak interfaces are favoured in CMCs, the interfacial debond energy is usually ignored in analyzing matrix cracking in CMCs. Including the interfacial debond energy in a model of fiber bridging has been shown to increase the steady state matrix cracking stress, but the effect is small for material parameters representative of current CMCs [88].

The protection by interfacial debonding of a fiber inside a cracked coating has been modeled [89]. Experimental work continues on interfacial characterization [90–92].

Acknowledgements

BNC was supported by AFOSR contract No. F49620-94-C, FWZ by the ARPA URI program, ONR contract No. N0014-92-J-1808. AG Evans, F Leckie, DB Marshall, and PD Morgan kindly reviewed sections of the manuscript.

References and recommended reading

Papers of particular interest, published within the annual period of review, have been highlighted as:

- of special interest
- of outstanding interest

1. Nair SV, Jakus K (Eds): *High Temperature Mechanical Behaviour of Ceramic Composites*. Boston: Butterworth-Heinemann; 1995.
2. Lehman RL, El-Rahaiby SK, Wachtman JB Jr (Eds): *Handbook on Continuous Fiber-reinforced Ceramic Matrix Composites*. Westerville, Ohio: American Ceram Society; 1995.
3. Vagaggini E, Domergue J-M, Evans AG: Relationships between hysteresis measurements and the constituent properties of

ceramic matrix composites: I, theory. *J Am Ceram Soc* 1995, 78:2709–2720.

This and the following paper provide an excellent demonstration of the development of constitutive laws from micromechanical arguments. Restricted to uniaxial loads.

4. Domergue J-M, Vagaggini E, Evans AG: Relationships between hysteresis measurements and the constituent properties of ceramic matrix composites: II, experimental studies on unidirectional materials. *J Am Ceram Soc* 1995, 78:2721–2731. See the above comment in [3*].

5. Domergue J-M, Heredia FE, Evans AG: Hysteresis loops and the inelastic deformation of 0/90 ceramic matrix composites. *J Am Ceram Soc* 1996, 79:161–170.

6. Hild F, Larsson P-L, Leckie FA: Uncoupled and coupled approaches to predict macrocrack initiation in fiber reinforced ceramic matrix composites. *Comp Struct* 1994, 29:365–377.

7. Burr A, Hild F, Leckie FA: Micro-mechanics and continuum damage mechanics. *Arch Appl Mech* 1995, 65:437–456.

8. Burr A, Hild F, Leckie FA: Continuum description of damage in ceramic-matrix composites. *Eur J Mech A - Solids* 1996, in press.

A powerful approach to formulating constitutive laws for multiaxial loads. Includes relation to the micromechanics of multiple cracking via energy considerations, with the crack density inferred from modulus measurements.

9. Hild F, Burr A, Leckie FA: Matrix cracking and debonding of ceramic-matrix composites. *Int J Solids Struct* 1996, 33:1209–1220.

10. Baste S, El Bouazzaoui R: An experimental investigation of stiffness reduction and cracks geometry in a unidirectional brittle matrix composite. *J Comp Mater* 1996, 30:282–308.

11. Hild F, Burr A, Leckie FA: Fiber breakage and fiber pull-out of fiber-reinforced ceramic-matrix composites. *Eur J Mech A - Solids* 1995, 13:731–749.

12. Genin GM, Hutchinson JW: Composite laminates in plane stress: constitutive modeling and stress redistribution due to matrix cracking. *J Amer Ceram Soc* 1996, in press.

Plane stress constitutive relations for CMCs are developed and implemented in a finite element code. A compelling demonstration is presented of the utility of the model in calculating stress and strain distributions around notches or holes.

13. Baste S, El Bouazzaoui R: Cracking orientation and induced anisotropy of a ceramic matrix composite under off-axis loading. *J Mater Sci* 1996, 31:1575–1584.

14. Cady CM, Mackin TJ, Evans AG: Silicon carbide/calcium aluminosilicate: a notch-insensitive ceramic-matrix composite. *J Am Ceram Soc* 1995, 78:77–82.

15. Heredia FE, Spearing SM, Mackin TJ, He MY, Evans AG: Notch effects in carbon matrix composites. *J Am Ceram Soc* 1995, 78:2817–2827.

16. Mall S, Bullock DE, Pemot JJ: Tensile fracture behaviour of fibre-reinforced ceramic-matrix composite with hole. *Composites* 1994, 25:237–242.

17. Mackin TJ, Purcell TE, He MY, Evans AG: Notch sensitivity and stress redistribution in three ceramic-matrix composites. *J Am Ceram Soc* 1995, 78:1719–1728.

Stress redistribution around notches in several CMCs has been monitored using stress pattern analysis from thermo-elastic emission (SPATE). The maximum stress concentration diminishes with increasing applied stress, but remains significant at the point of fracture. The terminal level of stress concentration coupled with the notched strength indicates that the local tensile strength must be greater than the value measured in a standard uniaxial tensile test. Although the authors do not point it out, this implies that the failure stress must be volume-dependent and should follow weakest link scaling laws.

18. Mackin TJ, Perry KE, Epstein JS, Cady C, Evans AG: Strain fields and damage around notches in ceramic-matrix composites. *J Am Ceram Soc* 1996, 79:65–73.

The strain fields ahead of sharp notches have been measured in several CMCs using moiré interferometry. The strain concentrations at the notch tips are unaffected by the nonlinearity in the stress-strain response, but because of the nonlinear material response, the stress concentration must be reduced. Such measurements are crucial for understanding notch sensitivity and validating constitutive laws for CMCs.

19. Shercliff HR, Beaumont PWR, Vekinis G: Direct observation of the fracture of CAS-glass/SiC composites: part II notched tension. *J Mater Sci* 1994, 29:4184–4190.

20. Droillard C, Voisard P, Heibst C, Lamon J: Determination of fracture toughness in 2-D woven SiC matrix composites made by chemical vapor infiltration. *J Am Ceram Soc* 1994, 78:1201-1211.
 21. Droillard C, Lamon J: Fracture toughness of 2-D woven SiC/SiC CVI-composites with multilayered interphases. *J Am Ceram Soc* 1996, 79:849-858.
- This is a thought provoking demonstration that stronger interfaces can yield tougher composites, depending on the details of microcracking in the inter-phase region.
22. Curtin WA: Stochastics and their role in structural performance. *Curr Opin Solid State Mater Sci* 1996, 1:674-678.
 23. Evans AG, Zok FW: Review: the physics and mechanics of fibre-reinforced brittle matrix composites. *J Mater Sci* 1994, 29:3857-3896.
- This review compiles knowledge about the mechanical performance of CMCs. The most comprehensive models available and the status of experimental assessments are presented. Emphasis is placed on the stress-strain response in tension and shear, the ultimate tensile strength, notch sensitivity, fatigue, stress corrosion, and creep. Many references are cited.
24. He MY, Wu B, Suo Z: Notch-sensitivity and shear bands in brittle matrix composites. *Acta Metall Mater* 1994, 42:3065-3070.
- Notch sensitivity of class II CMCs is modeled using line springs to describe material nonlinearity within both shear bands and mode I damage zones ahead of the crack tip. A simple relation to describe the trends in notched strength with notch size is proposed: $\sigma/\sigma_0 = (1 + \pi a_0/EI)^{-1/2}$ where a_0 is the initial notch strength, σ and σ_0 are the notched and unnotched strengths, E is Young's modulus measured in the loading direction and I is the fracture energy (measured on a large, notched specimen). Excellent correlation with numerical simulations confirms the earlier finding that notched strength is relatively insensitive to the details of bridging laws.
25. Gu P: Notch sensitivity of fiber-reinforced ceramics. *Int J Fracture* 1995, 70:253-266.
 26. Xia ZC, Hutchinson JW, Evans AG, Budiansky B: On large scale sliding in fiber-reinforced composites. *J Mech Phys Solids* 1994, 42:1139-1158.
- Models of matrix cracking in which large scale sliding (fiber/matrix/slip zones large relative to the crack length) is taken into account compared with traditional line spring models. Crack tip stress intensity factors are not strongly influenced, but the stress concentration in bridging fibers at notches is found to be substantially overestimated by line spring models, which are therefore conservative estimators of strength.
27. Wang M, Laird C: Damage and fracture of a cross woven C/SiC composite subject to compression loading. *J Mater Sci* 1996, 31:2065-2069.
- A thorough and useful account of failure mechanisms.
28. Wang M, Laird C: Characterization of microstructure and tensile behavior of a cross-woven C-SiC composite. *Acta Mater* 1996, 44:1371-1387.
- Complements the preceding paper ([27]):
29. Evans AG, Zok FW, McMeeking RM: Fatigue of ceramic matrix composites. *Acta Metall Mater* 1995, 43:859-875.
 30. Holmes JW, Sørensen BF: Fatigue behaviour of continuous fiber-reinforced ceramic matrix composites. In *High Temperature Mechanical Behaviour of Ceramic Composites*. Edited by Nair SV, Jakus K. Boston, Massachusetts: Butterworth-Heinemann; 1995.
- This review provides a general overview of fatigue degradation and failure. The discussion is based predominantly on experimental measurements and observations.
31. Mall S, Weidenaar WA: Tension-compression fatigue behaviour of fibre-reinforced ceramic matrix composite with circular hole. *Composites* 1995, 26:631-636.
 32. Morris WL, Cox BN, Marshall DB, Inman RV, James MR: Fatigue mechanisms in graphite/SiC composites at room and high temperature. *J Am Ceram Soc* 1994, 77:792-800.
 33. Shercliff HR, Vekins G, Beaumont PWR: Direct observation of the fracture of CAS-glass/SiC composites: part 1 delamination. *J Mater Sci* 1994, 29:3643-3652.
 34. Kaute DAW, Shercliff HR, Ashby MF: Modelling of fiber bridging and toughness of ceramic matrix composites. *Scripta Metall Mater* 1995, 32:1055-1060.
 35. Hutchinson JW, Lu TJ: Laminar delamination due to thermal gradients. Cambridge, Massachusetts: Harvard University; 1995. [Report No. MECH-253].
- The essential mechanics of a critical technological problem are laid out. Indispensable for designing thermal barriers.
36. Dransfield K, Baillie C, Mai Y-W: Improving the delamination resistance of CFRP by stitching - a review. *Comp Sci Tech* 1994, 50:305-317.
 37. Cox BN, Flanagan G: *Handbook of analytical methods for textile composites. Contractor Report to NASA Langley*. Thousand Oaks, California: Rockwell Science Center; 1996, in press.
- A review of mechanisms and models for textile composites, developed for polymer composites, but largely applicable to CMCs.
38. Lu TJ and Hutchinson JW: Role of fiber stitching in eliminating transverse fracture in cross-ply ceramic composites. *J Am Ceram Soc* 1995, 78:251-253.
- A valuable demonstration of how concepts from the mechanics of bridged cracks lead the way to understanding the control of delamination by textile reinforcement.
39. Cox BN, Massabò R, Kedward KT: The suppression of delaminations in curved structures by stitching. *Composites* 1996, in press.
 40. Lu TJ, Hutchinson JW: Effect of matrix cracking and interface sliding on the thermal expansion of fibre-reinforced composites. *Composites* 1995, 26:403-414.
 41. Lu TJ, Hutchinson JW: Thermal conductivity and expansion of cross-ply composites with matrix cracks. *J Mech Phys Solids* 1995, 43:1175-1198.
- The thermal expansion and conductivity of CMCs containing periodic matrix cracks are analyzed, with numerical results extended by analytical solutions.
42. Ning Q-G, Chou T-W: A closed-form solution of the transverse effective thermal conductivity of woven fabric composites. *J Comp Mater* 1995, 29:2280-2315.
 43. Hasselman DPH, Donaldson KY: Thermal conductivity of continuous fiber-reinforced ceramic-matrix composites. In *Handbook on Continuous Fiber-Reinforced Ceramic Matrix Composites*. Edited by Lehman RL, El-Rahaiby SK, Wachtman JB Jr. West Lafayette, Indiana: Ceramics Information Analysis Center; 1995:547-583.
 44. Weber CH, Löfvander JPA, Evans AG: Creep anisotropy of a continuous-fiber-reinforced silicon carbide/calcium aluminosilicate composite. *J Am Ceram Soc* 1994, 77:1745-1752.
 45. Henager CH Jr, Jones RH: Subcritical crack growth in CVI silicon carbide reinforced with NicalonTM fibers: experiment and model. *J Am Ceram Soc* 1994, 77:2381-2394.
- An early member of a definitive set of papers reporting observations on matrix cracking in CMCs with creeping fibers.
46. Jones CR, Henager CH Jr, Jones RH: Crack bridging by SiC fibers during slow crack growth and the resultant fracture toughness of SiC/SiC₂ composites. *Scripta Metall Mater* 1995, 33:2067-2072.
- Key observations of the central failure mechanism in an important class of CMCs under static loads at high temperature.
47. Lamouroux F, Vallès JL, Steen M: Influence of damage on the creep behaviour of ceramic matrix composites. *Comp Engng* 1995, 5:1379-1386.
- Further evidence that fiber creep allows subcritical matrix crack growth.
48. Henager CH Jr, Jones RH, Windisch CF Jr, Stackpoole MM, Bordia R: Time-dependent, environmentally assisted crack growth in NicalonTM-fiber-reinforced SiC composites at elevated temperatures. *Metall Mater Trans A* 1996, 27A:839-849.
 49. Cox BN, Marshall DB, McMeeking RM, Begley MR: Matrix cracking in ceramic matrix composites with creeping fibers. *Proceedings of the IUTAM Symposium on Nonlinear Analysis of Fracture*. Edited by Willis JR. Dordrecht, The Netherlands: Kluwer; 1996, in press.
 50. Begley MR, Evans AG, McMeeking RM: Creep rupture in ceramic matrix composites with creeping fibers. *J Mech Phys Solids* 1995, 43:727-740.
- Very useful constitutive laws are defined for the bridging effect of creeping fibers, but the reader should check [53] for remarks on the conjectured steady state cracking condition which is then used for analyzing crack growth.
51. El-Azab A, Ghoniem NM: Investigation of incubation time for sub-critical crack propagation in SiC-SiC composites. *J Nucl Mater* 1995, 219:101-109.
 52. Gwo T-J, Nair SV: Creep crack growth in fiber reinforced composites with rate dependent bridging - role of a viscous fiber matrix interface. *Mech Mater* 1996, in press.

53. Begley MR, Cox BN, McMeeking RM: Time dependent crack growth in ceramic matrix composites with creeping fibers. *Acta Metall Mater* 1995, 43:3927-3936.
 54. Cox BN, Marshall DB: Crack initiation in fiber-reinforced brittle laminates. *J Am Ceram Soc* 1996, 79:1181-1188.
 55. Mumm DR, Morris WL, Dadkhah MS, Cox BN: High temperature crack growth in ceramic composites. In *Thermal and Mechanical Test Methods and Behaviour of Continuous-Fiber Ceramic Composites*, ASTM STP 1309. Philadelphia: ASTM; 1996.
 56. Weber CH, Kim KT, Heredia FE, Evans AG: High temperature deformation and rupture in SiC-C composites. *Mater Sci Eng A* 1995, 196:25-31.
 57. Bodet R, Bourrat X, Lamon J, Naslain R: Tensile creep behaviour of a silicon carbide-based fibre with a low oxygen content. *J Mater Sci* 1995, 30:661-667.
 58. El Azab A, Ghoniem NM: Postirradiation fiber debonding and pull-out in SiC-SiC composites. *J Nucl Mater* 1994, 212:845-848.
 59. Jones RH, Henager CH Jr: Fusion reactor application issues for low activation SiC/SiC composites. *J Nucl Mater* 1995, 219:55-62.
 60. Evans AG, Zok FW, McMeeking RM, Du ZZ: Models of high-temperature, environmentally-assisted embrittlement in ceramic matrix composites. *J Am Ceram Soc* 1996, in press.
 61. Heredia FE, McNulty JC, Zok FW, Evans AG: Oxidation embrittlement probe for ceramic-matrix composites. *J Am Ceram Soc* 1995, 78:2097-2100.
- The prevalence of stress oxidation at intermediate temperatures is demonstrated on several CMC systems containing Nicalon™ fibers with either C, BN/SiC, or C/B coatings. The phenomenon is manifested in a reduction in strength or rupture time, along with diminished fiber pullout lengths on the fracture surface.
62. Jones RH, Henager CH Jr, Windisch CF Jr: High temperature corrosion and crack growth of SiC-SiC at variable oxygen partial pressures. *Mater Sci Eng A* 1995, 198:103-112.
 63. Sheldon BW, Sun EY, Nutt SR, Brennan JJ: Oxidation of BN-coated SiC fibers in ceramic matrix composites. *J Am Ceram Soc* 1996, 79:539-543.
 64. Cutler WA, Zok FW, Lange FF: Mechanical behavior of several hybrid ceramic matrix composite laminates. *J Am Ceram Soc* 1996, 79:1825-1833.
 65. Morgan PED, Marshall DB: Ceramic composites of monazite and alumina. *J Am Ceram Soc* 1995, 78:1553-1563.
- The revelation of monazites as interface coatings. This discovery will come to be viewed as a major breakthrough.
66. Morgan PED, Marshall DB, Housley RM: High-temperature stability of monazite-alumina composites. *Mater Sci Eng A* 1995, 195:215-222.
- Monazite is chemically stable in alumina between 1400°C and 1600°C over long periods, provided it is free of alkali metals and divalent elements.
67. Tu W-C, Lange FF, Evans AG: Concept for a damage-tolerant ceramic composite with "strong" interfaces. *J Am Ceram Soc* 1995, 79:417-424.
- The attainment of tough CMCs by surrounding fiber bundles (as in a textile) by a weak matrix is demonstrated.
68. Lange FF, Tu WC, Evans AG: Processing of damage-tolerant, oxidation-resistant ceramic matrix composites by a precursor infiltration and pyrolysis method. *Mater Sci Eng A* 1995, 195:145-150.
 69. Ota T, Takahashi M, Hibi T, Ozawa M, Suzuki S, Hikichi Y: Biomimetic process for producing SiC "wood". *J Am Ceram Soc* 1995, 78:3409-3411.
 70. Lu TJ: Crack branching in all-oxide ceramic composites. *J Am Ceram Soc* 1996, 79:266-274.
 71. Cox BN: Modeling three-dimensional composites. In *Advanced Technology for Design and Fabrication of Composite Materials and Structures* (Torino, 1993). Edited by Sih GC, Carpinteri A, Surace G. Amsterdam: Kluwer; 1995:49-62.
 72. Cox BN: Lockup, chains, and the delocalization of damage. *J Mater Sci* 1996, in press.
- The concept of imparting damage tolerance through the use of systematic internal defects and lock-up mechanisms is explored, with reference to several material classes. A model system of steel chains in an epoxy matrix provides a particularly vivid demonstration. Reinforcement geometry may be tailored to greatly enhance damage tolerance while maintaining high strength.
73. Hilmas G, Brady A, Abdali U, Zywicki G, Halloran J: Fibrous monoliths: non-brittle fracture from powder-processed ceramics. *Mater Sci Eng A* 1995, 195:263-268.
 74. Nakano K, Kamiya A, Nishino Y, Imura T, Chou T-W: Fabrication and characterization of three-dimensional carbon fiber reinforced silicon carbide and silicon nitride composites. *J Am Ceram Soc* 1995, 78:2811-2814.
 75. Zhien L, Jianjun Y, Zhiyun X: The interface, microstructure and mechanical properties of C/LAS glass-ceramic composites. *J Mater Sci* 1995, 30:399-404.
 76. Kawai C, Wakamatsu S: Fabrication of C/SiC composites by an electrodeposition/sintering method and the control of the properties. *J Mater Sci* 1996, 31:2165-2170.
 77. Chawla KK, Xu ZR, Ha J-S: Processing, structure, and properties of mullite fiber/mullite matrix composites. *J Eur Ceram Soc* 1996, 16:283-299.
 78. Shin D-W, Auh KH, Knowles KM: SiC fibre/borosilicate glass composite (part 2) - factors controlling the mechanical properties. *J Ceram Soc Japan* 1995, 103:409-417.
 79. Parthasarathy TA, Barlage DR, Jero PD, Kerans RJ: Effect of interfacial roughness parameters on the fiber pushout behavior of a model composite. *J Am Ceram Soc* 1995, 78:3232-3236.
 80. Parthasarathy TA, Marshall DB, Kerans RJ: Analysis of the effect of interfacial roughness on fiber debonding and sliding in brittle matrix composites. *Acta Metall Mater* 1994, 42:3773-3784.
- An attractively simple micromechanical model of interface roughness is supported by test data in the material studied.
81. Huang CM, Zhu D, Xu Y, Mackin T, Kriven WM: Interfacial properties of SiC monofilament reinforced β' (-SiAlON) composites. *Mater Sci Eng A* 1995, 201:159-168.
 82. Peters PWM, Martin E, Quenisset JM: Slip and frictional shear stresses in ceramic matrix composites. *J Comp Mater* 1995, 29:550-572.
 83. Cox BN: Life prediction for bridged fatigue cracks. In *Life Prediction Methodology for Titanium Matrix Composites*, ASTM STP 1253. Edited by Johnson WS, Larsen JM, Cox BN. Philadelphia: ASTM; 1996.
 84. Kerans RJ: Issues in the control of fiber-matrix interface properties in ceramic composites. *Scripta Metall Mater* 1994, 31:1079-1084.
 85. Kerans RJ, Jero PD, Parthasarathy TA: Issues in the control of fiber/matrix interfaces in ceramic composites. *Comp Sci Tech* 1994, 51:291-296.
 86. Kerans RJ: The role of coating compliance and fiber/matrix interfacial topography on debonding in ceramic composites. *Scripta Metall Mater* 1995, 32:505-509.
 87. Sørensen BF, Holmes JW: Effect of loading rate on the monotonic tensile behavior of a continuous-fiber-reinforced glass-ceramic matrix composite. *J Am Ceram Soc* 1996, 79:313-320.
- Interfacial friction is shown to be rate dependent.
88. Budiansky B, Evans AG, Hutchinson JW: Fiber-matrix debonding effects on cracking in aligned fiber ceramic composites. *Int J Solids Struct* 1995, 32:315-328.
 89. Ochiai S, Hojo M: Reduction in energy release rate for mode I fracture of a fibre with a cracked coating layer due to small-scale interfacial debonding. *J Mater Sci* 1996, 31:2027-2034.
 90. Chawla N, Holmes JW, Mansfield JF: Surface roughness characterization of Nicalon™ and Hi-Nicalon™ ceramic fibers by atomic force microscopy. *Mater Charact* 1995, 35:199-206.
 91. Lamon J, Rebillat F: Microcomposite test procedure for evaluating the interface properties of ceramic matrix composites. *J Am Ceram Soc* 1995, 78:401-405.
 92. Morscher GN, Martinez-Fernandez J, Purdy MJ: Determination of interfacial properties using a single-fiber microcomposite test. *J Am Ceram Soc* 1996, 79:1083-1091.

MATRIX CRACKING IN CERAMIC MATRIX COMPOSITES WITH CREEPING FIBERS

B. N. COX and D. B. MARSHALL
Rockwell Science Center
1049 Camino Dos Rios
Thousand Oaks, CA 91360

R. M. McMEEKING and M. R. BEGLEY
Dept. Mechanical and Environmental Engineering
University of California, Santa Barbara
Santa Barbara, CA 93106

1. Introduction

High strength can be achieved in ceramic fibers by manufacturing them as fine-grained polycrystals. Unfortunately, fine-grained fibers are prone to creep, because grain boundaries provide easy paths for diffusion. The matrix in many composites, whether formed by chemical vapor infiltration or by some other route, has a much coarser grain structure. Therefore, service life of CMCs reinforced by fine-grained fibers can be limited by fiber creep at temperatures where the matrix remains elastic. This paper is concerned with how fiber creep affects the failure by matrix cracking of a CMC under monotonic loading.

Of primary interest is the passage to failure of 0/90° laminates, which offer at least a partial solution to the requirement of strength under transverse loads. The first damage observed in these materials under loads aligned with the 0° fibers is matrix cracking, which initiates in the 90° plies [1,2]. In many applications, failure may be considered to occur when these matrix cracks grow into through cracks by crossing the entire composite. 1) *Stiffness critical applications*. As long as matrix cracks remain comparable in size to the ply thickness, they cause a relatively minor reduction in the composite stiffness, because crack openings are limited by the crack length [3]. However, when matrix cracks traverse the entire composite, the separated pieces of matrix sustain average strains much lower than those in the fibers. The contribution of the matrix to the composite modulus is then severely degraded. 2) *Hermeticity*. As long as matrix cracks remain small and unconnected, they do not compromise the ability of the composite to act as a seal or liner, impermeable to gases. However, gas permeability obviously rises dramatically in the presence of through cracks. 3) *Hostile environments*. Matrix cracks admit

corrosive gases into the interior of the composite, where they attack fibers and the fiber/matrix interfaces. Composite strength and toughness can then fall away very quickly. Even small matrix cracks will introduce some corrosive gases. However, degradation may be limited to near-surface regions and relatively harmless until through cracks form, at which point failure will usually be imminent [4].

At room temperature, a lower bound exists to the stress at which cracks initiating in neighboring 90° plies link up to form through cracks. The bound obtains regardless of the presence of matrix flaws or flaws in clusters of fibers. The lower bound is a certain critical matrix cracking stress, σ_{crit} , to be introduced below. While σ_{crit} varies to some extent with laminar dimensions and residual stresses, it is easily characterized for a single material and remains a fundamental, robust engineering parameter for failure at room temperature.

At high temperatures where fibers creep, this useful simplicity is lost. The critical matrix cracking stress, which now takes a temperature dependent value $\sigma_{crit}(T)$, is still a bound for *rate independent* cracking, i.e., the immediate response to load, but subcritical crack growth mediated by fiber creep will eventually lead to through cracks at stresses much lower than σ_{crit} [5,6]. Lifetime becomes a function of temperature and stress, dictated by the rate of subcritical crack growth. This is the subject considered here.

Fiber creep will also affect the residual ultimate strength of the composite. In applications where matrix cracking is not fatal per se, changes in residual strength must also be modeled. Some remarks will be made on the role of subcritical matrix crack growth on residual strength, but this issue will otherwise be left for future research.

2. Initial, Rate-Independent Matrix Cracking

In $0/90^\circ$ laminates loaded in the 0° fiber direction, the first manifestation of matrix cracking is tunneling cracks in the 90° plies [1,2]. The tunneling cracks initiate at intrinsic flaws in the 90° plies, which, being loaded transversely, tend to be weaker than the 0° plies. If any stable phase of matrix cracking occurs, it consists of the subsequent spreading of the cracks produced by tunneling into the adjacent 0° plies. The stable phase of growth occurs in the plane strain configuration indicated in Fig. 1a. Before discussing details of the initiation of matrix cracks by tunneling, it is helpful to examine the factors governing the stability and stress levels of the plane strain phase.

Within the plane strain crack, the 90° ply acts effectively as a sharp notch or unbridged interval of width $2h_{90}$, while fiber bridging in the 0° plies acts in the intervals $h_{90} < |x_1| < a$ to shield the crack tip, where x_1 and the crack length a are defined in Fig. 1a. A useful model of the relation between the bridging tractions p and the crack opening displacement $2u$ is [7,8]

$$p = \frac{2fE}{(1-f)E_m} \left[\frac{\tau E_f u}{R} \right]^{1/2} \quad (1)$$

where τ is the interfacial friction stress (a function of temperature); f is the fiber volume fraction; R is the fiber radius; E_f and E_m are the fiber and matrix moduli; and $E = fE_f + (1-f)E_m$. While this relation is based on several assumptions that may not always be valid in a given CMC [9], it is likely to indicate trends quite well.

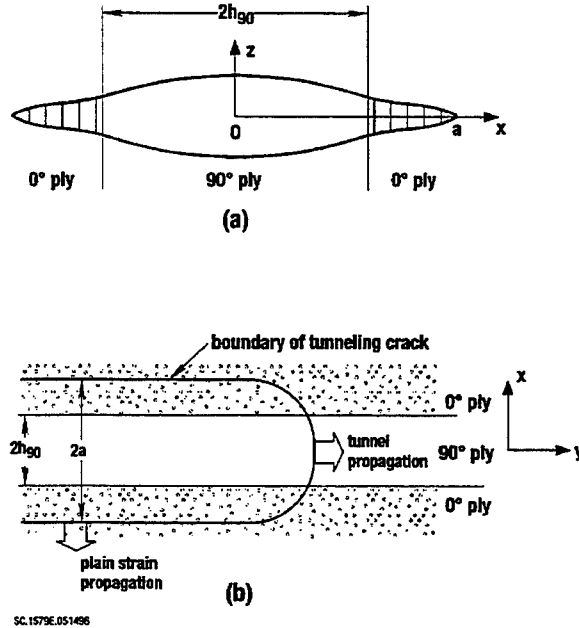


Figure 1. (a) Schematic of a plane strain crack spreading from a 90° ply. (b) Schematic of a tunneling crack propagating along a 90° ply and lapping into the adjacent 0° plies.

Crack propagation is assumed here to occur when the crack tip stress intensity factor, K_{tip} , takes a critical value $K_c = \sqrt{E' \Gamma_0}$, where E' is an effective modulus for the laminate [3] and Γ_0 is the effective fracture energy for the matrix crack in the 0° ply. This criterion implies that the matrix is an elastic, brittle material.

Because p is an increasing function of u and crack propagation occurs at a nonzero value of K_{tip} , the steady state crack configuration can be attained for long bridged cracks where the critical stress for propagation, σ_p , becomes independent of the crack length [10]. This limiting stress is the matrix cracking

stress, σ_{mc} . It can be readily deduced from $p(u)$ by evaluating the complementary energy density [11]:

$$\sigma_{mc} = \left[\frac{6\eta^2 E_f E^2 \Gamma_0}{R(1-f)^2 E_m^2} \right]^{1/3} \quad (2)$$

A characteristic length, the "bridging length scale," a_m , is associated with the traction law, $p(u)$. For the model of fiber bridging underlying Eq. (1), it has the form [7,10]

$$a_m = \frac{\pi E'}{4} \left(\frac{3\Gamma_0}{2} \right)^{1/3} \left[\frac{4\eta^2 E_f E^2}{R(1-f)^2 E_m^2} \right]^{-2/3} \quad (3)$$

The stability of the plane strain phase of crack growth is determined entirely by the ratio, h_{90}/a_m , of the 90° ply half-width to the bridging length scale (Fig. 2). If $h_{90}/a_m < 8/3\pi^2$, $\sigma_p(a)$ is a decreasing function; crack growth is unstable and always requires an applied stress $\sigma_a > \sigma_{mc}$. If $h_{90}/a_m > 8/3\pi^2$, $\sigma_p(a)$ is an increasing function; crack growth is stable, commencing at some $\sigma_a < \sigma_{mc}$. (The critical ratio $8/3\pi^2$ is found by equating the critical stress for a Griffith crack of size h_{90}/a_m to the steady state matrix cracking stress, σ_{mc} .)

Whatever the value of h_{90} , σ_p eventually reaches the matrix cracking stress, σ_{mc} , approaching close to it for crack lengths large compared to a_m . It is for this reason that σ_{mc} serves as a design limit for forming long matrix cracks for *any* distribution of flaws. In current CMCs, a_m is typically ~ 0.1 mm at room temperature [10]. Thus, $h_{90}/a_m > 8/3\pi^2$ in most cases, so that crack growth is stable; while $\sigma_p \approx \sigma_{mc}$ for cracks ~ 1 mm or more.

Now consider the events leading up to the propagation of a plane strain crack. The critical stress for tunnel crack propagation can be computed from energy considerations [12,13]. When the tunneling crack is long, the critical stress approaches a constant asymptote, σ_t , which is a function $\sigma_t(d)$ of the distance, $d = a - h_{90}$, to which the tunneling crack laps into the adjacent 0° plies as it propagates along the 90° ply. This function depends on the 90° ply width and the ratio $\eta = \Gamma_{90}/\Gamma_0$ of the effective fracture toughnesses of the 90° and 0° plies. The minimum, $\sigma_t^{(\min)}$, of $\sigma_t(a)$ is generally a lower bound to the initiation stress for matrix cracking. The initiation stress will be significantly higher than $\sigma_t^{(\min)}$ only if intrinsic flaws are much less than the 90° ply width.

Estimates for existing CMCs suggest this is not usually the case. The sum $h_{90} + d_{\min}$, where d_{\min} is the value of d corresponding to $\sigma_t = \sigma_t^{(\min)}$, will be the

half-width of the plane strain crack created by the tunneling event. For $\eta < 1/2$, $d_{\min} = 0$; the tunneling crack is confined entirely to the 90° ply. Some nonzero increment in the applied load will be required before propagation of the newly created plane strain crack into the 0° plies occurs. For $\eta > 1/2$, $d_{\min} > 0$; and in this case it can be shown that the tunneling crack simultaneously satisfies the criterion for propagation as a plane strain crack into the 0° plies [14,15]. Any increase in load after the tunneling crack has formed will be accompanied immediately by its broadening in the plane strain crack configuration [15].

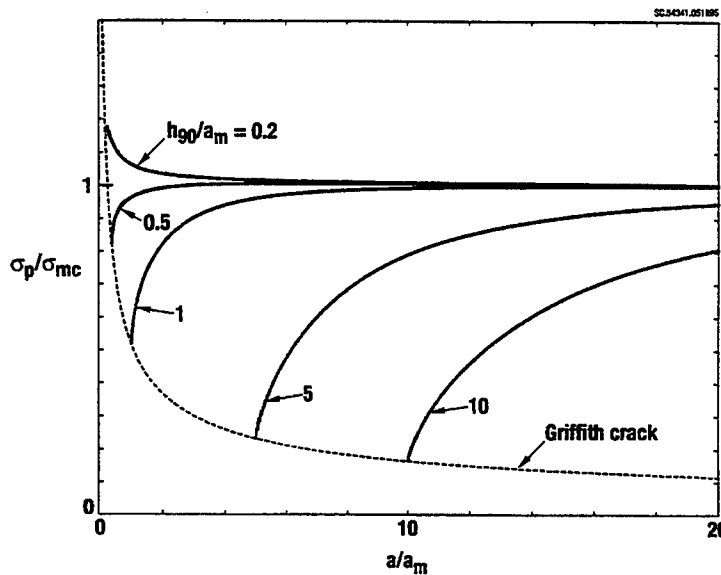


Figure 2. The critical stress for plane strain crack growth.

The correct value of the toughness ratio, η , is difficult to specify for some particular CMC from microstructural considerations alone. It will probably always have to be measured. However, the range $0 \leq \eta \leq 1$ seems reasonable for composites with identical materials in the 0° and 90° plies [15].

One further condition must be satisfied for a stable phase of plane strain cracking to occur. The tunneling crack must not penetrate beyond the adjacent 0° ply during its formation. If it does, it will enter new unbridged zones, i.e., the next 90° plies, the critical stress for its formation will drop, and the initiating crack will radiate unstably out in all directions without limit. This consideration imposes bounds on the minimum ratio, h_0/h_{90} , of the 0° and 90° ply half-widths for stable cracking, given a value of the toughness ratio, η . A stability map can thus be created from solutions to the tunneling problem (Fig.

3). Figure 3 shows the approximate location of a typical SiC-SiC composite on the map, as well as the repositioning that would be expected if values of the micro-structural parameters f (volume fraction), R (fiber radius), τ (friction stress), or η (toughness ratio) were halved.

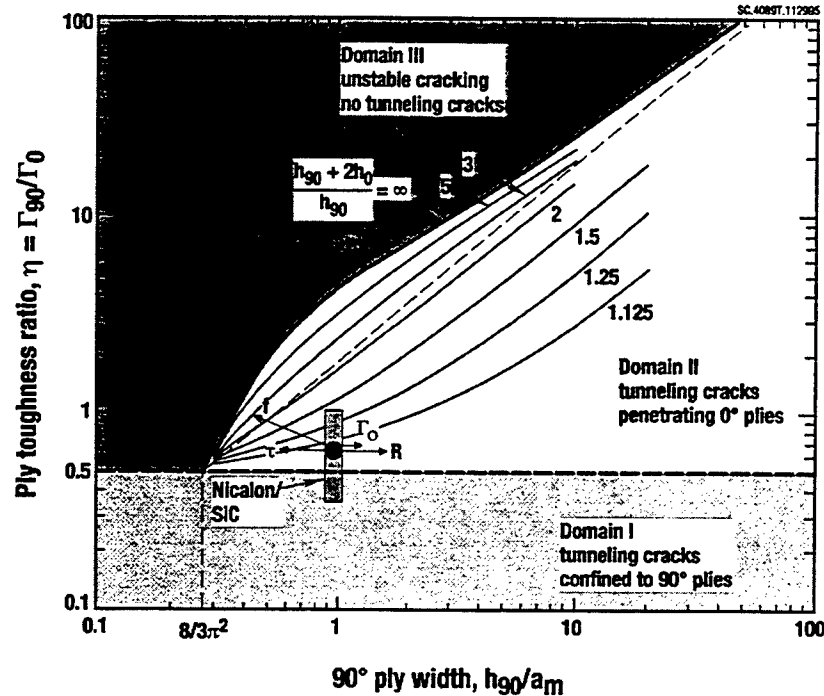


Figure 3. Map showing the regimes where a phase of stable plane strain crack growth can follow crack initiation by tunneling.

Figure 4 shows an alternative view of the role of ply widths in the cracking process. Here the boundaries of stable and unstable cracking are plotted out against the 90° ply half-width, h_{90} , for the fixed ratio $h_{90}/h_0 = 1$. One solid curve shows the critical stress for a plane strain crack (no bridging) of width $2h_{90}$. The higher solid curve shows the stress at which the plane strain crack curve intersects the far boundary of the first 0° plies, i.e., $\sigma_p(h_{90} + 2h_0)$. All stresses are normalized against σ_{MC} , the limiting critical stress for an infinite crack wholly contained in an infinite (hypothetical) 0° ply. The horizontal dashed lines show the stress values at which crack initiation will occur by tunneling for several values of the toughness ratio, η . Here it is assumed that an initial flaw comparable to or slightly greater than the 90° ply widths pre-exists, so that the steady state tunneling stress, σ_t , is appropriately taken as the initiation stress. If only smaller flaws exist, the dashed line should be raised. Whether a stable phase of plane strain crack growth exists is determined by

where the horizontal dashed line meets the vertical line drawn at the given value of 90° ply width, h_{90}/a_m . This point is denoted P.

If $\eta < 1/2$, P will fall below the Griffith curve. In other words, after initiation by tunneling, a further load increment to σ_G will be required before the crack extends stably in plane strain. This stable growth will terminate when the applied load rises to $\sigma_p(h_{90} + 2h_0)$.

If $1/2 < \eta < \eta_{crit}$, P will fall between the curve $\sigma_p(h_{90} + 2h_0)$ and the Griffith curve (the case shown in Fig. 4). Here η_{crit} is the critical value of η for the ply width ratio unity in Fig 3. Plane strain crack growth will follow immediately after crack initiation upon further load increase. Once again, stable growth will terminate when the applied load reaches $\sigma_p(h_{90} + 2h_0)$.

If $\eta > \eta_{crit}$, P will fall above the curve $\sigma_p(h_{90} + 2h_0)$ and unlimited unstable cracking will accompany crack initiation.

Thus $\sigma_p(h_{90} + 2h_0)$ should be identified with the engineering design limit, σ_{crit} . Whatever the ply toughness ratio, any matrix cracks will arrest without exceeding the first 0° plies at all stresses below $\sigma_{crit} = \sigma_p(h_{90} + 2h_0)$.

3. Subcritical Crack Growth Mediated by Fiber Creep

Whenever crack arrest depends on fiber bridging, it will give way to subcritical crack growth at high temperatures because of fiber creep. Thus, subcritical crack growth will fix a finite lifetime for all applied loads between σ_G and σ_{crit} in Fig. 4.

A bridging law for creeping fibers coupled to the matrix by friction takes the relatively simple form

$$\dot{u} = 2\lambda p[\dot{p} + \beta p] \quad (4)$$

provided: there are no rate effects in the interfacial friction; fiber creep is confined to the slip zone adjacent to the matrix crack by the stress concentration due to the crack; the matrix remains elastic; and fiber creep follows a linear law

$$\dot{\epsilon}_f = \dot{\sigma}_f / E_f + \beta \sigma \quad (5)$$

where ϵ_f and σ_f are the fiber strain and stress and β is a creep coefficient [5]. For general fiber creep laws, an explicit relation between u and p and their time derivatives cannot always be derived; but this is unlikely to have any qualitative effect on the subcritical crack growth problem.

The condition for matrix crack extension is

$$K_{tip} = K_a - K_b = K_c \quad (6)$$

where K_a is the applied stress intensity factor and K_b its reduction due to bridging. Consider the differential

$$dK_{tip} = \frac{\partial K_{tip}}{\partial a} da + \frac{\partial K_{tip}}{\partial t} dt \quad (7)$$

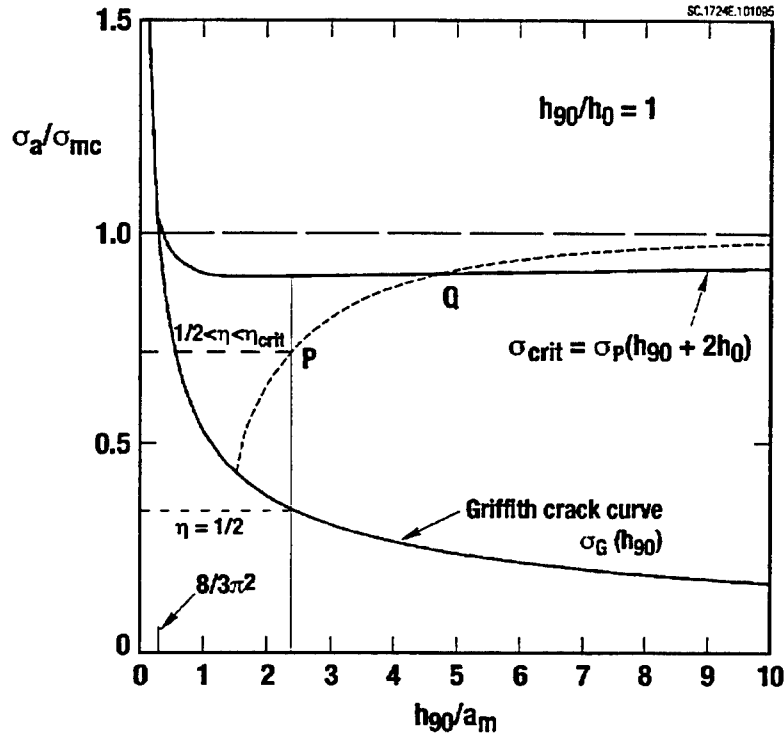


Figure 4. Diagram defining σ_G and σ_{crit} , which bound the domain where life at high temperature will be determined by subcritical plane strain crack growth; and showing schematically the boundary between stresses for which fiber creep rupture follows subcritical crack propagation and vice versa.

For stable rate-independent growth, which is the regime of interest, the first term must be negative. The second term is positive, reflecting the decay of bridging. Maintenance of the condition Eq. (6) implies $dK_{tip} = 0$ and via Eq. (7) there follows a governing differential equation for the crack velocity, da/dt . Numerical methods for solving this equation may be found in Refs. 6 and 16.

Typical solutions for the crack velocity are shown in Fig. 5. Essential characteristics are as follows. 1) The velocity history can be divided into an initial deceleration transient; and a quasi-steady state at long crack lengths, defined by increasing insensitivity of da/dt to the initial conditions [6]. ("Quasi-steady state" is preferred to "steady state" because there is no invariant of the motion as $a \rightarrow \infty$ [16].) The deceleration transient is dominated by creep relaxation of fibers right next to the 90° ply, while the quasi-steady state is dominated by the loading history of fibers in a small, propagating zone just behind the crack tip [6]. 2) Unless the 0° ply width is much greater than the 90° ply width, crack propagation across the first 0° ply (whose limits are not marked in Fig. 5), which is followed by catastrophic cracking and therefore defines lifetime in the sense of this paper, is spent entirely in the deceleration transient. 3) The velocity and therefore the time to failure are very strong functions of the applied stress, with $da/dt \rightarrow \infty$ and lifetime $t_c \rightarrow 0$ as $\sigma_a \rightarrow \sigma_{mc}$. 4) At long crack lengths, the crack continues to accelerate, but increasingly slowly.

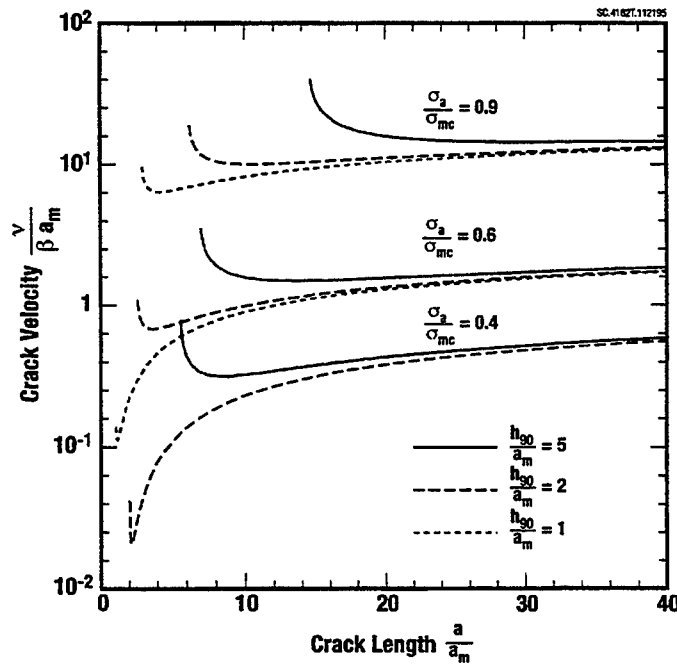


Figure 5. Crack growth rate histories for cracks bridged by creeping fibers (from [6]). Curves are shown for three different 90° ply widths and three different applied stress levels. The initial crack length, which exceeds the 90° ply width for the cases shown, is defined by arrest of the rate-independent plane strain crack that grows from the initiating tunneling crack. The calculated crack growth is pursued well into hypothetically semi-infinite 0° plies.

4. Other Aspects of Composite Failure

4.1 FIBER FAILURE BY CREEP RUPTURE

In the calculations of Fig. 5, fibers were assumed never to fail. In reality, they will fail by creep rupture if the fiber strain exceeds some critical value, ϵ_{crit} . Fiber failure may occur either after through cracks have formed or during the phase of subcritical crack growth. The former will always be the case for applied stresses, σ_a , sufficiently close to or above σ_{mc} , since crack propagation will then be either very fast or dynamic (depending on whether σ_a is above or below σ_{crit}). Because subcritical matrix crack propagation rates are such strong functions of applied stress, there will be a transition to fiber failure during subcritical propagation as σ_a is reduced. The velocity becomes vanishingly small as the applied load approaches the minimum, σ_G , required for penetration of the initiating tunneling crack into the 0° plies. Lower velocities imply an increasing time for the accumulation of fiber creep strain; and the available time increases much faster than the fiber's creep rate declines [6]. New experiments are required to confirm this transition.

4.2 CRACK PROPAGATION FOLLOWING FIBER FAILURE IN THE SMALL SCALE BRIDGING LIMIT

In the domain where fiber failure occurs during subcritical crack growth, the surviving bridging zone will often be much smaller than other crack and specimen dimensions. Small scale bridging conditions will then apply. After some growth, the crack configuration will approximate a steady state configuration governed solely by the applied stress intensity factor, K_a . The velocity will approach a steady state value, V_{ss} , which will be a function of K_a rather than directly of crack length. Complete solutions for this steady state have been presented in Ref. [17]. The solutions show many similarities to those for equilibrium craze zones in polymers, e.g., Refs. [18-21], but also some distinct features peculiar to the mechanics of brittle matrix composites [17]. In particular, crack growth occurs only when K_a exceeds K_c . At the lowest stresses, i.e., small $K_a - K_c$

$$V_{ss} \sim (K_a - K_c)^{3/2} \epsilon_{crit}^{1/2}, \quad (8)$$

where ϵ_{crit} is the critical fiber strain. Small $K_a - K_c$ is probably the most important regime for the present context, since fiber failure during subcritical crack growth occurs only for stresses just above σ_G , which means that K_a is near K_c .

As illustrated by the asymptotic result Eq. (8), the crack velocity following fiber failure increases much faster than when the fibers remain intact (cf. Fig. 5). For practical purposes, the onset of fiber failure in the wake of a subcritical crack could be considered equivalent to structural failure.

4.3 THE LIMITS OF SINGLE CRACK MODELS

The constitutive model of Eq. (4) was derived for a single matrix crack and the resulting crack growth curves were all calculated in the absence of any stress redistribution effects that might arise from similar, nearby cracks. At room temperature, multiple matrix cracks are the common case; and rather than being noninteracting, their separation is in fact determined by marginal overlap between their interfacial slip zones. In a body with multiple matrix cracks, the overlap ought to be factored into the bridging law for creeping fibers. Multiple cracks should indeed be expected in a smooth specimen. But at high temperatures, recent experiments on *notched* SiC/SiC composites have shown that while multiple cracks do initiate, only one propagates very far, so that the problem reverts to that of a single dominant matrix crack [22]. Whether multiple or single cracks will occur at high temperatures in the presence of blunt stress concentrators remains a topic of current research.

When arrays of cracks arise in the 90° plies in smooth laminates, crack interaction effects ought to be computed, e.g., by employing weight functions for arrays of cracks instead of those for single cracks [13]. Crack interactions will accelerate the formation of through cracks via crack coalescence. For an isolated matrix crack growing away from a 90° ply through neighboring 0° plies, unstable growth to a through crack will commence when it has reached the far side of the 0° plies. If two cracks grow towards one another into the same 0° ply from successive 90° plies, they each need cross only half the 0° ply before coalescence leads to catastrophic cracking; and their mutual interaction will accelerate even this diminished phase of subcritical crack growth. The boundary marked σ_{crit} in Fig. 4 will move down, because of the stricter limits that must be satisfied for the initiation (tunneling) phase to terminate in crack arrest. How far down the boundary will move will depend on how the 0° ply half-width, h_0 , compares to the bridging length scale, a_m . If $h_0/a_m \gg 1$, the change will be slight, because the rate-independent plane strain cracking stress, $\sigma_p(a)$, will approach close to the limit σ_{mc} before crack interaction effects become significant. If $h_0 \sim a_m$, the fall in σ_{crit} will be considerable, but readily calculated [13]. The failure map retains the same appearance.

Even when multiple cracks exist, the trends and failure maps presented here will remain qualitatively true. The overlap of slip zones does not change the essential features of the bridging constitutive law, namely that p is an increasing function of u and decays with time. Furthermore, the law already contains implicit assumptions about micromechanics which are doubtful in detail. The constitutive law of Eq. (4) serves as a good guide to possible fracture behavior, with its details *always* understood to require empirical calibration, preferably using fracture data rather than micromechanical tests [9]. Whatever the exact form chosen for a bridging law like Eq. (4), once it is calibrated against experiments, it will probably yield accurate predictions for a wide range of other stress levels.

Acknowledgments BNC was supported under AFOSR Contract No. F49620-94-C-0030; DBM under Rockwell Independent R&D Funding; and RMM and MRB under the ARPA University Research Initiative (ONR Contract No. N-0014-92-J-1808).

References

1. D.S. Beyerle, S.M. Spearing, and A.G. Evans, "Damage Mechanisms and the Mechanical Properties of a Laminated 0/90 Ceramic/Matrix Composite," *J. Amer. Ceram. Soc.* **75**, 3321-30 (1992).
2. F. Lamouroux, M. Steen, and J.L. Valles, "Uniaxial Tensile and Creep Behaviour of an Alumina Fibre-Reinforced Ceramic Matrix Composite: I-Experimental Study," *J. European Ceram. Soc.*, in press.
3. Z.C. Xia, R.R. Carr, and J.W. Hutchinson, "Transverse Cracking in Fiber-Reinforced Brittle Matrix, Cross-Ply Laminates," *Acta Metall. Mater.* **41**, 2365-75 (1993).
4. F. Heredia, J.C. McNulty, F.W. Zok, and A.G. Evans, "Oxidation Embrittlement Probe for Ceramic Matrix Composites," *J. Amer. Ceram. Soc.* **78**, 2097-2100 (1995).
5. M.R. Begley, A.G. Evans, and R.M. McMeeking, "Creep Rupture in Ceramic Matrix Composites with Creeping Fibers," *J. Mech. Phys. Solids* **43**, 727-40 (1995).
6. M.R. Begley, B.N. Cox, and R.M. McMeeking, "Time Dependent Crack Growth in Ceramic Matrix Composites with Creeping Fibers," *Acta Metall. Mater.* **43**, 3927-36 (1995).
7. D.B. Marshall, B.N. Cox, and A.G. Evans, "The Mechanics of Matrix Cracking in Brittle-Matrix Fiber Composites," *Acta Metall. Mater.* **33**, 2013-21 (1985).
8. L.N. McCartney, "Mechanics of Matrix Cracking in Brittle-Matrix Fibre-Reinforced Composites," *Proc. Roy. Soc. London A* **409**, 329-50 (1987).
9. B.N. Cox, "Life Prediction for Bridged Cracks," in *Life Prediction for Titanium Matrix Composites*, ed. W.S. Johnson, J. Larsen, and B.N. Cox, ASTM STP (ASTM, Philadelphia, 1995), in press.
10. B.N. Cox and D.B. Marshall, "Concepts for Bridged Cracks in Fracture and Fatigue," *Acta Metall. Mater.* **42**, 341-63 (1994).
11. D.B. Marshall and B.N. Cox, "A J Integral Method for Calculating Steady State Matrix Cracking Stresses in Composites," *Mechanics of Materials* **7**, 127-33 (1988).
12. S. Ho and Z. Suo, "Tunneling Cracks in Constrained Layers," *J. Appl. Mech.* **60**, 890-4 (1993).
13. Z.C. Xia and J.W. Hutchinson, "Matrix Cracking of Cross-Ply Ceramic Composites," *Acta Metall. Mater.* **42**, 1933-45 (1994).
14. J.L. Beuth, "Cracking in Thin Bonded Films in Residual Tension," *Int. J. Solids Structures* **29**, 1657-75 (1992).

15. B.N. Cox and D.B. Marshall, "Crack Initiation in Brittle Fiber Reinforced Laminates," *J. Amer. Ceram. Soc.*, in press.
16. B.N. Cox and L.R.F. Rose, "Time or Cycle Dependent Crack Bridging," *Mechanics of Materials* **19**, 39-57 (1994).
17. M.R. Begley, B.N. Cox, R.M. McMeeking, "Creep Crack Growth with Small Scale Bridging in Ceramic Matrix Composites," submitted to *Acta Metall. Mater.*
18. W.G. Knauss, "Time Dependent Fracture and Cohesive Zones," *Journal of Engineering Materials and Technology* **115**, 262-7 (1993).
19. L.-O. Fager, J.L. Bassani, C.-Y. Hui, and D.-B. Xu, "Aspects of Cohesive Zone Models and Crack Growth in Rate-Dependent Materials", *International Journal of Fracture* **52**, 119-44 (1991).
20. E.J. Kramer and E.W. Hart, "Theory of Slow, Steady Crack Growth in Polymer Glasses," *Polymer* **25**, 1667-78 (1984).
21. R.A. Schapery, "A Theory of Crack Initiation and Growth in Viscoelastic Media," *International Journal of Fracture* **11**, 141-59 (1975).
22. D.R. Mumm, W.L. Morris, M.S. Dadkhah, and B.N. Cox, "High Temperature Crack Growth in Ceramic Composites," *Thermal and Mechanical Test Methods and Behaviour of Continuous-Fiber Ceramic Composites*, ASTM STP 1309, ed. M.G. Jenkins, S.T. Gonczy, E. Lara-Curzio, N.E. Ashbaugh, and L.P. Zawada (ASTM, Philadelphia, 1996).

Delamination Resistance of Two Hybrid Ceramic-Composite Laminates

 Willard A. Cutler,^{*,†} Frank W. Zok,^{*} and Fred F. Lange^{*}

Materials Department, University of California, Santa Barbara, California 93106

 Panos G. Charalambides^{*}

 Department of Mechanical Engineering, The University of Maryland-Baltimore County,
 Baltimore, Maryland 21228

Hybrid laminar composites that are comprised of alternating layers of ceramic sheets and fiber-reinforced ceramic-matrix composite (CMC) layers exhibit attractive mechanical properties, including a high first cracking stress and a high strain to failure. To achieve these properties, a strong bond must exist between the ceramic and CMC layers; otherwise, delamination will occur readily between the layers. The present study focuses on the delamination resistance of such laminates at ambient and elevated temperatures. The delamination resistance of interfaces that have been subjected to mixed-mode loading has been measured for two different hybrid composites by using edge-notched flexure specimens. At low temperatures, delamination occurs by a process that involves multiple matrix cracking within the CMC layers normal to the fibers, followed by cracking of the matrix parallel to the fibers at or near the ceramic/CMC interface. The corresponding fracture energies are typically in the range of $\sim 100\text{--}300\text{ J/m}^2$ —comparable to the delamination resistance of the CMC itself. At elevated temperatures, delamination occurs via cavitation and rupture of the matrix within the CMC layers at or near the ceramic/CMC interface, with an attendant loss in toughness (to $\sim 10\text{--}30\text{ J/m}^2$). The loss in toughness occurs most rapidly at temperatures that are close to the strain point of the matrix phase; this represents the life-limiting temperature for this class of composites.

I. Introduction

HYBRID laminar composites are fabricated by bonding together alternating layers of a monolithic ceramic and a fiber-reinforced ceramic-matrix composite (CMC) at elevated temperatures, using the matrix phase of the CMC as the bonding agent. A variety of such composites have previously been fabricated and their properties have been characterized.^{1,2} A distinct advantage of this compositing scheme over conventional fiber CMCs is that the constituent layers can be first fabricated independently of each other, following a route that optimizes their respective mechanical properties. Subsequently, the layers can be selected and combined in such a way that the ceramic layers impart a high cracking stress (provided that they are stiff and strong) and the CMC layers provide a high strain to failure and good damage tolerance. This process-

ing route can provide considerable flexibility and tailorability in mechanical properties.

To obtain good structural properties in the hybrid laminates, the layers must be strongly bonded to each other. Laminates with weak interfaces are susceptible to delamination under out-of-plane tensile loading. Under in-plane loading, delamination may also occur, as a result of cracks that form in the monolithic ceramic layers perpendicular to the interfaces and deflect into the interfaces. Such effects are important both in uniaxial tension and in bending. The problem of delamination in weakly bonded systems can be exacerbated in bend tests that are performed on relatively short beams, wherein the shear stresses between the outer and inner loading pins can precipitate shear delamination prior to tensile cracking of the layers. When delamination occurs, the layers bend essentially independently of each other, and each has a linear stress gradient, from tension to compression (provided that the frictional resistance is small). The subsequent tensile failure occurs at a significantly lower load level. Such effects have been demonstrated at ambient temperatures in several different laminates¹⁻³ and are expected to be equally important at elevated temperatures.

Recent studies have demonstrated the importance of delamination in controlling both the flexural and tensile properties of these laminates.^{2,3} At sufficiently high temperatures, their mechanical properties rapidly degrade. This degradation is manifested in the development of extensive delamination along or near the ceramic/CMC interfaces. Evidently, the delamination resistance is strongly temperature dependent. The purpose of the present study is to experimentally examine the temperature dependence of the delamination resistance of two different ceramic/CMC laminates and, in particular, to identify the critical temperature at which the degradation is most acute. It is demonstrated that the delamination resistance steeply decreases at temperatures that roughly correspond to the strain point⁴ of the matrix material within the CMC layers of these laminates.

II. Experimental Procedure

Two different hybrid laminates were studied. Both were fabricated with dense SiC sheets that were $\sim 0.5\text{ mm}$ thick (Hexoloy SA, Carborundum Co., Niagara Falls, NY). The CMC layers⁵ were comprised of either NicalonTM SiC fibers (Nippon Carbon, Tokyo, Japan) within a glass matrix (aluminosilicate glass, Corning 1723, Corning, NY) or of Nicalon fibers in a glass-ceramic matrix (calcium aluminosilicate glass-ceramic, Corning-CAS, Corning). Table I lists the strain, annealing, and

B. N. Cox—contributing editor

Manuscript No. 191281. Received January 13, 1997; approved April 22, 1997.

Supported in part by the DARPA University Research Initiative Program at UCSB under Office of Naval Research Contract No. N00014-92-J-1808. Author WAC was supported by Corning (Corning, NY). Author PGC was supported by the National Science Foundation under Grant No. CMS 94-96209.

^{*}Member, American Ceramic Society.

[†]Now with Corning, Corning, NY.

⁴Usually, the key changes in the flow characteristics of glasses are characterized by the strain point, the annealing point, and the softening point; these correspond to viscosities of $10^{14.5}$, 10^{13} , and $10^{7.6}\text{ P}$, respectively.^{4,5} Physically, the strain point represents the temperature below which the glass behaves essentially elastically, the annealing point is the temperature at which internal stresses are relieved within a period of minutes, and the softening point is the temperature at which the glass readily flows at low stresses.

⁵CMC layers were supplied as unfired fiber-matrix prepreps (Corning).

Table I. Critical Temperatures for CMC Matrices[†]

Matrix	Strain point (°C)	Annealing point (°C)	Softening point (°C)
Glass (Corning 1723)	~665	~710	~910
Glass-ceramic (Corning CAS)	~1140 [‡]	~1245 [‡]	Not available

[†]Data supplied by the manufacturer (Corning, Corning, NY). [‡]Apparent value based on beam-bending viscosity of bulk beams.

softening temperatures of the glass and glass-ceramic matrix materials.[‡] In one laminate system, the SiC sheets were bonded to the CMC layers by using the glass matrix of the CMC, and, in the other, the SiC sheets were bonded to the CMC layers with the glass-ceramic matrix of the CMC. Fabrication details and room-temperature properties of these laminates have been reported elsewhere.²

The delamination resistance, Γ_{IC} , was measured using edge-notched, four-point flexure tests.^{6,7} The laminates were composed of one unidirectional CMC layer that was sandwiched between two ceramic layers (Fig. 1(a)). This geometry was chosen because of its simplicity and because of the need to keep the loading pins in contact with an elastic (nondeforming) medium over the entire range of testing temperatures. Solutions for the delamination strain energy release rate for this three-layer configuration, as well as for the five-layer configuration (Fig. 1(b)), are presented in the Appendix. These solutions were obtained for well-developed delamination cracks for which steady-state conditions apply, as discussed elsewhere.^{6,7} Delamination was assumed to occur along or at close proximity to the interface of the outermost ceramic layer with the first fiber-reinforced layer. The homogeneous ceramic layers were considered to be linear elastic and isotropic, with a Young's modulus E_c , a Poisson's ratio ν_c , and a thickness t_c . On the other hand, the fiber-reinforced layers were considered to be linear elastic and orthotropic, with longitudinal and transverse moduli E_1 and E_2 (respectively), in-plane major and minor Poisson's ratios ν_{12} and ν_{21} (respectively), and a thickness t_f . This thickness of the fiber-reinforced layers was set equal to st , where s is an arbitrary proportionality constant.

As shown in the Appendix and Table A-I, the nondimensional delamination energy release rate is dependent on the bimaterial dissimilarity constant (λ) and the layer-thickness ratio (s) (as given in the Appendix, Eqs. (A-10) and (A-9), respectively). The systems that are under consideration are characterized by a moderate elastic dissimilarity ($\lambda \approx 2.0$). The normalized steady-state energy release rate is plotted against s for various λ values in Figs. A-2 and A-3. The calculations

indicate that, for the systems that are under consideration, firstly delamination is more likely to occur in the specimen configuration in which one fiber layer is sandwiched between two ceramic layers (Fig. 1(a)), relative to the configurations that contain a larger number of alternating layers, such as that which is shown in Fig. 1(b). The analysis that is presented in the Appendix neglects residual stresses, because their effects have been shown³ to be negligible for the systems that are studied herein.

Specimens for testing were cut from larger panels, parallel to the fiber direction. Typical specimen dimensions were ~1.7 mm thick \times 3.6 mm wide \times 50 mm long. One transverse face which exposed the CMC layer was polished to a 1 μ m finish to facilitate observations of damage evolution, as described below. One of the SiC layers was notched using a diamond blade to a depth of ~80% of its thickness (not shown in Fig. 1). Sharp precracks were introduced at the tips of the notches by loading the specimens in three-point bending at room temperature. These cracks did not deflect into the ceramic/CMC interface but did travel across the interface into the CMC layer a short distance (~10–20 μ m) and then arrested (Fig. 2). For the subsequent calculations of the energy release rates, the crack depth was considered to be equal to the thickness of the outer SiC layer, which was measured with a micrometer prior to processing.

The precracked specimens were subsequently loaded in four-point flexure, using inner and outer loading spans of 19 and 39 mm, respectively. The tests were performed at temperatures ranging from ambient to 910°C for the glass-matrix composite and to 1350°C for the glass-ceramic-matrix composite. The effects of oxidation embrittlement that occur in Nicalon-containing CMCs^{8–11} were precluded by testing in a stagnant argon environment. Prior to testing, the furnace was evacuated to $\sim 5 \times 10^{-6}$ torr ($\sim 6.7 \times 10^{-4}$ Pa) and subsequently backfilled and flushed with argon three times. The tests were performed in a hydraulic testing machine (Model 810 with a Centorr vacuum furnace, MTS Systems, Eden Prairie, MN). Prior to loading, the specimens were heated at a rate of 10°C/min to the prescribed temperature and held at that temperature for 10 min. The majority of the tests were conducted at a crosshead displacement rate of 0.05 mm/min. Some of the elevated temperature tests were performed at displacement rates of 0.001, 0.08, and 1.0 mm/min.

Damage evolution was monitored in two ways. At room temperature, the polished surfaces were viewed using *in-situ* stereomicroscopy. At high temperatures, it was accomplished by interrupting the tests, cooling the specimens rapidly to ambient temperature ($>50^\circ\text{C}/\text{min}$), and examining them via either optical microscopy or scanning electron microscopy (SEM). After examination, the specimens were placed back

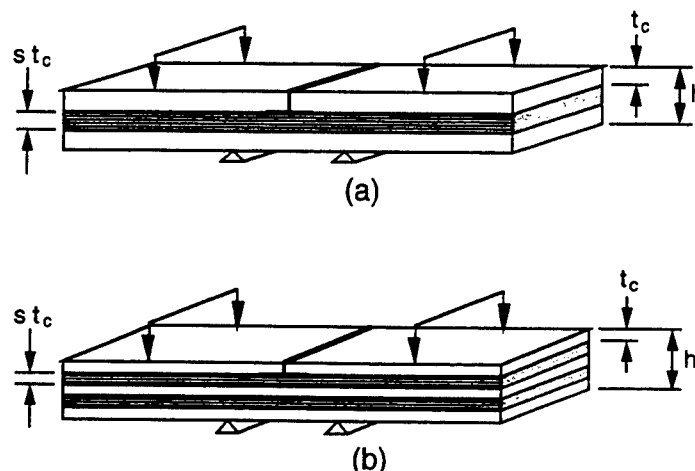


Fig. 1. Testing geometries for beams with (a) one fiber layer sandwiched between two dense ceramic layers (SiC for present experiments) and (b) two fiber layers sandwiched between three ceramic layers.

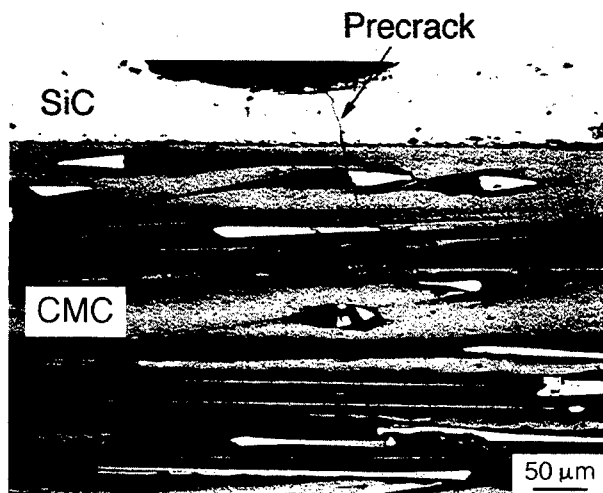


Fig. 2. Micrograph of a precrack emanating from a notch and penetrating into the CMC layer.

into the test fixture and loaded to a higher stress level at the same temperature. This procedure was repeated until the experiment was terminated. The tests were terminated when either the load attained a plateau (steady-state) level, independent of displacement, or the load decreased suddenly (the load decreases were associated with the formation of additional cracks in the SiC). There was no difference in the mechanical behavior of the interrupted and uninterrupted tests. Typically one to three tests were performed for each temperature and loading rate. The critical energy release rates that were associated with delamination were obtained from the plateau loads and the solutions for strain energy release rates (see Appendix). In some instances, a plateau stress was not obtained; instead, a second crack formed in the outer SiC layer, which caused a sudden load decrease. When this occurred, the test was terminated; if a delamination crack had formed prior to the load decrease, the peak load was used to calculate a lower-bound estimate of the steady-state delamination resistance. Changes in the Young's modulus of the CMC with temperature were neglected for these calculations.

After testing, the specimens were examined via optical microscopy and SEM. In some instances, the fracture surfaces were exposed by peeling away the top SiC sheet and examined via SEM.

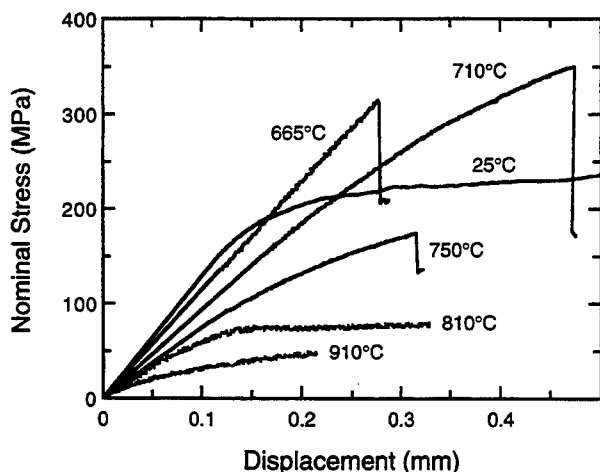


Fig. 3. Nominal-stress-versus-displacement curves for SiC/glass-CMC hybrid composites tested at the temperatures noted.

III. Results and Observations

(1) Laminates with Nicalon/1723 Glass CMC

Figure 3 shows the curves of nominal bending stress versus crosshead displacement for the edge-notched specimens. The curves generally exhibit (i) an initial linear elastic region, (ii) a transient region in which damage occurs ahead of the precrack and the response gradually softens (manifested in a decreasing tangent modulus), and (iii) a plateau (steady-state) stress at which extensive delamination occurs at or near the ceramic/CMC interface. At room temperature, the initial nonlinearity in the stress-displacement response was associated with the formation of matrix cracks that were oriented roughly normal to the interface (Fig. 4(a)). These cracks were typically ~200 μm in length and spaced ~50–100 μm apart. At higher stress levels (approaching the plateau), delamination cracks were observed emanating from the precrack at or near the CMC/ceramic interface. In some instances, the delamination crack followed a somewhat tortuous path through the CMC layer, which resulted in some fiber bridging by inclined fibers (Fig. 4(b)). Similar bridging processes have been observed previously in CMCs under transverse Mode-I loading conditions.¹² However, most of the delamination crack followed a path either along the interface or through the glass matrix near the interface (within ~10 μm). Subsequent examination of the delaminated SiC surfaces revealed remnants of the glass, which was consistent with

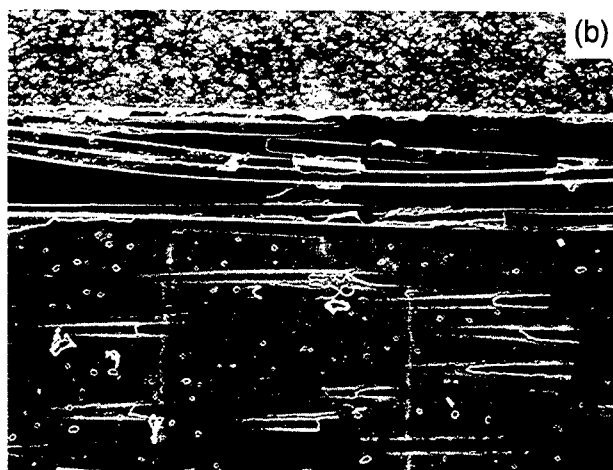
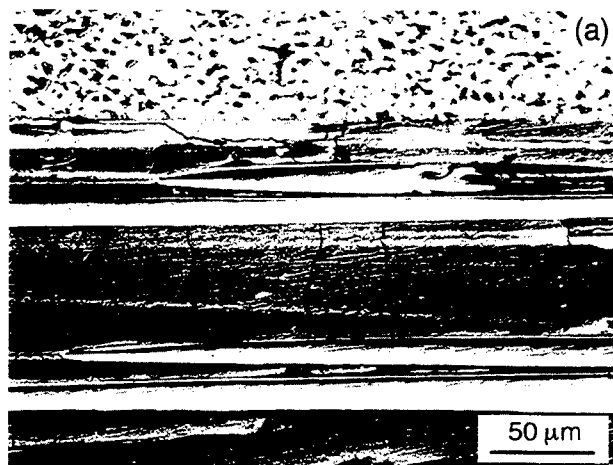


Fig. 4. Delamination in the SiC/Nicalon 1723 glass laminate at room temperature, showing (a) accompanying Mode I cracking in the glass matrix and (b) matrix cracking combined with fiber bridging.

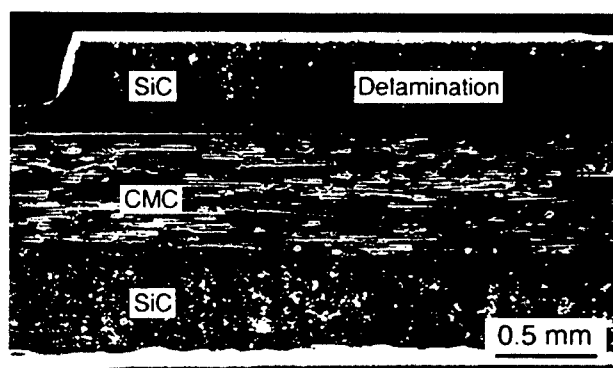


Fig. 5. Low-magnification view of delamination at room temperature.

the observations of the dominant crack propagating partially through the CMC itself rather than along the interface. The delamination resistance was in the range of 140–210 J/m². These values are only slightly lower than those that were measured using double-cantilever-beam specimens (in Mode I) of the CMC itself (~250 J/m²).¹²

At 710°C (the annealing point of the glass), delamination proceeded in a similar fashion (Fig. 5), although the peak stress was considerably higher and no plateau was obtained, because of the formation of an additional crack in the SiC. The delamination resistance that was estimated from the peak load was ~470 J/m²—approximately three times the corresponding room-temperature value. This increase is thought to be due to the reduction in the flow resistance of the glass and the resulting increase in its toughness. Similar behavior was obtained at 750°C, although delamination and cracking of the SiC both occurred at lower stresses.

At 810°C, a well-defined plateau stress was obtained. In this case, there was no evidence of matrix cracks of the type that are shown in Fig. 4(a). Instead, delamination occurred by a process of cavitation and rupture through the glass matrix very near the ceramic/CMC interface (Fig. 6), with a resistance of only ~20 J/m². Similar observations were made for the specimen that was tested at 910°C (the softening point of the glass), although there was more damage within the bulk of the CMC layer (Fig. 7) and the delamination resistance was reduced even more (to ~9 J/m²).

Estimates of the steady-state delamination resistance, which were obtained from the peak loads, are plotted in Fig. 8. The

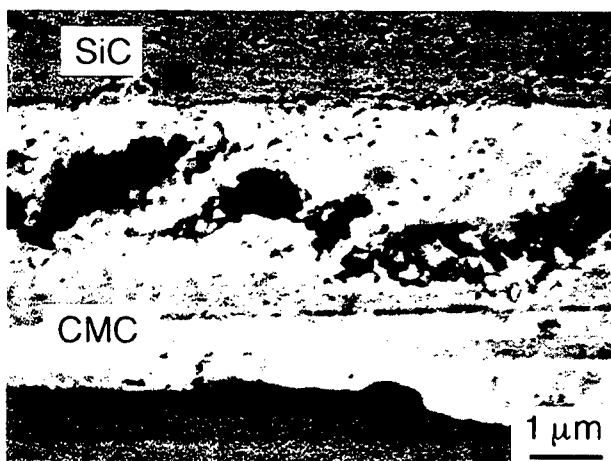


Fig. 6. Micrograph of cavitation near the SiC/glass-CMC laminate interface at 810°C.

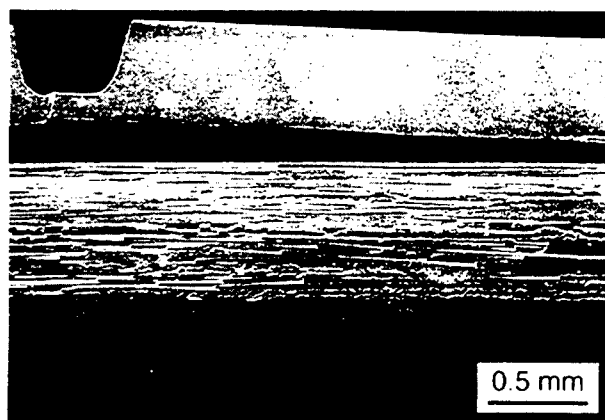


Fig. 7. Damage within the bulk of the CMC layer at 865°C.

data points that are accompanied by arrows indicate that a plateau stress had not been obtained during testing, which suggests that the actual toughness is somewhat higher. Evidently, the interfacial toughness first increases as the temperature increases, up to approximately the annealing point of the glass, but subsequently decreases at higher temperatures, as matrix cavitation becomes the dominant mode of failure.

The effects of the imposed displacement rate (0.001, 0.08, and 1.0 mm/min) on delamination resistance were determined at 865°C, i.e., between the annealing and softening points of the glass matrix. Figure 9 shows the stress-displacement curves and the delamination resistances that have been obtained from these tests. In each of these cases, there was considerable damage in the bulk of the CMC, although failure ultimately occurred at or near the ceramic/CMC interface. The resistance increased approximately an order of magnitude as the displacement rate increased.

(2) Laminates with Nicalon-Glass-Ceramic CMC

Figure 10(a) shows the stress-versus-displacement curves for the laminates that contain the Nicalon-CAS-glass-ceramic CMC. Similar trends were observed in the temperature dependence of the delamination resistance (Fig. 10(b)), although there were some subtle differences in the fracture characteristics. Notably, at low temperatures (<1000°C), delamination proceeded through the CMC itself, at a relatively large distance from the ceramic/CMC interface (~100–300 μm) (Fig. 11). No steady-state toughness was obtained at these temperatures, probably because of the tortuosity of the crack path and the

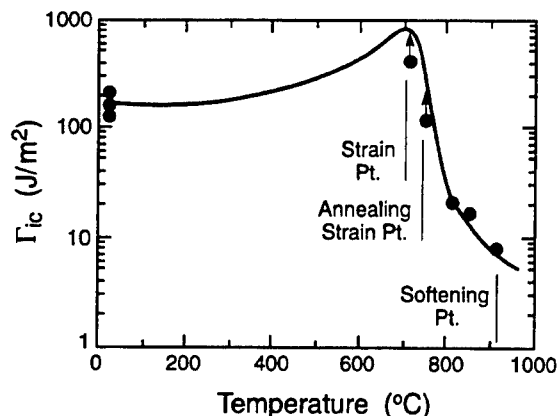


Fig. 8. Variation in delamination resistance with temperature for the SiC/glass-CMC system.

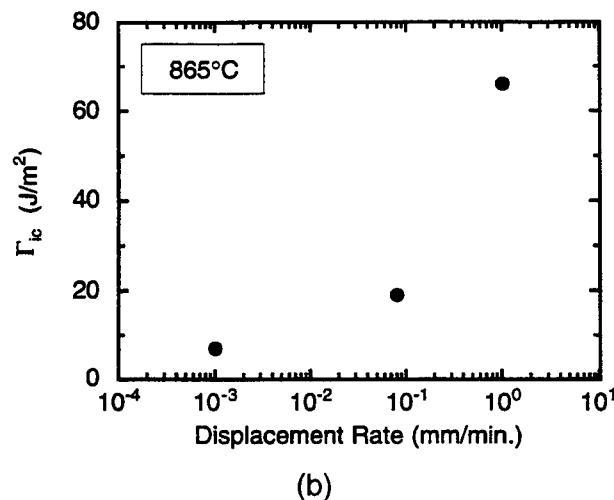
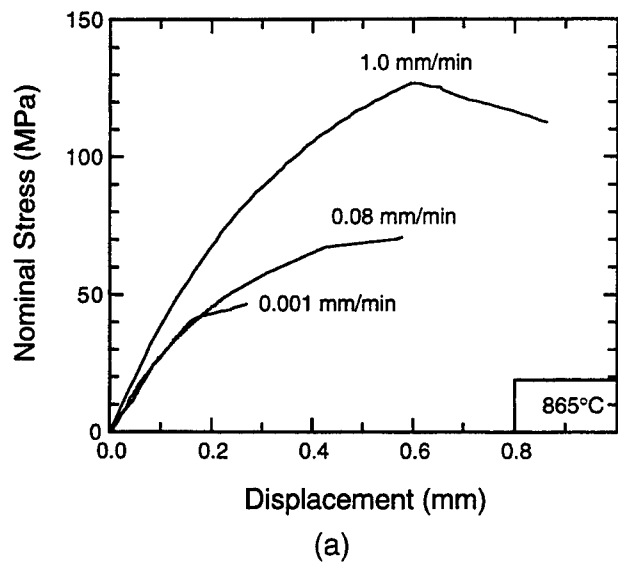


Fig. 9. Effects of loading rate on (a) the nominal-stress-versus-displacement curves for the SiC/glass-CMC laminates and (b) the delamination resistance, at 865°C.

occurrence of fiber bridging, which, in turn, result in an increasing fracture resistance with crack growth (i.e., *R*-curve behavior).

At temperatures in the range of ~1000°–1250°C, delamination occurred “cleanly” along the ceramic/CMC interface, with minimal damage or cracking elsewhere in the CMC, and with some evidence of ductile ligaments spanning the crack. This material is likely the intergranular glass phase that is invariably present in glass-ceramic materials. Relatively well-defined plateau stresses were obtained. The corresponding delamination resistance was essentially constant in this temperature range (~20–25 J/m²). Examination of the SiC surfaces after delamination revealed isolated islands of remnant CAS matrix that was bonded to the SiC (Fig. 12). Similar observations were made on the specimen that was tested at 1350°C, although there was evidence of more cavitation damage within the CAS both near the SiC/CMC interface and within the bulk of the CMC layer (Fig. 13). This test was terminated because of the formation of a crack in the SiC on the compressive side of the specimen. The delamination resistance was estimated to be greater than ~6 J/m².

The effects of loading rate on the delamination resistance at

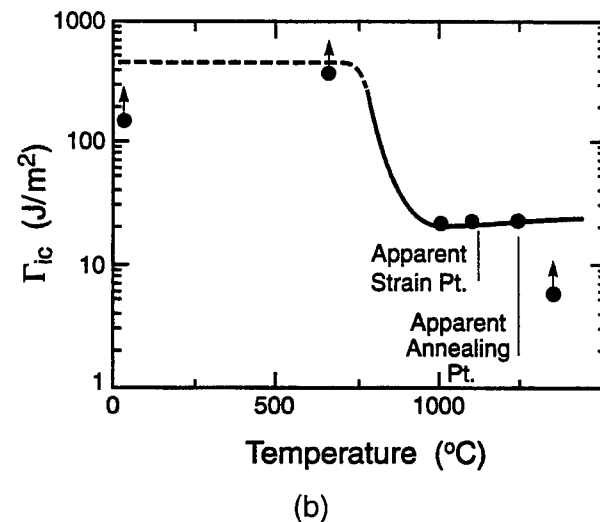
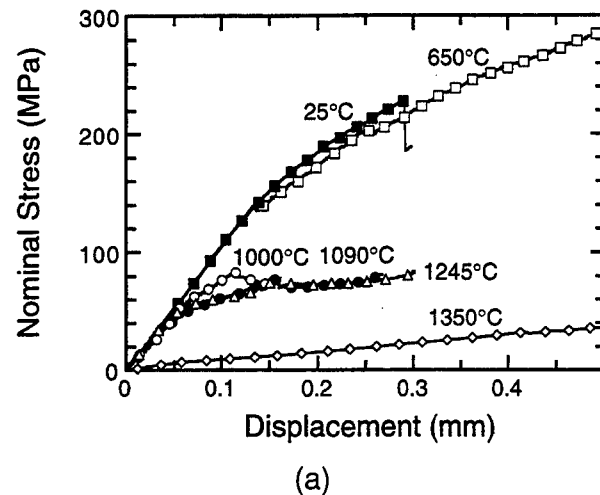


Fig. 10. Effects of test temperature on (a) the nominal-stress-versus-displacement curves and (b) the delamination resistance, for the SiC/glass-ceramic laminates.

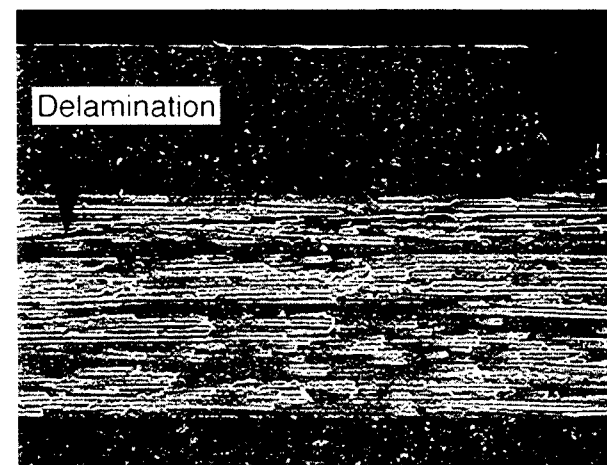


Fig. 11. Delamination in the SiC/glass-ceramic CMC at 650°C.

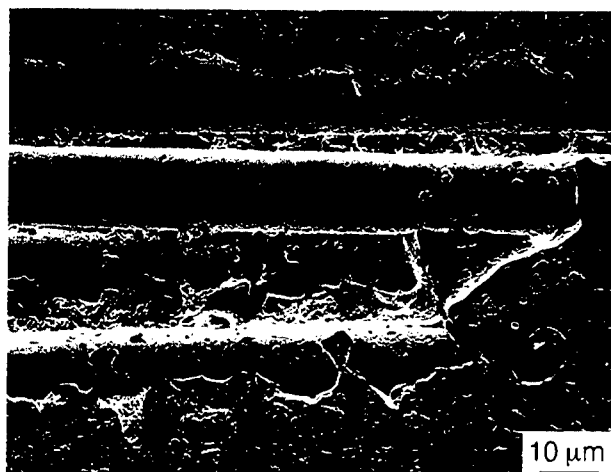


Fig. 12. Micrograph of an island of glass-ceramic matrix attached to the SiC.

a temperature of 1100°C were also examined. Qualitatively, the trends are similar to those of the glass-matrix system (Fig. 14), although two of the three tests were terminated because of cracking of the SiC.

IV. Discussion

The temperature dependence of the fracture mode and the delamination resistance of the SiC/Nicalon 1723 glass CMC can be correlated with the changes in the viscosity of the glass matrix (Table I). The delamination resistance in this system decreases steeply, by more than an order of magnitude, at a temperature near the annealing point. Near this same temperature, the fracture mode changes from one of brittle fracture of the glass matrix with attendant fiber bridging to one of localized flow, cavitation, and rupture within the glass near the SiC/CMC interface. Similar correlations exist for the laminates that contain the CAS–Nicalon CMC, although the transition seems to occur at a slightly lower temperature in relation to the strain point of the CAS. (The absolute temperature of the transition in the CAS laminate is higher, because of the more-refractory nature of the glass-ceramic.) These materials contain some residual glassy phase at the grain boundaries, which seems to control the fracture resistance at higher temperatures; this is believed to be the cause of the lower transition tempera-

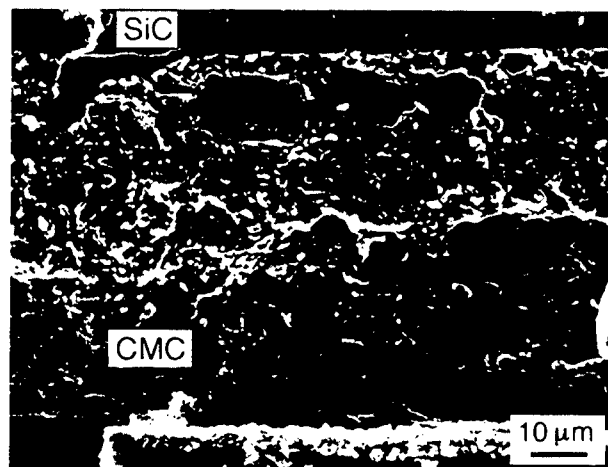


Fig. 13. Cavitation in the SiC/glass-ceramic-CMC laminate near the SiC/CMC interface at 1350°C.

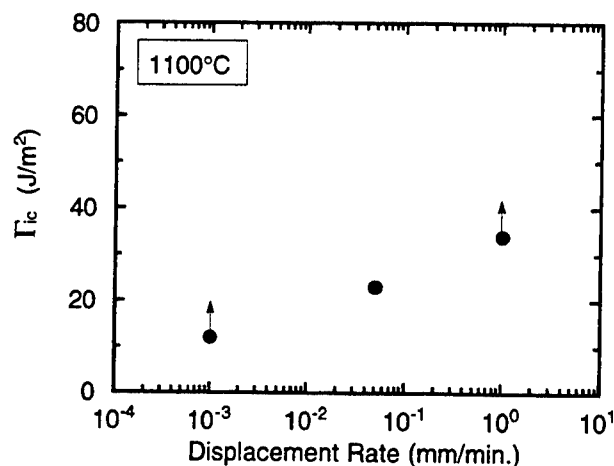


Fig. 14. Effects of loading rate on the delamination resistance of the SiC/glass-ceramic laminates at 1100°C.

ture in the CAS system. It is expected that the transition temperature could be elevated further through the use of a matrix material with a higher degree of crystallinity. In addition, the observed increase in crack-growth resistance with increased loading rate is consistent with reported observations of sub-critical crack growth that is caused by creep cavitation in glass ceramics,¹³ which, again, is consistent with the role of the viscosity of the matrix phase.

Some of the edge-notched flexure tests did not yield definitive values for the delamination resistance, which is a result of cracking of the ceramic sheets prior to the attainment of a steady state. Such tests provide only a lower-bound estimate of the delamination resistance. The incidence of this cracking does not seem to correlate with the test temperature or other characteristics of the test procedure or material properties and is probably associated with the stochastic nature of the strength of the ceramic.

The calculated values of delamination resistance are based on the implicit assumption that delamination occurs in a planar fashion at the SiC/CMC interface and that the zone of damage is confined to a small region that is adjacent to the interface. In some instances, the zone of microcracks extends ~200 μm into the CMC; in others, the delamination crack deviates gradually from the plane of the interface, by as much as ~300 μm. These effects may become important when the corresponding lengths become comparable to the layer thickness (~0.5–1 mm in the present experiments). The magnitude of those effects can be probed experimentally by measuring the delamination resistance in thicker test specimens.

V. Conclusions

The delamination resistance of the hybrid laminates is sensitive to the matrix phase within the CMC, because this is the bonding agent between the ceramic and the CMC layers. For

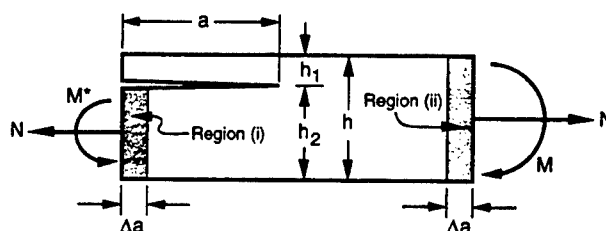


Fig. A-1. Schematic of a symmetric half of delaminated composite beam subjected to combined axial loading and bending.

Table A-I. Normalized Laminate Stiffnesses

Laminate stiffness [†]	Configuration in Fig. 1(a)		Configuration in Fig. 1(b)	
	Region (i)	Region (ii)	Region (i)	Region (ii)
\hat{A}_{11}	$\frac{1+s\lambda}{s+2}$	$\frac{2+s\lambda}{s+2}$	$\frac{2(1+s\lambda)}{3+2s}$	$\frac{3+2s\lambda}{3+2s}$
\hat{B}_{11}	$\frac{s}{2} \left[\frac{1-\lambda}{(s+2)^2} \right]$	0	$\frac{s(1-\lambda)}{(3+2s)^2}$	0
\hat{D}_{11}	$\frac{1}{12} \left[\frac{1}{(s+2)^3} \right]$	$\frac{1}{12} \left[\frac{1}{(s+2)^3} \right]$	$\frac{1}{3} \left[\frac{1}{(3+2s)^3} \right]$	$\frac{1}{12} \left[\frac{1}{(3+2s)^3} \right]$
	$\times (\lambda s^3 + 3s^2 + 3s\lambda + 1)$	$\times [\lambda s^3 + 6(1+s)^2 + 2]$	$\times [3s(1+\lambda)(1+s) + 2(1+s^3\lambda)]$	$\times [8\lambda s^3 + 12s^2(2+\lambda) + 6s(8+\lambda) + 27]$

[†]The equations for \hat{A}_{11} , \hat{B}_{11} , and \hat{D}_{11} are as follows: $\hat{A}_{11} = A_{11}/(Q_c h)$, $\hat{B}_{11} = B_{11}/(Q_c h^2)$, and $\hat{D}_{11} = D_{11}/(Q_c h^3)$, where $Q_c = E_c/(1-\nu_c^2)$.

the hybrid laminates that contain the glass-matrix CMC, the delamination resistance can be correlated with the viscosity of the glass matrix; it is relatively insensitive to temperature, up to the annealing point of the glass matrix, and subsequently diminishes rapidly with further increases in temperature. For the laminates that contain the more-refractory glass-ceramic, the delamination resistance is maintained to higher temperatures, approaching the strain point of the glass-ceramic. Beyond these temperatures, the failure mode changes to one that involves flow, cavitation, and rupture, which results in substantial reductions in the delamination resistance. In this regime, the resistance is sensitive to the loading rate, which is a consequence of the viscoplastic nature of the matrix phase.

APPENDIX

The steady-state strain energy release rate, G_{ss} , for a bimaterial specimen that contains one layer of each material is found elsewhere.^{3,7} Solutions for two other beam geometries that are of greater interest to the present work (see Fig. 1) are presented here. The G_{ss} value is obtained from the difference in the strain-energy densities ahead of and behind the crack tip, using a cutting and pasting operation to simulate virtual crack exten-

sion (Fig. A-1). It is expressed as the sum of the strain energy release rate functions that are produced by the applied moment (G_M), the axial forces (G_N), and the coupled effects of the two (G_{NM}). The results are

$$G_{ss} = \frac{S^2 h^2 \cos^2 \Phi}{3\bar{D}} (G_N \tan^2 \Phi + G_{NM} \tan \Phi + G_M) \quad (A-1)$$

where

$$G_M = \frac{1}{\left(1 - \frac{\hat{B}_{11}^2}{\hat{A}_{11}\hat{D}_{11}}\right)_i} \left(\frac{1}{8\hat{D}_{11}} \right)_i - \left[\frac{1}{8\hat{D}_{11}} \right]_{ii} \quad (A-2)$$

$$G_N = \frac{1}{\left(1 - \frac{\hat{B}_{11}^2}{\hat{A}_{11}\hat{D}_{11}}\right)_i} \left(\frac{1}{8} \right) \left(\frac{1}{\hat{A}_{11}} + 2\bar{y} \frac{\hat{B}_{11}}{\hat{A}_{11}\hat{D}_{11}} + \bar{y}^2 \frac{1}{\hat{D}_{11}} \right)_i - \left(\frac{1}{8\hat{A}_{11}} \right)_{ii} \quad (A-3)$$

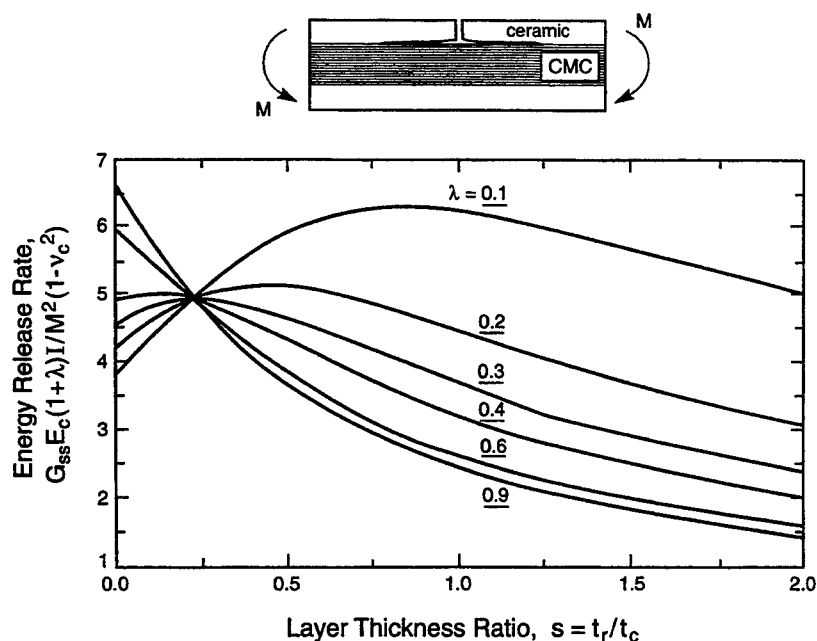


Fig. A-2. Variation in the normalized energy release rate, \hat{G} , with the layer-thickness ratio s (equal to t_r/t_c) and the elastic dissimilarity constant, λ , in the range of 0.1–0.9. Results were obtained assuming delamination of the top ply in a three-layer composite, as shown in the schematic above the graph.

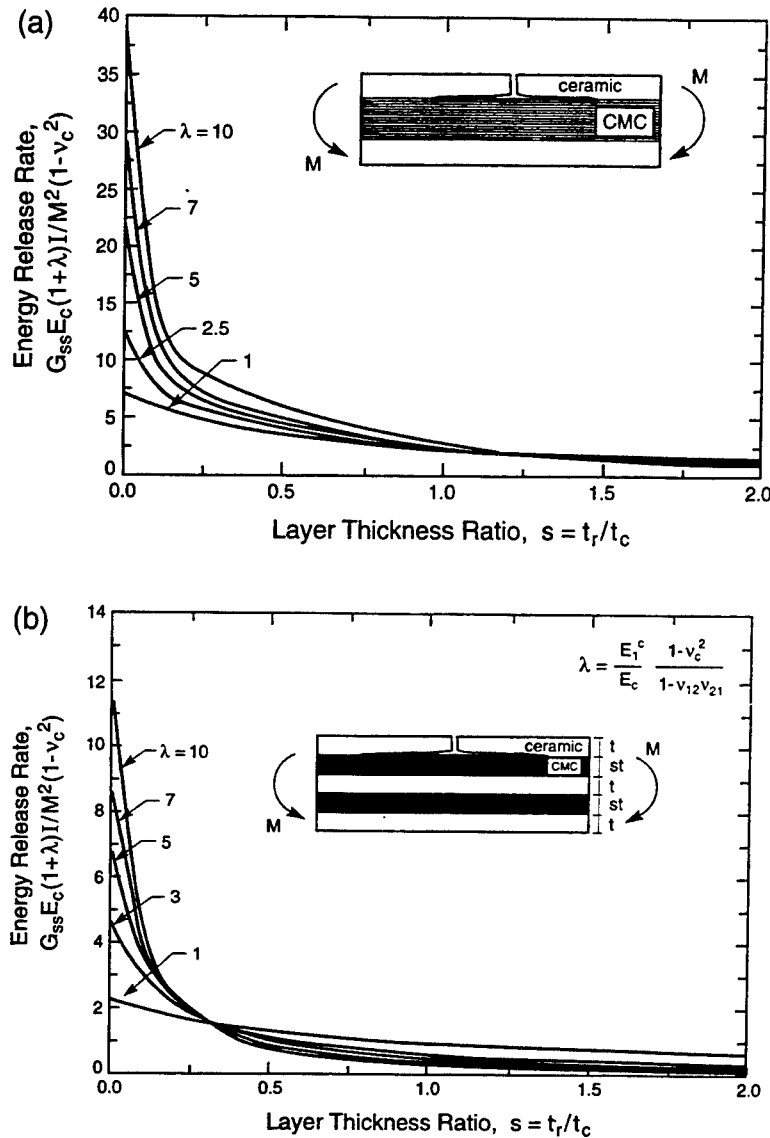


Fig. A-3. Variation in the normalized energy release rate, \hat{G} , with the layer-thickness ratio s (equal to t_r/t_c) for (a) a three-layer composite and (b) a five-layer composite. Results were obtained using elastic dissimilarity constant, λ , values in the range of 1.0–10.0.

$$G_{NM} = \frac{1}{\left(1 - \frac{\hat{B}_{11}^2}{\hat{A}_{11}\hat{D}_{11}}\right)_i} \left(\frac{1}{4}\right) \left(\frac{\hat{B}_{11}}{\hat{A}_{11}\hat{D}_{11}} + \bar{y} \frac{1}{\hat{D}_{11}}\right)_i \quad (\text{A-4})$$

$$\bar{y} = \frac{\xi}{2(1 + \xi)} \quad (\text{A-5})$$

$$\bar{D} = \left(\frac{E_c}{1 - \nu_c^2}\right) \frac{h^2}{12} \quad (\text{A-6})$$

$$S = \frac{M}{h \cos \Phi} = \frac{Pl}{2bh \cos \Phi} \quad (\text{A-7})$$

$$\xi = \frac{h_1}{h_2} \quad (\text{A-8})$$

$$s = \frac{t_r}{t_c} \quad (\text{A-9})$$

$$\lambda = \frac{E_1^r}{E_c} \left(\frac{1 - \nu_c^2}{1 - \nu_{12}^r \nu_{21}^r} \right) \quad (\text{A-10})$$

$$\tan \Phi = \frac{Nh}{M} \quad (\text{A-11})$$

Here, E_c and ν_c are the Young's modulus and Poisson's ratio, respectively, of the precracked (ceramic) layer; P is the plateau load, l the distance between the inner and outer loading points, b the specimen width, and h the specimen height. The thickness of the uncracked and cracked layers are, respectively, h_1 and h_2 , and t_c and t_r are the thickness of the ceramic and CMC-reinforced layers, respectively. M is the applied moment, and N is the applied normal force; the normalized stiffnesses— \hat{A}_{11} , \hat{B}_{11} , and \hat{D}_{11} —for the two regions that are illustrated in Fig. A-1 are found in Table A-1. Some typical results are plotted in Figs. A-2 and A-3.

References

- ¹C. A. Folsom, F. W. Zok, F. F. Lange, and D. B. Marshall, "Mechanical Behavior of a Laminar Ceramic/Fiber-Reinforced Epoxy Composite," *J. Am. Ceram. Soc.*, **75** [11] 2969–75 (1992).

²W. A. Cutler, F. W. Zok, and F. F. Lange, "Mechanical Behavior of Several Hybrid CMC Laminates," *J. Am. Ceram. Soc.*, **79** [7] 1825-33 (1996).

³W. A. Cutler, "Processing and Mechanical Behavior of High Temperature Hybrid Laminated Composites"; Ph.D. Dissertation. University of California. Santa Barbara, CA, 1995.

⁴(a) "Standard Test Method for Softening Point of Glass," ASTM Designation C 338-93. *1996 Annual Book of ASTM Standards*, Vol. 15.02, pp. 100-102. American Society for Testing and Materials, Philadelphia, PA. (b) "Standard Test Method for Annealing Point and Strain Point of Glass by Beam Bending," ASTM Designation C 598-93. *ibid.*, pp. 154-58.

⁵D. C. Boyd and D. A. Thompson, "Glass," *Kirk-Othmer: Encycl. Chem. Technol.*, 3rd Ed., **11** [3] 807-80 (1980).

⁶P. G. Charalambides, H. C. Cao, J. Lund, and A. G. Evans, "Development of a Test Method for Measuring the Mixed Mode Fracture Resistance of Bimaterial Interfaces," *Mech. Mater.*, **8**, 269-83 (1990).

⁷P. G. Charalambides, J. Lund, A. G. Evans, and R. M. McMeeking, "A Test Specimen for Determining the Fracture Resistance of Bimaterial Interfaces," *J. Appl. Mech.*, **56**, 77-82 (1989).

⁸T. Mah, M. G. Mendiratta, A. P. Katz, R. Ruh, and K. S. Mazdhyasni, "High-Temperature Mechanical Behavior of Fiber-Reinforced Glass-Ceramic-Matrix Composites," *J. Am. Ceram. Soc.*, **68** [9] C-248-C-251 (1985).

⁹J. J. Brennan, "Interfacial Characterization of Glass and Glass-Ceramic Matrix/Nicalon SiC Fiber Composites," *Mater. Sci. Res.*, **20**, 546-60 (1986).

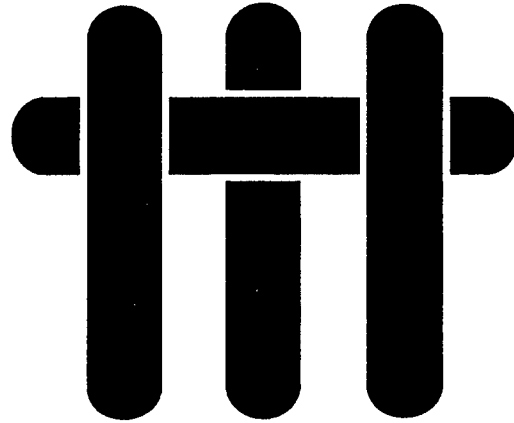
¹⁰L. Filipuzzi, G. Camus, R. Naslain, and J. Thebault, "Oxidation Mechanisms and Kinetics of 1D-SiC/C/SiC Composite Materials: I, An Experimental Approach," *J. Am. Ceram. Soc.*, **77** [2] 459-66 (1994).

¹¹F. E. Heredia, J. C. McNulty, F. W. Zok and A. G. Evans, "Oxidation Embrittlement Probe for Ceramic-Matrix Composites," *J. Am. Ceram. Soc.*, **78** [8] 2097-100 (1995).

¹²S. M. Spearing and A. G. Evans, "The Role of Fiber Bridging in the Delamination Resistance of Fiber-Reinforced Composites," *Acta Metall. Mater.*, **40** [9] 2191-99 (1992).

¹³K. S. Chan and R. A. Page, "Origin of the Creep-Crack Growth Threshold in a Glass-Ceramic," *J. Am. Ceram. Soc.*, **75** [3] 603-12 (1992). □

M A T E R I A L S



LIMIT STRESS CONDITIONS FOR WEAKLY BONDED FIBER COMPOSITES SUBJECT TO TRANSVERSE BIAXIAL TENSILE LOADING

Z.-Z. Du* and F.W. Zok

Materials Department
University of California
Santa Barbara, California 93106

*Now at Hibbitt, Karlsson and Sorensen, Inc.
1080 Main St.
Pawtucket, RI 02860

Submitted to International Journal of Solids and Structures

April, 1997

Revised September, 1997

ABSTRACT

This paper focuses on the limit stress conditions of metal matrix composites reinforced with weakly-bonded continuous fibers subject to general biaxial tensile loading normal to the fiber direction. The study is performed using unit cell models, with the fibers being treated as either perfectly rigid or perfectly compliant. The cells are first analyzed using finite element methods (FEM) and the results used to construct yield surfaces in stress space. A simpler analytical model based on net-section yielding is also developed and the results compared with the ones obtained by FEM. Though the latter approach provides a reasonable first order estimate of the limit stress, it generally underestimates the values obtained from the FEM calculations: a result of stress gradients acting along the failure plane. The effects of stress gradients are incorporated into the net-section yielding model through an analytical solution based upon the slip line field around a circular hole. This approach yields analytical predictions which are generally in very good agreement with the FEM results.

1. INTRODUCTION

The plastic flow and creep properties of continuous fiber-reinforced metal matrix composites (MMCs) exhibit varying degrees of anisotropy, depending on the properties of the constituents (matrix, fibers and interfaces) and the fiber architecture. In unidirectionally reinforced materials, the properties measured along the axis of the fibers are usually dominated by the fibers and are superior to those of the matrix alloy alone (Jansson et al., 1991; Weber, et al., 1994). In contrast, under transverse or shear loading, the properties are matrix-dominated. Even in the best of circumstances, wherein the fibers are well-bonded to the matrix, the contributions from the fibers are relatively small except at very high fiber volume fractions ($\geq 50\%$). This type of behavior is exemplified by the Al/Al₂O₃ and Al/B systems (Jansson and Leckie, 1992). In systems comprised of SiC fibers in Ti alloys, the interfaces between the fibers and the matrix are weak because of the presence of C coatings. In these systems, the transverse and shear properties fall below those of the matrix alone (Jansson et al., 1991; Jansson and Leckie, 1994; Weber et al., 1995). Typically, the ratio of axial to transverse tensile strengths in Ti/SiC composites at ambient temperature is ~ 4 . At elevated temperatures, the matrix strength decreases, causing an increase in the anisotropy of the composite strength (Weber et al., 1995). The strength anisotropy has important implications regarding the design of structural components using MMCs, particularly under conditions of multiaxial stress. Indeed, this anisotropy represents one of the most severe drawbacks associated with this class of composite and may limit the use of MMCs in structural applications.

The transverse flow and creep properties of *well-bonded* fiber-reinforced MMCs under uniaxial loading have been studied by numerous investigators through calculations based on finite element methods (FEM) (Teply and Dvorak,

1988; Brockenbrough and Suresh, 1990; Brockenbrough et al., 1991; Nakamura and Suresh, 1993; Zahl et al., 1994; Du and McMeeking, 1994). A relatively comprehensive series of numerical results is documented in Zahl et al. (1994). One of the key results emanating from these studies is that, at sufficiently large strains, the ratio of the composite flow stress, $\sigma_c(\epsilon)$, to that of the matrix, $\sigma_m(\epsilon)$, reaches a constant (steady-state) value, dependent only of the fiber volume fraction, f , and the hardening characteristics of the matrix. The transient response preceding this steady-state persists for strains that are typically in the range of $\sim (1-5) \epsilon_0$, with ϵ_0 being the yield strain of the matrix. For modest values of f (< 0.35), the steady state strength ratio is given approximately by $\sigma_c(\epsilon)/\sigma_m(\epsilon) \approx 2/\sqrt{3} \approx 1.15$; the main role of the fibers is to constrain the matrix from contracting along the fiber direction, leading to conditions of plane strain. Substantial elevations in strength are only obtained for high fiber volume fractions ($f > 0.5$).

The influence of thermal residual stress on the transverse tensile response of well-bonded systems has been examined also (Nakamura and Suresh, 1993, Böhm and Rammerstorfer, 1991). A general result is that the steady-state strength ratio, $\sigma_c(\epsilon)/\sigma_m(\epsilon)$, is *independent* of the thermal stress; the thermal stress only influences the transient response. The magnitude of the transient effect depends on the thermal misfit strain and the flow and hardening characteristics of the matrix.

Limited numerical studies have been conducted for materials with *weak interfaces*, subject to uniaxial tensile loading transverse to the fibers (Nimmer et al., 1991; Gunawardena et al., 1993). In these cases, the composite strength is less than the yield strength of the matrix alone. The effects of thermal residual stress and frictional sliding along the fiber/matrix interfaces have also been considered. In cases where the matrix thermal expansion coefficient, α_m , exceeds that of the fibers, α_f (a characteristic of most MMCs), the interface experiences a residual normal compression following cooling from the processing temperature. Consequently, the

remote stress required to separate the interface is higher than that in a residual stress-free composite. Comparisons of the FEM calculations with experimental data on a Ti/SiC composite indicate that the condition for interface separation is one in which the local normal stress across the interface becomes positive (Gunawardena et al., 1993). This result suggests that the interfaces have essentially zero normal strength and the fibers are held in place by the residual compression stress acting across the interface. Clearly the residual stress alters the initial transient part of the stress-strain response, but, as in the case of well-bonded systems, the steady-state plastic response is unaffected. Frictional sliding at the interface appears to play only a minor role in the flow response. FEM calculations have been conducted using a Coulomb friction law to characterize the sliding resistance of the interface and indicate that the flow response of the composite remains essentially unchanged for friction coefficients in the range, $\mu = 0$ to 1 (Gunawardena et al., 1993).

The models of the flow response of continuous fiber composites have been limited to *uniaxial* loading. In practice, however, these materials are expected to be subjected locally to multiaxial stress states, even in components that are nominally loaded principally in just one direction. The multiaxiality arises because of stress concentrations, such as those present at regions where the components are joined to monolithic alloys. To motivate the current work, one specific example is cited. Ti/SiC composites are being considered for use in actuator piston rods for aircraft engines. The rods are comprised essentially of a hollow thin-walled tube of unidirectionally reinforced Ti/SiC. The tubes are clad on both the inside and the outside with layers of monolithic Ti, and the ends of the tubes are attached to monolithic Ti end fittings of rather complex shape. Though the loads are applied principally along the tube axis, there is some degree of bending, which causes tensile hoop and radial stresses near the ends of the tube (Du, et al., 1996). An

understanding of the effect of this triaxiality on the flow and fracture response of Ti/SiC composites is needed in order to produce reliable designs.

The current work represents an initial attempt at developing models and solutions for plastic failure of weakly-bonded fiber reinforced MMCs subject to multiaxial stress states. In this paper, the scope is restricted to *biaxial tensile loading transverse to the fiber direction* in unidirectional materials. Fully multiaxial (3D) conditions have yet to be addressed. The emphasis is on the *plastic limit stress conditions*; no consideration is given to other failure modes. As such, the predicted failure stresses are expected to be upper bounds to the stresses that composites may support in actual components. The effects of the fiber volume fraction, the spatial arrangement of the fibers, and the direction of loading in relation to the fiber arrangement are considered. The results are based on both FEM and analytical calculations. The results are used to construct the yield surfaces using stress parameters that characterize the mean and deviatoric components of the stress state.

2. CELL MODELS AND CONSTITUENT PROPERTIES

The flow properties of the composites are examined through the analysis of unit cell models. For this purpose, the fibers are assumed to be distributed on a periodic array and the loading directions, relative to the directions characterizing the symmetry of the array, are prescribed. The periodic idealization is a good representation of most Ti/SiC composites wherein the fibers are distributed uniformly through the matrix; it may be a less accurate representation of composites produced by melt infiltration because of the more random fiber distribution. Figure 1 shows the periodic nature of the fibers in a typical Ti/SiC composite.

The present study focuses on unit cells derived from the hexagonal and square fiber arrangements. Two typical unit cells and finite element grids for a fiber

volume fraction, $f = 0.35$, are shown in Fig. 2. Similar cells were constructed for fiber volume fractions of $f = 0.25$ and 0.50 . This range of volume fractions brackets the range found in all Ti/SiC composites of commercial interest. Uniaxial tension was simulated by imposing uniform tensile displacements on one pair of cell faces and calculating the corresponding average surface traction, either σ_{xx} or σ_{yy} . The faces normal to the applied stress were required to remain planar in order to maintain compatibility with adjacent cells. Moreover, plane strain conditions were imposed in the z -direction (along the fiber axis). For the square array, tensile loading on either pair of cell faces yields identical results because of the symmetry of the cell. In contrast, for the hexagonal array, the two loading configurations yield different results, since the axes that characterize the symmetry of the cell do not coincide with the principal loading axes. The two loading configurations are subsequently distinguished from one another by the directions of loading in relation to the closed-packed direction (CPD) of the fibers; in Fig. 1(b), loading along the x -axis is *normal* to the CPD whereas loading along the y -axis is *parallel* to the CPD.

Biaxial loading was simulated by prescribing the boundary displacements on the two orthogonal directions to be proportional to one another and subsequently calculating the limiting values of the two stress components, σ_{xx} and σ_{yy} . The ratio of displacements was varied in order to obtain a range of stress ratios, σ_{xx}/σ_{yy} .

Most of the calculations were based on the assumption that the matrix is elastic, perfectly-plastic, with Young's modulus, E_m , Poisson's ratio, ν , and yield stress, σ_o and yield strain, $\epsilon_o = \sigma_o/E_m$. In some cases, the matrix response was assumed to follow the Ramberg-Osgood flow law. For uniaxial tensile loading, this law is given by

$$\epsilon/\epsilon_o = \sigma/\sigma_o + \alpha(\sigma/\sigma_o)^n \quad (1)$$

where σ and ϵ are the axial stress and strain, respectively; α is a numerical coefficient, taken to be $3/7$; n is the hardening exponent; σ_0 is a reference stress and ϵ_0 is the corresponding reference strain. Eqn. (1) was generalized to multiaxial stress states using small strain J_2 flow theory. For deformations much greater than the elastic ones, the stresses and strains at a material point increase in proportion to each other under proportional loading and the resulting solution is equivalent to that for J_2 deformation theory. The resulting strain field is then the same as the strain *rate* field for a creeping material with a power-law creep exponent of n . This equivalence implies that the solutions obtained for power-hardening are also applicable to power-law creep (Odqvist, 1966).

The fibers are treated in one of two ways: either perfectly rigid (with a Young's modulus, $E_f = \infty$) or perfectly compliant ($E_f = 0$). The latter assumption is equivalent to treating the fibers as holes. For cases where the fibers are rigid, the interface is assumed to have zero normal tensile strength.

In the light of the introductory comments regarding the absence of any effects of thermal stress on the limit stress conditions, the thermal stresses are not incorporated into the analysis. Despite this simplification, the present results for the transient response are expected to be applicable at high temperatures and low stresses, wherein the thermal stresses have adequate opportunity to relax through matrix creep. In contrast, the predicted transient at low temperatures may be subject to some uncertainty, depending on the magnitude of the thermal misfit strain.

Finite element calculations were performed using a commercial code, ABAQUS (1994), on a Convex mainframe. The matrix was discretized using isoparametric second-order hybrid elements with reduced integration in order to avoid problems of mesh-locking associated with incompressible deformation. For the cases where the fibers were perfectly rigid, interface elements were introduced to simulate the contact between the matrix and the fibers.

The cells were also analyzed using an analytical approach based on net-section yielding. For this purpose, the potential planes along which yielding can occur were first identified from the FEM results. Figs. 1(c) and (d) show schematics of the approximate locations of these planes within the unit cells. For the hexagonal array, three such planes exist, denoted by A, B and C. Analogous planes exist for the square array, denoted D, E and F, though only two of them are unique (D and E). The average normal and shear stresses acting on each of these planes were then calculated in terms of the applied stresses assuming that the stresses are distributed uniformly along these planes. Finally, the local stresses were combined with the Mises yield criterion for plane strain conditions in order to obtain the limiting values of the remote stress components. This approach generally leads to conservative estimates of the limit stress; stress gradients along the expected failure planes cause an elevation in the limit stress. This elevation can, in turn, trigger plastic failure along *other* planes.

The effects of the stress gradients have been incorporated explicitly into the net-section yielding model using the slip-line solution for yielding ahead of a circular notch. The same result is obtained by considering the expansion of a thick-walled circular cylinder subject to uniform biaxial tension. It will be demonstrated that the results predicted by the modified version of this model are generally in excellent agreement with the FEM results. This approach is described in further detail in Sections 3 and 4.

3. FEM RESULTS

3.1 Uniaxial Tension

Figure 2(a) shows the transverse stress-strain curves for composites with three different fiber volume fractions in a hexagonal array, with the load applied

parallel to the CPD. The solid and dashed lines are the results obtained for composites with rigid and perfectly compliant fibers, respectively. The corresponding results for the hexagonal array loaded *normal* to the CPD and the square array are given in Figs. 2(b) and (c), respectively. For the hexagonal arrays, the limiting strength values are only slightly higher for composites containing rigid fibers than for those containing perfectly compliant fibers (by $\sim 2\text{-}14\%$), whereas for the square arrangements they are essentially *independent* of the fiber modulus.

A summary of the uniaxial limit strengths is presented in Fig. 3. The results indicate that the strengths decrease approximately linearly with increasing fiber volume fraction and reach values of $\sim (0.2\text{-}0.3)$ at a volume fraction, $f = 0.5$. For the hexagonal arrays, the limit strengths are higher when the load is applied normal to the CPD than when it is applied parallel to the CPD. This trend is contrary to the one observed for composites with strongly bonded interfaces, wherein the transverse strength is found to be nearly independent of the loading direction (Zahl et al., 1994).

To gain further insight into the effects of the fiber modulus and the fiber arrangement on the flow response of the composite, the evolution of matrix plasticity within the composite has also been calculated. Figure 4(a) illustrates this behavior in a composite with rigid fibers in a hexagonal arrangement loaded *normal* to the CPD and a fiber volume fraction of 0.35. Figure 4(b) shows the corresponding results for a composite with perfectly compliant fibers. In both cases, plasticity initiates in the equatorial regions around the fibers. As the applied strain is increased, the plastic zone initially spreads in both the radial and hoop directions around the fibers. For the composite with perfectly compliant fibers, the plasticity subsequently spreads along the ligament joining nearest-neighbor fibers, at an angle of $\sim 30^\circ$ to the loading direction. Once this ligament is completely yielded, the limit stress is attained. In the composite with rigid fibers, the plasticity initially spreads in a similar manner. However, the additional constraint associated with the fiber

causes the plasticity to also spread in the direction normal to the loading axis, ultimately forming two plastic ligaments: one at 30° and the other at 90° to the loading axis. The same trends in the evolution of the plasticity were obtained for the other fiber volume fractions, $f = 0.25$ and 0.5 . For the composites loaded *parallel* to the CPD, similar trends were again observed, with the exception that the plasticity remains confined to the ligaments between nearest-neighbor fibers, at 60° to the loading direction (Fig. 4(c)); it does not spread extensively along the plane normal to the loading direction.

Typical results for the square fiber arrangements are shown in Fig. 4(d). The plasticity again initiates in the equatorial regions around the fibers. For the high volume fractions, $f = 0.35$ and 0.5 , it subsequently spreads normal to the loading direction, forming a plastic ligament between adjacent fibers. Essentially identical behavior is obtained for both rigid and perfectly compliant fibers, in accord with the strong similarities in the limit stresses presented in Fig. 2(c). For the lowest volume fraction, $f = 0.25$, the plasticity initially spreads along the normal plane in a similar fashion. However, as the tip of this plastic zone approaches the cell boundary, a plastic zone develops and spreads along the cell diagonal (at $\sim 45^\circ$ to the loading direction). Plastic failure ultimately occurs along this inclined plane.

In a subsequent section, an analytical model of net-section yielding is developed, based upon the assumption that the stresses are uniformly distributed along the potential failure planes. To assess the validity of this assumption, the distributions in stress have been calculated using FEM. Some representative results for the square fiber array with $E_f = \infty$ are shown in Fig. 5. For the two highest volume fractions, $f = 0.35$ and 0.5 , the matrix separates from the fibers along the equatorial plane ($x = 0$) and, consequently, the transverse stress, σ_{yy} , in the matrix at this point is zero and the longitudinal stress is equivalent to the plane strain flow stress, $(2/\sqrt{3}) \sigma_0$. However, at positions away from the interface along the plane $x = 0$,

the transverse stress is tensile, increasing approximately linearly with position, y/R . In order for the effective stress to remain at the flow stress, the corresponding longitudinal stress σ_{xx} along this plane follows a similar increasing trend with y/R . Similar results are obtained from both $f = 0.35$ and 0.5 . For $f = 0.25$, the interface along the equatorial plane remains intact at the limit stress. At this point, the transverse stress in the matrix is compressive ($\sim -0.15 \sigma_0$) and thus the longitudinal stress is below the plane strain flow stress: $\sim (2\sqrt{3} - 0.15) \sigma_0 \approx \sigma_0$. However, both σ_{xx} and σ_{yy} increase with the distance, y/R , in essentially the same way as they do for the higher volume fractions. One notable exception is the slight decay in σ_{xx} and σ_{yy} at positions close to the cell boundary ($y/R \approx 1.8$). This decay is associated with the small elastic region along this plane. As noted earlier, plastic failure ultimately occurs along an inclined plane, at $\sim 45^\circ$ to the loading direction, not along the $x = 0$ plane.

The separation of the interfaces at the two highest fiber volume fractions and the stress gradients along the $x = 0$ plane are associated with the imposed boundary conditions along the cell edges, $y = W$. Had this boundary been allowed to remain traction-free, the matrix would have contracted laterally near the equatorial plane due to the yielding. The imposed condition that the cell boundary remain planar results in the development of transverse *tensile* stresses near the equatorial plane. However, since the average normal traction on this boundary must be zero, balancing compressive stresses are also developed at other points on the boundary. Examples of these stress distributions for the square fiber arrays are shown on Fig. 5(c). It is of interest to note that the peak values of the transverse tension are comparable to the corresponding values of the longitudinal limit stress, indicating a rather high degree of stress triaxiality.

For the hexagonal fiber arrays, the stress distributions are somewhat different. When the load is applied parallel to the CPD, the stresses remain relatively uniform

along the failure plane (at $\sim 60^\circ$ to the loading direction). This behavior is shown by the contour maps of σ_{xx} and σ_{xy} in Fig. 6. The results obtained for the hexagonal array loaded normal to the CPD were similar to those for the square array with the lowest fiber volume fraction. Notably, stress gradients were present along the yielded portion of the normal plane (A), though failure ultimately occurred on the inclined plane (B). The stresses along the failure plane were relatively uniform, as for the case where the load is applied parallel to the CPD.

Limited numerical studies have also been conducted for composites with a strain-hardening matrix. Figure 6(a) shows the effects of the hardening exponent, n , on the stress-strain curves for composites with rigid fibers in a hexagonal arrangement loaded normal to the CPD. In this case, the flow stress of the composite, $\sigma_c(\epsilon)$, is normalized by the flow stress of the matrix alone, $\sigma_m(\epsilon)$, at the same applied strain. The strength ratio, $\sigma_c(\epsilon)/\sigma_m(\epsilon)$, asymptotically approaches a constant value at strains of the order $\epsilon/\epsilon_0 \geq 20-50$. The asymptotic values of the strength ratio are plotted against the hardening exponent in Fig. 6(b) for composites with three different fiber volume fractions. Evidently the asymptotic stress ratio is very insensitive to n when the fibers are perfectly compliant and essentially *independent* of n when the fibers are rigid. Moreover, the differences between perfectly compliant and rigid fibers decrease with increasing n ; for $n \geq 0.2$, the two limit stress ratios are within $\sim 2-3\%$ of one another.

The trends in the limiting strength ratio with the hardening exponent differ from the results obtained for well-bonded fiber and particulate composites. In the well-bonded systems, the limiting strength ratio increases substantially with n ; for example, in the case of spherical particulate reinforcements, it increases from 1.28 to 1.67 as n is increased from 0 to 0.2 (Brockenbrough and Zok, 1995). Similar increases are obtained in the well-bonded fiber-reinforced systems (Zahl et al., 1994). Moreover, the magnitude of the strains required to obtain the limiting strength are

very much higher in the composites with weakly bonded interfaces. Typically, in the well-bonded systems, the asymptotic level is reached within $\varepsilon/\varepsilon_0 \sim 2-5$ (depending on f and n): about an order of magnitude smaller than the values obtained for the weakly-bonded systems.

3.2 Biaxial Tension

A series of FEM calculations were performed for biaxial loading of the square and hexagonal fiber arrays with $f = 0.35$. The limiting values of the two stress components are plotted in Fig. 8. Also shown for comparison is the yield surface for a monolithic metal under plane strain loading conditions, given by

$$\sigma_{xx} - \sigma_{yy} = \pm \frac{2\sqrt{3}}{3} \sigma_0 \quad (2)$$

For the square array, the composite yield surface is symmetric about the line $\sigma_{xx} = \sigma_{yy}$ because of the symmetry of the cell. In the regime $\sigma_{xx}, \sigma_{yy} > 0$, yielding occurs when *either* σ_{xx} or σ_{yy} reaches a critical value, $\sim 0.46 \sigma_0$, independent of the other stress component. As the stresses become negative, the shape of the yield surface changes. In the limit wherein both σ_{xx} and σ_{yy} are $\ll 0$, the yield surface approaches that of the monolithic metal (given by Eqn. 2). In this limit, similar results would be expected for *well-bonded* fiber composites. Yield surfaces with similar shapes have been developed for the compaction of an array of plastic cylinders, though the stresses are compressive and the cell geometry is different (Akisanya and Cocks, 1995).

The yield surface for the hexagonal array exhibits several slightly different features. (i) It is not symmetric about $\sigma_{xx} = \sigma_{yy}$. (ii) The composite is somewhat stronger in the x-direction (normal to the CPD) than in the y-direction. (iii) There is

only a small portion of the yield surface that does not depend on both stress components (top right corner of Figure 8).

Figure 9 shows the stress distribution along the failure plane in the square array for uniform biaxial tensile loading. Evidently the distributions are almost identical to those obtained for *uniaxial* loading (compare with Figs. 5(a) and (b)). These similarities can be rationalized in terms of the transverse stresses that develop under uniaxial loading, as described previously. These similarities are manifested in the insensitivity of the limiting values of one of the applied stresses, σ_{xx} , to the other, σ_{yy} , as seen in Fig. 8.

4. NET-SECTION YIELDING MODEL

4.1 Uniaxial Tension

The FEM calculations show that the limit stresses are insensitive to the modulus of the fibers. For fiber volume fractions typical of most Ti/SiC composites, $f \sim 0.35$, the difference in strengths between the rigid fibers and the perfectly compliant ones is negligible for the square fiber array and only $\sim 6-7\%$ for the hexagonal arrays. The results indicate that the composite behaves essentially the same as a matrix containing an array of holes. This result, in turn, suggests that the limit stress may be calculated on the basis of net-section yielding, neglecting the contributions from the fibers. Such an approach is developed here.

The situation in which the fibers are in a hexagonal array and loaded normal to the CPD is considered first (Fig. 1(c)). From the geometry, the cell height, H , and the cell width, L , are related to the fiber volume fraction, f , and the fiber radius, R , through the relations

$$\frac{H}{2R} = \sqrt{\frac{\sqrt{3}}{8} \frac{\pi}{f}} \quad (3)$$

and

$$\frac{L}{2R} = \sqrt{\frac{\sqrt{3}}{24} \frac{\pi}{f}} \quad (4)$$

In this configuration, plasticity tends to develop along one of two planes: the first at $\sim 30^\circ$ to the loading direction (B in Fig. 1(c)), and the other along the equatorial plane normal to the loading direction (A). The limit strength of the composite is then expected to be the lower of the stress levels required to cause yielding along these two planes. In calculating the critical stress levels, it is assumed initially that the stresses are distributed uniformly along each of the two planes, with no stress or strain concentrations arising from the holes.

Across plane B, both a normal tensile stress, σ_B , and a shear stress, τ_B , are present. The relations between these stresses and the applied stress, σ_{xx}^∞ , are obtained from equilibrium considerations. The relations are

$$\frac{\tau_B}{\sigma_B} = \frac{\cos(\pi/6)}{\cos(\pi/3)} = \sqrt{3} \quad (5)$$

and

$$\sigma_{xx} \sqrt{\frac{\sqrt{3}}{24} \frac{\pi}{f}} = \frac{\tau_B \sqrt{3}}{2} \left[\sqrt{\frac{\sqrt{3}}{6} \frac{\pi}{f}} - 1 \right] + \frac{\sigma_B}{2} \left[\sqrt{\frac{\sqrt{3}}{6} \frac{\pi}{f}} - 1 \right] \quad (6)$$

Under plane strain conditions, the effective (Mises) stress, $\bar{\sigma}_B$, corresponding to these two stresses is [10]:

$$\bar{\sigma}_B = \sqrt{\frac{3}{4} \sigma_B^2 + 3\tau_B^2} \quad (7)$$

Yielding occurs when $\bar{\sigma}_B = \sigma_o$. Combining Eqns. (5) through (7) with the yield criterion gives the limiting value of the remote stress, σ_{xx}^ℓ :

$$\frac{\sigma_{xx}^\ell}{\sigma_o} = \frac{8}{\sqrt{39}} \left[1 - \sqrt{2\sqrt{3} \frac{f}{\pi}} \right] \quad (8)$$

Plane A is subjected only to a tensile stress, σ_A , given by

$$\frac{\sigma_A}{\sigma_{xx}} = \left[1 - \sqrt{\frac{2\sqrt{3} f}{\pi}} \right]^{-1} \quad (9)$$

The effective stress on this plane is

$$\bar{\sigma}_A = \frac{\sqrt{3}}{2} \sigma_A \quad (10)$$

Combining Eqns. (9) and (10) with the yield criterion gives the limiting stress as:

$$\frac{\sigma_{xx}^\ell}{\sigma_o} = \frac{2}{\sqrt{3}} \left[1 - \sqrt{2\sqrt{3} \frac{f}{\pi}} \right] \quad (11)$$

Comparison of Eqns. (8) and (11) shows that the limit stress predicted by Eqn. (11) is always the lower of the two; the ratio of the stresses is $4/\sqrt{13} \approx 1.11$.

The same approach is used to evaluate the limit stresses for hexagonal fiber arrays loaded *parallel* to the CPD (along the y-direction). The two potential failure planes are B and C. The limit stresses for yielding along these two planes are

$$\frac{\sigma_{yy}^{\ell}}{\sigma_o} = \frac{8\sqrt{7}}{21} \left[1 - \sqrt{2\sqrt{3} \frac{f}{\pi}} \right] \quad (\text{Plane B}) \quad (12)$$

and

$$\frac{\sigma_{yy}^{\ell}}{\sigma_o} = \frac{2\sqrt{3}}{3} \left[1 - \sqrt{\frac{2\sqrt{3}}{3} \frac{f}{\pi}} \right] \quad (\text{Plane C}) \quad (13)$$

The value predicted by Eqn. (12) is always the lower of the two.

For the square fiber array, the cell dimension, W , is related to R and f through

$$\frac{W}{2R} = \frac{1}{4} \sqrt{\frac{\pi}{f}} \quad (14)$$

The limit stresses are

$$\frac{\sigma_{xx}^{\ell}}{\sigma_o} = \frac{\sigma_{yy}^{\ell}}{\sigma_o} = \frac{4\sqrt{15}}{15} \left[1 - \sqrt{\frac{2f}{\pi}} \right] \quad (\text{Plane E}) \quad (15)$$

and

$$\frac{\sigma_{xx}^{\ell}}{\sigma_o} = \frac{\sigma_{yy}^{\ell}}{\sigma_o} = \frac{2\sqrt{3}}{3} \left[1 - 2\sqrt{\frac{f}{\pi}} \right] \quad (\text{Planes D and F}) \quad (16)$$

where sections D, E and F are indicated on Fig. 1(d). Eqn. (16) predicts the lower of the two limit stress for all values of f .

The limit stresses predicted by Eqns. (8), (11), (12), (13), (15) and (16) are plotted as a function of fiber volume fraction in Fig. 10. (These predictions are labeled as "Simple Net-Section Model" to distinguish them from the modified version which is described below.) For comparison, the results obtained from the FEM calculations are also shown.

For the hexagonal array loaded parallel to the CPD (Fig. 10(a)), the net-section prediction is in excellent agreement with the FEM results: the differences being $< 2\%$ for both $f = 0.25$ and 0.35 and $\sim 9\%$ for $f = 0.5$. The net-section model also correctly predicts that plastic failure should occur along the inclined plane, B. These correlations are consistent with the uniformity in the stresses across this plane, shown in Fig. 6.

For the hexagonal array loaded normal to the CPD (Fig. 10(b)), the net-section model predicts failure along plane A; in contrast, the FEM results indicate that it occurs along plane B at a somewhat higher stress. This discrepancy appears to be associated with the stress gradients along plane A, leading both to an elevation in the flow stress and a transition in the failure plane from A to B. Indeed, the net-section predictions for plane B are in very good agreement with the FEM results. (The effects of the stress gradients on the limit stress for plane A are presented later.)

For the square array, the net-section model predicts failure along the normal planes, D or F, depending on whether the load is applied in the x- or y- directions. The FEM results indicate that, for $f = 0.35$ and 0.5 , failure does indeed occur along these planes, though at stress levels that are higher than the net-section predictions. The FEM results also indicate, that for $f = 0.25$, failure occurs along the inclined plane, E, rather than D or F. The net-section prediction for plane E at this volume fraction is in good agreement with the FEM result.

The stress gradients acting along the planes normal to the loading direction have previously been analyzed for the case of a rectangular bar containing a circular hole of radius, R , subject to uniaxial tensile loading (Hill, 1989; Kaliszky, 1989). In this case, the slip-line field around the hole consists of a series of logarithmic spirals. Within the plastic zone, the stresses acting across the plane of minimum cross section are

$$\frac{\sigma_{yy}}{\sigma_o} = \frac{2\sqrt{3}}{3} \ln(r/R) \quad (17)$$

and

$$\frac{\sigma_{xx}}{\sigma_o} = \frac{2\sqrt{3}}{3} (1 + \ln r/R) \quad (18)$$

where r is the radial distance measured from the center of the hole and x represents the direction of loading. Figure 5 shows comparisons between these predictions and the ones obtained from the FEM calculations for the square fiber array subject to uniaxial loading. Good correlations are obtained for the two highest volume fractions. For the lowest volume fraction, the two follow similar increasing trends with y/R , though the analytical results are somewhat higher than the numerical ones. This discrepancy is due to the contact of the matrix with the fiber along the equatorial plane and the resulting compressive stress acting normal to the interface.

The solutions for the stress gradients can be used to modify the predicted limit stresses. This is accomplished by multiplying the results in Eqns. 11 and 15 by a numerical coefficient, λ , defined by the ratio of the average normal stress, $\hat{\sigma}$, acting along the failure plane perpendicular to the loading direction (obtained from the

slip-line solution) to the plane strain yield stress, $(2\sqrt{3}/3)\sigma_o$. In general, λ is given by

$$\lambda \equiv \frac{\sqrt{3} \hat{\sigma}}{2 \sigma_o} = \frac{\sqrt{3}}{2(r_o - R) \sigma_o} \int_R^{r_o} \sigma_{\theta\theta}(r) dr \quad (19)$$

where r_o is the limiting distance, taken as W for the square array, and either H or L for the hexagonal array depending on the loading direction. λ is obtained by substituting Eqn. (17) into (19) along with the appropriate value of r_o , and then combining the result with the relationship between the cell dimensions and the fiber volume fraction (either Eqn. (3), (4) or (14)). For the square array, the result is:

$$\lambda = \frac{\ell n\left(\frac{W}{R}\right)}{1 - \frac{R}{W}} = \frac{\ell n\left(\frac{1}{2} \sqrt{\frac{\pi}{f}}\right)}{1 - 2\sqrt{\frac{f}{\pi}}} \quad (20)$$

For the hexagonal array loaded normal to the CPD, it is

$$\lambda = \frac{\ell n\left(\frac{L}{R}\right)}{1 - \frac{R}{L}} = \frac{\ell n\left(\sqrt{\frac{\sqrt{3} \pi}{6 f}}\right)}{1 - \sqrt{\frac{2\sqrt{3} f}{\pi}}} \quad (21)$$

and for the hexagonal array loaded parallel to the CPD, it is

$$\lambda = \frac{\ell n \sqrt{\frac{\sqrt{3} \pi}{2 f}}}{1 - \sqrt{\frac{2\sqrt{3} f}{3 \pi}}} \quad (22)$$

Figures 10(b) and (c) show the predictions obtained from the modified versions of the net-section yielding model (incorporating the stress gradients). The solutions are obtained by multiplying the right side of Eqn. 15 by λ in Eqn. 20, and multiplying the right side of Eqn. 11 by λ in Eqn. 21. For the hexagonal array (Fig. 10(b)), the modified model predicts a limit stress for plane A which is higher than that needed for yielding along plane B, in accord with the FEM prediction that failure occurs on plane B. For the square array, the modified model yields predictions for yielding along plane E that are in excellent agreement with the FEM results for volume fractions at which failure does indeed occur along E ($f = 0.35$ and 0.5); for $f = 0.25$, it predicts a limit stress for E that exceeds that for planes D or F and thus correctly predicts the transition in the failure planes as the fiber volume fraction is reduced.

4.2 Biaxial Loading

The net-section yielding model has been extended to calculate the limiting yield surface of the composite under biaxial tensile loading. For this purpose, two stress parameters are introduced: a mean stress, σ_m , and a deviatoric stress, $\Delta\sigma$, defined by

$$\sigma_m \equiv (\sigma_{xx} + \sigma_{yy})/2 \quad (23)$$

and

$$\Delta\sigma \equiv (\sigma_{xx} - \sigma_{yy})/2 \quad (24)$$

where σ_{xx} and σ_{yy} are the stresses applied along the directions indicated in Fig. 1. These parameters have previously been used by others to describe the yield surfaces for porous materials (Akisanya and Cocks, 1995; Sofronis and McMeeking, 1992). The combinations of $\Delta\sigma$ and σ_m that lead to plastic collapse are calculated using the approach outlined above. Notably, the potential critical planes are identified, the average normal and shear stresses acting along each of these planes is evaluated and the stresses then combined with the Mises yield criterion. For planes oriented normal to either the x- or y- directions, the factor, λ , is also incorporated. (It can be shown readily that the stress gradients that occur around a cylindrical hole under uniform biaxial tension are identical to the ones described by Eqns. 17 and 18 for uniaxial tension, with σ_{yy} replaced by the hoop stress, $\sigma_{\theta\theta}$, and σ_{xx} replaced by the radial stress, σ_{rr} . Consequently, λ is expected to be independent of the imposed stress state.) The limit surface is obtained from the inner envelope of the yield surfaces calculated for all planes.

For the square fiber array, yielding can occur on planes D, E or F (Fig. 1(d)). The normal and shear stresses on plane E are

$$\sigma_E = \frac{\sigma_{xx} + \sigma_{yy}}{2(1 - \sqrt{2f/\pi})} = \frac{\sigma_m}{1 - \sqrt{2f/\pi}} \quad (25)$$

and

$$\tau_E = \frac{\sigma_{xx} - \sigma_{yy}}{2(1 - \sqrt{2f/\pi})} = \frac{\Delta\sigma}{(1 - \sqrt{2f/\pi})} \quad (26)$$

and the corresponding yield condition is

$$\left(\frac{\sigma_m}{\sigma_o}\right)^2 + \left(\frac{2\Delta\sigma}{\sigma_o}\right)^2 = \frac{4}{3}\left(1-2\sqrt{f/\pi}\right)^2 \quad (27)$$

Planes D and F are subjected only to normal stresses, given by

$$\sigma_D = \frac{\sigma_m + \Delta\sigma}{1-2\sqrt{f/\pi}} \quad (28)$$

and

$$\sigma_F = \frac{\sigma_m - \Delta\sigma}{1-2\sqrt{f/\pi}} \quad (29)$$

The yield conditions are

$$\frac{\sigma_m}{\sigma_o} + \frac{\Delta\sigma}{\sigma_o} = \pm \frac{2\sqrt{3}}{3} \lambda \left[1-2\sqrt{f/\pi}\right] \quad (\text{Plane D}) \quad (30)$$

and

$$\frac{\sigma_m}{\sigma_o} - \frac{\Delta\sigma}{\sigma_o} = \pm \frac{2\sqrt{3}}{3} \lambda \left[1-2\sqrt{f/\pi}\right] \quad (\text{Plane F}) \quad (31)$$

Eqns. (27), (30) and (31) are plotted in Fig. 11(a) for a fiber volume fraction, $f = 0.35$.

The inner surface along which yielding is predicted to occur is indicated by the shading. The FEM results are also shown in this figure.

Since the model neglects the contributions from the fibers, it is expected to be valid only when both σ_{xx} and σ_{yy} are positive. This condition can be written in terms of the two stress parameters as

$$-\sigma_m \leq \Delta\sigma \leq \sigma_m \quad (32)$$

This result is plotted on Fig. 11 as two dotted lines. Within this regime, yield occurs on planes D or F, depending on whether $\Delta\sigma$ is negative or positive; the stresses required for yielding on plane E are always higher and thus are not attained.

Yielding on plane E is predicted to occur when

$$\sigma_m/\sigma_o \lesssim 0.18 \quad (33)$$

Despite the fact that this range is outside of the one defined by Eqn. (32), the predictions remain in good agreement with the FEM results, suggesting that the model is accurate even when one of the stress components is somewhat negative. It should also be noted that, because of the symmetry of the unit cell, the yield surface is symmetric about the line $\Delta\sigma = 0$.

As noted earlier, the yield surface becomes insensitive to σ_m when $\sigma_m/\sigma_o \ll 0$. In this limit, the yield surface is expected to be essentially the same as that of a *well-bonded* fiber composite neglecting the differences associated with sliding vs. non-sliding interfaces. Yield is then predicted to occur when $|2\Delta\sigma|$ reaches the plane strain flow stress of the matrix, $(2/\sqrt{3})\sigma_o$, such that

$$\left| \frac{\Delta\sigma}{\sigma_o} \right| = 1/\sqrt{3} \approx 0.577 \quad (34)$$

Following the same approach, the limit surfaces for the hexagonal fiber arrays have also been obtained. The relevant results are

$$\frac{\sigma_m}{\sigma_o} + \frac{\Delta\sigma}{\sigma_o} = \pm \frac{2\sqrt{3}}{3} \lambda \left(1 - \sqrt{2\sqrt{3} f / \pi}\right) \quad (35)$$

for plane A;

$$\left(\frac{\sigma_m}{\sigma_o} - \frac{\Delta\sigma}{2\sigma_o}\right)^2 + 3\left(\frac{\Delta\sigma}{\sigma_o}\right)^2 = \frac{4}{3}\left(1 - \sqrt{2\sqrt{3} f / \pi}\right)^2 \quad (36)$$

for plane B; and

$$\frac{\sigma_m}{\sigma_o} - \frac{\Delta\sigma}{\sigma_o} = \pm \frac{2\sqrt{3}}{3} \lambda \left(1 - \sqrt{2f / \sqrt{3} \pi}\right) \quad (37)$$

for plane C.

The yield surfaces for $f = 0.35$ are plotted in Fig. 11(b), along with the FEM results and the lines defined by Eqn. (32). For this fiber array, the axes that define the symmetry of the cell are different from those defining the principal stresses; consequently, the yield surfaces are not symmetric about $\Delta\sigma = 0$. The analytical results predict failure along plane B for most stress combinations, the exception being the region in the top right corner of the yield surface where failure occurs along plane A. The agreement between the analytical and numerical results is good for cases where $\Delta\sigma/\sigma_o$ is not zero. When it is zero (i.e. uniform biaxial tension), the analytical result for yielding along plane B is $\sim 20\%$ less than the numerical one. This discrepancy arises because, under uniform biaxial loading, stress gradients develop along plane B; indeed, in this limit, they are identical to those along plane A. As a result, the limit stress is underestimated. The more relevant result in this limit is the one for yielding along plane A, incorporating the effects of stress gradients. In this case, the analytical result is essentially identical to the numerical

one. In its present form, the net-section yielding model does not take into account *changes* in stress gradients with stress state: the gradients are either neglected altogether (as they should for yielding along inclined planes under near-uniaxial loading) or are included for all stress states (for planes oriented normal to the principal loading directions). The shear stresses acting along the inclined planes effectively eliminate the stress gradients. However, under uniform biaxial loading, these shear stresses vanish and the stress gradients become important.

The effects of fiber volume fraction on the yield surfaces for both types of fiber arrays are shown on Fig. 12. In these cases, only the inner yield surfaces from the analytical solutions are shown. The yield surfaces for the various volume fractions nest inside one another, expanding as f decreases. In the limit of $f \rightarrow 0$, the yield surface approaches that of a monolithic metal under plane strain conditions. It should be emphasized that the accuracy of the yield surfaces that lie outside the range $-\sigma_m \leq \sigma \leq \sigma_m$ may be questionable in some cases. Furthermore, for the hexagonal arrays, the predictions along $\Delta\sigma/\sigma_0 \approx 0$ are expected to be lower bounds to the actual limiting stresses.

5. CONCLUDING REMARKS

The limit stresses for biaxial loading of weakly-bonded unidirectional fiber composites have been evaluated and used to construct limit surfaces in an appropriate stress space. The limit stresses depend somewhat on the fiber array as well as the directions of loading but are insensitive to the fiber modulus. The limiting conditions are obtained when plastic failure occurs along the most favorably oriented plane within the matrix. Transitions in the failure plane can occur with changes in the fiber volume fraction or imposed stress state. Such effects can be accurately described through the use of a net-section yielding model,

incorporating the stress gradients that occur along planes oriented perpendicular to the principal loading directions. The attractive features of the net-section yielding model include its simplicity as well as the potential for extending it to other situations, including other fiber volume fractions and fiber arrangements, without recourse to the numerical calculations.

ACKNOWLEDGMENTS

Funding for this work was supplied by the DARPA University Research Initiative Program at UCSB under ONR contract N0014-92-J-1808. Fruitful discussions with R.M. McMeeking are gratefully acknowledged. The ABAQUS finite element code was made available by Hibbitt, Karlsson and Sorensen, Inc., Pawtucket, RI, through an academic license.

REFERENCES

- ABAQUS User Manual (1994), Hibbitt, Karlsson and Sorensen, Inc., 1080 Main Street, Pawtucket, RI.
- Akisanya, A.R. and Cocks, A.C.F. (1995) Stage I Compaction of Cylindrical Particles Under Non-hydrostatic Loading, *Journal of Mechanics and Physics of Solids*, **43**, 605-636.
- Böhm, H.J. and Rammerstorfer (1991) Micromechanical Investigation of the Processing and Loading of Fiber-reinforced Metal Matrix Composites, *Materials Science and Engineering*, **A135**, 185-188.
- Brockenbrough, J.R. and Suresh, S. (1990) Plastic Deformation of Continuous Fiber-Reinforced Metal Matrix Composites: Effects of Fiber Shape and Distribution, *Scripta Metallurgica et Materialia*, **24**, 325-30.
- Brockenbrough, J.R., Suresh, S., and Wienecke, H.A. (1991) Deformation of Metal-Matrix Composites with Continuous Fibers: Geometrical Effects of Fiber Distribution and Shape, *Acta Metallurgica et Materialia*, **39**, 735-52.
- Brockenbrough, J.A. and Zok, F.W. (1995) On the Role of Particle Cracking in Flow and Fracture of Metal Matrix Composites, *Acta Metallurgica et Materialia*, **43**, pp. 11-20.
- Du, Z-Z. and McMeeking, R.M. (1994) Control of Strength Anisotropy of Metal Matrix Fiber Composites, *Journal of Computer-Aided Materials Design*, **1**, 243-264.
- Du, Z-Z., Leckie, F.A. and Burr, A. (1996) Design with Titanium Matrix Composites: Case Studies," in preparation.
- Gunawardena, S.R., Jansson, S. and Leckie, F.A. (1993) Modeling of Anisotropic Behavior of Weakly Bonded Fiber Reinforced MMCs, *Acta Metallurgica et Materialia*, **41**, 3147-56.
- Hill, R. (1989) *The Mathematical Theory of Plasticity*, Clarendon Press, Oxford, pp. 245-252.

- Jansson, S. and Leckie, F.A., (1992) Mechanical Behaviour of a Continuous Fiber-Reinforced Aluminum Matrix Composite Subjected to Transverse and Thermal Loading, *Journal of Mechanics and Physics of Solids*, **40**, 593-612.
- Jansson, S., Dève, H. and Evans, A.G. (1991) The Anisotropic Mechanical Properties of a Ti Matrix Composite Reinforced with SiC Fibers, *Metallurgical Transactions*, **22A**, 2975-2984.
- Jansson, S., and Leckie, F.A. (1994) Transverse Tensile and Inplane Shear Strength of Weakly Bonded Fiber Reinforced MMCs Subjected to Cyclic Thermal Loading, *Mechanics of Materials*, **18**, 205-212.
- Kalishky, S. (1989) *Plasticity: Theory and Engineering Applications*, Elsevier, Amsterdam, pp. 205-208.
- Nakamura, T. and Suresh, S. (1993) Effects of Thermal Residual Stresses and Fiber Packing on Deformation of Metal Matrix Composites, *Acta Metallurgica et Materialia*, **41**, 1665-1681.
- Nimmer, R.P., Bankert, R.J., Russell, E.S., Smith, G.A. and Wright, P.K. (1991) Micromechanical Modeling of Fiber Matrix Interface Effects in Transversely Loaded SiC/Ti-6-4 Metal Matrix Composites, *Journal of Composites and Technological Research*, **13**, 3-13.
- Odqvist, F.K.G., (1966) *The Mathematical Theory of Creep and Creep Rupture*, Oxford University Press.
- Sofronis, P. and McMeeking, R.M. (1992) Creep of Power-Law Material Containing Spherical Voids, *Trans. ASME*, **59**, S88-S95.
- Teply, J.L. and Dvorak, G.J. (1988) Bounds on Overall Instantaneous Properties of Elastic-Plastic Composites, *Journal of Mechanics and Physics of Solids*, **36**, 29-58.
- Weber, C.H., Du, Z-Z. and Zok, F.W. (1996) High Temperature Deformation and Fracture of a Fiber Reinforced Titanium Matrix Composite, *Acta Metallurgica et Materialia*, **44**, 683-695.

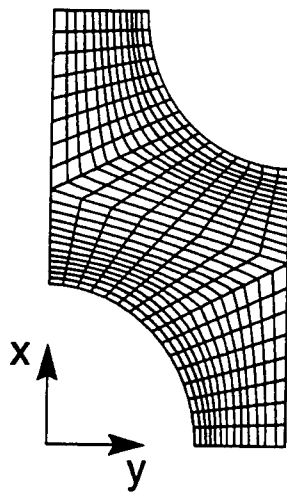
Zahl, D.B., Schmauder, S. and McMeeking, R.M. (1994) Transverse Strength of Metal Matrix Composites Reinforced with Strongly Bonded Continuous Fibers in Regular Arrangements, *Acta Metallurgica et Materialia*, **42**, 2983-2997.

FIGURES

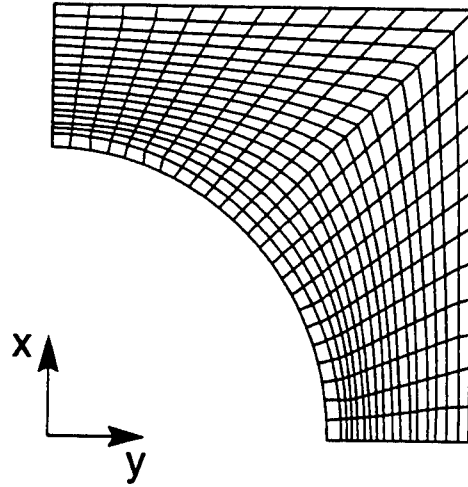
- Figure 1 Typical finite element grids for cells with a fiber volume fraction, $f = 0.35$: (a) square arrangement, (b) hexagonal arrangement. In (a), the load is applied parallel to the close-packed direction (either the x- or y-directions). In (b), the load is applied either parallel (y) or perpendicular (x) to the close packed direction. (c) and (d) show cell dimensions and the potential planes along which plastic failure can occur.
- Figure 2 Stress-strain curves for composites with (a) a hexagonal array of fibers loaded normal to the CPD, (b) a hexagonal array of fibers loaded parallel to the CPD and (c) a square fiber array. The solid lines represent the results for perfectly rigid fibers and the dashed lines are for perfectly compliant fibers.
- Figure 3 Trends in the uniaxial limit stress with the fiber volume fraction for both hexagonal and square fiber arrangements, where the fibers are (a) rigid, or (b) perfectly compliant.
- Figure 4 Evolution of matrix plasticity (indicated by shaded regions) with applied strain, for (a), (b) hexagonal arrays loaded normal to the CPD, (c) hexagonal array loaded parallel to the CPD, and (d) square array. In all cases, the fiber volume fraction is 0.35.
- Figure 5 Distributions of (a) transverse and (b) longitudinal stresses along the failure plane ($x = 0$), and (c) transverse stress along the cell boundaries ($y = W$).
- Figure 6 Contour maps showing distributions in the longitudinal and shear stresses, σ_{yy} and σ_{xy} for a hexagonal fiber array loaded parallel to the CPD. Note the uniformity in these stresses across the ligament joining the two fibers.
- Figure 7 Effects of the matrix hardening exponent on (a) the stress-strain response and (b) the asymptotic strength ratio, for composites with rigid fibers in a hexagonal array loaded normal to the CPD. The stresses are normalized by the flow stress of the matrix alone at the same applied strain.
- Figure 8 Limit stresses for biaxial loading: (a) square and (b) hexagonal fiber arrays.
- Figure 9 Stress distributions along failure plane ($x = 0$) for uniform biaxial tensile loading of a square fiber array with $f = 0.35$. Also shown for comparison are the predictions based on the uniform expansion of a cylinder (Eqns. 17 and 18).
- Figure 10 Comparisons of analytical predictions of limit stresses for uniaxial loading with those obtained using FEM.

Figure 11 Limiting yield surfaces for composites with $f = 0.35$: (a) square and (b) hexagonal fiber arrays.

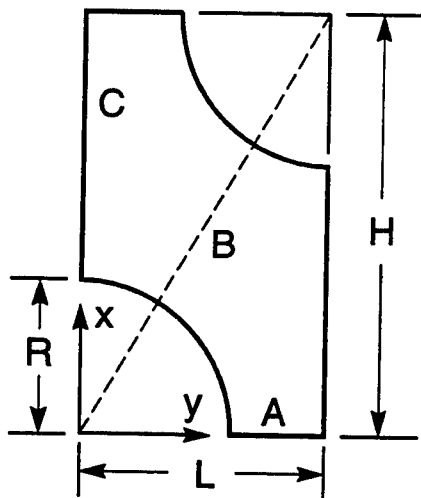
Figure 12 Effects of fiber volume fraction on the yield surfaces for (a) square and (b) hexagonal fiber arrays.



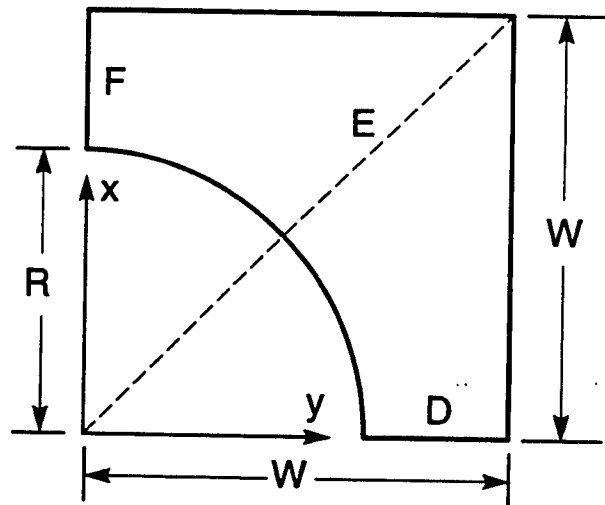
(a)



(b)



(c)



(d)

Figure 1

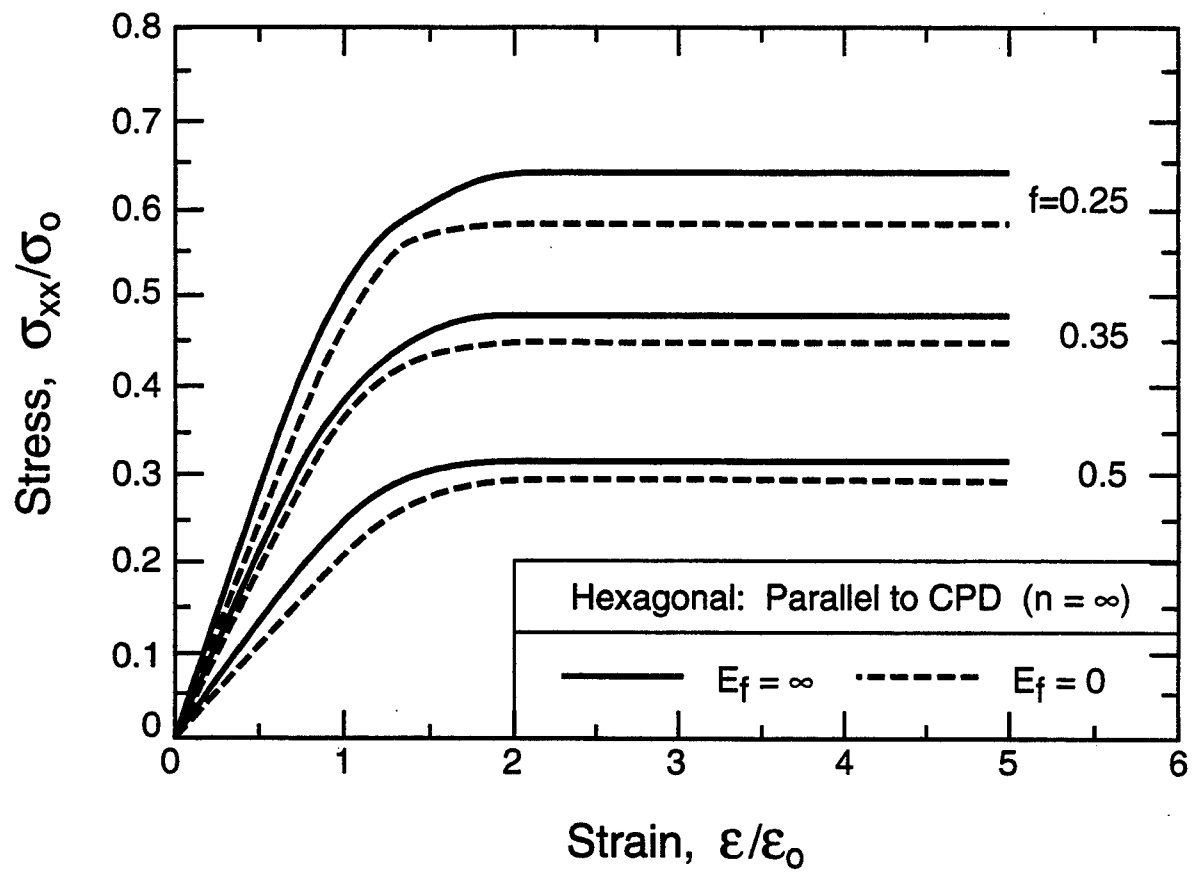


Figure 2

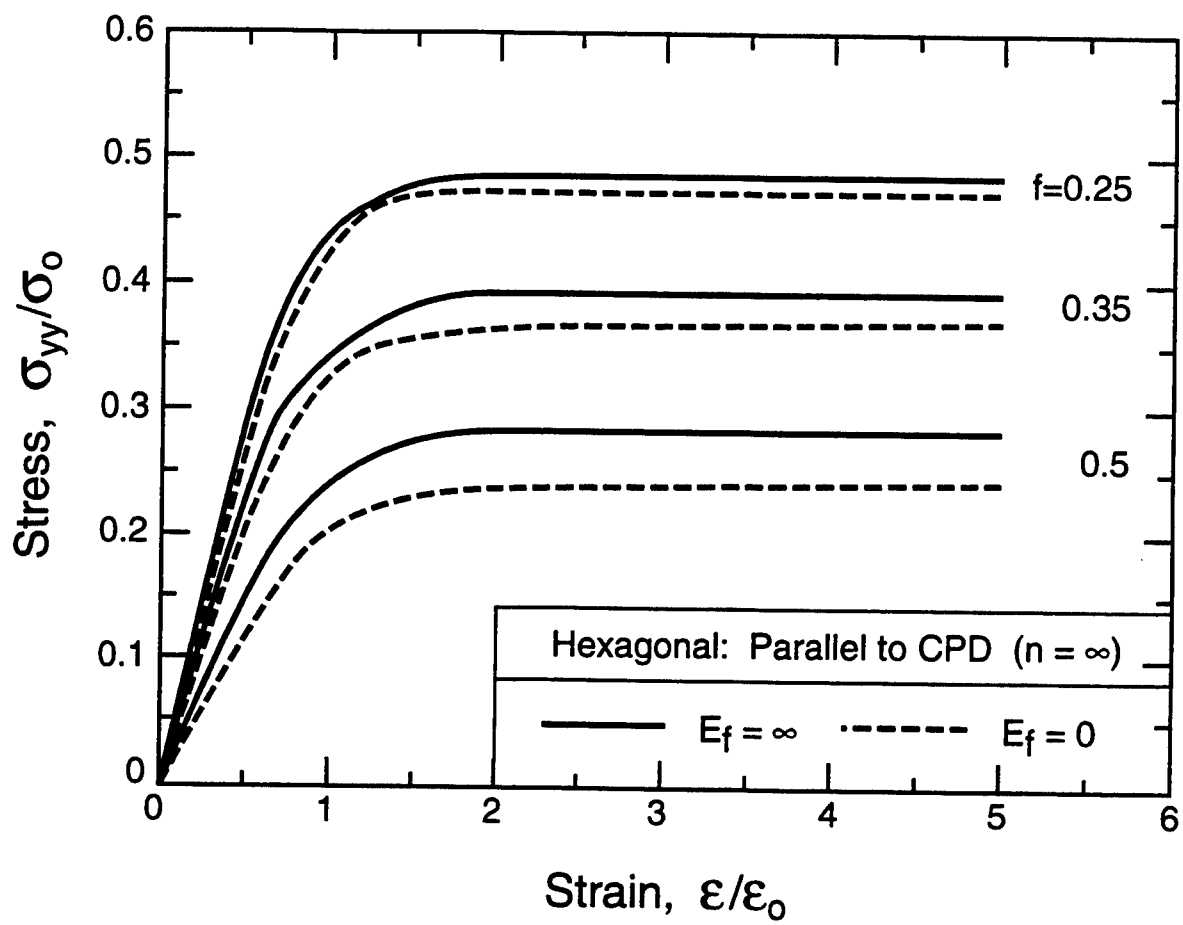


Figure 2(b)

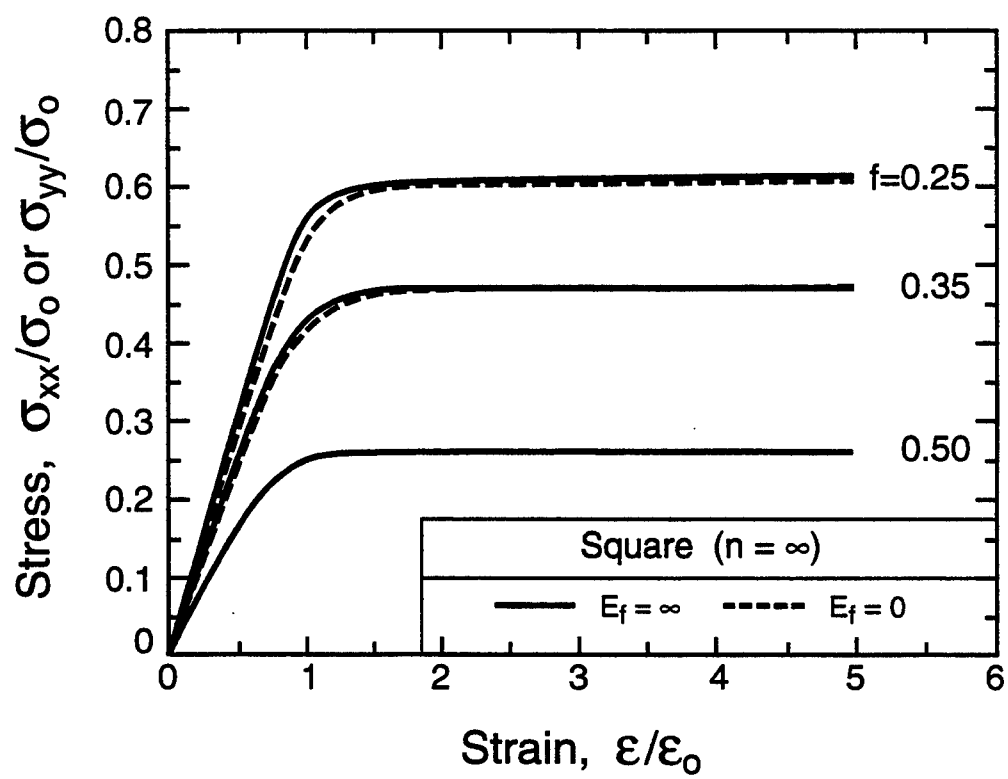


Figure 2(c)

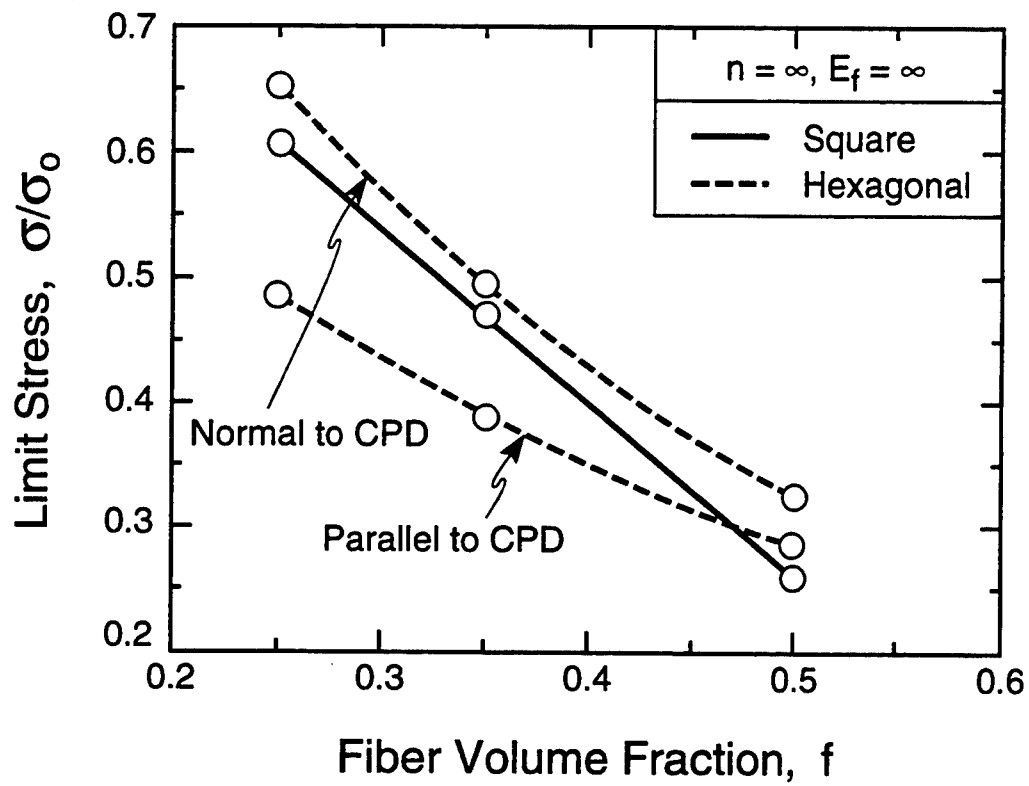


Figure 3(a)

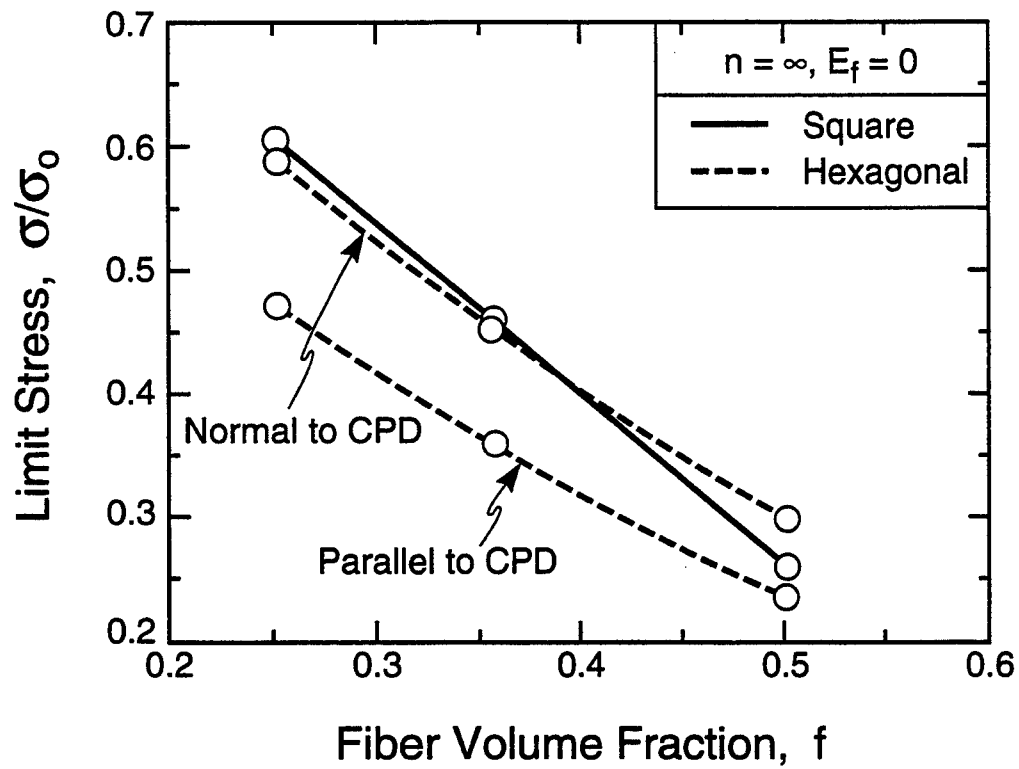


Figure 3(b)

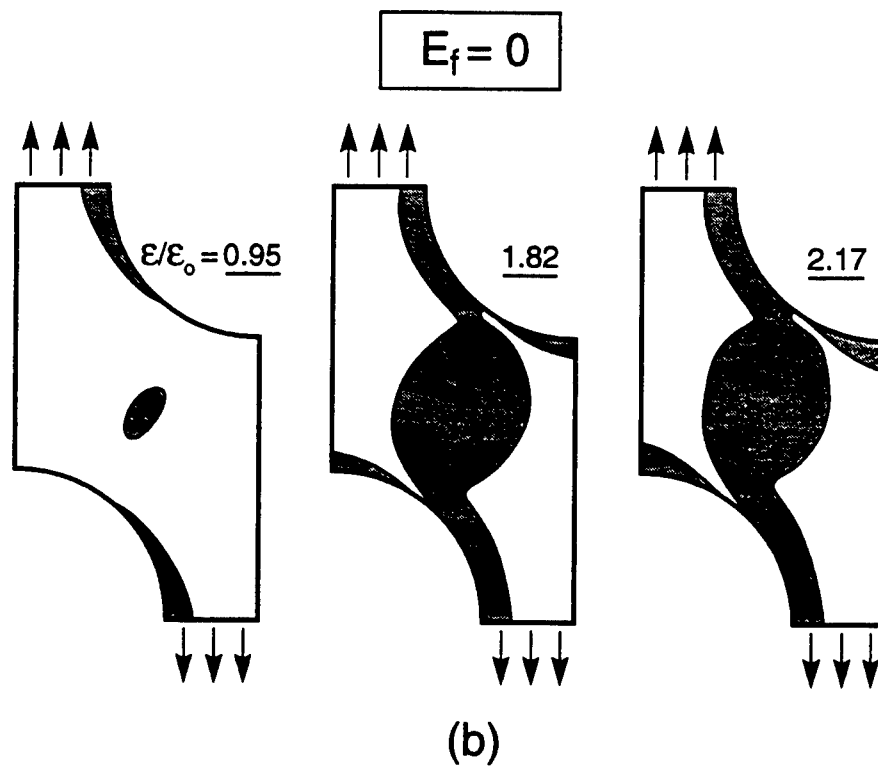
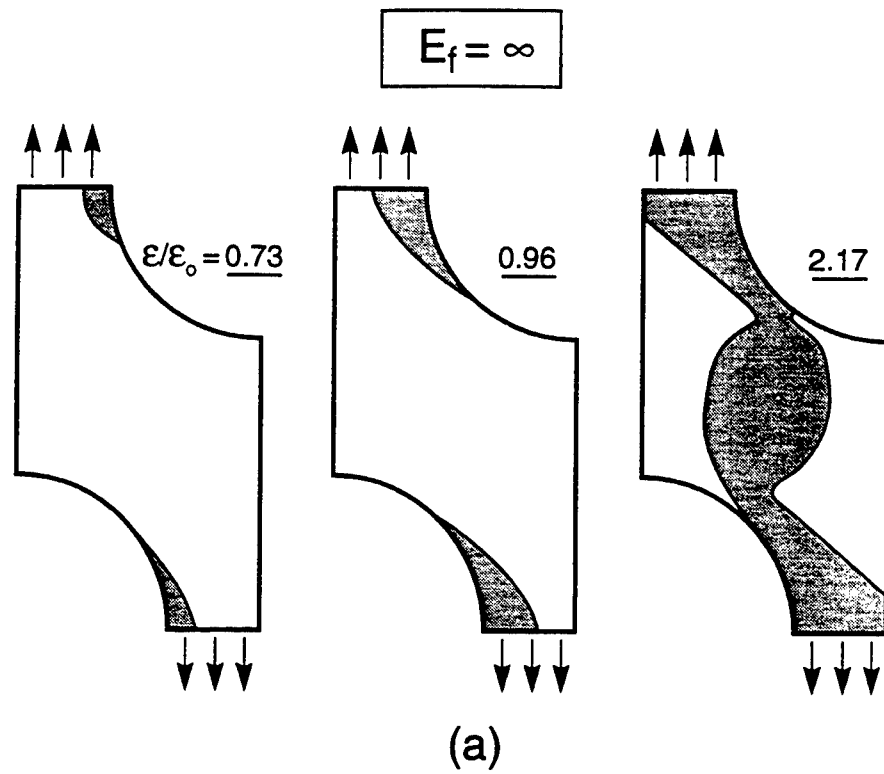
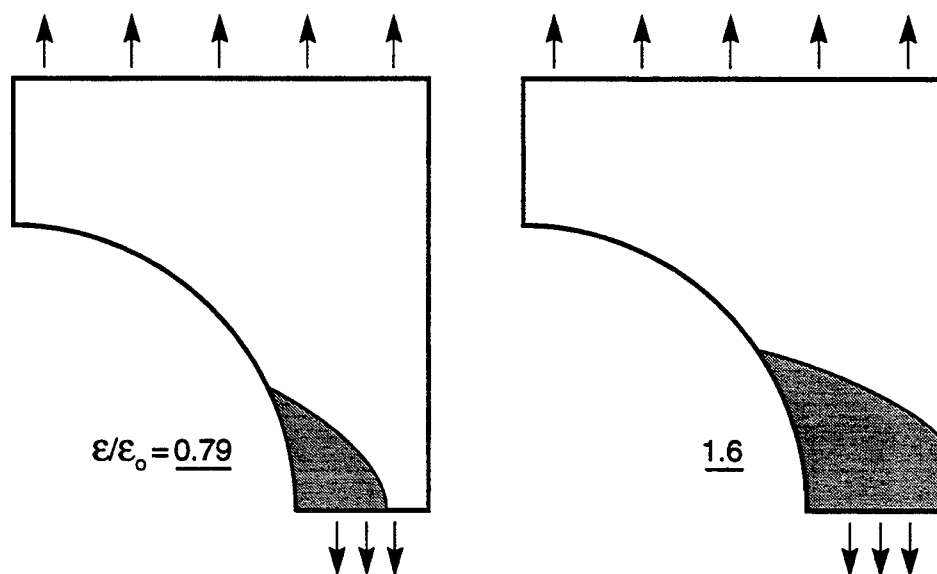


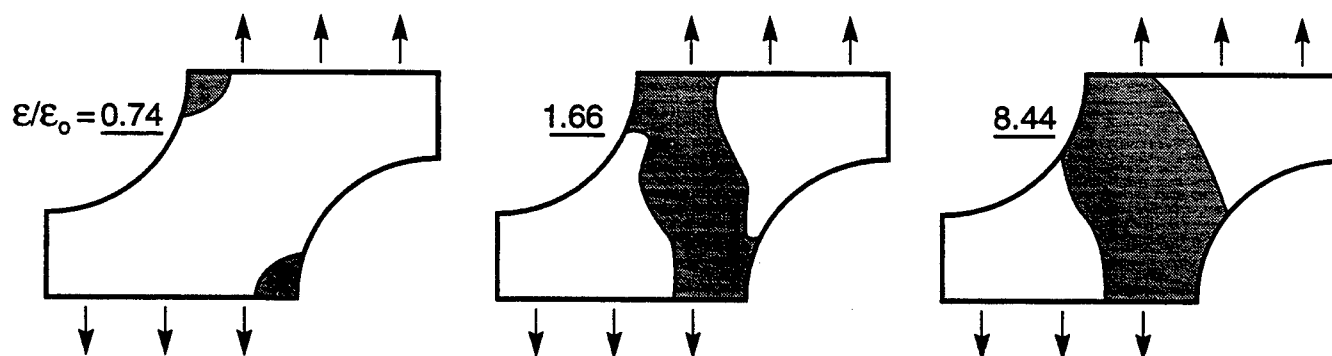
Figure 4

$$E_f = \infty$$



(c)

$$E_f = \infty$$



(d)

Figure 4

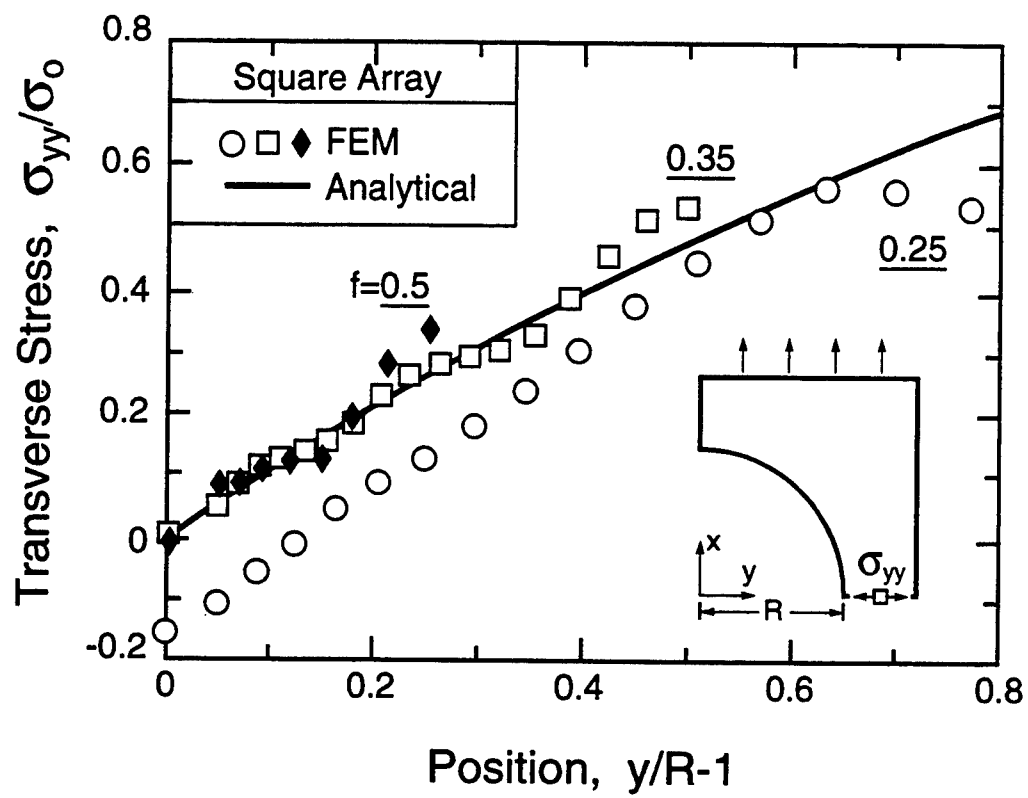


Figure 5(a)

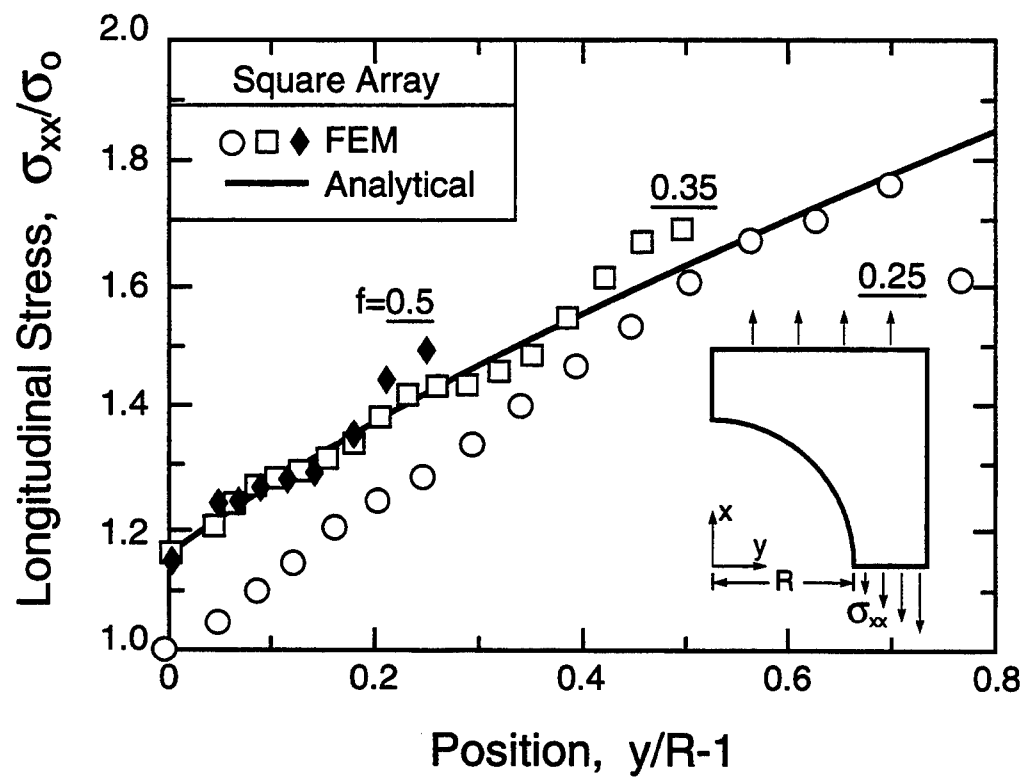


Figure 5(b)

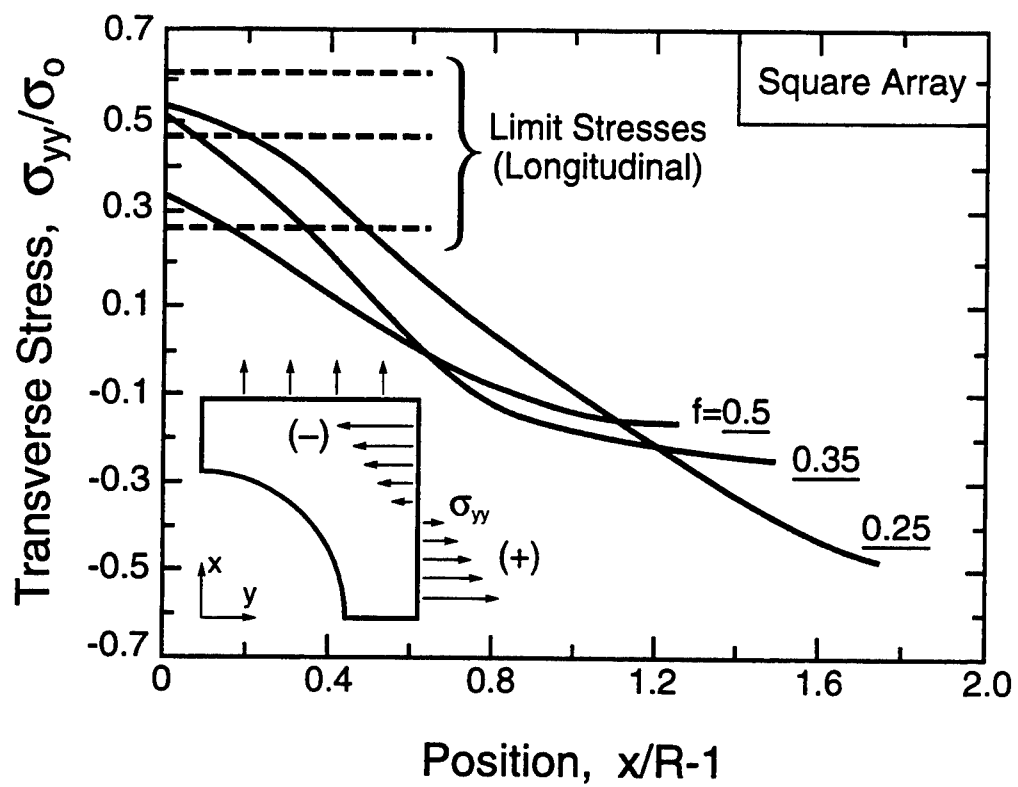
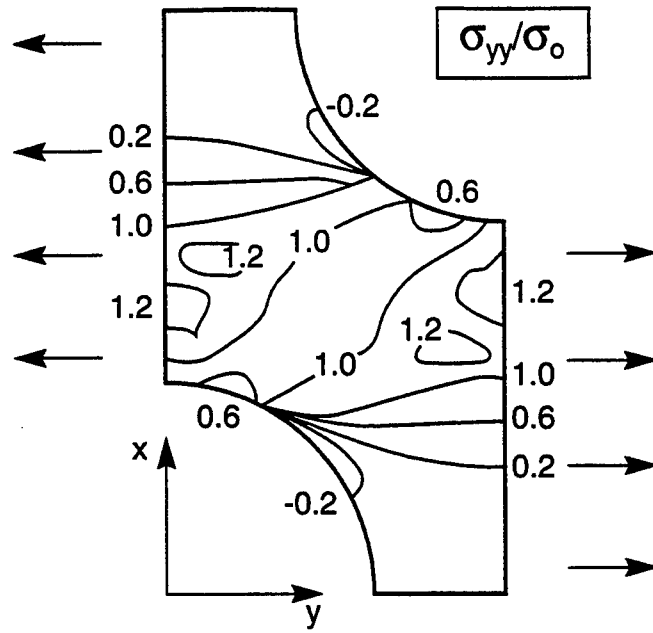
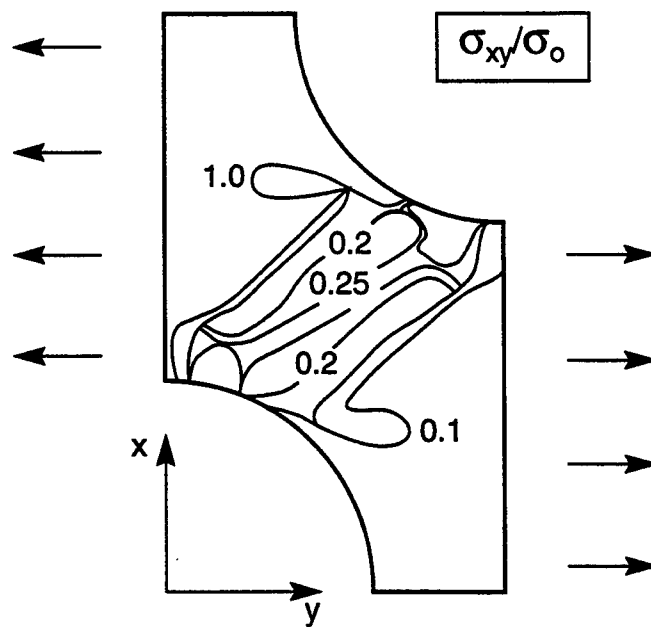


Figure 5(c)



(a)



(b)

Figure 6

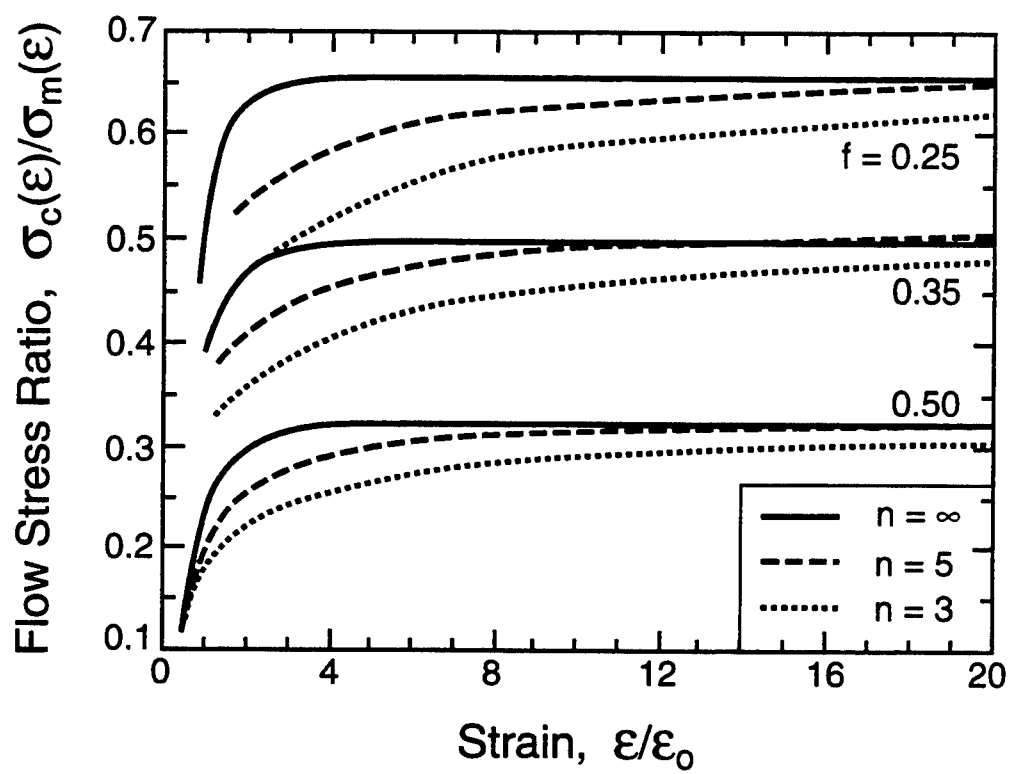


Figure 7(a)

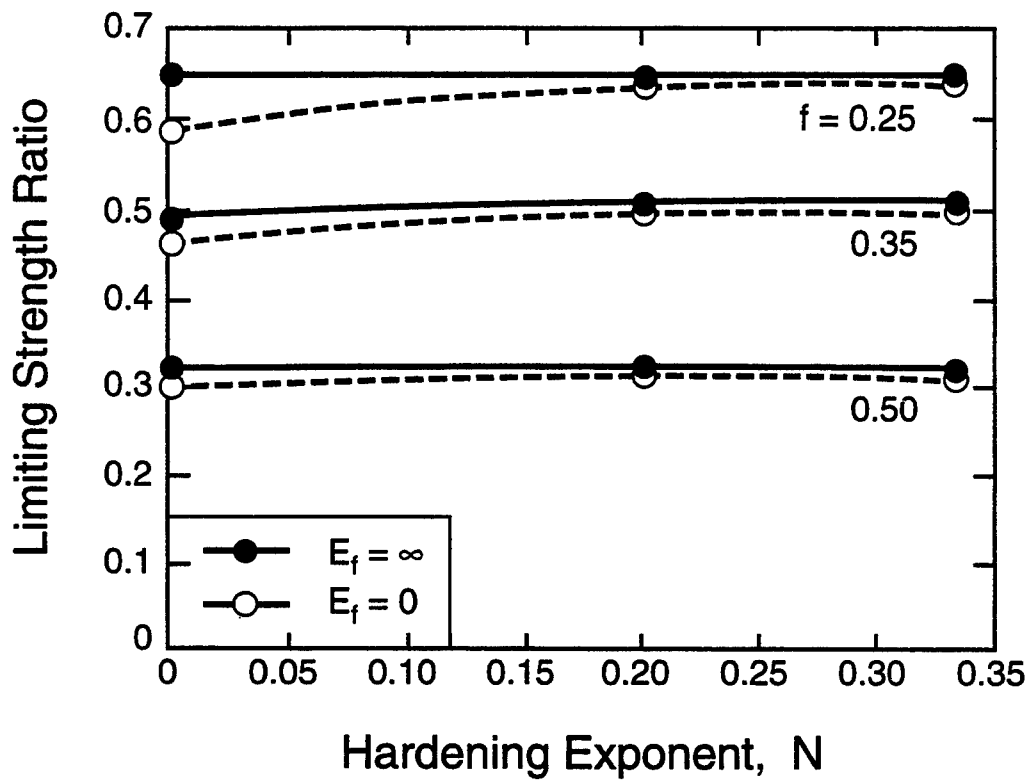


Figure 7(b)

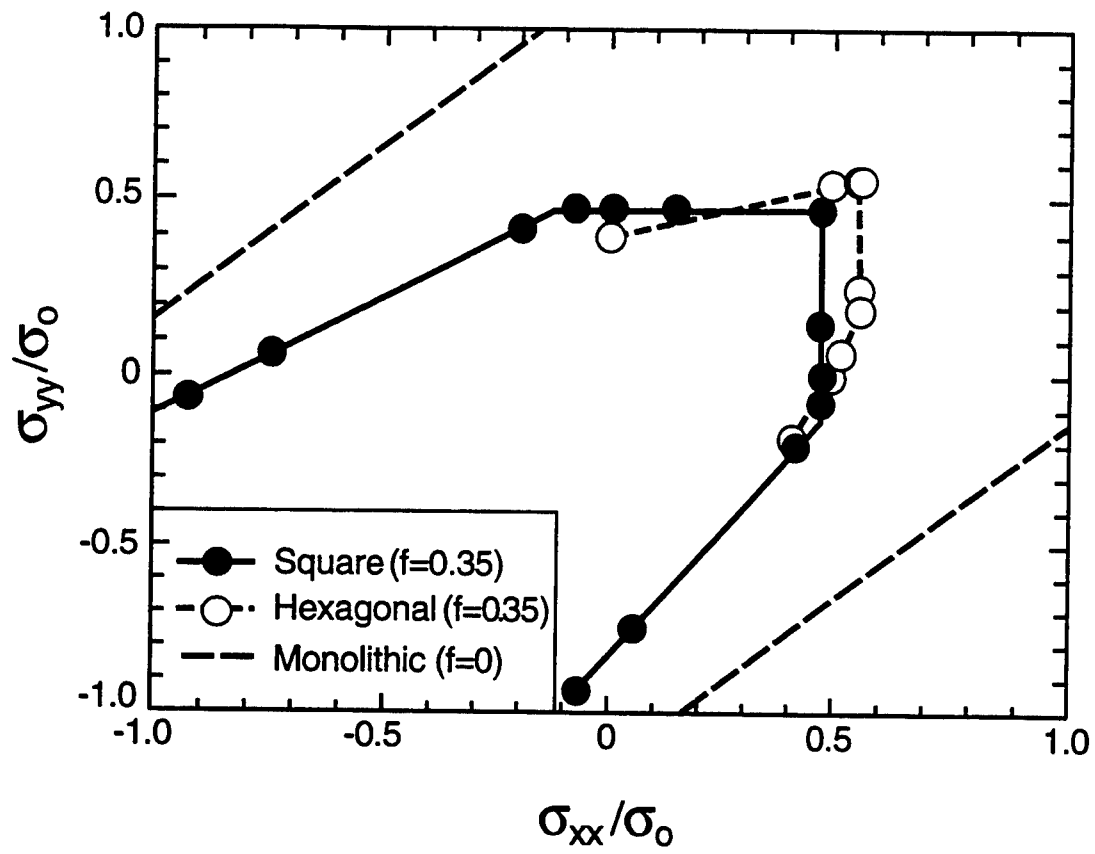


Figure 8

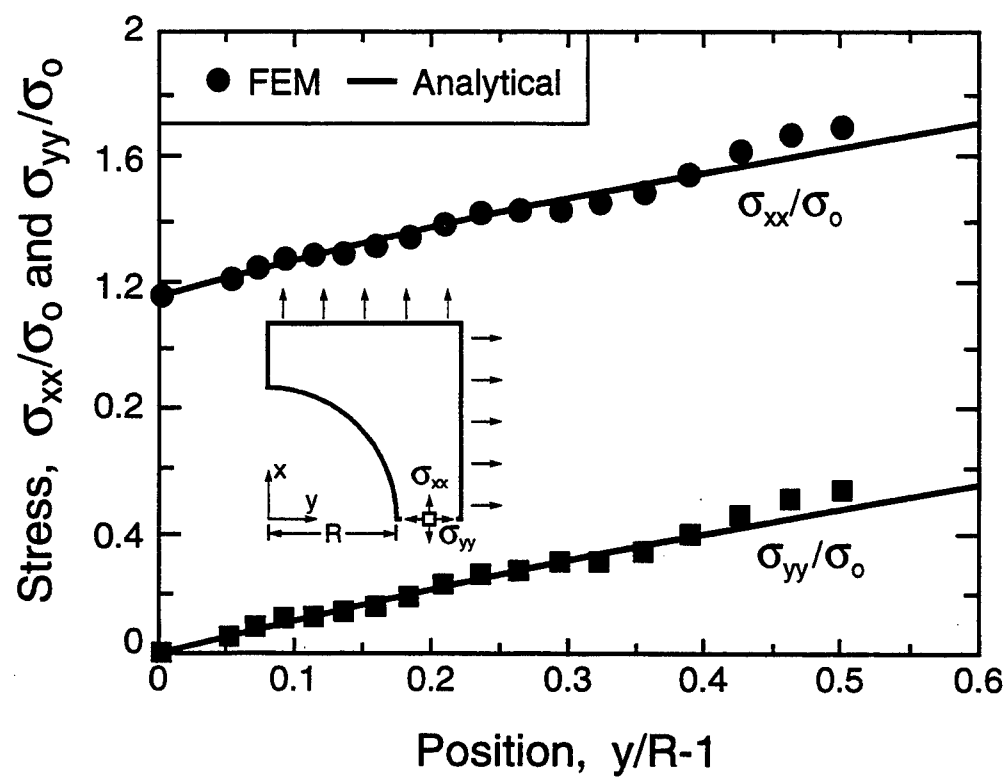


Figure 9

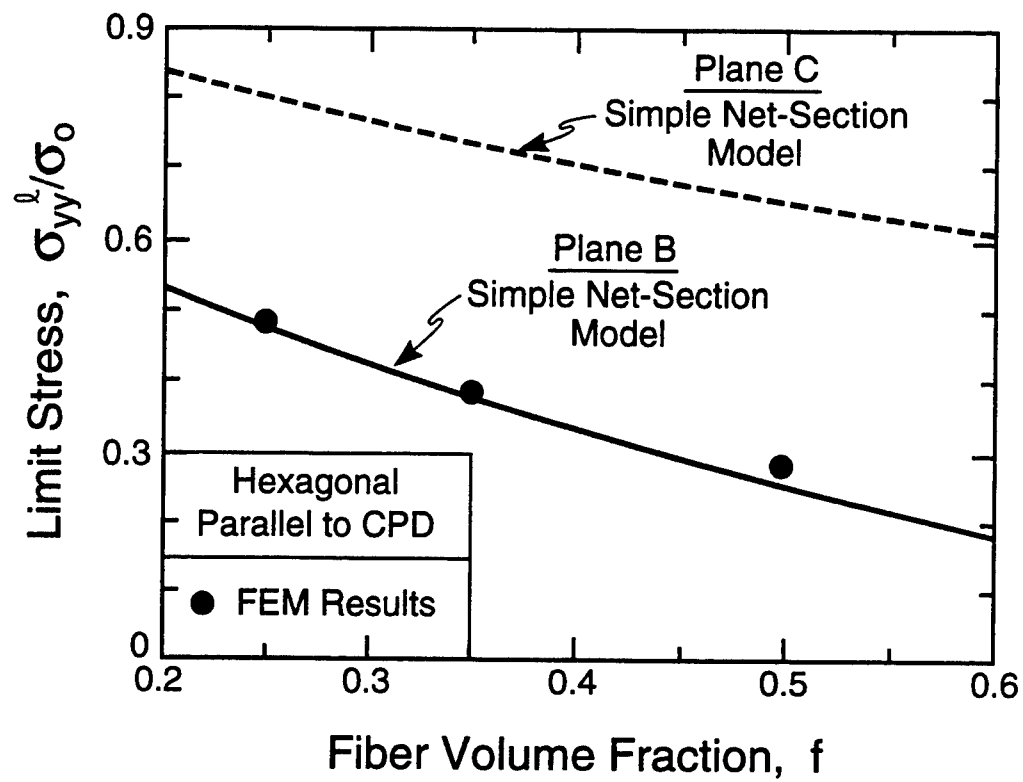


Figure 10(a)

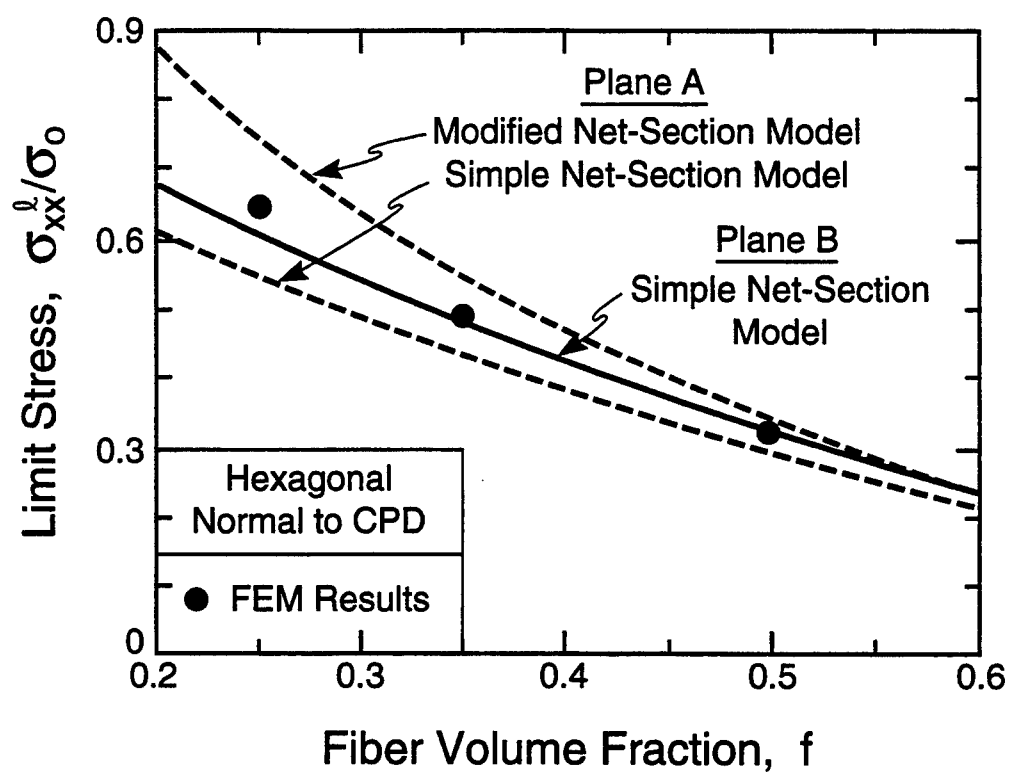


Figure 10(b)

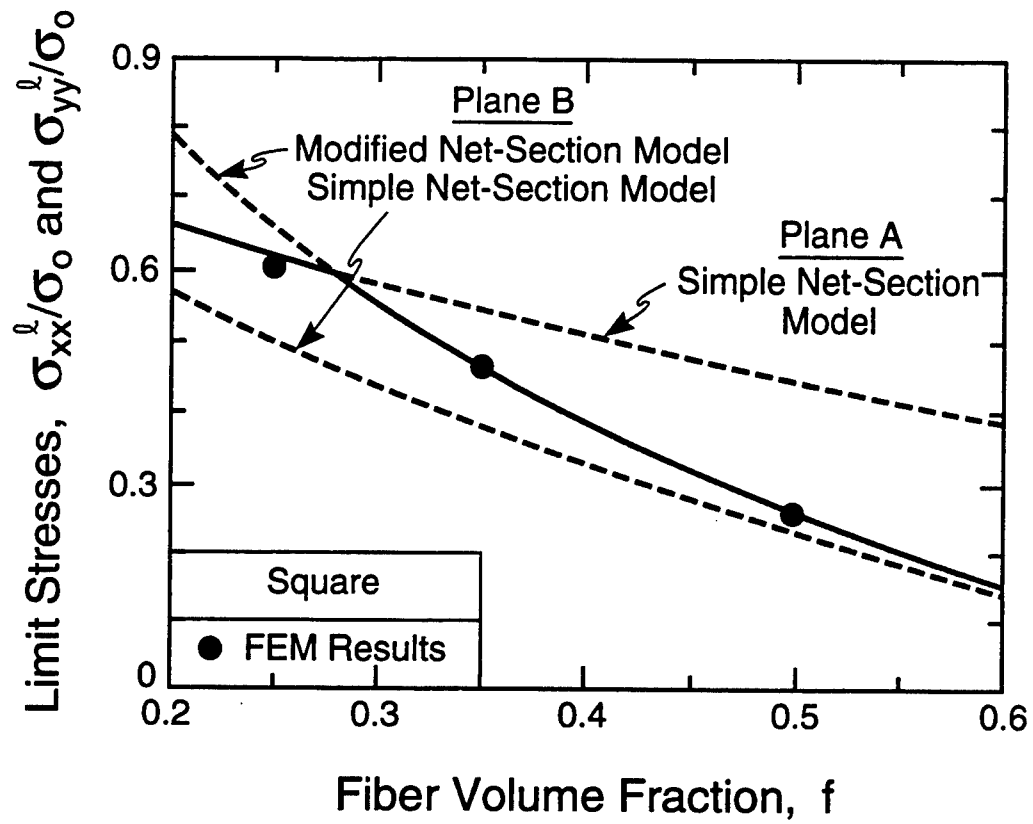


Figure 10(c)

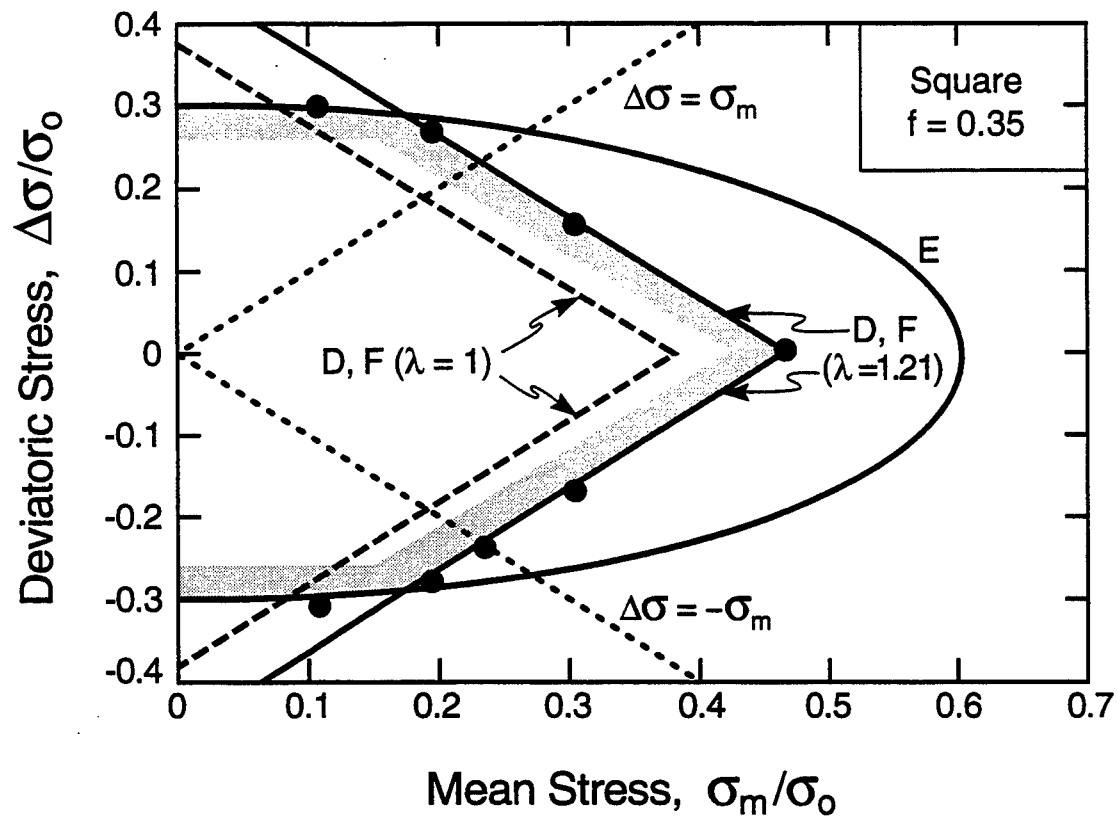


Figure 11(a)

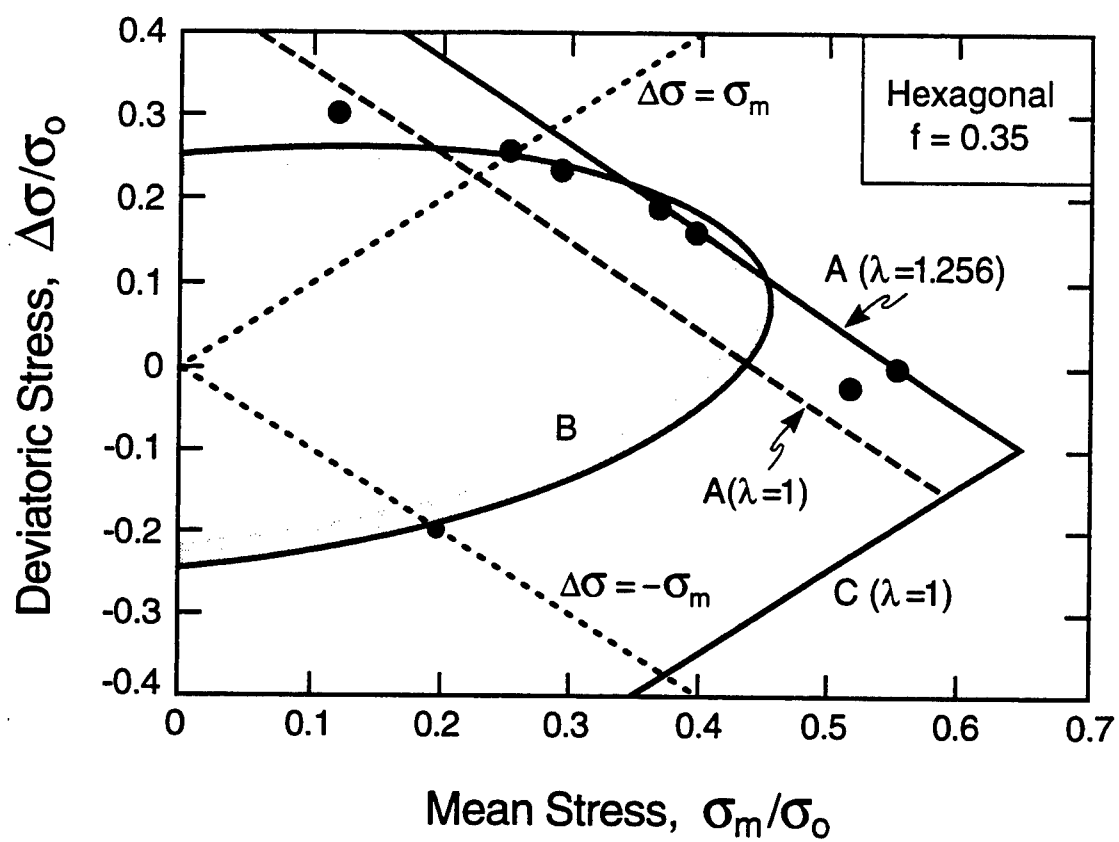


Figure 11(b)

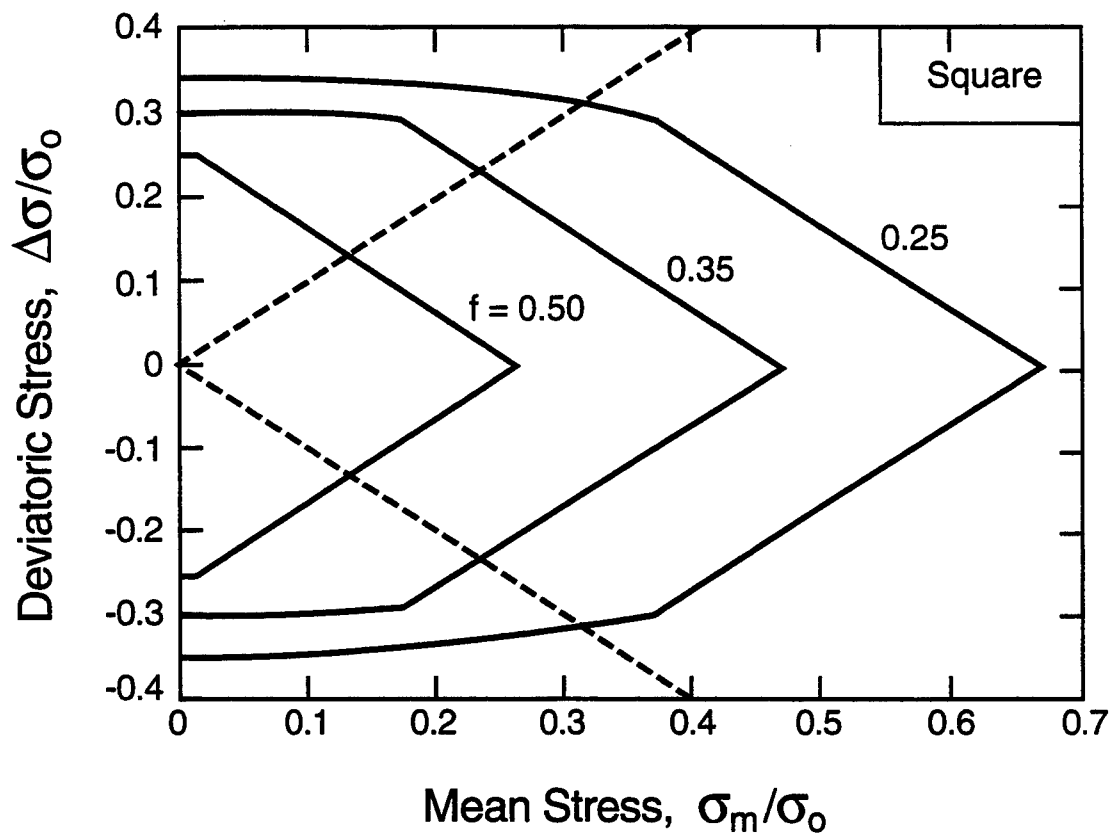


Figure 12(a)

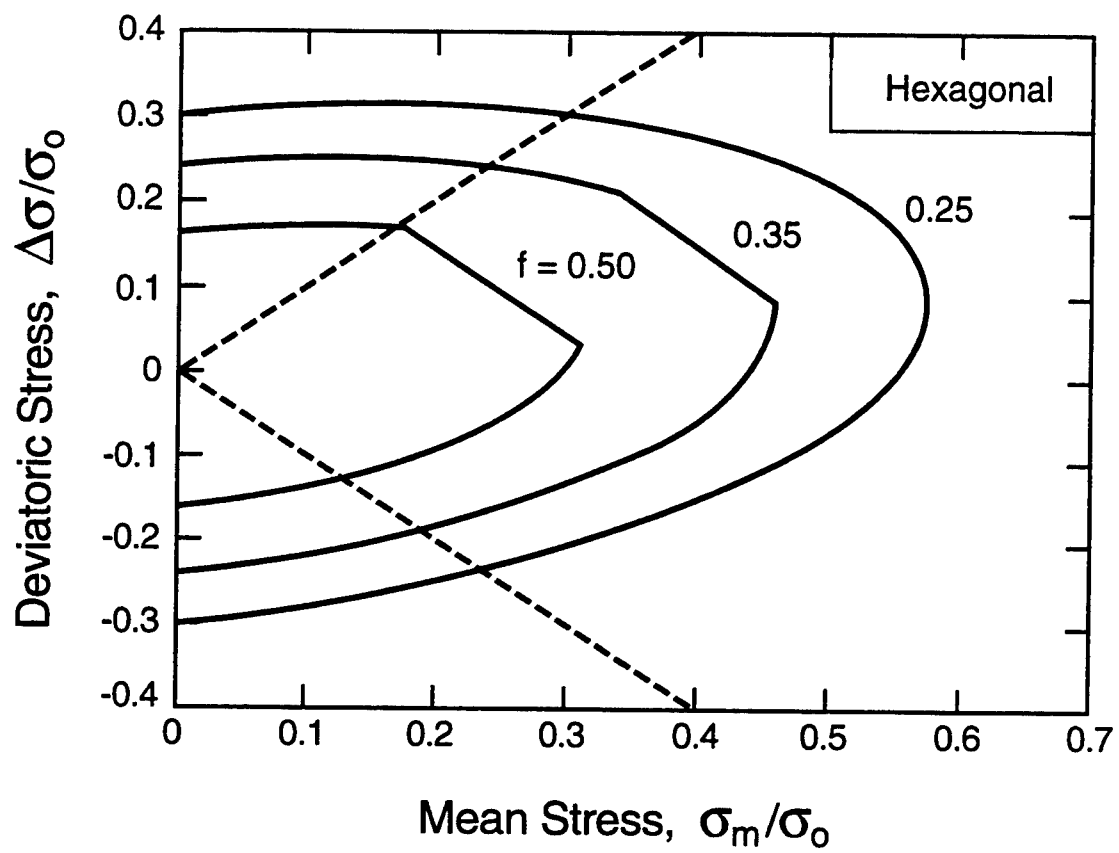


Figure 12(b)

Models of High-Temperature, Environmentally Assisted Embrittlement in Ceramic-Matrix Composites

Anthony G. Evans,* Frank W. Zok,* Robert M. McMeeking, and Zheng Z. Du

Materials Department, University of California, Santa Barbara, California 93106-5050

The intermediate-temperature oxidation embrittlement, or "pest," effect found in ceramic-matrix composites (CMCs) is shown to have features analogous to stress corrosion cracking. The behavior involves crack growth upon oxidation of the fibers or the fiber coatings to form an oxide that weakens the fibers. It has reaction- and diffusion-controlled regimes. The former occurs at low stresses. The latter occurs at higher stresses. It is controlled by oxygen ingress through the matrix cracks. There is also a crack growth threshold. Expressions for the crack velocity above the threshold are derived as well as the stress dependence of the rupture life.

I. Introduction

CERAMIC-MATRIX composites (CMCs) with non-oxide fibers are subject to a "pest" phenomenon. This is manifest as an embrittlement that predominates at intermediate temperatures between about 500° and 900°C.¹⁻⁹ It occurs at stresses above that needed to cause matrix cracks (typically, 0–100 MPa).¹⁰ It is caused by oxygen ingress from the atmosphere through the cracks. The oxygen locally reacts with the fibers. The reaction product weakens the fibers and may also modify their debonding and friction characteristics. The weakened fibers respond to the stress concentration at the perimeter of unbridged crack segments,^{11,12} causing the cracks to extend. This process repeats until the remaining fibers are unable to support the load and the composite fails. Models describing this embrittlement process are developed. The models predict the time-to-failure in terms of nondimensional parameters.

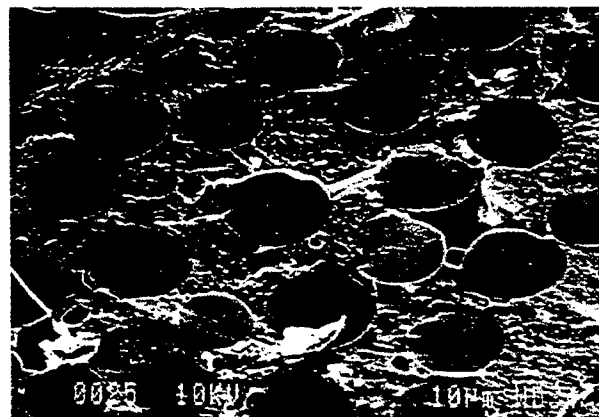
The embrittlement phenomenon occurs under both static and cyclic loading, at temperatures around the "pest" temperature, T_p . Some experimental results presented in other articles^{9,13} (Figs. 1 and 2) are summarized in order to motivate the concepts used in the present analysis. Measurements performed on a unidirectional MAS/SiC composite in air at 750°C provide a vivid demonstration of the phenomenon. When this material is subject to cyclic stress (amplitude, $\Delta\sigma = 235$ MPa), and stress ratio (minimum/maximum), $R = 0.05$, fracture occurs after ~1200 cycles. The corresponding rupture time is 43 min. In contrast, the same material tested at room temperature, subject to the same loads, had an infinite life. The fracture surface after testing at 750°C exhibits substantial embrittlement, characterized by a region around the periphery ~0.7 mm wide in which the fibers fail along the plane of the matrix crack (Figs. 1(a,b)). Fiber pullout occurs within the central (unembrittled) region, comprising about half the cross section. The net-section stress on this central region at the onset of fracture is comparable to

the ultimate tensile strength of the pristine composite,¹³ indicating that the fiber strengths in this region have not been altered by oxidation.

When experiments are performed subject to static load, at a stress equivalent to the peak in the cyclic test, rupture occurs in 41 min, essentially identical to that found in the cyclic tests. Similar embrittlement features are observed on the fracture surface (Fig. 2). The similarities in the rupture times and in the embrittlement features suggest that fracture is controlled by the peak applied stress with no intrinsic cyclic mechanism.



(a)



(b)

Fig. 1. Scanning electron micrographs of fatigue fracture surface of MAS/SiC: (a) inclined overview; (b) close-up of the fracture surface within the embrittled region.

M. Thouless—contributing editor

Manuscript No. 192656. Received May 2, 1995; approved February 26, 1996.

*Member, American Ceramic Society.

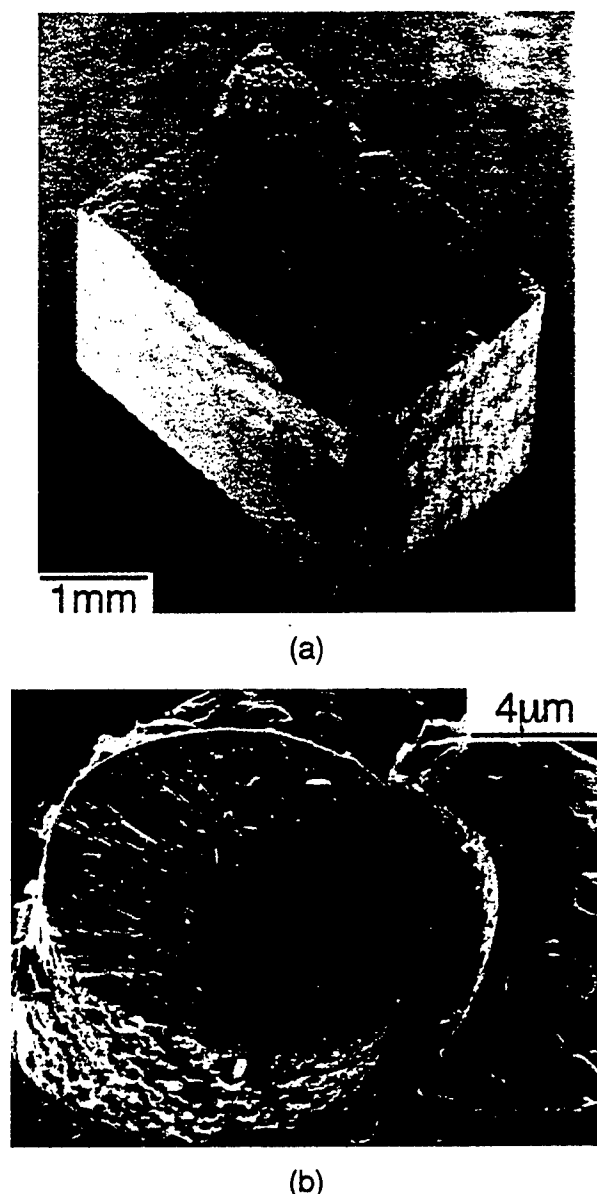


Fig. 2. Fracture surface of specimen subjected to static loading: (a) overview; (b) close-up of fiber in embrittled region.

Consequently, the embrittlement models emphasize the kinetic effects that occur under load. They are expected to apply to both static and cyclic loading.

II. Preliminaries

The models to be developed are based on the above experimental findings. They invoke a degradation zone that spreads through the composite, resulting in a time-dependent tensile strength, once the stress has exceeded that needed to introduce matrix cracks, reminiscent of stress corrosion cracking.^{14,15} The discontinuous nature of the matrix cracks in CMCs^{10,16,17} dictates the actual mechanisms. In 0/90 CMCs, the cracks are discontinuous because they form first in the 90° plies and only partially penetrate the 0° plies (Fig. 3). In unidirectional CMCs, crack interactions cause them to be discontinuous.^{18,19} Degradation occurs according to two rate-limiting phenomena:^{14,15} (i) When the gas flow within the cracks is relatively rapid, all of the fibers bridging those cracks connected to the surface oxidize and weaken simultaneously. When they have degraded sufficiently to fail, the surface cracks extend across the weakened

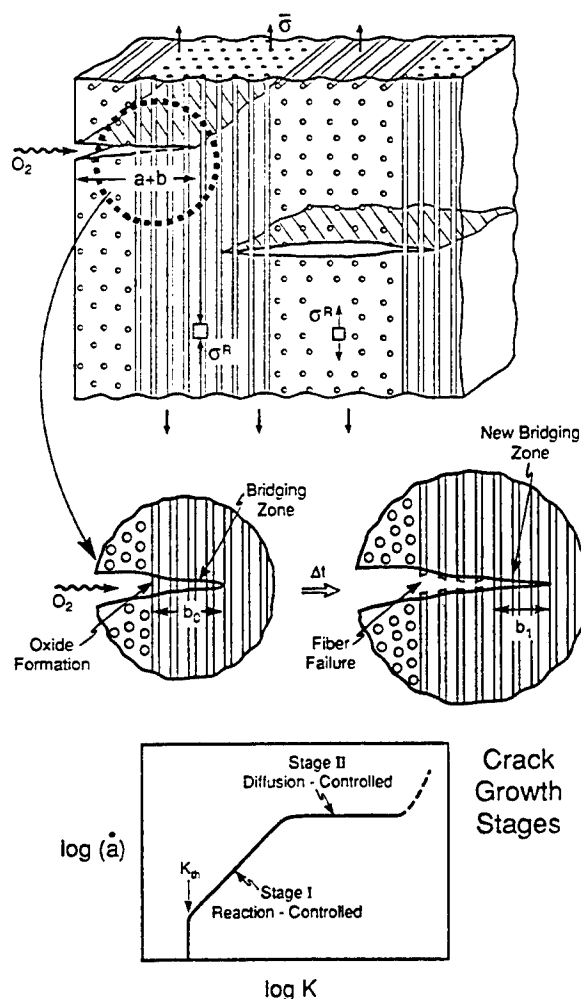


Fig. 3. Schematic illustrating the mechanism of oxidation embrittlement.

zone and form new crack segments bridged by pristine fibers (Fig. 3). This new bridged region again gradually weakens and fails. The process continues in a manner resembling stage I, reaction-controlled, stress corrosion cracking.^{18,19} (ii) When the narrow matrix crack opening inhibits the ingress of oxygen and the egress of the gaseous reaction products (typically CO_2), oxygen gradients develop along the crack. The outmost fibers then oxidize and degrade most rapidly. Thereafter, the fibers fail sequentially, resulting in a fiber degradation front that progresses into the composite. This process is similar to stage II, diffusion-controlled, stress corrosion cracking¹⁸ (Fig. 3). Analyses of each of these phenomena are presented and a critical assessment made of the parameters that specify the regions of dominance.

In some cases, the oxygen can slowly penetrate the material through narrow connecting channels along gaps in the fiber coatings (Fig. 4). This process acts in concert with (i) and (ii) by uniformly degrading the interior fibers and allowing the composite to fail prematurely. This case is not incorporated in the present models.

The overall model is schematically illustrated in Fig. 3. The matrix cracks have an opening displacement governed by the applied stress.¹⁰ The fibers are initially intact. With time, oxygen from the environment diffuses through the cracks and initiates oxidation of the fibers. The oxide thickness increases with time and partially consumes some of the fibers. This process reduces the strength of the fibers.²⁰ It may also affect the friction

stress at the interface. There is a stress concentration on the fibers at the perimeters of the unbridged cracks.¹² When the weakening diminishes the fiber strength below this concentrated stress, the fibers fail. The process then repeats and the unbridged cracks continue to grow. Eventually, the composite fails.

There are three principal phenomena to be modeled: (a) the reduced strength of the fibers with oxide layers, (b) the stress concentration in the fibers at the perimeters of unbridged crack segments, and (c) the oxygen concentration within the matrix cracks, which is coupled with the thickness of the oxide reaction product on the fibers. The philosophy is to use the simplest level of analysis that provides physically realistic results. Then, analytic expressions can be provided in terms of nondimensional parameters with coefficients and exponents to be calibrated by experiment. The basic concept is illustrated for non-oxide fibers in an oxide matrix, but could be readily extended to non-oxide matrices.

III. Fiber Weakening

An initial matrix crack is introduced upon the application of a stress σ .²¹ A portion of this crack, length a , is considered to be unbridged, whereas another segment, length b , is bridged by intact fibers (Fig. 3). For a 0/90 composite, the initial value a_0 would be the ply thickness, h . For a unidirectional composite, a_0 would refer to a manufacturing flaw. Upon subsequent isothermal exposure at temperature T , oxygen reacts with each of the bridging fibers to form an oxide reaction product, thickness d . For diffusion-controlled oxide growth, exemplified by SiO_2 on either SiC or Si_3N_4 fibers, d has the temporal form²²

$$\dot{d} = \Omega D_0 c X_0 / d \quad (1)$$

where D_0 is the oxygen diffusivity in the oxide, X_0 is the mole fraction of oxygen in the atmosphere at the fiber location, c is the molar gas concentration, and Ω is the molecular volume of oxygen. The diffusivity D_0 is Arrhenius and has the form

$$D_0 = D_0^* \exp(-Q_0/R_g T) \quad (2)$$

where Q_0 is the activation energy for oxygen diffusion through the oxide, D_0^* is the reference diffusivity, and R_g is the gas constant. For a uniform oxygen concentration, this oxide thickness can be re-expressed as

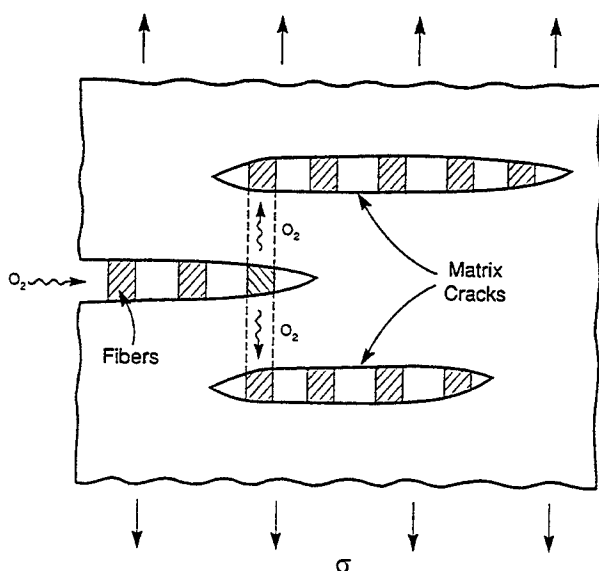


Fig. 4. Schematic of oxygen ingress between matrix cracks, through the fiber coatings.

$$d = \sqrt{2\Omega D_0 c X_0} \sqrt{t} = H \sqrt{t} \quad (3)$$

where H is the parabolic rate constant, which would not normally be steady-state, because X_0 can vary with time and fiber location in the matrix crack.

The formation of the oxide weakens the fibers. The oxide layer is assumed to behave as a surface flaw.²³ When the oxide thickness becomes large enough to cause weakening, the scaling relation for the fiber strength S should then be $S \sim 1/\sqrt{d}$. The consequent strengths are

$$S = S_0 \quad (t < t_0) \quad (4a)$$

$$S = S_0(t_0/t)^{1/4} \quad (t > t_0) \quad (4b)$$

where t_0 is the time taken for the fibers to be weakened below their initial strength, S_0 . This occurs when the oxide thickness is d_0 , related to t_0 by Eq. (3). Note that t_0 decreases as T increases, in accordance with the temperature dependence of the diffusivity, D_0 .

IV. Stress Concentrations

The incidence of fiber failure is governed by the magnitude of the concentrated stress, σ_c , acting on the row of fibers at the edge of the unbridged segment of the matrix crack. This stress is given by (Fig. 5)^{11,12}

$$\sigma_c = \left(\frac{\sigma}{f}\right) \sqrt{1 + \eta^{2/3}} \quad (5)$$

with

$$\eta = \frac{3\pi\beta f^2 E_f E_a \tau}{(1-f)^2 E_m^2 A R \sigma}$$

where τ is the interface friction stress, R is the fiber radius, f is the fiber volume fraction, E_f and E_m are Young's moduli of the fiber and matrix, respectively, E is the longitudinal composite modulus, and A is an anisotropy factor of order unity.¹¹ The coefficient β is a large-scale slip coefficient:¹² $\beta \approx 1/3$ for typical f and E_f/E_m .

V. Oxide Thickness

As oxygen from the environment diffuses through the cracks and initiates oxidation of the fibers, there is a time-dependent distribution of the oxygen mole fraction X_0 along the crack, x .^{24,25} There is a corresponding distribution of the thickness d of the oxide layers on the fibers (Fig. 6). These problems are

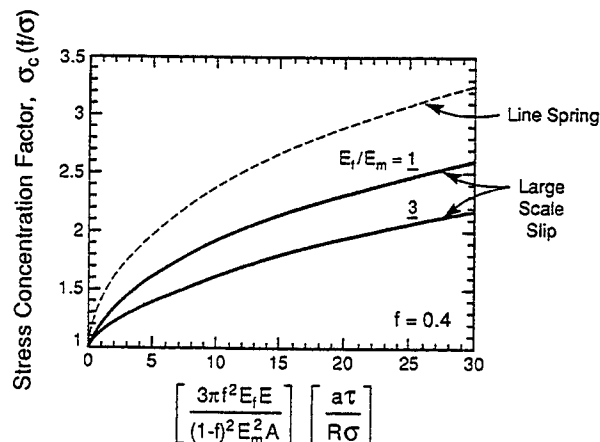


Fig. 5. Stress concentration, σ_c , on fibers at perimeter of unbridged crack, length a .^{11,12}

coupled, such that $X_o(x,t)$ and $d(x,t)$ must be solved simultaneously. The problem is inherently transient and has no steady state.* The solution depends upon the pressure and composition of the gas within the crack. Conservation of the oxygen passing along the crack requires that²⁶

$$\frac{\partial(cX_o)}{\partial t} + \frac{\partial(cX_o v)}{\partial x} + \frac{\partial j_o}{\partial x} + \phi_o = 0 \quad (6)$$

where v is the molar average velocity of gas in the crack, c is its molar concentration, x is the position along the crack, j_o is the molar oxygen flux, and ϕ_o is the molar rate of oxygen absorption per unit volume of space in the crack. The gas is considered to be a two-component mixture including oxygen and an unreactive gas, say, nitrogen. The oxygen flux j_o , given by²⁴

$$j_o = -c\bar{D} \frac{\partial X_o}{\partial x} \quad (7)$$

occurs relative to the mixture moving at velocity v . The diffusivity \bar{D} has Knudsen and molecular contributions, with the slower process being dominant. The Knudsen diffusion coefficient for a narrow channel is

$$D_k = \frac{2\Delta}{3} \sqrt{\frac{8R_g T}{\pi M_o}} \quad (8)$$

where M_o is the molar mass of oxygen. For small crack openings Δ , D_k is assumed to control \bar{D} .

*In a previous treatment of this problem, Lamouroux et al.²⁴ make the erroneous initial assumption that steady state exists and they use a steady-state differential equation.

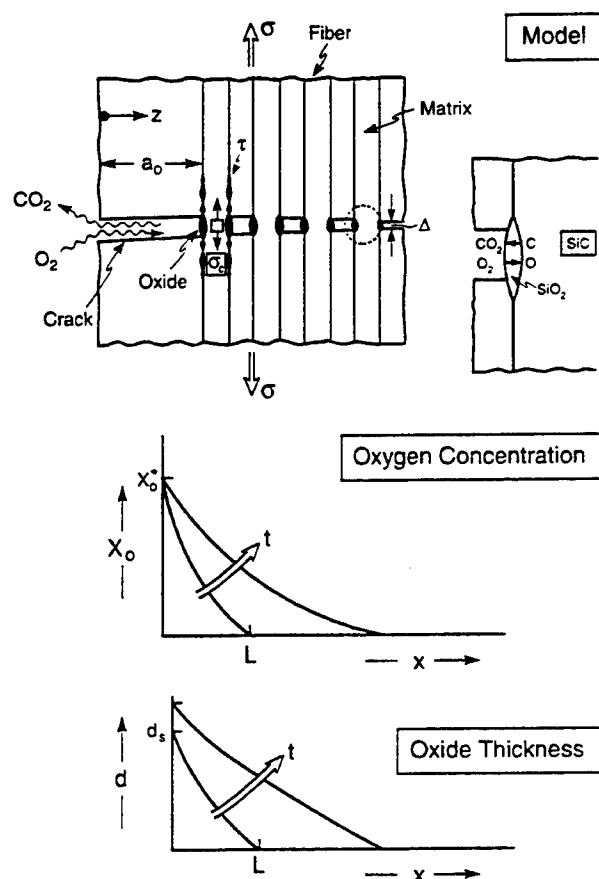


Fig. 6. Schematic of oxygen concentration gradient in the crack and the corresponding gradient in oxide thickness.

The velocity of the gas mixture in the crack occurs by convection to replenish oxygen as it is lost in the oxidation process. It is assumed that gas ingress occurs without resistance, so that the mixture everywhere in the crack is at ambient temperature and pressure. The molar concentration c is therefore uniform and constant. Consideration of Eq. (6), together with an equivalent for the inert gas, gives

$$c \frac{\partial v}{\partial x} + \phi_o = 0 \quad (9)$$

From Eq. (1), the molar rate of oxygen consumed by the reaction with the fibers and the coatings is

$$\phi = \lambda f D_o c X_o / R d \quad (10)$$

where f is the volume fraction of fibers in the composite and λ is the length of the fibers oxidized at each matrix crack, divided by the crack opening. The parameter λ is assumed to be constant and uniform in the crack.

Combination of Eqs. (6), (7), and (10) then yields

$$\frac{\partial X_o}{\partial t} + \frac{\partial(X_o v)}{\partial x} - \bar{D} \frac{\partial^2 X_o}{\partial x^2} + \frac{\lambda f D_o X_o}{R d} = 0 \quad (11)$$

This equation has been solved simultaneously with Eq. (9), subject to integration of Eq. (1).²⁷ The initial conditions are everywhere $X_o = 0.2$ and $d = 0$. The boundary conditions are $X_o = 0.2$ at $x = 0$, as well as $dX_o/dx = 0$ and $v = 0$ at the crack center. Upon using literature data for SiC, the key results²⁷ (Fig. 7) demonstrate how the oxygen concentration gradient develops, upon initial matrix cracking, as the oxygen penetrates the composite through the cracks. There are corresponding trends in the oxide thickness (Fig. 8). At longer times, the oxygen concentration becomes relatively uniform. This happens quickly as \bar{D}/D_o becomes relatively large.

In order to apply these results to oxidation embrittlement, an analytical approximation is required for the oxide thickness. Inspection of Fig. 8 indicates that

$$\sqrt{d} \approx \sqrt{d_s} - x/\sqrt{L} \quad (12)$$

where d_s is the oxide thickness at the surface and L is a penetration depth, having the functional form²⁷

$$L = \xi R \bar{D} / D_o f \quad (13)$$

where ξ is a nondimensional fitting coefficient. Note that L decreases as the temperature increases, because more oxygen is consumed to create an oxide reaction product.

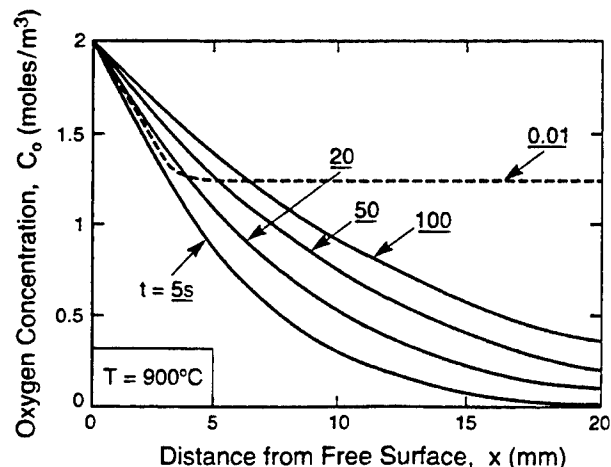


Fig. 7. Variations in oxygen concentration in the crack at 900°C calculated for diffusivities relevant to Nicalon fibers in CMCs.²⁷

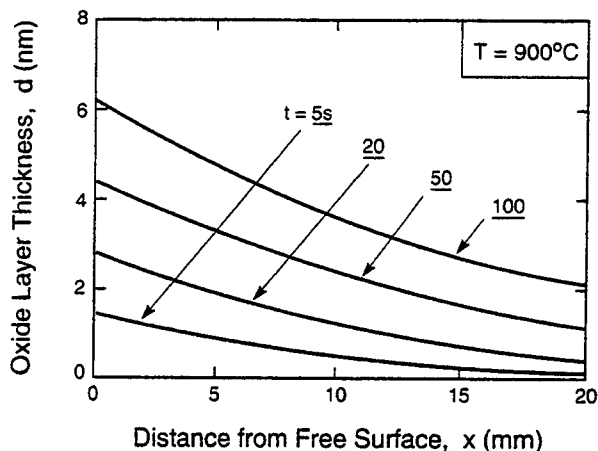


Fig. 8. Variations in oxide thickness on the fibers at 900°C calculated for diffusivities relevant to Nicalon fibers.²⁷

VI. Crack Growth

(1) Reaction Controlled

When the crack is propagating slowly, such that the oxygen concentration in the crack is uniform, all of the fibers within the crack are expected to fail when their strength, S , decreases to the concentrated stress, σ_c . This occurs at a time Δt , which can be obtained from Eqs. (4) and (5) as

$$\frac{\Delta t}{t_0} = \left(\frac{fS_0}{\sigma} \right)^4 [1 + \eta^{2/3}]^{-2} \quad (14)$$

When the fibers fail, the unbridged crack extends by b , the original bridging zone size, causing another bridged segment to form. The magnitude of b for finite length cracks does not have a simple analytical form. For present purposes, the solution for a semi-infinite crack (Fig. 9) is used as an approximation. It is given by¹²

$$\frac{b}{R} \approx \frac{(3\sqrt{\pi}/4)^{2/3}}{5} \left(\frac{1-f}{f} \right)^{1/3} \left[\frac{\sigma}{\tau} \sqrt{\frac{a+b}{R}} \right]^{2/3} \times \left[\sigma \sqrt{\frac{\pi(a+b)}{E\Gamma_m(1-f)}} - 1 \right] \quad (15)$$

where Γ_m is the matrix fracture toughness. For most cases of interest, the initial unbridged crack is relatively large, $a \gg b$ (as in 0/90 composites, with initial ply cracks), whereupon Eq. (15) simplifies to

$$\frac{b}{R} \approx \frac{(3\sqrt{\pi}/4)^{2/3}}{5} \left(\frac{1-f}{f} \right)^{1/3} \left[\frac{\sigma}{\tau} \sqrt{\frac{a}{R}} \right]^{2/3} \times \left[\sigma \sqrt{\frac{\pi a}{E\Gamma_m(1-f)}} - 1 \right] \quad (16)$$

The effective crack velocity at constant applied stress σ and fixed friction stress τ is

$$\dot{a} \approx b/\Delta t \quad (17)$$

Hence, from Eqs. (14) and (16),

$$\frac{d\alpha}{d\hat{t}} = A\alpha^{1/3} [B\sqrt{\alpha} - 1] [1 + C\alpha^{2/3}]^2 \quad (18)$$

where $\alpha = a/R$, $\hat{t} = \Delta t/t_0$,

$$A = 0.24(\sigma/fS_0)^4 (1-f)^{1/3} (\sigma/\tau)^{2/3} / f^{1/3}$$

$$B = \sigma \sqrt{\frac{\pi R}{E\Gamma_m(1-f)}}$$

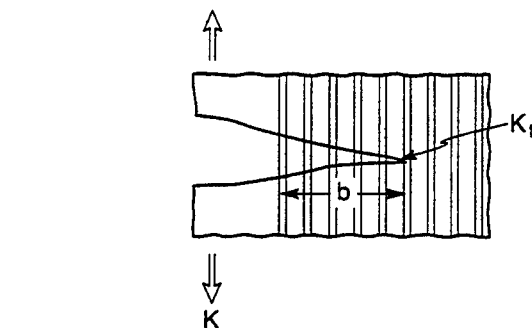
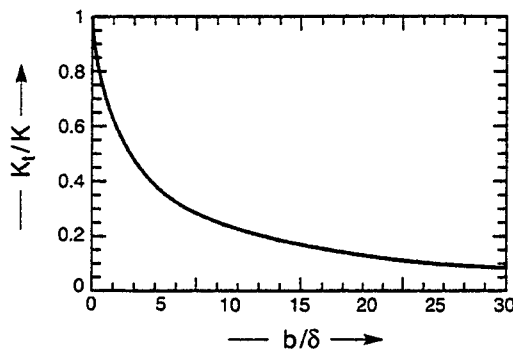


Fig. 9. Ratio of crack tip stress intensity, K_t , to applied value, K , as a function of bridging zone size, b , normalized by a length dimension,⁷ $\delta = (3AEK/\beta^2)^{2/3}$, where $\beta = [4f^2 E_r E^2 \tau / R(1-f)^2 E_m^2]^{1/2}$.

$$C = \left[\frac{3\pi f^2 \tau}{(1-f)^2 \sigma} \right]^{2/3}$$

Rearranging identifies an expression for the time t_c taken for the unbridged crack to grow from its initial size a_0 to a larger size, a , at constant stress σ and fixed τ as

$$\int_{a_0}^a [\alpha^{-1/3} (B\sqrt{\alpha} - 1)^{-1} (1 + C\alpha^{2/3})^{-2}] d\alpha = A\hat{t}_c \quad (19)$$

Plotting yields the characteristics summarized in Fig. 10.

It is apparent that the behavior can be separated into two regions:

(i) A threshold below which the crack cannot propagate is given by $B\sqrt{\alpha} < 1$. Inserting the definitions of B and α identifies a threshold stress S_{th} and a threshold stress intensity factor K_{th} below which there is no crack growth,

$$K_{th} = \sqrt{E\Gamma_m(1-f)} \quad (20)$$

where $K_{th} = S_{th}\sqrt{\pi a}$. The threshold arises because the matrix crack cannot extend when $K < K_{th}$, even in the absence of bridging fibers. A second requirement is that

$$\sigma < 3\pi f^2 \tau a / (1-f)^2 R \quad (21)$$

(ii) Above the threshold, the crack extends according to a power-law growth rate given by

$$d\alpha/d\hat{t} \approx ABC^2 \alpha^{13/6} \quad (22a)$$

or

$$\dot{a}t_0 = \left[\frac{0.7}{f^{5/3}(1-f)^{17/6}} \right] \left[\frac{\tau^{2/3}}{S_0^4 \sqrt{E\Gamma_m R^{2/3}}} \right] K^{13/3} \quad (22b)$$

where K is the stress intensity factor. The power-law dependence is again reminiscent of stress corrosion cracking.

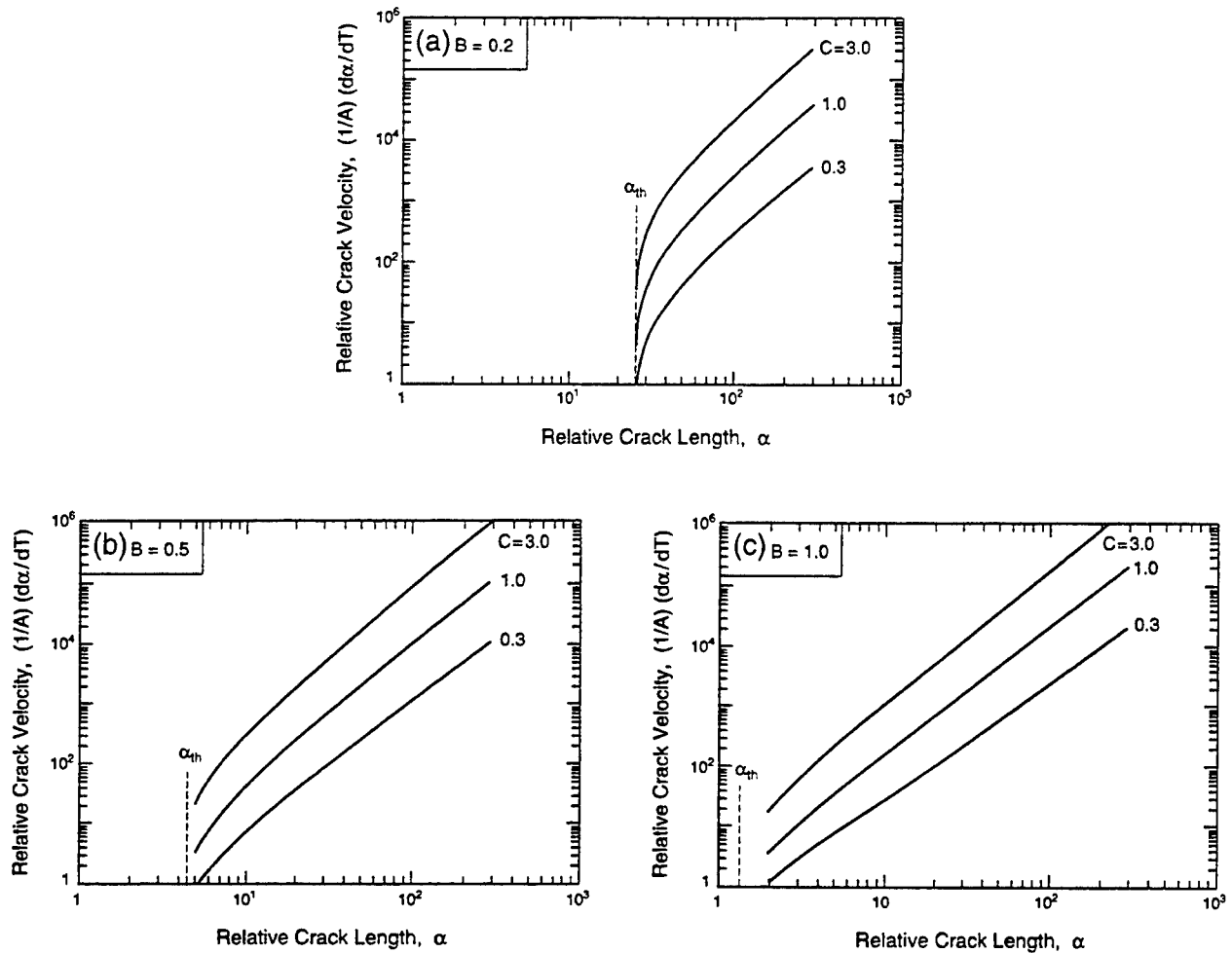


Fig. 10. Trends in nondimensional crack velocity $d\alpha/dT$ with crack length α . Note that there is a threshold α_{th} below which $d\alpha/dT \rightarrow 0$. Above the threshold, there is a power-law dependence of $d\alpha/dT$ on α .

The propagation time, Δt_c , for a crack to extend from a_0 to a is

$$\Delta t_c = \frac{(6/7)}{ABC^2} (R/a_0)^{7/6} [1 - (a_0/a)^{7/6}] \quad (23a)$$

or in actual time

$$\frac{\Delta t_c}{t_0} = 0.1 f^{5/3} (1-f)^{17/6} \left[\frac{S_0^4 \sqrt{E\Gamma_m}}{(\sigma^{13/3} \tau^2)^{1/3} R^{1/2}} \right] \left(\frac{R}{a_0} \right)^{7/6} \left[1 - \left(\frac{a_0}{a} \right)^{7/6} \right] \quad (23b)$$

where the initial unbridged crack size a_0 is equal to the ply thickness h for 0/90 composites.

(2) Diffusion Controlled

When the magnitude of the oxygen penetration distance L (Eq. (13)) is small, diffusion-controlled crack growth can occur. The situation is depicted in Fig. 6. The bridged segment contains fibers subject to an oxide thickness distribution given by Eq. (12). A steady state may then be envisaged in which the weakest fibers at the perimeter of the unbridged zone fail, causing the entire bridged configuration to extend by the fiber spacing, s . The process repeats at time intervals, Δt_1 , governed by the oxide thickness, d_1 , that exists at the next row of fibers. The corresponding crack velocity would be

$$\dot{a}_s = s/\Delta t_1 \quad (24)$$

According to this scheme, the oxide thickness, d_1 , is obtained from Eq. (12) as

$$\sqrt{d_1} = \sqrt{d_c} - s/\sqrt{L} \quad (25)$$

Here, d_c is the critical oxide thickness at which the fibers fail, obtained from Eqs. (3) to (5) as

$$d_c = d_0 (S_0 f / \sigma)^2 / (1 + \eta^{2/3}) \quad (26)$$

The time Δt_1 is related to the difference between d_1 and d_c . It is given approximately by Eq. (3) as

$$\Delta t_1 \approx [(d_c - d_1)/H]^2 \quad (27)$$

An assumption is now needed about the location within the crack where the oxygen concentration is atmospheric. Since the crack openings are much larger in the unbridged than the bridged regions of the crack,¹⁴ it is assumed that this location occurs at the end of the unbridged crack. Then, combining Eqs. (25) to (27) gives

$$\Delta t_1 = 4(S_0 f / \sigma)^4 (s/L)^2 (1 + \eta^{2/3})^{-2} \quad (28)$$

Note that upon comparison with reaction-controlled behavior, Eq. (14), $\Delta t_1 \equiv 4 \Delta t_1 (s/L)^2$.

Since $s = 2R/\sqrt{f}$, the crack velocity becomes,

$$\dot{a}_{t_0} = (\xi^2/8) f^{5/2} R (\bar{D}/D_0)^2 (\sigma/S_0)^4 (1 + \eta^{2/3})^2 \quad (29a)$$

or

$$\dot{a}_{t_0} = (1/8) (L^2/R) f^{9/2} (\sigma/S_0)^4 (1 + \eta^{2/3})^2 \quad (29b)$$

This is the stage II, steady-state velocity \dot{a}_s of the matrix crack. It is independent of crack length, but still dependent on stress.

It can be compared with Eq. (22) for stage I, reaction-controlled propagation. By equating \dot{a} to \dot{a}_c , the transition from stage I to stage II could be specified, as well as the corresponding crack length, a_c .

The overall behavior is sketched in Fig. 11(a). The threshold stress intensity factor, K_{th} , is indicated. The slope, $\dot{a}(K)$, in the reaction-controlled stage I is 13/3. Diffusion-controlled stage II is subject to constant crack velocity, at fixed applied stress, σ ; but this velocity does depend on σ .

The propagation time in stage II, Δt_c , is

$$\Delta t_c = (a_c - a_i) / \dot{a}_c \quad (30)$$

where a_c is the crack size at which the remaining composite is unable to support the load.

A net section stress criterion can be used for a_c , because of the notch insensitivity of most CMCs, subject to fiber pullout.²⁸ Composite failure then happens when the net-section stress reaches the ultimate tensile strength, S . This condition obtains when the crack length a_c becomes

$$a_c/w = 1 - \sqrt{\sigma/S} \quad (31)$$

where w is the width of the section that supports the load in the absence of embrittlement.

VII. Rupture Time

The rupture life predicted by the model has the features depicted in Fig. 11(b). When $K < K_{th}$, the life is essentially infinite. When $K > K_{th}$, the life t_f can be estimated from $\dot{a}(K)$ (Eqs. (23) and (30)), in the normal manner, by separating the variables and integrating the crack length from its initial value,

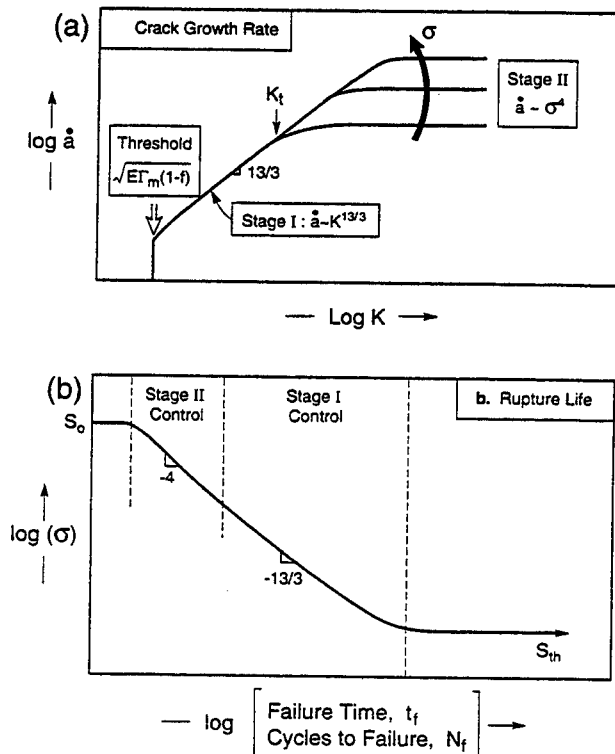


Fig. 11. Schematic of trends in the rupture life with applied stress, showing the reaction-controlled and diffusion-controlled regimes: (a) crack growth rate \dot{a} , as a function of stress intensity factor, K ; (b) rupture life t_f , as a function of applied stress, σ . The threshold, as well as stages I and II, are identified.

a_0 , to the critical value, a_c .^{15,29} A similar analysis may be used to obtain the cycles to failure, N_f , when the loading is cyclic.²⁹

If the unexposed fibers retain their original strength, the propagation time in stage I, Δt_c , scales according to

$$\Delta t_c = 0.1 t_0 \left[\frac{S_0 \sqrt{E \Gamma_m} R^{2/3}}{(\sigma^{13/3} \tau)^{1/3} h^{7/6}} \right] \left[1 - \left(\frac{h}{a_i} \right)^{7/6} \right] f^{5/3} (1 - f)^{17/6} \quad (32)$$

where t_0 must be calibrated by experiment. The term S_0 reflects the influence of the initial fiber strength, Γ_m , the effect of matrix toughness, and τ the influence of the friction stress. For a specific composite (fixed S_0 , Γ_m , τ) a further simplification is

$$\Delta t_c = t_0 (\sigma_*/\sigma)^{13/3} [1 - (h/a_i)^{7/6}] \quad (33)$$

where σ_* is a reference stress, which may change with time if τ is affected by oxidation.

At low stresses, the fracture time is controlled by Δt_c , through the rate of growth of the oxide reaction product on the fibers. It is strongly temperature and stress dependent. The rupture time decreases as either the temperature or the stress increases. At high stresses, fracture may become controlled by oxygen diffusion along the matrix crack. In this regime, as temperature increases, more oxygen is consumed near the crack mouth to form an oxide of greater thickness, such that less oxygen penetrates into the material through the cracks (smaller L). The growth rate of the cracks, \dot{a} , may thus diminish as the temperature increases, dependent on the relative magnitudes of t_0 and L . The resultant behavior is characteristic of a "pest" phenomenon, with a maximum embrittlement occurring at intermediate temperature. This effect has been noted previously and elaborated in other articles.^{24,25} It is again similar to stress corrosion.^{18,19} However, this is not the only (or perhaps even the predominant) source of the "pest" effect. Two other factors may be more important, both associated with the temperature dependence of the viscosity of the oxide reaction product: (i) At high temperatures, the oxide can flow into the matrix cracks. This process may block access of oxygen to the composite interface. (ii) Oxide flow also diminishes the severity of the fiber strength degradation by alleviating stress concentrations in the fibers caused by the oxide. All of these possibilities require further experimental and theoretical assessment before the "pest" effect can be fully explained.

When narrow pathways exist between neighboring matrix cracks, through gaps at the interfaces, the internal fibers can degrade, changing S_0 in Eq. (29). The reduced strengths could be obtained from Eqs. (1) and (4) if the gas-phase concentration and composition inside the composite were known. In some cases, these factors are controlled by carbon, present as either a fiber coating or a residue. Then CO and CO₂ are produced internally at a rate that limits the O₂/CO₂ ratio, enabling slow, controlled oxidation of the internal fibers. In other cases, there are oxygen sinks in the material, such as B. Analysis of these effects is beyond the scope of the present study.

VIII. Concluding Remarks

A kinetic model has been presented that describes the ingress of oxygen through matrix cracks, as well as its reaction with the fibers and fiber coatings to cause stress oxidation cracking in non-oxide CMCs. The results of the model are given in the form of nondimensional groups of kinetic parameters that need to be calibrated by a few critical experiments. Once calibrated, the results could be used to predict the behavior over a wide range of conditions.

The present model does not have features that explicitly suppress stress oxidation at high temperatures. This phenomenon is attributed to temperature conditions that sufficiently diminish the viscosity of the oxide reaction products that they can flow and impede oxygen access, as well as ameliorate the weakening of the oxidized fibers. Additional modeling would be needed to introduce these effects in a systematic manner.

References

- ¹J. J. Brennan and K. M. Prewé, "Silicon Carbide Fiber-Reinforced Glass-Ceramic Matrix Composites Exhibiting High Strength and Toughness," *J. Mater. Sci.*, **17**, 2371–83 (1982).
- ²J. J. Brennan, "Interfacial Characterization of Glass and Glass-Ceramic Matrix/Nicalon Fiber Composites"; p. 561 in *Tailoring of Multiphase Ceramics*, Edited by R. E. Tressler et al. Plenum Press, New York, 1986.
- ³J. J. Brennan, "Interface Chemistry and Bonding in Fiber Reinforced Glass-Ceramic Matrix Composites"; 231–39 in *Ceramic Microstructures: The Role of Interfaces*, Edited by J. A. Pask and A. G. Evans. Plenum, New York, 1988.
- ⁴J. J. Brennan, "Interfacial Studies of Chemical Vapor Infiltrated Ceramic Matrix Composite," *Mater. Sci. Eng.*, **A126**, 203–23 (1990).
- ⁵R. F. Cooper and K. Chyung, "Structure and Chemistry of Fiber-Matrix Interfaces in Silicon Carbide Fiber-Reinforced Glass-Ceramic Composites: An Electron Microscopy Study," *J. Mater. Sci.*, **22**, 3148–60 (1987).
- ⁶R. L. Stewart, K. Chyung, M. P. Taylor, and R. F. Cooper, "Fracture of SiC Fiber/Glass-Ceramic Composites as a Function of Temperature"; pp. 33–51 in *Fracture Mechanics of Ceramics, Vol. 7, Composites, Impact, Statistics, and High-Temperature Phenomena*, Edited by R. C. Bradt, A. G. Evans, D. P. H. Hasselman, and F. F. Lange. Plenum Press, New York, 1986.
- ⁷E. Bischoff, M. Rühle, O. Sbaizero, and A. G. Evans, "Microstructural Studies of the Interfacial Zone of a SiC-Fiber-Reinforced Lithium Aluminosilicate Glass-Ceramic," *J. Am. Ceram. Soc.*, **72**, 741–45 (1989).
- ⁸L. A. Bonney and R. F. Cooper, "Reaction-Layer Interfaces in SiC-Fiber-Reinforced Glass Ceramics: A High-Resolution Scanning Transmission Electron Microscopy Analysis," *J. Am. Ceram. Soc.*, **73**, 1916–21 (1990).
- ⁹F. Heredia, J. McNulty, F. Zok, and A. G. Evans, "Oxidation Embrittlement Probe for Ceramic-Matrix Composites," *J. Am. Ceram. Soc.*, **78** [8] 2097–100 (1995).
- ¹⁰A. G. Evans and F. W. Zok, "Review: The Physics and Mechanics of Fibre-Reinforced Brittle Matrix Composites," *J. Mater. Sci.*, **29**, 3857–96 (1994).
- ¹¹B. Budiansky and Y. L. Cui, "On the Tensile Strength of a Fiber-Reinforced Ceramic Composite Containing a Crack-like Flaw," *J. Mech. Phys. Solids*, **42**, 1–19 (1994).
- ¹²Z. C. Xia, I. W. Hutchinson, A. G. Evans, and B. Budiansky, "On Large Scale Sliding in Fiber-Reinforced Composites," *J. Mech. Phys. Solids*, **42**, 1139–58 (1994).
- ¹³J. McNulty, F. W. Zok, and A. G. Evans, "Fatigue and Rupture of Ceramic Matrix Composites at Elevated Temperature"; unpublished work.
- ¹⁴S. M. Wiederhorn, "Effects of Water Vapor on Crack Growth in Glass," *J. Am. Ceram. Soc.*, **50**, 407–14 (1967).
- ¹⁵S. M. Wiederhorn, "Subcritical Crack Growth in Ceramics"; pp. 613–46 in *Fracture Mechanics of Ceramics*, Vol. 2, Edited by R. C. Bradt et al. Plenum Press, New York, 1974.
- ¹⁶Z. C. Xia and I. W. Hutchinson, "Matrix Cracking of Cross-Ply Ceramic Composites," *Acta Metall. Mater.*, **42**, 1933–45 (1994).
- ¹⁷R. Y. Kim and N. Pagano, "Crack Initiation in Unidirectional Brittle Matrix Composites," *J. Am. Ceram. Soc.*, **74**, 1082–90 (1991).
- ¹⁸S. M. Spearing and F. W. Zok, "Matrix Crack Spacing in Brittle Matrix Composites," *Acta Metall. Mater.*, **40**, 2033–43 (1992).
- ¹⁹S. M. Spearing and F. W. Zok, "Stochastic Aspects of Matrix Cracking in Brittle Matrix Composites," *J. Eng. Mater. Technol.*, **115**, 314 (1994).
- ²⁰M. D. Thouless, O. Sbaizero, L. S. Sigl, and A. G. Evans, "Effect of Interface Mechanical Properties on Pullout in a SiC-Fiber-Reinforced Lithium Aluminum Silicate Glass-Ceramic," *J. Am. Ceram. Soc.*, **72**, 525–45 (1989).
- ²¹C. Xia, R. R. Carr, and I. W. Hutchinson, "Matrix Cracking in Cross Ply Ceramic Matrix Composites," *Acta Metall. Mater.*, **41**, 2365 (1993).
- ²²J. A. Costello and R. E. Tressler, "Isotope Labelling Studies of the Oxidation of Silicon Carbide at 1000° and 1300°C," *J. Electrochem. Soc.*, **131**, 8, 1944–47 (1984).
- ²³T. Helmer, H. Peterlik, and K. Kromp, "Coating of Carbon Fibers—The Strength of Fibers," *J. Am. Ceram. Soc.*, **78**, 133–36 (1995).
- ²⁴F. Lamouroux, R. Naslain, and J.-M. Thébaud, "Kinetics and Mechanisms of Oxidation of 2D Woven C/SiC Composites: I. Experimental Approach," *J. Am. Ceram. Soc.*, **77**, 2049–57 (1994).
- ²⁵F. Lamouroux, R. Naslain, and J.-M. Thébaud, "Kinetics and Mechanisms of Oxidation of 2D Woven C/SiC Composites: II. Theoretical Approach," *J. Am. Ceram. Soc.*, **77**, 2058 (1994).
- ²⁶D. R. Poirier and G. M. Geiger, *Transport Phenomena in Materials Processing*. The Metallurgical Society, Warrendale, PA, 1994.
- ²⁷Z. Z. Du and R. M. McMeeking, "Oxidation of Fibers Exposed by Matrix Cracks in Ceramic Matrix Composites"; unpublished work.
- ²⁸C. M. Cady, T. J. Mackin, and A. G. Evans, "Silicon Carbide/Calcium Aluminosilicate: A Notch-Insensitive Ceramic-matrix Composite," *J. Am. Ceram. Soc.*, **78**, 77–82 (1995).
- ²⁹A. G. Evans and E. R. Fuller, "Crack Propagation in Ceramic Materials under Cyclic Loading Conditions," *Metall. Trans.*, **5**, 27 (1994). □

Creep damage in SiC/SiC composites

A.G. Evans^a, C. Weber^b

^a*Division of Applied Sciences, Harvard University, Cambridge, MA 02138, USA*

^b*Materials Department, University of California, Santa Barbara, CA 93106, USA*

Received 27 February 1995

Abstract

In SiC/SiC composites, the matrix has greater creep resistance than the fibers. The consequent fiber deformation has been shown to transfer sufficient stress onto the matrix that, above a threshold, matrix cracks propagate across the 0° plies. This process increases the compliance of the composite and reloads the fibers, resulting in creep rates dominated by the fibers. The extent of the compliance change is limited by the high temperature interface friction stress, τ , through its effect on the crack density. After creep, τ is diminished substantially from its room-temperature magnitude, resulting in low crack densities and extensive fiber pull-out. A matrix-cracking solution for composites with creeping fibers has been used to correlate the experimentally determined rates of compliance change and the creep strain.

Keywords: Creep; Deformation; SiC/SiC composites; Matrix cracking

1. Introduction

The high-temperature performance of ceramic-matrix composites (CMCs) is usually limited by one of two phenomena: embrittlement or creep [1-6]. The longevity of *non-oxide* CMCs is presently governed by their susceptibility to a "pest" problem that operates in the temperature range 500 to 900 °C. This problem is being addressed by attending to the chemistry of the fibers and interfaces. Should this limitation be resolved, creep would become the temperature-limiting phenomenon, as it is now in oxide CMCs. High strength CMCs are typically made with fine-grained fibers. Such fibers are susceptible to creep and rupture, causing high-temperature composite performance to be fiber-creep-limited [7,8]. This situation is addressed in the present article.

There are two basic situations to be considered when CMCs are creep-limited, dependent on the relative creep strengths of the fibers and the matrix. When the fibers have the greater creep resistance, matrix deformation transfers stress to the fibers in accordance with the McLean model [9]. Consequently, for most situations of practical interest, the composite response to loading

along one fiber axis is controlled *solely by the creep properties of the fibers*. Such behavior has been demonstrated for SiC/CAS composites [10]. When the fibers have a lower creep resistance than the matrix, the composite response is less obvious. Within this category there appear to be two behaviors, dependent on the relative stiffness of the matrix: (a) if the matrix has a high compliance, as in SiC/C composites, elastic straining of the matrix occurs readily, and composite creep is still controlled by the fibers [11]; (b) high-stiffness matrices, exemplified by SiC/SiC, behave differently [5,6]. Composites of the latter type are examined in this study.

2. Theoretical background

In CMCs comprising fibers that creep in an elastic matrix, fiber creep transfers stress to the matrix [4-6]. This causes matrix cracking. The cracking in turn diminishes the matrix stiffness. This enables the fibers to reload, inducing further creep. The interaction between fiber creep and matrix cracking is the principal theme of this paper. The available theoretical results that relate to these phenomena are summarized as background to the experimental study and for the interpretation of the results.

* Corresponding author.

2.1. Creep-induced matrix cracking

Previous analysis has demonstrated that matrix cracks propagate as creep relaxes the fiber-bridging tractions [4,5]. The benchmarking of this behavior for 0/90 composites is provided by two bounds: (a) a threshold stress σ_{th} and (b) a steady-state crack velocity v_s . For 0/90 CMCs, matrix cracks first form in the 90° plies and partially penetrate the 0° plies (Fig. 1). Threshold behavior obtains when the stress σ is small enough to assure that these cracks do not extend, even though the fibers creep. This condition is characterized by a threshold stress [4]

$$\sigma_{th} = \sqrt{\frac{2E_m\Gamma_m(1-f)}{\pi h}} \quad (1)$$

where E_m is the Young's modulus of the matrix, Γ_m is its fracture energy, f is the fiber volume fraction in the plies and h is the ply thickness. When $\sigma < \sigma_{th}$, creep is transient and governed by the McLean model [9].

When $\sigma > \sigma_{th}$, the crack extends into the 0° plies as fiber creep occurs. The trends in crack velocity are depicted in Fig. 2. An upper bound is evident, associated with a steady-state velocity v_s . For fibers subject to linear creep with viscosity η , this velocity is given by [4]

$$v_s = \left(\frac{3\pi}{16}\right) \left(\frac{2fE_f}{E} + 1\right) \left[\frac{(1-f)E_m^2}{\eta\sigma_{mc}^2}\right] g(\sigma/\sigma_{mc}) \quad (2)$$

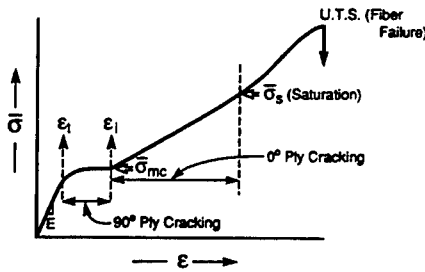
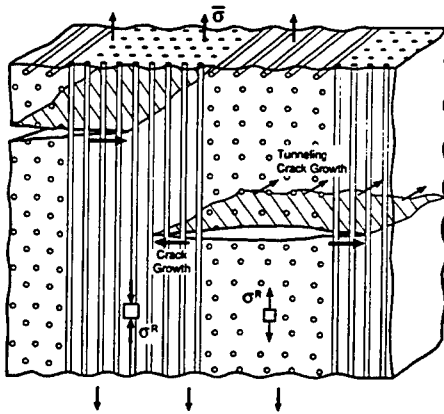


Fig. 1. Schematic of cracking events in 0/90 composites.

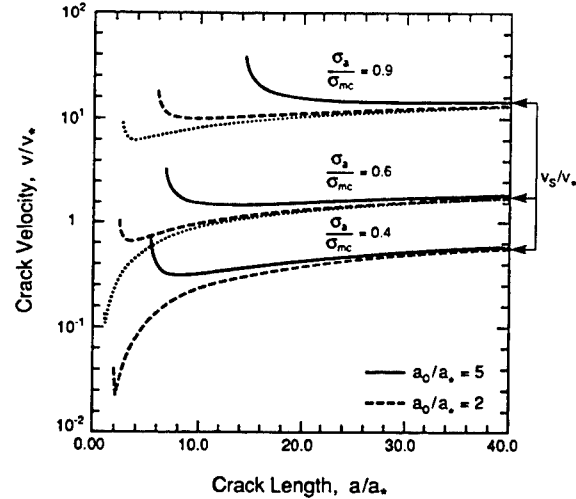


Fig. 2. Crack velocity predictions for 0/90 CMCs with creeping fibers: v^* and a^* are reference velocity and crack length, respectively, defined in Ref. [4].

where E_f is the Young's modulus of the fibers, E is the composite modulus, σ_{mc} is the steady-state matrix cracking stress in the absence of creep, and g is a function given approximately by [4]

$$g(\sigma/\sigma_{mc}) \approx [1 - (\sigma/\sigma_{mc})^b]^{-1} \quad (3)$$

where b is an exponent ($b = 3$).

The velocity can be related to a reference time, Δt , required to extend the cracks across the 0° plies as

$$\Delta t \equiv h/v_s = \left(\frac{16}{3\pi}\right) \frac{h\eta\sigma_{mc}^2[g^{-1}(\sigma/\sigma_{mc})]}{(1-f)\Gamma_mE_m^2(2fE_f/E+1)}$$

The properties of SiC/SiC composites needed to estimate Δt are summarized in Table 1 [12–14].

When Nicalon fibers are used, one complication is the *time dependence* of the viscosity, caused by grain coarsening [7,10]. This would not be a problem for microstructurally stable fibers, such as α -SiC and α -Al₂O₃. However, for Nicalon fibers [10]

$$\eta = (\sigma_0/f\dot{\epsilon}_0)(t/t_0)^x \quad (5)$$

Table 1
Properties of SiC/SiC composites

Property	Magnitude	Comment
E_m	300 GPa	Porous matrix [12,13]
E_f	200 GPa	Measured [7]
f	0.4	Within plies
E	260 GPa	Measured [12]
σ_{mc}	140 MPa	Measured [12,13]
Γ_m	10 J m ⁻²	Columnar grains [2]
h	200 μm	
t_0	10 ⁻⁶ s	1200 °C [10]
τ	50 MPa	Room temperature [13]
σ_{th}	60 MPa	Eq. (1)

where σ_0 is a reference stress (1 MPa), $\dot{\epsilon}_0$ is a reference strain rate, t is time, and t_0 is a temperature-dependent time constant (Table 1), with $\alpha \approx 0.9$.

2.2. Debonding and friction

There are several indicators of debonding and friction that may be used to probe the effects of temperature and creep on the interface response when matrix cracks are present:

(1) The most direct indication is provided by measurement and analysis of the hysteresis strains, as elaborated elsewhere [13,15]. A parameter related to these strains having particular relevance is the friction index \bar{L} , which is dependent on the friction stress τ and the crack spacing d in accordance with [13,15]

$$\tau = \frac{b_2(1 - a_1 f)^2 R \omega^2}{4 E_m f^2 \bar{L} d} \quad (6)$$

where b_2 and a_1 are coefficients of order unity [16], R is the fiber radius, and ω is a load partitioning factor between 1 and 2. The magnitude of \bar{L} can be obtained from the inverse tangent modulus (ITM) or the width of the hysteresis loop. The hysteresis strains may also be used to assess the magnitude of the interface toughness [15].

(2) When the matrix cracks in the 0° plies reach saturation, the crack spacing d_s relates to τ , such that [17]

$$\tau = \frac{(1 - f) E_m (\sigma - \sigma_i) R}{f E d_s} \quad (7)$$

where σ_i is the debond stress, which is related to the interface toughness [16].

(3) The fiber pull-out length p provides yet another measure of the interface friction stress. The relationship when there is multiple matrix cracking is given by [18]

$$\tau = R S_c \lambda(m) / p \quad (8)$$

where S_c is the characteristic strength of the fibers at the test temperature, with m being the Weibull modulus and $\lambda(m) \approx 0.25$ for typical m ($= 3-5$) [2,18]. The strength S_c is inferred from the ultimate tensile strength (UTS), measured after creep testing, S_u , using the relation [18]

$$S_c = \frac{S_u}{f F(m)} \quad (9)$$

where $F(m) \approx 0.7$ for Nicalon fibers in CMCs.

2.3. Compliance

The compliance is related primarily to the matrix crack densities in both the 0° and 90° plies, and their morphologies. When all of the cracks in the 90° plies extend across the 0° plies, the relationship has the

simple form [19]

$$\frac{E}{E^*} - 1 = C_1 \left(\frac{h}{d} \right) \left[1 + 2 \left(\frac{R D_1}{h C_1} \right) \right] \quad (10)$$

where E is the initial modulus, E^* is the diminished modulus after matrix cracking, d is the crack spacing; C_1 and D_1 are coefficients of order unity that depend primarily on elastic properties and fiber volume fractions. Before the cracks penetrate the 0° plies, the same result applies, but with the second term in the square parenthesis being zero [19]. Solutions for other crack configurations are not available.

3. Experiments

3.1. Procedures

The experimental studies are performed on a 0/90 SiC/SiC composite with a plain weave, having the microstructure and room temperature properties elaborated elsewhere [12–14]. The tests are performed in tension in an inert (Ar) atmosphere within a servohydraulic loading frame. The loads are applied to the specimen by water-cooled stainless steel friction grips. The furnace is resistance-heated with W elements. The displacements are measured in the hot zone by a mechanical extensometer, held in contact with the specimen by means of a small spring. All experiments are performed at 1200°C . The tests are conducted subject to load control, and the displacements recorded. Periodic (relatively rapid) unloading and reloading cycles are used to assess changes in constituent properties as the experiments proceed [13,15].

Some tests are interrupted prior to failure. The loads are removed and the specimens cooled to allow investigation of the creep damage by performing scanning electron microscopy (SEM) observations of the surfaces. Others are loaded to failure after completion of the creep test in order to measure the retained strength. These samples are also examined by SEM.

3.2. Results

The creep rates measured at 1200°C , at three stress levels (50, 75 and 110 MPa) are plotted in Fig. 3. The deformation is transient, as in other CMCs reinforced with Nicalon fibers [6,10–11]. The evolution of the hysteresis loops indicates the changes that occur in the material as creep proceeds. There are no significant changes upon creep testing at 50 MPa, but at the higher stresses both the compliance and loop width increase as creep proceeds (Fig. 4). The inverse tangent moduli (ITMs) may be obtained from the reload strains [13,15] (Fig. 5). These provide information about the constituent properties and their variation during creep, as

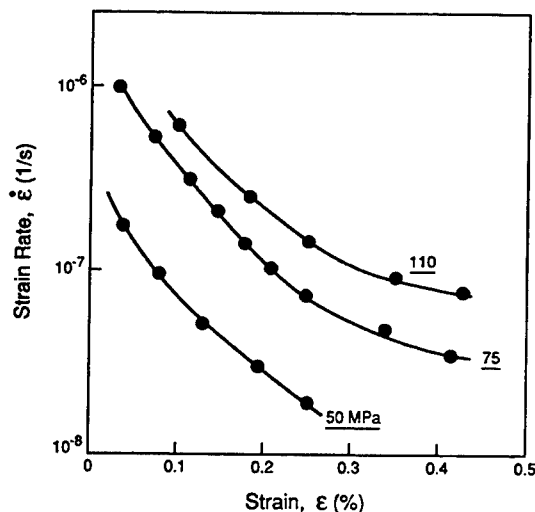


Fig. 3. Creep rate as a function of strain upon testing at 1200 °C at the indicated stresses.

elaborated below. Note that the ITMs have a linear stress dependence. This feature is characteristic of a material with a low interface toughness [15]. It contrasts with the behavior found at room temperature on the same composite [12,15].

SEM observations conducted after interrupting the tests performed at 110 MPa reveal matrix cracks (Figs. 6(a) and 6(b)). These cracks extend across the 0° plies after about 10 h. At longer times, they extend across several 0/90 plies. The crack opening displacements ($\delta \approx 7 \mu\text{m}$) are substantially larger than those evident after room-temperature testing [12]. The crack spacings ($\delta \approx 600 \mu\text{m}$) are also relatively large, indicative of a much lower friction stress than that at room temperature [13] (Table 1). It appears as if the cracks originate at large pores in the 90° plies (Fig. 6(b)) and then extend continuously across several neighboring 0/90 plies (Fig. 6(a)).

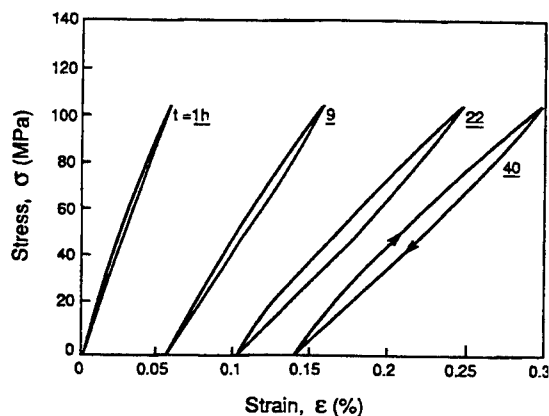


Fig. 4. Hysteresis strains measured upon periodic unloading and reloading after testing at 1200 °C for different times at 110 MPa.

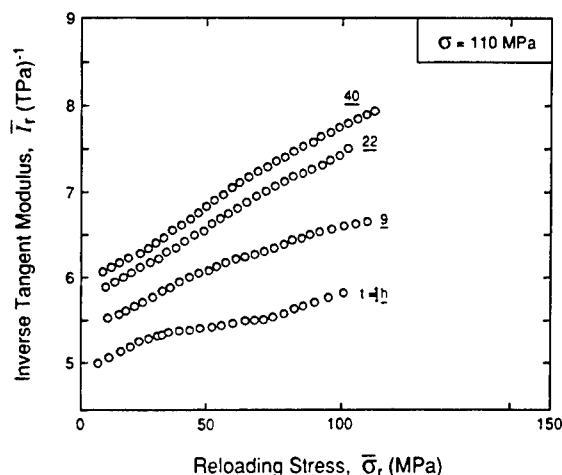


Fig. 5. Inverse tangent moduli evaluated from the reload hysteresis strains.

Specimens tested to failure after completion of the creep test at 110 MPa had a retained strength, $S_u \approx 300$ MPa, larger than the room-temperature UTS [12,13]. The corresponding characteristic strength [18] (Eq. (9)) is $S_c \approx 2.1$ GPa. These specimens also exhibited appreciable fiber pull-out (Fig. 6(c)), with an average pull-out length p of 400 μm . At room temperature [17] the corresponding magnitude is $p = 30 \mu\text{m}$, again indicative of a reduced friction stress after creep testing.



Fig. 6. SEM observations of matrix cracks formed after testing in creep at 1200 °C to a strain of about 0.5% at a stress of 110 MPa: (a) overview; (b) close-up of one matrix crack; (c) fiber pull-out upon loading to failure after creep testing.

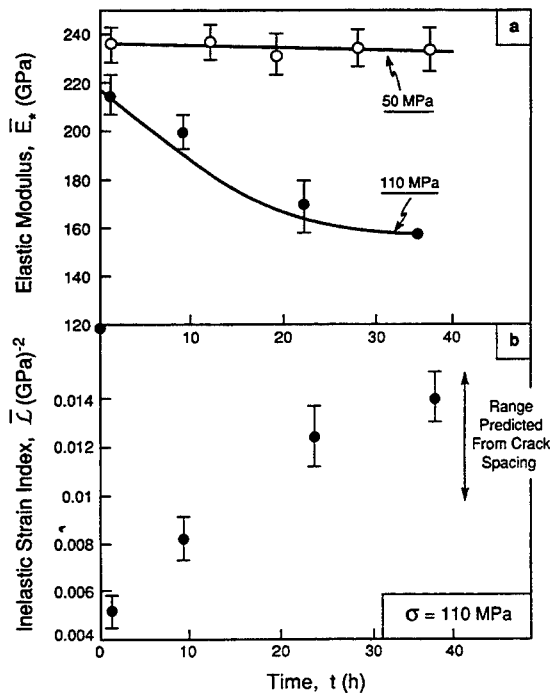


Fig. 7. Variations in (a) the elastic modulus and (b) the friction index with strain evaluated from the ITMs (Fig. 5).

4. Analysis

4.1. Compliance changes

Hysteresis loop analysis performed using procedures described elsewhere [13,15] gives the changes in the compliance and friction index plotted in Fig. 7. At the lowest applied stress ($\sigma = 50$ MPa) there is transient creep, but the modulus remains invariant. These findings suggest that this applied stress is below the crack growth threshold. Indeed, by using the constituent properties indicated in Table 1, the predicted threshold, $\sigma_{th} \approx 60$ MPa, is found to be consistent with the observations. At higher stresses, 75 MPa and above, the cracks propagate and the modulus decreases. These changes are assessed using Eq. (10). For SiC/SiC (Table 1) and at the low crack densities found in the present experiments (Fig. 6(a)), the coefficients are [19] $D_1 \approx 1.8$ and $C_1 \approx 1.2$. Hence, the modulus ratio should change by about 15% as the cracks extend across the 0° plies. The data (Fig. 7(a)) indicate *larger* changes, because the cracks have a configuration that differs from that used to obtain Eq. (10). Instead of being continuous, the cracks originate in the 90° plies and extend across several neighboring plies. The next step would be to establish the geometric evolution of matrix cracks in order to provide a predictive capability.

4.2. Friction stress

The friction stress is estimated in three different ways. The matrix crack spacing in the 0° plies upon saturation, d_s , provides a preliminary estimate. If the debond stress σ_i is considered to be small, because the interface toughness is small, then Eq. (7) gives $\tau \approx 2$ MPa. This value also predicts a friction index \bar{L} (Eq. (6)) similar to the measured magnitude (Fig. 7(b)). Moreover, inserting the measured fiber pull-out length, $p = 400$ μ m, into Eq. (8) gives $\tau = 6$ MPa. Values in the range 2–6 MPa are much smaller than at room temperature [13], where $\tau \approx 50$ MPa. The lower magnitude of τ after creep at high temperature might be rationalized using rough fiber sliding models [20], but an explicit attempt is not made here. One important effect is the diminished residual stress at 1200 $^\circ$ C. Another might be the greater fiber compliance at this temperature.

4.3. Crack growth

The reference time for crack growth (Eq. (4)) may be used to rationalize the rates at which the compliance changes and the composite creeps. Two of the parameters in this formula need to be interpreted before proceeding:

- (1) The matrix cracking stress σ_{mc} is expected to differ from the room-temperature magnitude.
- (2) The fiber viscosity changes with time, and the crack velocity diminishes as it propagates. Because of these complicating factors, it is only possible to assess overall consistency between the observations and the model. Explicit predictions cannot be made.

There are two counteracting effects on σ_{mc} as the temperature changes: one associated with the diminished τ and the other with the reduced residual stress [2]. These effects are assumed to annul.

Based on the time for cracks to grow across the 0° plies (about 10 h at 110 MPa), the average fiber viscosity is obtained from Eq. (5) as $\eta = 10^{15}$ Pa s⁻¹. With this viscosity, the reference time is obtained from Eq. (4), using the information from Table 1, as $\Delta t \approx 10^4$ s. This is indeed comparable to the time found for the cracks to grow across the 0° plies. It would thus appear feasible to use Eq. (4), with a compliance model, to predict the creep characteristics, whenever the fibers have fixed viscosity.

5. Concluding remarks

The creep rate of SiC/SiC above a threshold stress is dominated by the creep viscosity of the fibers, because the stress transferred onto the matrix causes cracks. There is a consequent decrease in stiffness, which degrades the material, reloads the fibers and allows creep

to continue. The stiffness decrease depends on the crack morphology and density. This density, in turn, is affected by the interface friction stress: smaller values give lower densities and a diminished stiffness degradation. In this SiC/SiC composite, the friction stress is found to be much lower after creep at high temperature than at room temperature. The temperature sensitivity might be attributed to a reduction in residual stress.

The rate at which the modulus decreases and creep occurs depends on the rate of matrix crack growth. This rate has been assessed from a steady-state bridging model with creeping fibers. However, a superior appreciation for the applicability of the model will be gained when CMCs with microstructurally stable fibers become available.

One implication of this work is that the creep performance of CMCs must be addressed by improving the creep resistance of the fibers. Increasing the creep resistance of the matrix does not have an appreciable effect and, moreover, is accompanied by creep-induced reductions in stiffness.

References

- [1] J.J. Brennan, in J.A. Pask and A.G. Evans (eds.), *Ceramic Microstructures: The Role of Interfaces*, Plenum, New York, 1988.
- [2] A.G. Evans and F.W. Zok, *J. Mat. Sci.*, 29 (1994) 3857–3896.
- [3] F.A. Heredia, J. McNulty, F.W. Zok and A.G. Evans, *J. Amer. Ceram. Soc.*, 78 (1995) 2097–2100.
- [4] M.R. Begley, B.N. Cox and R.M. McMeeking, *Acta Metall. Mater.*, 43 (1995) 3927–3931.
- [5] C.H. Heneger and R.H. Jones, *Mat. Sci. Eng. A*, 166 (1993) 2365.
- [6] G.E. Hilmas, J.W. Holmes, R.T. Bhatt and J.A. DiCarlo, in N.P. Bansal (ed.), *Advances in Ceramic-Matrix Composites*, *Ceramic Transactions*, Vol. 38, American Ceramic Society, Westerville, OH, 1993, pp. 291–304.
- [7] R.E. Tressler and J. DiCarlo, in R. Naslain et al. (eds.) *High Temperature Ceramic Matrix Composites*, Woodhead, UK, 1993, pp. 33–49.
- [8] H.J. Frost and M.F. Ashby, *Deformation Mechanism Maps*, Pergamon Press, Oxford, UK, 1982.
- [9] M. McLean, *Compos. Sci. Technol.*, 23 (1985) 37.
- [10] C.H. Weber, J.P.A. Lofvander and A.G. Evans, *J. Amer. Ceram. Soc.*, 77 (1994) 1745–1786.
- [11] C. Weber, H. Kim, X. Bourrat and A.G. Evans, *Mat. Sci. Eng., A196* (1995) 25–31.
- [12] L. Guillaumat, *Ph.D. Thesis*, Laboratoire des Composites Thermostructuraux, Domaine Universitaire, Bordeaux, France, March 1993.
- [13] J.M. Domergue and A.G. Evans, *J. Amer. Ceram. Soc.*, 79 (1996) 161–179.
- [14] R. Naslain, *J. Alloys Comp.*, 188 (1992) 42.
- [15] J.M. Domergue, E. Vagaggini and A.G. Evans, *J. Amer. Ceram. Soc.*, 78 (1995) 2721–2731.
- [16] J.W. Hutchinson and H.M. Jensen, *Mech. Mater.*, 9 (1985) 37.
- [17] M.Y. He, B.X. Wu, A.G. Evans and J.W. Hutchinson, *Mech. Mater.*, 18 (1994) 213–229.
- [18] W.A. Curtin, *J. Amer. Ceram. Soc.*, 74 (1991) 2837.
- [19] Z. Xia and J.W. Hutchinson, *Acta Metall. Mater.*, 42 (1994) 1933–1945.
- [20] T.A. Parthasarathy, D.B. Marshall and R. Kerans, *Acta Metall. Mater.*, 42 (1994) 3773.

Composite Laminates in Plane Stress: Constitutive Modeling and Stress Redistribution due to Matrix Cracking

Guy M. Genin and John W. Hutchinson*

Harvard University, Cambridge, Massachusetts 02138

Plane-stress constitutive relations for laminate composites undergoing matrix cracking are developed that can be fit to data from uniaxial tests. The constitutive equations are specialized to brittle-matrix composites in the form of crossplies and quasi-isotropic laminates. The effect of nonlinear stress-strain behavior on stress redistribution around holes and notches in laminate plates is illustrated.

I. Introduction

FIBER-REINFORCED brittle-matrix composites are of technological interest as potential lightweight materials for high-temperature environments. Design with brittle-matrix composites is typically based on linear elastic stress analyses, and components made of such composites are usually constructed so as to avoid all cracking at design loads. This approach is unduly conservative for certain classes of fiber-reinforced ceramic-matrix composites that possess appreciable "ductility" associated with matrix cracks that leave the fibers intact. Allowance for some matrix cracking at points of high stress concentration can considerably increase the load-carrying capabilities of some of these materials. In these laminates, the nonlinear stress-strain behavior associated with matrix cracking can redistribute and reduce stresses in regions of high stress concentration, similar to the way that plastic deformation accommodates stress concentration in metals.

An example of a composite that displays some ductility is coated silicon carbide (SiC) fibers embedded in a glass (calcium aluminosilicate, CAS) matrix. When SiC/CAS laminae are stacked in a (0°/90°) crossply configuration and loaded in uniaxial tension, the stress-strain behavior of the laminate is as shown in Fig. 1(A), as reported by Cady¹ and Beyerle *et al.*² The material responds linearly to the point at which the matrix material begins to crack, then loses stiffness as an increasing number of matrix cracks form.^{2,3} The cracks that are growing in the matrix material deflect into the low-toughness fiber/matrix interfaces, given an appropriate fiber coating, and eventually arrest,^{4,5} leaving the fibers intact. When the matrix material becomes saturated with cracks, all the load is taken by the fibers, which deform in a linear elastic fashion until failure. When the fibers do start to fail, they do not necessarily break at the matrix-crack plane; consequently, they continue to provide some load-carrying capacity because of frictional pullout. The data shown in Fig. 1(A) has been taken under nominally load-controlled conditions. If the data had been taken in a controlled-displacement tensile test, a portion of the stress-strain curve with decreasing stress after the peak would be observed.

Figure 1(A) also shows the Cady data¹ for the strain transverse to the loading direction in a uniaxial tensile test that has

been conducted parallel to a set of fibers in the SiC/CAS crossply. The material experiences the usual Poisson contraction in the linear range; however, as matrix cracks deflect into the fiber/matrix interfaces and the fibers become increasingly debonded, the transverse strain is largely uncoupled from the uniaxial stress and the strain increments reverse sign. By the point at which the matrix material becomes saturated with cracks, some composites actually experience an expansion in the transverse direction.

Figure 1(B) shows the uniaxial and transverse strains resulting from a controlled-force tensile test that has been conducted at an angle of 45° to the fiber directions in a SiC/CAS crossply. The curves illustrate a different behavior from that exhibited in the previous loading, with extensive straining at nominally constant stress once matrix cracking is underway. The matrix cracks still form perpendicular to the direction of the maximum principal stress; however, now the fibers are not oriented to carry the applied stress nearly as effectively as when the stress acts parallel to one set of fibers. If the matrix were not present, the crossed fibers would simply deform by a "scissoring" mechanism. The uncracked matrix suppresses this mechanism but matrix cracking permits its partial operation. The density of matrix cracks at saturation is generally much higher for the 45° loading than for the 0° loading. This effect may be increased by a porous matrix or strong elastic anisotropy in the fibers. However, the matrix cracking stress and even the elastic modulus for loading at an angle of 45° to the fiber directions may be higher or lower than the corresponding quantities for loading parallel to the fibers, depending on the properties of the constituents of a laminate. Transverse to the loading direction, the response of the SiC/CAS laminate differs significantly from the transverse response that is observed in Fig. 1(A). After the 45° matrix cracking stress is attained, the composite experiences continued negative transverse straining with strains on the order of the strain in the direction of loading. This behavior is readily understood in terms of the scissoring mechanism.

The stress-strain curve for the SiC/CAS crossply subject to a shear stress applied parallel to the fibers is shown in Fig. 1(C). It is quite similar to the curve for uniaxial tension at an angle of 45° to the fibers, with the composite exhibiting comparable ductility.

Brittle-matrix laminates that are suitable for engineering have a tendency to be one of two types. Either they behave as SiC/CAS, with a strain to failure both in tension parallel to the fibers and in shear that exceeds the linear elastic strain for the corresponding failure load by a moderate amount, or they exhibit brittle behavior in tension with a much larger strain to failure in shear, as in carbon-carbon (C/C) composites. An example of the stress-strain behavior of the latter, as reported by Turner *et al.*,⁶ Heredia,⁷ and Evans,⁸ is shown in Fig. 2. Both types of materials are attractive in that they have been observed to redistribute stresses around stress concentrations, sometimes to the point that elastic stress concentrations are completely eliminated before the material fails.⁹⁻¹³ Such behavior is termed notch insensitivity. In this work, it will be shown that changes in stiffness due to matrix cracking contribute to the notch insensitivity observed in components made of SiC/CAS laminates by forcing the redistribution of stresses away from regions of high

B. N. Cox—contributing editor

Manuscript No. 192578. Received May 30, 1995; approved October 25, 1996. Supported in part by the ARPA University Research Initiative (Subagreement P.O. KK-3007 with the University of California, Santa Barbara, under ONR Prime Contract No. N00014-92-J1808) and the Division of Applied Sciences, Harvard University. *Member, American Ceramic Society.

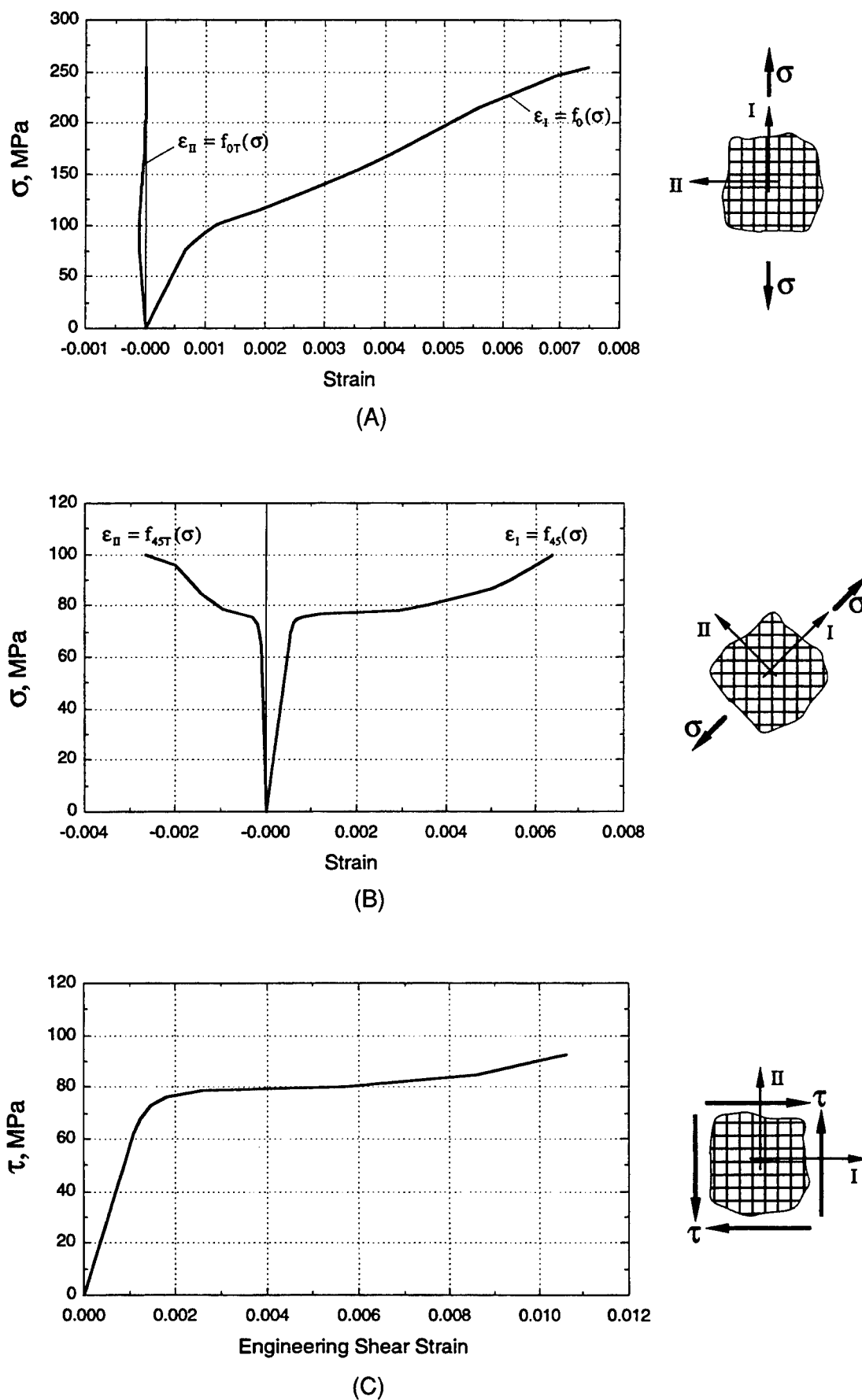


Fig. 1. Stress-strain behavior of a SiC/CAS crossply in (A) uniaxial tension parallel to the fibers, (B) uniaxial tension at an angle of 45° to the fibers, and (C) pure shear in the fiber axes. Data is from Cady¹ and Beyerle *et al.*²

stress concentration. However, in components made of the C/C composite, matrix cracking can actually serve to intensify stress concentrations; the observed notch insensitivity in C/C components is due to phenomena that occur after the carbon fibers begin to fracture.

Stress analysis that accounts for notch insensitivity allows for less-conservative design. The goal of the engineer, and the goal of the present work, is to predict the notch sensitivity of a brittle-matrix laminate in a particular configuration and, thereby, accurately assess the ultimate load and failure mechanism for a component made of these brittle-matrix laminate materials.

Fundamental to such an analysis is a constitutive law that accounts for the inelastic material response of these composites. Although a substantial amount of literature exists for the prediction of the mechanical behavior of laminates of different material systems and stackings based on micromechanical analysis (e.g., Xia and coworkers^{14,15} and Dvorak and coworkers¹⁶⁻¹⁸), the micromechanical approach to design is invariably too complicated to use for generating the constitutive response needed in component stress analysis. Although a few attempts have been made to actually design very simple laminate components from micromechanical analyses for metal-matrix and polymer-matrix composites (e.g., Kennedy and Wang¹⁹ and Dvorak *et al.*²⁰), most efforts to develop computational methods of stress analysis to aid in the design of components of brittle-matrix laminates have led to two categories of constitutive relations: continuum damage laws and phenomenological stress-strain laws similar to those for elastic-plastic solids.

Continuum damage mechanics attempt to curve fit experimental data with a set of damage parameters that are considered to be internal variables that evolve with the loading history. Various schemes for modeling the state of degradation of either a lamina or a laminate have included scalar variables,²¹⁻²⁶ damage vectors,²⁷ and even damage tensors (e.g., Talreja²⁸ and Allen *et al.*²⁹). The approach adopted in the present paper is the phenomenological approach. The focus is on behavior under proportional plane stressing, and the development of the constitutive law parallels that of the deformation theory of plasticity. This entails using data from stress-strain tests and, ignoring details of the internal mechanisms that produce this behavior, creating a scheme that reproduces the input tests and estimates the mechanical behavior for all other multiaxial loadings.

Several phenomenological constitutive models exist in the literature, each of which treats either individual laminae or entire laminates as plane-stress continua and has been designed

to model only proportional loading. Petit and Waddoups³⁰ proposed an incrementally linear orthotropic model, in which the incremental shear and tensile moduli at each point within each lamina are updated to equal the tangent moduli of the stress-strain curves corresponding to the tensile and shear stresses at the beginning of a loading increment. Although their model completely neglects the behavior of the material transverse to the loading direction and, thus, is not applicable to multiaxial stress states, Petit and Waddoups³⁰ did successfully predict tensile stress-strain curves for uniaxial loadings in different orientations on applying their scheme to laminate composites of different lay-ups, with the laminae constrained by the condition that points in neighboring layers must move together.

Hahn and Tsai,³¹ focusing on materials such as the C/C composite, whose behavior is shown in Fig. 2, modeled the behavior of a lamina by combining linear elasticity for the normal components of stress and strain with a nonlinear elastic curve-fit of the shear behavior. Hahn³² later specialized this model to the case of a 0/90 laminate. Surret and Vautrin³³ proposed a curve-fit of the nonlinear behavior for loading perpendicular to the fibers in a lamina, in addition to a curve-fit of the nonlinear shear behavior, and then also successfully reproduced off-axis uniaxial test results in a unidirectional laminate. These simple constitutive models are limited in that they are incapable of modeling inelastic behavior that occurs for loading in the fiber axes, such as that observed for the SiC/CAS composite in Fig. 1, and also fail to reproduce the often-reported observation that the maximum inelastic strain in a brittle-matrix laminate occurs in the direction of the largest principal stress. Nevertheless, several authors (e.g., Chang *et al.*³⁴) have analyzed multidirectional laminate composites by applying a single lamina constitutive law, similar to that of Hahn and Tsai,³¹ to each of the individual laminae of a composite in the manner of Petit and Waddoups³⁰ and have obtained reasonable qualitative results. Other authors^{35,36} used the linear elastic properties of a 0/90 laminate combined with a nonlinear elastic curve-fit of shear behavior in a manner similar to that of Hahn.³²

The current work presents a plane-stress constitutive model for proportional loading of (0/90) laminate composites that is based on three uniaxial measurements. The formulation also applies to laminates of a (0/±45/90) configuration. The model predicts all additional sets of data that are available for the two material systems introduced above. The model is then used in component-stress analysis and accurately replicates experimental observations and measurements.

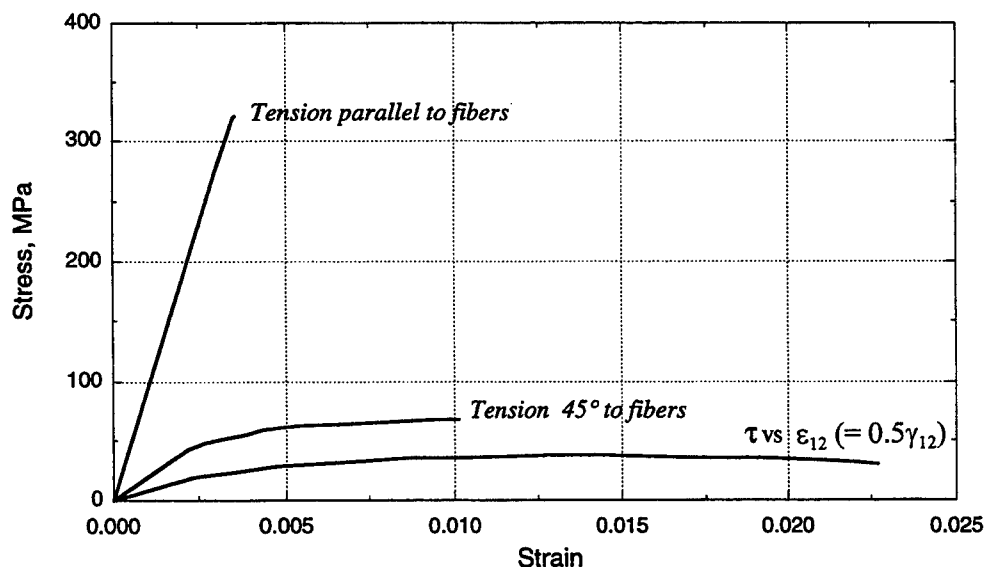


Fig. 2. Stress-strain curves for a C/C crossply (from Turner *et al.*,⁶ Heredia,⁷ and Evans⁸).

II. Constitutive Model

This section develops a plane-stress constitutive model for symmetrically stacked brittle-matrix laminates. In the first part, the model is developed for "specially orthotropic" laminates, i.e., laminates that possess cubic in-plane symmetry. The most common examples of these are laminates stacked with a (0/90) configuration and laminates stacked with a (0/±45/90) configuration in which the number of individual plies with a ±45° orientation differs from the number of plies with 0° and 90° orientations. Although the formulation is valid for both systems, attention is focused on the (0/90) configuration.

In the second part, the model is developed for laminates that possess in-plane isotropy. Two common configurations of laminae that produce "quasi-isotropic" laminates are the (0/±60) and (0/±45/90) configurations, the latter only when equal numbers of laminae are oriented in each of the four directions. The constitutive equations for quasi-isotropic laminates are shown to be a special case of the constitutive equations for the crossply laminates.

(1) Crossply Laminates

The most-reliable data on which to base a plane-stress constitutive model are uniaxial stress-strain tests. Let the results of a stress-strain test parallel to the fibers in a crossply composite be denoted by $\epsilon_1 = f_0(\sigma_1)$ for strain parallel to the fibers, in terms of applied stress, and $\epsilon_{11} = f_{0T}(\sigma_1)$ for strain transverse to the loading direction, in terms of applied stress, as depicted in Fig. 1(A). The following is proposed for proportional multiaxial loading when the principal axes of stress and strain are aligned with the fibers:

$$\epsilon_1 = f_0(\sigma_1) + f_{0T}(\sigma_{11}) \quad (1a)$$

and

$$\epsilon_{11} = f_0(\sigma_{11}) + f_{0T}(\sigma_1) \quad (1b)$$

This assumes that no interaction exists between these two principal stress components, which is justified on the grounds that matrix cracking perpendicular to one stressing direction decouples the straining in the other direction.

The axes at an angle of 45° to the fiber axes also are symmetry axes. For loading in which the principal axes of stress are aligned at an angle of 45° from the fibers in a crossply, the strains share the same principal axes and are considered here to be given by relations similar to those in Eqs. (1):

$$\epsilon_1 = f_{45}(\sigma_1) + f_{45T}(\sigma_{11}) \quad (2a)$$

and

$$\epsilon_{11} = f_{45}(\sigma_{11}) + f_{45T}(\sigma_1) \quad (2b)$$

In these equations, $f_{45}(\sigma_1)$ represents strain in the loading direction for a uniaxial tension test conducted at an angle of 45° to the fiber directions, and $f_{45T}(\sigma_1)$ represents strain transverse to the loading direction for this test, as shown in Fig. 1(B).

An important connection follows from the requirement that, for equibiaxial loading with $\sigma_1 = \sigma_{11} = \sigma$, the orientation of the principal axes is indeterminate and the strains from Eqs. (1) must match the strains from Eqs. (2). Consequently, $f_{45T}(\sigma)$ may be written in terms of the other three functions as

$$f_{45T}(\sigma) = f_0(\sigma) + f_{0T}(\sigma) - f_{45}(\sigma) \quad (3)$$

In principle, experimental stress-strain data for any three of the four functions appearing in Eqs. (1) and (2) could be chosen, with the fourth given by Eq. (3). In this work, data for the three functions on the right-hand side of Eq. (3) will be input into the model, whereas $f_{45T}(\sigma)$ follows from Eq. (3).

From this point, the formulation continues as a recipe for the stresses in terms of the strains. This is necessary because, for materials of the type being considered, stress component ranges vary significantly for various multiaxial states, whereas strain components are much less restricted. We define $\Sigma_0(\epsilon_1, \epsilon_{11})$ as the inverse of Eqs. (1), such that

$$\sigma_1 = \Sigma_0(\epsilon_1, \epsilon_{11}) \quad (4a)$$

and

$$\sigma_{11} = \Sigma_0(\epsilon_{11}, \epsilon_1) \quad (4b)$$

The reduction in stresses due to matrix cracking at prescribed ϵ_1 and ϵ_{11} , when the principal loading axes coincide with the fiber directions, is the difference between the stresses that would result if no cracking occurred and Σ_0 . The "stress deficits" for loading in the fiber axes are defined as

$$\Delta\sigma_1^0 = \frac{E_0}{(1 - \nu_0^2)}(\epsilon_1 + \nu_0\epsilon_{11}) - \Sigma_0(\epsilon_1, \epsilon_{11}) \quad (5a)$$

and

$$\Delta\sigma_{11}^0 = \frac{E_0}{(1 - \nu_0^2)}(\epsilon_{11} + \nu_0\epsilon_1) - \Sigma_0(\epsilon_{11}, \epsilon_1) \quad (5b)$$

where E_0 and ν_0 are, respectively, the elastic modulus and Poisson's ratio for uniaxial loading parallel to the fibers.

Similarly, for the case when the principal axes of loading lie at an angle of 45° to the fiber directions, denote the inverse of Eq. (2) as $\sigma_1 = \Sigma_{45}(\epsilon_1, \epsilon_{11})$ and $\sigma_{11} = \Sigma_{45}(\epsilon_{11}, \epsilon_1)$ and let the stress deficits due to matrix cracking be given by

$$\Delta\sigma_1^{45} = \frac{E_{45}}{(1 - \nu_{45}^2)}(\epsilon_1 + \nu_{45}\epsilon_{11}) - \Sigma_{45}(\epsilon_1, \epsilon_{11}) \quad (6a)$$

and

$$\Delta\sigma_{11}^{45} = \frac{E_{45}}{(1 - \nu_{45}^2)}(\epsilon_{11} + \nu_{45}\epsilon_1) - \Sigma_{45}(\epsilon_{11}, \epsilon_1) \quad (6b)$$

Here, E_{45} is the elastic modulus for uniaxial loading in the axes at an angle of 45° to the fiber directions; ν_{45} , which is the Poisson's ratio in these axes, can be expressed in terms of E_0 , ν_0 , and E_{45} , using Eq. (3), as

$$\nu_{45} = 1 - \frac{E_{45}}{E_0}(1 - \nu_0) \quad (7)$$

Now consider principal strains $(\epsilon_1, \epsilon_{11})$ in principal axes oriented at an arbitrary angle θ from the fiber directions. The principal axes of stress deficits due to matrix cracking are considered to coincide with the principal strain axes. The stress deficits in these axes are assumed to be given by interpolation between the stress deficits in the 0° and 45° orientations, according to

$$\Delta\sigma_1 = \Delta\sigma_1^0 \cos^2 2\theta + \Delta\sigma_1^{45} \sin^2 2\theta \quad (8a)$$

and

$$\Delta\sigma_{11} = \Delta\sigma_{11}^0 \cos^2 2\theta + \Delta\sigma_{11}^{45} \sin^2 2\theta \quad (8b)$$

where the stress deficits $\Delta\sigma_1^0$, $\Delta\sigma_{11}^0$, $\Delta\sigma_1^{45}$, and $\Delta\sigma_{11}^{45}$ are given in terms of $(\epsilon_1, \epsilon_{11})$ by Eqs. (5) and (6). On rotating back to the fiber axes, one obtains the plane-stress relation for stresses associated with proportional straining to $(\epsilon_1, \epsilon_2, \gamma_{12} = 2\epsilon_{12})$:

$$\sigma_1 = \frac{E_0}{(1 - \nu_0^2)}(\epsilon_1 + \nu_0\epsilon_2) - \Delta\sigma_1 \cos^2 \theta - \Delta\sigma_{11} \sin^2 \theta \quad (9a)$$

$$\sigma_2 = \frac{E_0}{(1 - \nu_0^2)}(\epsilon_2 + \nu_0\epsilon_1) - \Delta\sigma_1 \sin^2 \theta - \Delta\sigma_{11} \cos^2 \theta \quad (9b)$$

and

$$\tau = \frac{E_{45}}{2(1 + \nu_{45})}\gamma_{12} - (\Delta\sigma_1 - \Delta\sigma_{11}) \sin \theta \cos \theta \quad (9c)$$

Of the five possible sets of data that could be used as a foundation for the constitutive relations, only three are used. The fact that the constitutive behavior can be modeled with

only three of these five tests is a requirement in the elastic range; beyond the elastic range, this is an assumption that must follow from Eqs. (1) and (2). The validity of this assumption is assessed by evaluating the predictions of the model against the two neglected uniaxial tests: the shear strain, in terms of shear stress, and the transverse strain, in terms of stress applied at an angle of 45° to the fibers. For both of these tests, exact expressions for strains, in terms of stresses, follow from Eqs. (1) and (2). The expression for the transverse strain, in terms of stress applied at an angle of 45°, has been derived above and is given in Eq. (3).

For an applied shear stress, the strains are readily obtained by considering the principal stress state, which occurs in the axes of symmetry at an angle of 45° to the fibers, then rotating back to the fiber axes. In the principal axes, the strain state is given by

$$\epsilon_I = f_{45}(\tau) + f_{45T}(-\tau) \quad (10a)$$

and

$$\epsilon_{II} = f_{45}(-\tau) + f_{45T}(\tau) \quad (10b)$$

where, again, $f_{45T}(\sigma)$ is given by Eq. (3).

Rotating back into the fiber axes, the following expressions are found for the strains that result from the application of a shear stress:

$$\gamma_{12} = 2\epsilon_{12} = f_{45}(\tau) - f_{45}(-\tau) - f_{45T}(\tau) + f_{45T}(-\tau) \quad (11a)$$

and

$$\epsilon_{11} = \epsilon_{22} = \frac{1}{2}(f_{45}(\tau) + f_{45}(-\tau) + f_{45T}(\tau) + f_{45T}(-\tau)) \quad (11b)$$

Before matrix cracking occurs, $f_{45}(-\tau) = -f_{45}(\tau)$ and $f_{45T}(-\tau) = -f_{45T}(\tau)$; therefore, $\epsilon_{11} = \epsilon_{22} = 0$. However, once the matrix begins to crack, the model predicts that a specimen loaded in pure shear will expand.

Predictions for the two sets of data that are not included as input into the model are plotted against the experimental data of Cady¹ for the SiC/CAS composite in Fig. 3. The predictions are obtained from the above expressions by matching f_0 , f_{45} , and f_{0T} to the uniaxial experimental data of Cady¹ for positive values of σ and by continuing the linear dependence on σ when σ is negative. The slight discrepancy between theory and experiment in the elastic range is due to experimental error; the measured elastic constants are not quite consistent with each other. Figure 3 shows excellent correlation between the experimental and theoretical curves.

(2) Quasi-Isotropic Laminates

The above approach is applicable to symmetric laminates of any stacking. A case of particular interest is the case of composites with isotropic in-plane behavior, which requires only two input equations. Two examples of such composites, to within a reasonable approximation, are composites with lay-ups of (0°, ±60°) and (0°, ±45°, 90°), which are usually referred to as being quasi-isotropic. As above in Eqs. (1) and (2), the formulation begins with the following proposal for strains in terms of stresses in any set of principal loading axes:

$$\epsilon_I = f(\sigma_I) + f_T(\sigma_{II}) \quad (12a)$$

and

$$\epsilon_{II} = f(\sigma_{II}) + f_T(\sigma_I) \quad (12b)$$

where $f(\sigma)$ and $f_T(\sigma)$ are, respectively, the data for axial and transverse strains, in terms of stress, for any in-plane uniaxial tensile loading.

As before, let $\Sigma(\epsilon_I, \epsilon_{II})$ represent the solution of Eqs. (12) for σ_I , in terms of the principal strains, and $\Sigma(\epsilon_{II}, \epsilon_I)$ represent the solution for σ_{II} ; the strains resulting from any applied loading

will produce the principal stresses $\Sigma(\epsilon_I, \epsilon_{II})$ and $\Sigma(\epsilon_{II}, \epsilon_I)$. Define θ as the angle from the x_1 - x_2 axes to the principal axes. Transforming the stress tensor back into the x_1 - x_2 axes yields the following relations for arbitrary plane-stress loading:

$$\sigma_I = \Sigma(\epsilon_I, \epsilon_{II}) \cos^2 \theta + \Sigma(\epsilon_{II}, \epsilon_I) \sin^2 \theta \quad (13a)$$

$$\sigma_{II} = \Sigma(\epsilon_{II}, \epsilon_I) \cos^2 \theta + \Sigma(\epsilon_I, \epsilon_{II}) \sin^2 \theta \quad (13b)$$

and

$$\tau = (\Sigma(\epsilon_I, \epsilon_{II}) - \Sigma(\epsilon_{II}, \epsilon_I)) \sin \theta \cos \theta \quad (13c)$$

Equations (13) also follow directly from the crossply model. Noting that, for an isotropic composite, $f_0(\sigma) = f_{45}(\sigma) \equiv f(\sigma)$ and $f_{0T}(\sigma) = f_{45T}(\sigma) \equiv f_T(\sigma)$, Eqs. (1) and (2) match Eqs. (12). Still defining $\Sigma(\epsilon_I, \epsilon_{II})$ as the inverse of Eqs. (1) and (2), the stress deficits in the principal axes may be written as

$$\Delta\sigma_I = \frac{E}{(1 - \nu^2)}(\epsilon_I + \nu\epsilon_{II}) - \Sigma(\epsilon_I, \epsilon_{II}) \quad (14a)$$

and

$$\Delta\sigma_{II} = \frac{E}{(1 - \nu^2)}(\epsilon_{II} + \nu\epsilon_I) - \Sigma(\epsilon_{II}, \epsilon_I) \quad (14b)$$

With these stress deficits being identical in the 0° and 45° axes, Eqs. (8) become trivial. Then, when Eqs. (14) are substituted into Eqs. (9), the linear elastic parts of the two sets of equations cancel, and the quasi-isotropic model of Eqs. (13) is recovered.

III. Applications of Model to Stress Redistribution at Holes and Notches

Two boundary-value problems are now solved using the constitutive model, in conjunction with the finite-element method. Both illustrate how the model can be used to predict stress redistribution and the failure mechanism for composite plates containing holes and notches. Two types of material behavior are considered. The solutions generated for plates with edge-notches are compared with experimentally measured strains for this geometry. Because the constitutive equations proposed above are only intended to be valid to the point at which the first fibers begin to break, the calculations can be expected to retain accuracy only when the strains in the fibers are less than the fiber failure strain. Loads at which fibers are expected to begin to fail will be noted in the sequel.

The results show that matrix cracking accounts for a very large portion of the experimentally observed notch insensitivity that is observed in laminates such as the SiC/CAS composite in Fig. 1. However, the results also show that matrix cracking alone is insufficient to reduce stress concentrations in laminates such as the C/C composite in Fig. 2.

(1) Hole in a Plate

A plate of a crossply brittle-matrix laminate containing a circular hole of radius R is loaded with an applied displacement δ parallel to the fibers, as shown in the insets in Figs. 4(A) and (B). The SiC/CAS composite in Fig. 1 and the C/C composite in Fig. 2 are each considered. The behavior of each crossply is compared to that of the corresponding isotropic composite, whose tensile behavior in any direction is matched to the 0° tensile curve.

The nonlinear problems were solved by the finite-element method. An in-house constitutive subroutine was developed and incorporated into a commercial finite-element program (ABAQUS). The constitutive subroutine is designed such that the stress-strain data that are identified in the above section, together with the fiber orientations, are the only inputs. Although the subroutine is completely capable of incorporating nonlinear compressive behavior into the analyses, all materials considered were assumed to behave linearly in compression to highlight the effects of the inelastic tensile strains due to matrix cracking. Outside the linear elastic range in tension, iteration is required at each load step to obtain the stresses in terms of the

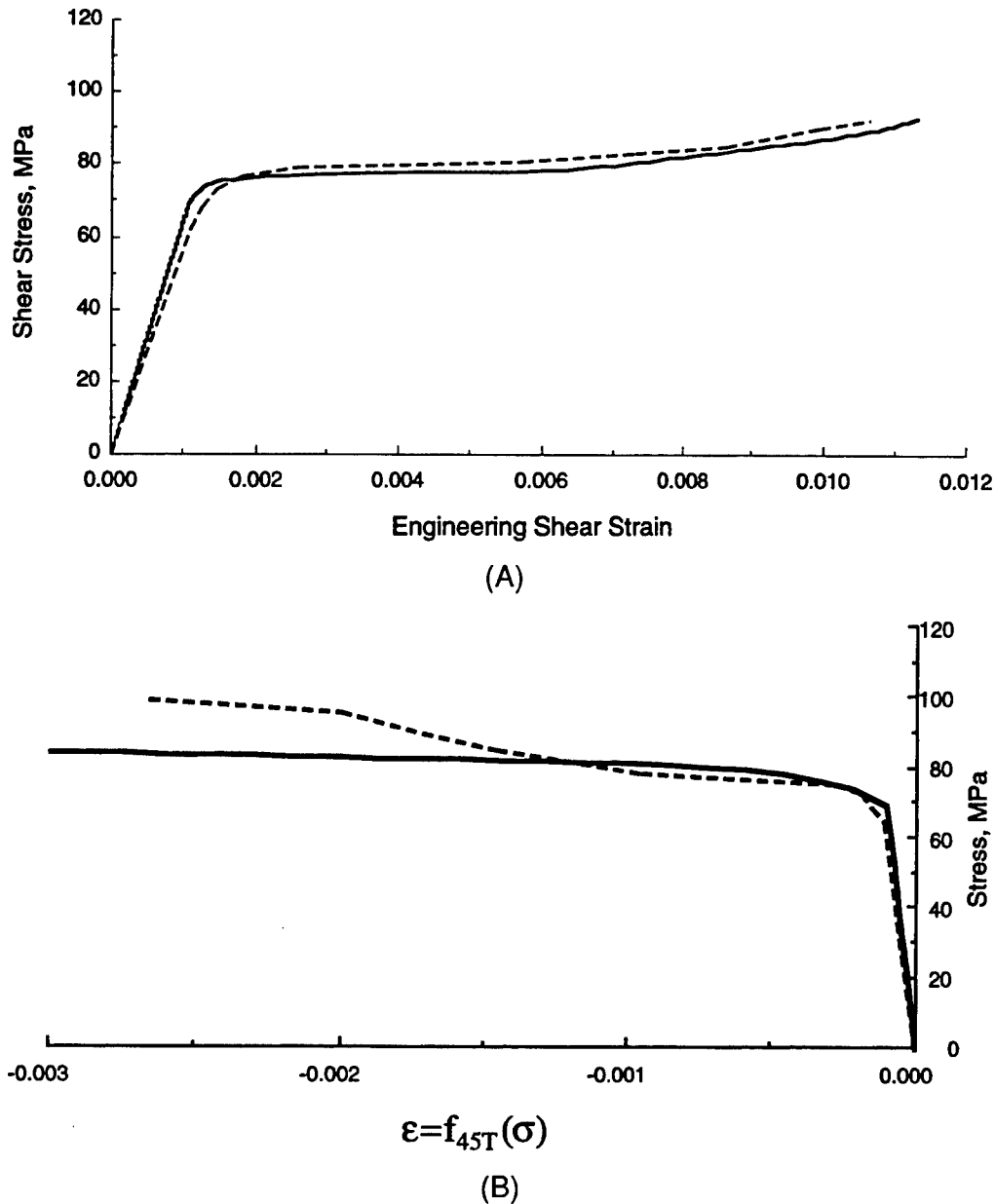


Fig. 3. Predictions for the response of the SiC/CAS crossply composite, compared to data from Cady¹ for (A) shear in the fiber axes and (B) strain transverse to a load applied at an angle of 45° to the fiber axes ((---) experiment and (—) prediction).

strains. Eight-noded quadratic elements have been selected for the analyses. Mesh studies have been conducted to ensure accuracy of the computed quantities.

Figures 4(A) and (B) show how the maximum stress concentration in the plate varies as the applied load increases. The point of maximum stress lies on the hole boundary at $(0, \pm R)$. In Figs. 4(A) and (B), this stress is normalized by the linear elastic stress concentration at $(0, \pm R)$. For the SiC/CAS crossply (which is isotropic in the elastic range) and the isotropic composites, this initial stress concentration, defined as the maximum stress divided by the mean stress across the ligament, is 2.5; for the C/C crossply, which is extremely anisotropic in the linear range, the initial stress concentration is 3.85. Solutions for these stress concentrations for the case of an infinite plate can be found in the literature by Green and Zerna.³⁷

The C/C composite is significantly weaker in tension at an angle of 45° to the fibers than it is in the fiber axes; consequently, matrix cracking is most pronounced on the boundary

of the hole, just behind the point $(0, \pm R)$, as illustrated in Fig. 4(A). As shear cracks develop in a fairly narrow band, leaving the majority of the material that is above the hole and over the ligament uncracked and linear elastic, the stress concentration at the hole increases as a result of the reduction in the tangential shear stiffness of the material directly behind the edge of the hole. Matrix cracking increases the overall compliance of the specimen; that is, it reduces the force increment required to further displace the upper boundary of the material above the hole. However, the cracking also causes the material to lose the shear stiffness necessary to distribute this force over the ligament and away from the hole boundary, and the end result is an increase in the stress concentration.

Despite the large shear concentrations, the C/C crossply will most likely begin to fail in tension, starting at the point $(0, R)$. Failure will occur in this fashion because the shear strain at every point throughout the domain is less than the shear strain that would cause failure in a shear test when the normal strain that would cause failure in a uniaxial tension test is exceeded.

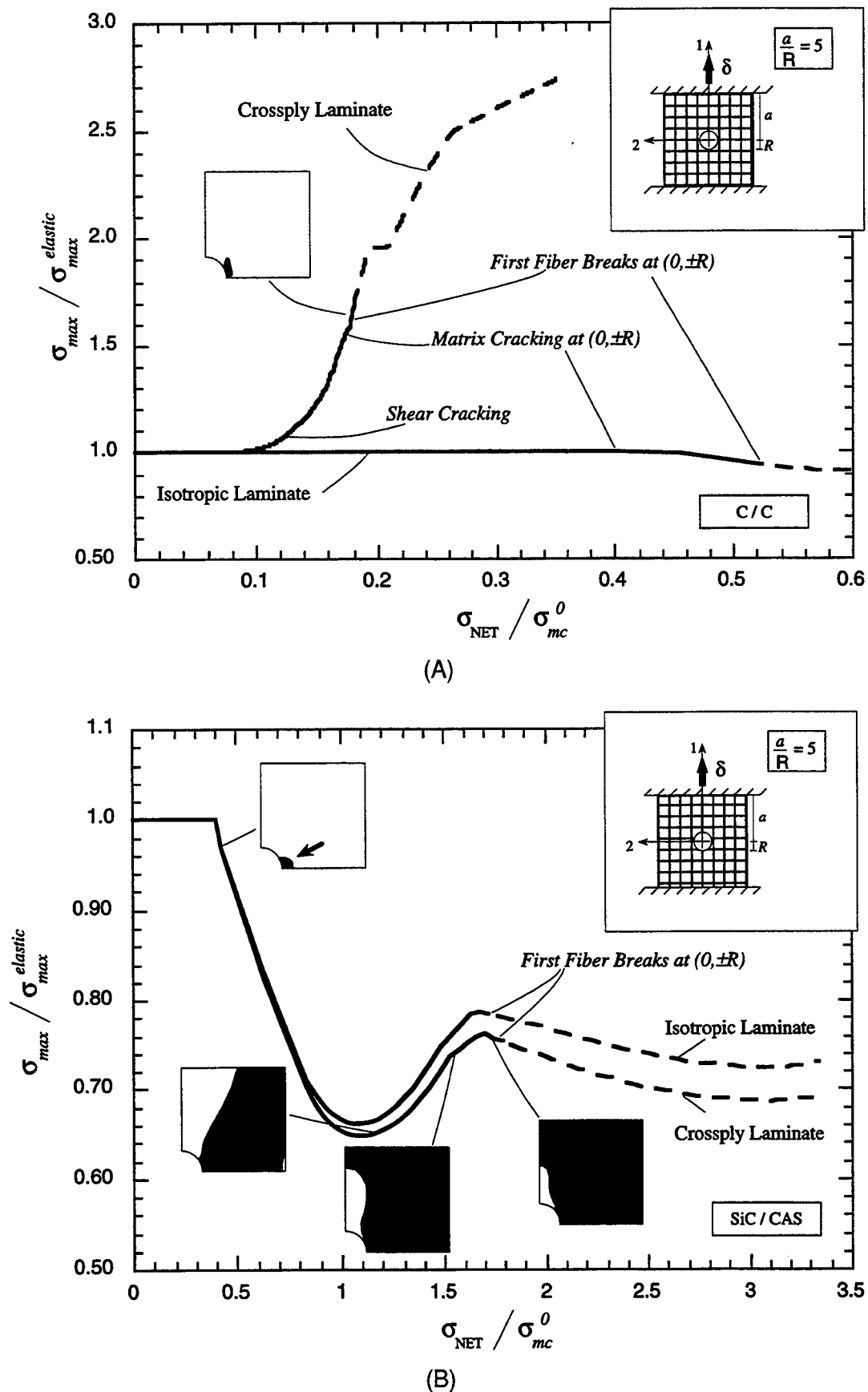


Fig. 4. Variation of stress concentration factor (SCF), $\sigma(0, \pm R) / \sigma_{\text{NET}}$, with respect to the net section stress, defined as the mean stress across the ligament for (A) C/C and (B) SiC/CAS composites. SCFs are normalized by the elastic SCFs (3.85 for the C/C crossply; 2.5 for the SiC/CAS crossply, which is isotropic in the elastic range). Shaded areas of the figures indicate the extent of matrix cracking in the specimens at specific loads.

The isotropic version of the C/C composite cracks first at the point (0,R). After a slight decrease in the stress concentration that is due to a small reduction in axial stiffness that occurs before the failure strain of the fibers is attained (cf. Fig. 2), the stress attains the value that would cause fiber failure in a uniaxial loading of the C/C crossply. The hypothetical isotropic version of this laminate can withstand a higher load than the crossply before fiber failure because of the substantially lower stress concentration. However, this does not necessarily imply that a quasi-isotropic composite is superior for this loading; a (0/±60) laminate, for example, would have a somewhat lower

ultimate stress than the crossply, which would have to be considered.

To accurately continue either of the above analyses beyond the point at which the first fiber fails, an analysis of the bridged, propagating crack would need to be performed. Nevertheless, to evaluate the impact of the decrease in axial stiffness on the stress concentration, the analysis is continued by extrapolating the input stress-strain data to the constitutive law as if no fiber failure had occurred. The dashed lines in Figs. 4(A) and (B) indicate that the small decrease in the stiffness of the material at the hole boundary that occurs just prior to the expected first

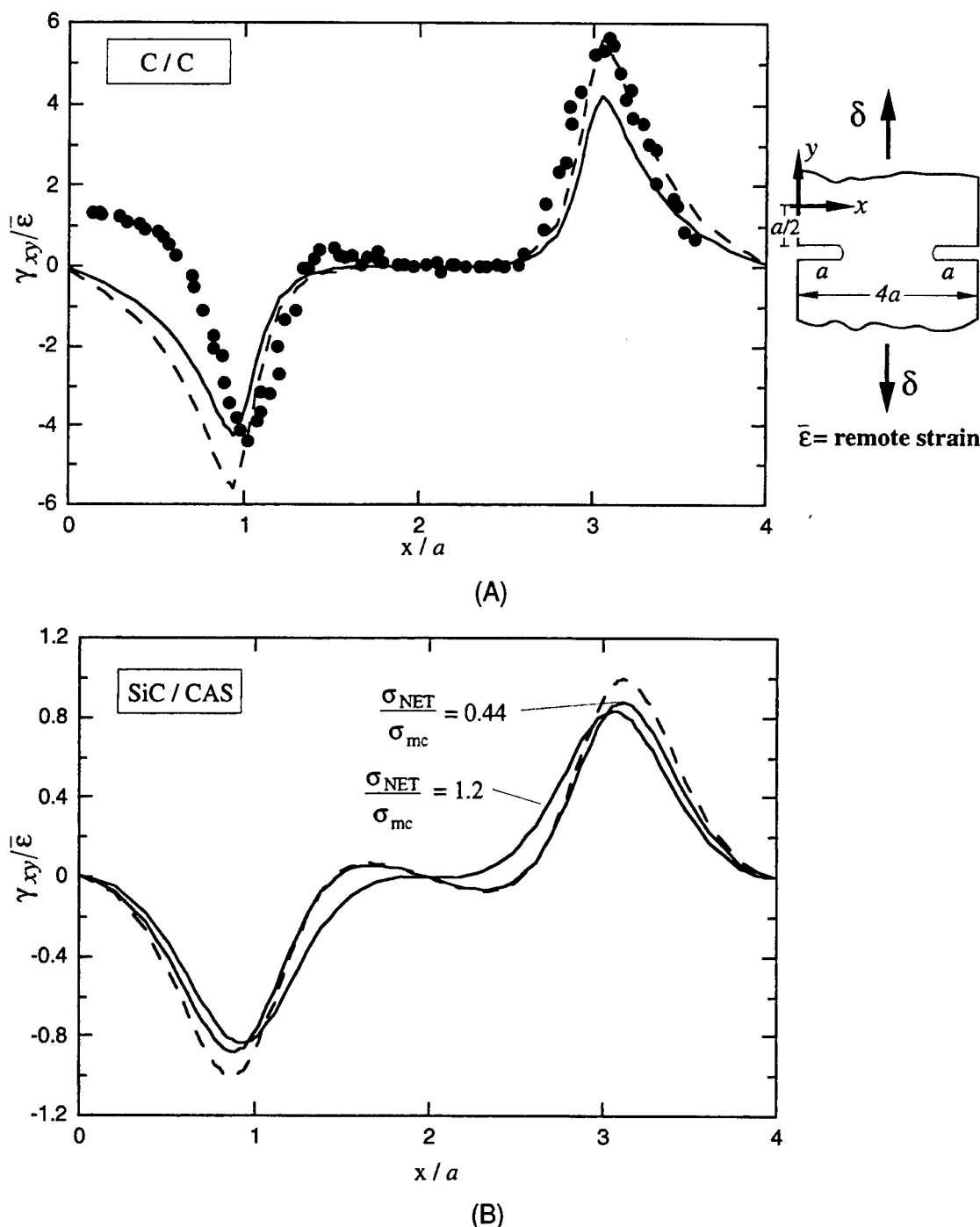


Fig. 5. Engineering shear strains ($\gamma = 2\epsilon_{12}$) along a line one-half notch length (i.e., $0.5a$) above the notches in double-edge-notched specimens constructed of (A) C/C (●) experiment (various loads), (---) elastic, and (—) $\sigma_{NET}/\sigma_{mc} = 0.1$ and (B) SiC/CAS (---) elastic. Experimental data plotted in Fig. 5(A) is from Evans.⁸

fiber failures, albeit an effective means of stress redistribution, is insufficient to reduce the stress concentration to beneath the linear elastic value for the C/C crossply.

The response of the SiC/CAS composite, whose matrix cracking strength at an angle of 45° to the fiber axes is comparable to its matrix cracking strength in the fiber axes (cf. Fig. 1), is shown in Fig. 4(B). For this material, matrix cracking first occurs on the hole boundary at the point $(0, R)$, and the stress concentration decreases steadily until matrix cracking extends from the hole boundary to the corners of the plate. The rate of increase of the stress concentration slows when the cracked region extends across the entire top of the plate, and the stress concentration then decreases slightly as cracks develop above the hole.

The curve corresponding to the isotropic version of the SiC/CAS laminate in Fig. 4(B) closely follows that of the crossply. Two conclusions can be drawn from this result. First, the tangent modulus of the material at the hole boundary is the most important parameter in the problem; any mechanism that can reduce the tangent modulus or extend the matrix cracking region of the uniaxial stress strain curve will contribute strongly to stress redistribution. Second, for crossplies that are isotropic in the linear range, the computationally more efficient isotropic material model provides an excellent approximation to the material behavior, assuming that the stress of interest in the body acts parallel to the fiber axes.

In all the cases considered, stressing is approximately proportional throughout the entire loading history (i.e., the relative

magnitudes of the stress components at each point are approximately independent of loading). This is essential if the nonlinear constitutive model introduced in this paper is to replicate material behavior accurately.

This simple example clearly shows the utility of the plane-stress analysis incorporating the nonlinear behavior of the material. In both cases, elastic stress concentrations are altered by the mechanism of matrix cracking, and the actual load at which failure may begin can be significantly higher or lower than that predicted by simple linear elastic analysis. The results show that, regardless of whether matrix cracking relieves or intensifies stress concentrations, a fair amount of cracking can occur locally at points of high stress within a component without destroying its integrity. The results emphasize the importance of inelastic straining in the direction of the fibers in redistributing stress.

(2) Double-Edge-Notched Specimens

A plate of a crossply brittle-matrix laminate with symmetric edge notches extending one quarter of the way across the section (notch length a) is loaded in tension, as shown in the inset of Fig. 5(A), and examined using the constitutive model for the same two composites that have been considered above. The loading is an applied displacement parallel to one set of fibers. This configuration closely replicates specimens for which experimental data has been obtained and which will be referenced below. The notch height is 3% of the specimen width and is very small compared to the height of the specimen. The notch tips are semicircular.

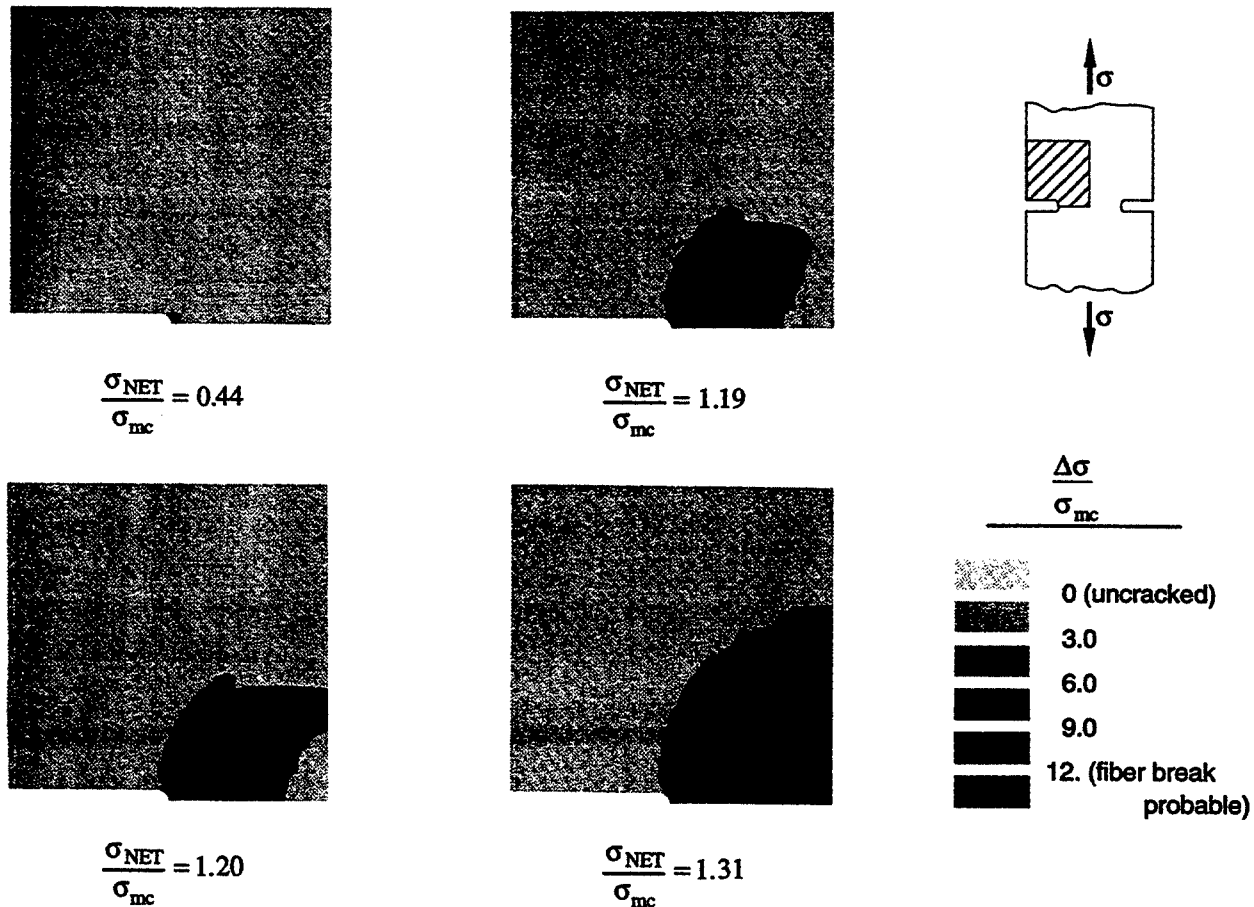


Fig. 6. Evolution of matrix cracking in a double-edge-notched SiC/CAS specimen loaded perpendicular to the notch plane. Outermost contour indicates the extent of the cracking region; inner contours indicate increased crack density. Extent of matrix cracking is described by the variable $\Delta\sigma$ (equal to $(1/\sigma_{mc})(\Delta\sigma_1^2 + \Delta\sigma_2^2)^{1/2}$), which is a normalized average of the stress deficits.

The boundary-value problems were again solved using the finite-element method. The solution procedure for the C/C specimen involved repeatedly stepping the applied displacement forward by a very small increment, iterating twice for the displacements within the domain, and proceeding to the next small displacement increment, regardless of whether equilibrium had been satisfied to within an acceptable tolerance. Convergence studies were conducted to ensure that the results presented here are independent of mesh size and displacement increment size. Convergence was attained with an analysis of 400 increments.

The solution for the SiC/CAS crossply was generated from the solution for a composite with a slightly stiffer 45° stress-strain curve. This solution served as the initial condition for each level of applied displacement.

Figures 5(A) and (B) show the engineering shear strain, γ_{xy} , normalized by the remote tensile strain, $\bar{\epsilon}$, away from the notched area, along a line one-half crack length above the notches for the SiC/CAS and the C/C composites. In each of Figs. 5(A) and (B), the dashed line corresponds to the shear strains from a linear elastic analysis, and the solid lines correspond to computed normalized shear strains at the values of the net section stress, σ_{NET} (equal to $P/(2a)$), indicated for loads P ranging up to the load at which fiber breakage is predicted to occur. P is calculated as part of the solution to the boundary-value problem.

Figure 5(A) contains the numerical predictions for the C/C system. Normalized shear strains are plotted for loads in the linear range and for the load at which fiber fracture is predicted

to begin. For the C/C composite, this occurs when the value of σ_{NET} is $\sim 10\%$ of the uniaxial matrix cracking stress, σ_{mc} . The shear-strain concentration is slightly reduced by matrix cracking but the straining remains almost proportional throughout the loading. This result is confirmed by experimental data reported by Evans,⁸ which is superimposed onto Fig. 5(A). The Evans data, which is for several loads up to and beyond the stress at which fiber breaking is predicted to begin, fall within the range of shear strains that are observed in the analysis. This experimentally verifies that the strains remain almost proportional and that the model provides a highly accurate prediction of the strain field.

The numerical results and the experimental data for the C/C composite indicate that shear strains are concentrated in sharp shear bands extending vertically just behind the notch tips, as will be more evident in a plot shown later. Note that the peak value of γ_{xy} is greater than $\bar{\epsilon}$ by a factor of >5 and is greater than the corresponding normalized strain level for the SiC/CAS composite in Fig. 5(B) by a factor of ~ 5 . This large difference is due to the strong anisotropy of the C/C material.

Figure 5(B) reveals that the shear-strain concentrations in the SiC/CAS specimen in the elastic range are much smaller than those in the C/C specimen, which is expected because of the almost isotropic elastic properties of the SiC/CAS laminate. Matrix cracking that occurs around the notch tip eases the shear-strain concentrations very slightly by the time the first fiber fails, at a net section stress of $\sim 130\%$ of the uniaxial matrix cracking stress. Despite this relatively small redistribution, the strains again remain almost proportional.

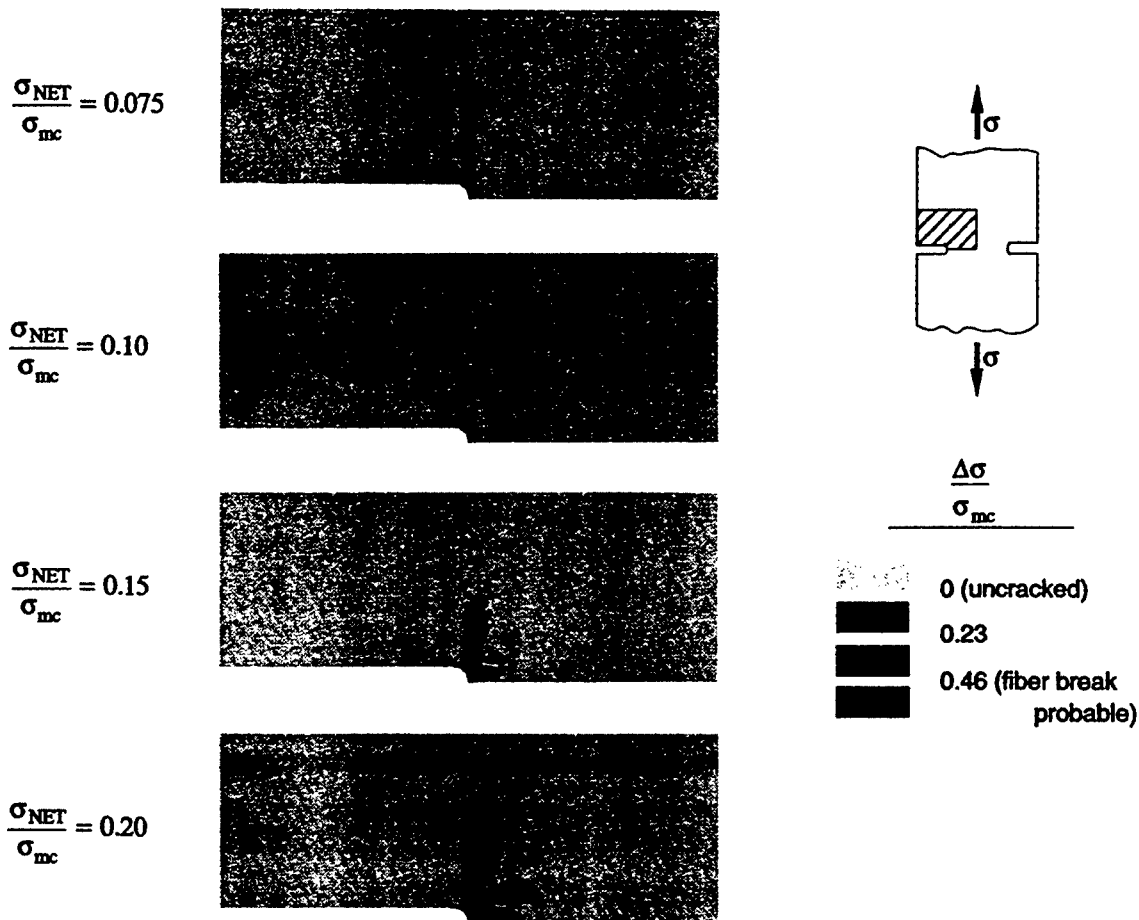


Fig. 7. Evolution of matrix cracking in a double-edge-notched C/C specimen loaded perpendicular to the notch plane. Outermost contour indicates the extent of the cracking region; inner contours indicate increased crack density. Extent of matrix cracking is described by the variable $\Delta\sigma$ (equal to $(1/\sigma_{mc})(\Delta\sigma_1^2 + \Delta\sigma_2^2)^{1/2}$), which is a normalized average of the stress deficits.

As in the case of a plate with a circular hole, cracking in the notched SiC/CAS specimen relieves stress concentrations, whereas cracking in the corresponding C/C specimen intensifies them. For the C/C specimen, the stress concentration, defined as the stress at the notch tip divided by the average stress across the ligament (σ_{NET}), is 10 for the elastic case, then increases to 14 at fiber failure. For the SiC/CAS specimen, the stress concentration decreases from the elastic value of 5.3 to ~ 2.5 at fiber failure.

The matrix cracking stress for an unnotched specimen of the C/C composite loaded parallel to one set of fibers is greater than that of the SiC/CAS composite by a factor of 4, and the stress at which fiber failure begins under such conditions is greater for the C/C composite by a factor of 1.25. However, because of the superior ability of the SiC/CAS composite to redistribute stresses through matrix cracking, the applied stress at which fiber failure is predicted to begin in the notched SiC/CAS specimen is higher than that predicted for the C/C composite. Stress redistribution due to matrix cracking more than doubles the load that is required to break fibers in the notched SiC/CAS specimen, relative to the load that is predicted based on the elastic stress concentration.

Figure 6 shows the development of matrix cracking in the SiC/CAS specimen. The contours are a normalized average of the principal stress deficits due to cracking: $\Delta\sigma \equiv (1/\sigma_{\text{mc}})(\Delta\sigma_1^2 + \Delta\sigma_2^2)^{1/2}$, where $\Delta\sigma_1$ and $\Delta\sigma_2$ are as defined in Eqs. (8a) and (8b), respectively. The outer contour, corresponding to where this quantity first becomes nonzero, depicts the extent of the region undergoing matrix cracking at a given load, and the inner contours indicate an increased crack density. The contour associated with the largest value of $\Delta\sigma$ shown indicates the stress decrease at which fiber failure would occur in a tensile test conducted at an angle of 45° to the fiber axes. Matrix cracks begin at the notch tips, then spread toward the center of the specimen. The first fiber failures are most likely to occur at the notch tips in the direction of the applied load.

Figure 7 shows the contours of maximum principal stress deficits that are predicted for the C/C composite. For this composite, cracking is initially concentrated in narrow shear bands above the notch tips, consistent with the behavior discussed earlier. A region of less-dense cracking develops along the ligament between the notches. For this specimen, fiber failure will most probably first occur on the notch boundaries, just behind the notch tips.

IV. Conclusions

Matrix cracking in brittle-matrix laminate composites can result in significant inelastic strain contributions, which, in turn, can lead to important stress redistribution at sites of high stress concentration. Matrix cracking can either ease or intensify stress concentrations. In this paper, a constitutive model has been presented that uses data from two uniaxial tests as input and is capable of predicting strains under proportional stressing for multiaxial plane-stress states. This model has been used to explore the effects of matrix cracking on stresses and strains in laminates containing holes and notches.

Acknowledgments: The authors are grateful to C. M. Cady, A. G. Evans, and F. E. Heredia for advice and assistance during the course of this research.

References

- ¹C. M. Cady; unpublished work.
- ²D. Beyerle, S. M. Spearing, and A. G. Evans, "Damage Mechanisms and the Mechanical Properties of a Laminated 0/90 Ceramic Matrix Composite," *J. Am. Ceram. Soc.*, **75**, 3321–30 (1992).
- ³B. Harris, F. A. Habib, and R. G. Cooke, "Matrix Cracking and the Mechanical Behaviour of SiC/CAS Composites," *Proc. R. Soc. London, A*, **437**, 109–31 (1992).
- ⁴M.-Y. He and J. W. Hutchinson, "Kinking of a Crack Out of an Interface," *J. Appl. Mech.*, **57**, 270–78 (1990).
- ⁵P. H. Geubelle and W. G. Knauss, "Crack Propagation at and near Bimaterial Interfaces: Linear Analysis," *J. Appl. Mech.*, **61**, 560–66 (1994).
- ⁶K. R. Turner, J. S. Speck, and A. G. Evans, "Mechanisms of Deformation and Failure in Carbon-Matrix Composites Subject to Tensile and Shear Loading," *J. Am. Ceram. Soc.*, **78**, 1841–48 (1995).
- ⁷F. E. Heredia; unpublished work.
- ⁸A. G. Evans; private communication.
- ⁹C. M. Cady, T. J. Mackin, and A. G. Evans, "Silicon Carbide/Calcium Aluminosilicate: A Notch-Insensitive Ceramic-Matrix Composite," *J. Am. Ceram. Soc.*, **78**, 77–82 (1995).
- ¹⁰T. J. Mackin, K. E. Perry, J. S. Epstein, C. Cady, and A. G. Evans, "Strain Fields and Damage around Notches in Ceramic-Matrix Composites," *J. Am. Ceram. Soc.*, **79**, 65–73 (1996).
- ¹¹C. M. Cady, K. E. Perry, and A. G. Evans, "Stress Redistribution around Mechanical Attachments in Ceramic-Matrix Composites," *Composites*, **26**, 683–90 (1995).
- ¹²A. G. Evans and F. W. Zok, "The Physics and Mechanics of Fibre-Reinforced Brittle Matrix Composites," *J. Mater. Sci.*, **29**, 3857–96 (1994).
- ¹³F. E. Heredia, S. M. Spearing, T. J. Mackin, M. Y. He, A. G. Evans, P. Mosher, and P. Brøndsted, "Notch Effects in Carbon Matrix Composites," *J. Am. Ceram. Soc.*, **77**, 2817–27 (1994).
- ¹⁴Z. C. Xia, R. R. Carr, and J. W. Hutchinson, "Transverse Cracking in Fibre-Reinforced Brittle Matrix, Cross-Ply Laminates," *Acta Metall. Mater.*, **41**, 2365–76 (1993).
- ¹⁵Z. C. Xia and J. W. Hutchinson, "Matrix Cracking of Cross-Ply Ceramic Composites," *Acta Metall. Mater.*, **42**, 1933–45 (1994).
- ¹⁶J. F. Wu, M. S. Shephard, G. J. Dvorak, and Y. A. Bahe-EI-Din, "A Material Model for the Finite Element Analysis of Metal Matrix Composites," *Compos. Sci. Technol.*, **35**, 347–66 (1989).
- ¹⁷N. Laws, G. J. Dvorak, and M. Hejazi, "Stiffness Changes in Unidirectional Composites Caused by Crack Systems," *Mech. Mater.*, **2**, 123–37 (1983).
- ¹⁸G. J. Dvorak, "Transformation Field Analysis of Inelastic Composite Materials," *Proc. R. Soc. London, A*, **437**, 311–27 (1992).
- ¹⁹T. C. Kennedy and M. Wang, "Three Dimensional, Nonlinear Viscoelastic Analysis of Laminated Composites," *J. Compos. Mater.*, **28**, 902–24 (1994).
- ²⁰G. J. Dvorak, Y. A. Bahe-EI-Din, and A. M. Wafa, "Implementation of Transformation Field Analysis for Inelastic Composite Materials," *Comput. Mech.*, **14**, 201–28 (1994).
- ²¹X. Aubard, J. Lamon, and O. Allix, "Model of the Nonlinear Mechanical Behavior of 2D SiC-SiC Chemical Vapor Infiltration Composites," *J. Am. Ceram. Soc.*, **77**, 2118–26 (1994).
- ²²F.-K. Chang and K.-Y. Chang, "A Progressive Damage Model for Laminated Composites," *J. Compos. Mater.*, **21**, 834–55 (1987).
- ²³D. Krajcinovic, "Damage Mechanics," *Mech. Mater.*, **8**, 117–97 (1989).
- ²⁴P. Ladeveze and E. Le Dantec, "Damage Modelling of the Elementary Ply for Laminated Composites," *Compos. Sci. Technol.*, **43**, 257–67 (1992).
- ²⁵A. Matzenmiller and J. Sackman, "On Damage Induced Anisotropy for Fiber Composites," *Damage Mech.*, **3**, 71–96 (1994).
- ²⁶D. R. Hayhurst, F. A. Leckie, and A. G. Evans, "Component Design-Based Model for Deformation and Rupture of Tough Fibre-Reinforced Ceramic Matrix Composites," *Proc. R. Soc. London, A*, **434**, 369–81 (1991).
- ²⁷R. Talreja, "A Continuum Mechanics Characterization of Damage in Composite Materials," *Proc. R. Soc. London, A*, **399**, 195–216 (1985).
- ²⁸R. Talreja, "Continuum Modeling of Damage in Ceramic Matrix Composites," *Mech. Mater.*, **12**, 165–80 (1991).
- ²⁹D. H. Allen, C. E. Harris, and S. E. Groves, "A Thermomechanical Constitutive Theory for Elastic Composites with Distributed Damage—I. Theoretical Development," *Int. J. Solids Struct.*, **23**, 1301–18 (1987).
- ³⁰P. H. Petit and M. E. Waddoups, "A Method of Predicting the Nonlinear Behavior of Laminated Composites," *J. Compos. Mater.*, **3**, 2–19 (1969).
- ³¹H. T. Hahn and S. W. Tsai, "Nonlinear Elastic Behavior of Unidirectional Composite Laminates," *J. Compos. Mater.*, **7**, 102–18 (1973).
- ³²H. T. Hahn, "Nonlinear Behavior of Laminated Composites," *J. Compos. Mater.*, **7**, 257–71 (1973).
- ³³Y. Suresh and A. Vautrin, "Plastic Behaviour of Fibrous Laminates," *Compos. Sci. Technol.*, **49**, 45–50 (1993).
- ³⁴F.-K. Chang, R. A. Scott, and G. S. Springer, "Failure Strength of Nonlinearly Elastic Composite Laminates Containing a Pin Loaded Hole," *J. Compos. Mater.*, **18**, 465–77 (1984).
- ³⁵S. M. Serabian and D. W. Oplinger, "An Experimental and Finite Element Investigation into the Mechanical Response of 0/90 Pin-Loaded Laminates," *J. Compos. Mater.*, **21**, 631–49 (1987).
- ³⁶H. Ho, J. Morton, and G. L. Farley, "Non-Linear Numerical Analysis of the Iosipescu Specimen for Composite Materials," *Compos. Sci. Technol.*, **50**, 355–65 (1994).
- ³⁷A. E. Green and W. Zerna, *Theoretical Elasticity*; pp. 350–51. Oxford University Press, London, U.K., 1968. □